FIRST PRINCIPLES STUDIES OF THE METAL-ORGANIC INTERFACE IN POROUS FRAMEWORKS

by

KHOA N. LE

A DISSERTATION

Presented to the Department of Chemistry and Biochemistry
and the Division of Graduate Studies of the University of Oregon
in partial fulfillment of the requirements
for the degree of
Doctor of Philosophy

September 2022

DISSERTATION APPROVAL PAGE

Student: Khoa N. Le

Title: First Principles Studies of The Metal-Organic Interface in Porous Frameworks

This dissertation has been accepted and approved in partial fulfillment of the requirements for the Doctor of Philosophy degree in the Department of Chemistry and Biochemistry by:

Shannon Boettcher	Chair
Christopher H. Hendon	Advisor
Julia Widom	Core Member
Christopher Wilson	Institutional Representative

and

Krista Chronister	Vice Provost for Graduate Studies

Original approval signatures are on file with the University of Oregon Division of Graduate Studies.

Degree awarded September 2022

© 2022 Khoa N. Le
All rights reserved.

DISSERTATION ABSTRACT

Khoa N. Le

Doctor of Philosophy

Department of Chemistry and Biochemistry

September 2022

Title: First Principles Studies of The Metal-Organic Interface in Porous Frameworks

Due to their generally poor conductivity, metal–organic frameworks (MOFs) have been limited in electrical applications. In this dissertation we explore structural deformation as a route to augmenting the electronic properties of these high surface area materials. We show that, under hydrostatic negative pressure, metallicity can be installed and we also elucidated the covalent characteristic of the metal-organic interface in 2D MOFs. Continuing our quest, we explore the deformation and phase change within 3D MOFs. Given the stability of metal-organic frameworks under numerous harsh conditions, bonding in MOFs has thought to be static. This project explores the metal-linker interface for a handful of carboxylate-based MOFs under various temperature conditions, which provides evident for dynamic bonding within these frameworks. Our insights to this phenomenon through the lens of density functional theory (DFT) combine with VT-DRIFT spectroscopy reveal specific vibrational modes coming from the carboxylate stretches that give rise to reversible metal-linker bonding within these materials. The metal-linker dynamics resemble the ubiquitous soft modes that trigger important phase transitions offering insights to several important events such as catalysis, negative thermal expansion, post-synthetic exchange that occurred in these frameworks. We applied the same methods onto Fe-based

porous frameworks and elucidated Fe metal centers possess properties such as spin-crossover transition, mixed-valency, and cooperativity which together enhance the material's transport properties. With these knowledges, we proposed a design principle of retroffitting 2D Fe-based MOFs into 3D analog to achieve highly conductive MOFs. This study contributes a fundamentally new perspective for the design of next-generation conductive metal–organic materials.

CURRICULUM VITAE

NAME OF AUTHOR: Khoa N. Le

GRADUATE AND UNDERGRADUATE SCHOOLS ATTENDED:

University of Oregon, Eugene, OR, USA
Western Washington University, Bellingham, WA, USA

DEGREES AWARDED:

Doctor of Philosophy, Physical and Computational Chemistry Division, 2022, University of Oregon
Master of Science, Physical and Computational Chemistry, 2021, University of Oregon
Bachelor of Science, Chemistry and Biochemistry, 2017, Western Washington University

AREAS OF SPECIAL INTEREST:

Computational Chemistry
Materials Chemistry
Physical Chemistry

PROFESSIONAL EXPERIENCE:

Research Assistant and Graduate Assistant, University of Oregon, Eugene, OR, USA
Pharmacist Assistant, Hoagland Pharmacy, Bellingham, WA, USA
Research Assistant, Western Washington University, Bellingham, WA, USA

GRANTS, AWARDS AND HONORS:

Renewable Energy Scholarship Foundation Award, 2021
Harvey E Lee Grad Scholarship Award, 2021

National Science Foundation - GRFP, 2020
Promising Scholar Scholarship Award, 2018
Scholar Week Selected Physical Chemistry Division Speaker, 2017
Scholar Week Science Excellent Poster Award, 2017
Oscar Edwin Olson Scholarship Award, 2016
Western Washington University Dean's List, 2011-2015
Bellingham Thomas Martina Horn Scholarship Award, 2011
BHS Class of '53 Scholarship Award, 2011
Academic Excellence Awards, 2011
AP Scholar with Honor Awards, 2011
Departmental Merit Awards, 2011
Champion of Diversity Candidate, 2010

PUBLICATIONS:

Kowalczyk, T.; **Le, K. N.**; Irle, S.; "Self-Consistent Optimization of Excited States within Density-Functional Tight-Binding," *J. Chem. Theory Comput*, **2016**

Le, K. N.; Hendon, C. H.; "Pressure-Induced Metallicity and Piezoreductive Transition of Metal-Centres in Conductive 2-Dimensional Metal–Organic Frameworks," *Phys. Chem. Chem. Phys.*, **2019**

Lee, S.-J.; Mancuso, J. L.; **Le, K. N.**; Malliakas, C. D.; Bae, Y.-S.; Hendon, C. H.; Islamoglu, T.; Farha, O. K.; "Time-Resolved in Situ Polymorphic Transformation from One 12-Connected Zr-MOF to Another," *ACS Mater. Lett*, **2020**

Mancuso, J. L.; Mroz, A. M.; **Le, K. N.**; Hendon, C. H.; "Electronic Structure Modeling of Metal–Organic Frameworks," *Chem. Rev.*, **2020**

Andreeva, A. B.; **Le, K. N.**; Chen, L.; Kellman, M. E.; Hendon, C. H.; Brozek, C. K.; "Soft Mode Metal-Linker Dynamics in Carboxylate MOFs Evidenced by Variable-Temperature Infrared Spectroscopy," *J. Am. Chem. Soc.*, **2020**

Szabo, R.; **Le, K. N.**; Kowalczyk, T.; "Multifactor Theoretical Modeling of Solar Thermal Fuels Built on Azobenzene and Norbornadiene Scaffolds," *Sustain. Energy Fuels*, **2021**

Le, K. N.; Mancuso, J. L.; Hendon, C. H.; "Electronic Challenges of Retrofitting 2D Electrically Conductive MOFs to Form 3D Conductive Lattices," *ACS Appl. Electron. Mater.*, **2021**

Andreeva, A. B.; **Le, K. N.**; Kadota, K.; Horike, S.; Hendon, C. H.; Brozek, C. K.; "Cooperativity and Metal–Linker Dynamics in Spin Crossover Framework Fe(1,2,3-Triazolate)2," *Chem. Mater.*, **2021**

McKenzie, J.; **Le, K. N.**;Bardgett, D. J.; Collins, K. A.; Ericson, T.; Wojnar, M. K.; Chouinard, J.; Golledge, S.; Cozzolino, A. F.; Johnson, D. C.; Hendon, C. H.; Brozek, C. K.; "Conductivity in Open-Framework Chalcogenides Tuned via Band Engineering and Redox Chemistry," *Chem. Mater.*, **2022**

Fabrizio, K.; **Le, K. N.**; Andreeva, A. B.; Hendon, C. H.; Brozek, C. K.; "Determining Optical Band Gaps of MOFs," *ACS Mater. Lett.*, **2022**

ACKNOWLEDGEMENTS

First and most importantly, I would like to thank my advisor **Dr. Christopher H. Hendon**. I appreciated all of your helps through the years, I honestly could not make it this far without your advice and your dedication. You're the reason I'm as successful as I am right now and I'm can't describe how much I appreciate your presence and guidance in life and in my academic career. Thank you so much Chris!

Next, I want to acknowledge and thank my committee members: **Dr. Shannon Boettcher**, **Dr. Julia Widom**, and **Dr. Christopher Wilson**. I dearly appreciate you guys advice and huge support through out my years at UO. This journey become so much easier and successful with you all serving as my mentors. Thank you so much! I also want to thank all of the professors I met at UO and all collaborators for your guidance and all the staffs member in the Chemistry Department for your kindness and helps every steps along the way.

I want to also acknowledge my bestest friend, **Alison Chang**, I don't know how to express my deep appreciation for you through words, but you are my rock since day one of the PhD and all of my accomplishments are there because of you both in life and in my academic career. I could not make it this far without your support. Thank you so much for being there for me through every up and down! You are much much and much appreciated!

I also want to thank **Lucas Gutterman**, my boyfriend for his encouragements and ambition for us as well as his supports through out my PhD. I appreciate the comfort you provided and your presence when I am not in the right mind, I also won't make it this far without you! Thank you so much!

I also want to thank my family members, especially **Minh N. Le**, my little sister for being there for me and my family when I'm not presence! Thanks sis!

I want to acknowledge my undergraduate advisor **Dr. Tim Kowalczyk** for his encouragements and his supports. He is the reason I made it into graduate school and I am very grateful for his presence in my life. I also want to acknowledge **Dr. Besty Raymond** and **Dr. Millie Johnson** for your guidance and being great role models. Thank you all of you guys for getting me where I am today!

Next, I want to thank many of my best friends and friends for their helps, their supports, and their advice. You guys are the best part of my PhD career and I am so happy I get to know all of you amazing people: **Austin Mroz**, **Jenna Mancuso**, **Joshua Davis**, **Emily McCracken**, **Marcella Buser**, **Elizabeth Radcliffe**, **Checkers Ray Marshall** (also for provided me this template), **Tekalign Debela**, **Robin Bumbaugh**, **Ashley Mapile**, **Nicole Morris**, and many more of you.

Lastly, I want to thank the **University of Oregon** and the **National Science Foundation** for provided me such great opportunity and a lovely community. This is one of the best journey in my academic career.

TABLE OF CONTENTS

Chapter Page

I. INTRODUCTION 1

1.1 A call for new material to address the energy crisis 1

1.2 Introducing Metal-Organic Frameworks 4

1.3 The disadvantages of 3D MOFs: poor electrical conductivity . . . 7

1.4 Conductive 2D MOFs: balancing between electrical conductivity and surface area 9

II. PRACTICAL GUIDE FOR MODELING POROUS FRAMEWORKS AND THE THEORY BEHIND COMPUTATIONAL CHEMISTRY 13

2.1 Density functional theory and electronic modeling 13

2.1.1 A short overview of QM/MM methods, Semi-empirical methods, and ab-initio methods 13

2.1.2 The Born-Oppenheimer approximation: separation of the electronic and the nuclear wavefunction 16

2.1.3 Density functional theory: replacing electronic particles with electron density 18

2.1.4 DFT functionals: LDA, GGA, meta-GGA, and hybrid exchange 20

2.2 Geometry Relaxation: Solid and Molecules 23

2.2.1 Electronic self-consistency and ionic iterations in an optimization calculation 23

2.2.2 Getting started: refining structure, setting up charge and multiplicity for condense phase calculation 24

2.2.3 Difficulty in obtaining the first ionic step convergence 30

Chapter Page

2.2.4 Local minimum and global minimum energy structure 31

2.2.5 Molecular Structure Optimization 32

2.3 Electronic Properties Modeling 33

2.3.1 An overview of band theory 33

2.3.2 EBS is plotted with k-vector in reciprocal space 34

2.3.3 Information to look for in EBS 36

2.3.4 Obtaining EBS and DOS 37

2.4 IR modeling with phonon calculations 38

2.4.1 Phonon calculation with finite difference method 38

2.4.2 Phonon calculation with density functional perturbation theory 39

2.4.3 Obtaining phonon modes and frequency using VASP 41

III. DYNAMIC BONDING OF THE METAL-LIGAND INTERFACE IN 3D MOFS 42

3.1 Examining metal-organic interface of 3D MOFs: Evidence of dynamic bonding in carboxylate-based MOFs. 42

3.1.1 An Overview of phase transition in MOFs: a case study of polymorphic transformation of a Zr-based MOF 42

3.1.2 Evidence of soft-mode in carboxylate-based MOFs 46

3.1.3 Dynamic bonding at the metal-linker interface and shallow potential energy surface allow phase transition in MOFs 49

3.1.4 Method 58

3.1.5 Conclusion 60

3.2 Dynamic bonding in non-carboxylated-based single-atom metal center: Fe-based versus others. 61

Chapter Page

3.2.1 Spin crossover transition as a unique property that only occur in $Fe(TA)_2$ in compare to the other analogs 61

3.2.2 Soft mode and its role in inducing spin crossover transition in $Fe(TA)_2$ 65

3.2.3 Another unique properties of Fe-based analog: cooperativity in MOFs 77

3.2.4 Method 81

3.2.5 Conclusion 82

3.3 Fe-based MOFs: Cooperativity differentiate MOFs from molecular solids 82

3.3.1 MOFs versus molecular solid analog 82

3.3.2 A closer look at how cooperativity in $Fe(TA)_2$ distinguishing the framework from similar molecular solid 85

3.3.3 Cooperativity's effect on the electronic properties of Fe-based MOFs 91

3.3.4 Method 93

3.3.5 Conclusion 95

IV. COVALENCY IN METAL-LIGAND INTERFACE IN 2D CONDUCTIVE MOFS 97

4.1 Evidence of Covalency in Metal-Linker Interface in 2D Conductive MOFs 97

4.1.1 The challenge of utilizing MOFs in electronic applications due to their ionic bonding characteristic 97

4.1.2 Pressure modulation as a way to probe the metal-organic interface in MOFs 99

4.1.3 Unusual redox behavior as evidence of covalency in metal-organic interface 102

4.1.4 Method 106

4.1.5 Conclusion 108

Chapter Page

4.2 Sheet Orientation and Its Relative Effects on Electronic Properties . . . 109

4.2.1 A proposed pathway to increase conductivity in MOFs: 2D metallic MOFs into 3D metallic MOFs . . . 109

4.2.2 Challenges in investigating 2D MOFs: A closer look at layers orientation's effect on electronic properties and the material's porosity . . . 114

4.2.3 Retroffitting of $Ni_2(HIB)_3$ revealing the role of d-orbital occupancy in maintaining the metal-organic interface covalency . . . 117

4.2.4 Conclusion . . . 119

4.3 The Effects of Metal Identity: Fe-based centers enhance conductivity and transport properties in porous frameworks . . . 120

4.3.1 Selecting the appropriate metal for retrofitting: a case study using open-framework chalcogenides . . . 120

4.3.2 High conductivity in Fe-based frameworks: the role of mixed-valency and oxidation level . . . 129

4.3.3 A 3D metallic MOF: retrofitted $Fe_3(HIB)_2$ . . . 135

4.3.4 Method . . . 140

4.3.5 Conclusion . . . 142

V. CONCLUSION . . . 144

REFERENCES . . . 151

LIST OF FIGURES

Figure Page

1. Global temperature plot shows temperatures in 2020 were the hottest on record. Temperatures were about 1°C over a baseline of 1951–80 average temperatures, or about 1.25°C above preindustrial levels. Increase in global temperature since 1850 confirm by various science institutions. Reprint with permission from "Global temperatures in 2020 tied record highs". Copyright 2022 by The American Association for the Advancement of Science and Copyright Clearance Center. 2

2. Chronological improvements in the conversion efficiencies of concentrator MJ and MJ solar cells in comparison with those of crystalline Si, GaAs, CIGS, and perovskite single-junction solar cells. Adapted with permission from "Multi-junction solar cells paving the way for super high-efficiency". Copyright 2022 by AIP Publishing and Copyright Clearance Center. 3

3. Metal-organic frameworks is a diverse class of materials due to its distinctive building blocks. 5

4. Illustrations of possible charge transport pathways in porous materials (a) through-bond pathway (b) extended conjugation pathway (c) through-space pathway. 7

5. 3D structure of MOF-5 which exhibits large band gap due to the ionic nature of it's metal-organic interface. This perhaps arise from the orbitals orientation of the metal center versus that of the BDC linkers. 8

6. (a) Cu-BHT, a non-porous structure (b) $La_{1.5}$(HOTP) with low conductivity but permanent pores (c) Ni_3(HITP)$_2$ with decent conductivity and slipping structure. 10

7. Proposed design principles to modify 2D MOFs to enhance their conductivity and increase their surface area. 11

Figure Page

8. Available computational methods ranging from low cost QM/MM methods for larger systems to ab-initio methods for smaller systems with much higher accuracy. 14

9. Density functional theory uses electron density to reduce the many particles electronic reality into a single self-interaction electronic cloud. 19

10. Jacob's Ladder for the five generation of DFT functionals, a depiction of accuracy versus computational cost of functionals and some representative examples 21

11. The reduction of a conventional cell into a primitive cell can reduce the number of atoms by multiple magnitudes minimizes the computational cost. 26

12. Octahedral Fe metal centers can adopt 4 different charge-multiplicity configurations. 29

13. Large numbers of atoms in close proximity allow MOs to form continuous bands. (a) significant energy is required to excite an electrons in a single atom (b) less energy is required for electron excitation as the number of atoms increase (c) overlap permits electrons to freely move between orbitals and/or bands. Notice the two bands do cross in this example, which is not necessarily the case for all materials. 34

14. An example of the first Brillouin zone of a hexagonal cell and its high symmetry points in the reciprocal space. 35

15. Energy gap between the conduction band and the valence band in (a) an insulator where the gap is significant large (b) semi-conductor where the gap is narrow and (c) a metal where there is no gap allows electron to enter the conduction band freely. 37

16. Schematic reaction energy profile and structure of kinetic product EHU-30 and thermodynamic product UiO-66 (C, black; H, pink; O, red; Zr, green). Reprinted with permission from ACS Materials Lett. 2020, 2, 5, 499–504.[1] Copyright 2022 American Chemical Society. 43

17. Band edge diagram and theoretical density of states for EHU-30 and UiO-66 demonstrating a subtle difference in frontier band characteristics. A depiction of the bent and linear linkers is additionally presented to illustrate the strain energy stored in the BDC units of EHU-30. Reprinted with permission from ACS Materials Lett. 2020, 2, 5, 499–504.[1] Copyright 2022 American Chemical Society. 45

18. Molecular Orbital (MO) Description of MOF Metal-Carboxylate Interactions (A) Schematic representation of C–O and M–O coupled anharmonic oscillators in metal-carboxylate complexes. (B) MO diagram of carbonyl bond in a carboxylate group. Reprinted with permission from J. Am. Chem. Soc. 2020, 142, 45, 19291–19299.[2] Copyright 2022 American Chemical Society. 50

19. Variable-temperature diffuse reflectance infrared Fourier transform spectra (VT-DRIFTS) and computed phonon modes of HKUST-1. (A) (Top) Experimental spectra collected between 100 and 200 °C under dynamic vacuum. (Bottom) Simulated peak positions of phonon modes with carboxylate character denoted by color intensity and labeled according to modes shown in panel B. (B) Representation of "asymmetric" and (C) "symmetric" carboxylate-based phonon modes projected at the Γ q-point. Reprinted with permission from J. Am. Chem. Soc. 2020, 142, 45, 19291–19299.[2] Copyright 2022 American Chemical Society. 52

20. Global curve fittings for representative spectra of the HKUST-1 asymmetric carboxylate stretch. Spectral deconvolution assumed two components with constant peak maxima but variable total areas. Fits produced a species centered at 1596 cm^{-1} (blue) and another at 1587 cm^{-1} (red). Markers denote experimental data and solid lines show Gaussian fits. Reprinted with permission from J. Am. Chem. Soc. 2020, 142, 45, 19291–19299.[2] Copyright 2022 American Chemical Society. 53

21. Equilibrium between "Tight" and "Loose" Ensembles of MOF Metal-Carboxylate Populations Existing near Thermoneutral Equilibrium (Top) Conversion of MOF metal-linker bonds between two ensemble-averaged states. (Bottom) Temperature-dependent free energies (ΔG) and relative population according to equilibrium constants derived from experimental data. Reprinted with permission from J. Am. Chem. Soc. 2020, 142, 45, 19291–19299.[2] Copyright 2022 American Chemical Society. 55

22. HKUST-1 equation of state. The blue point is the computed equilibrium structure, but other similar energy structures are accessible (emphasized in the yellow gradient). Unlike MOF-5, HKUST-1 a less smooth energy profile near the equilibrium structure. We highlight another minimum energy structure (red), which could be the "loose" geometry. Regardless, the potential energy surface is shallow around the minimum. M-O bond elongates more rapidly than the C-O bond. Reprinted with permission from J. Am. Chem. Soc. 2020, 142, 45, 19291–19299.[2] Copyright 2022 American Chemical Society. 56

23. MOF-5 equation of state. The blue point denotes the computed equilibrium structure, but other similar energy structures are accessible (emphasized in the blue gradient). The potential energy surface is shallow around the minimum. M-O bond elongates more rapidly than the C-O bond. Reprinted with permission from J. Am. Chem. Soc. 2020, 142, 45, 19291–19299.[2] Copyright 2022 American Chemical Society. 57

24. Representation of the $Fe(TA)_2$ metal node (a) and pore structure (b). Reprinted with permission from Chem. Mater. 2021, 33, 21, 8534–8545.[3] Copyright 2022 American Chemical Society. 63

25. Representation of Bonding and Hysteresis Phenomena in Spin Crossover Behavior (a) Thermal-induced bond expansion and soft modes. (b) Magnetic hysteresis and abrupt transitions with depictions of elastic interactions between neighboring ions. Reprinted with permission from Chem. Mater. 2021, 33, 21, 8534–8545.[3] Copyright 2022 American Chemical Society. 65

Figure Page

26. VT-DRIFT spectra of $Fe(TA)_2$. (a) Spectra collected at 623 and 173 K of HS and LS phases, respectively. (b) Computed vibrational modes corresponding to frequency regions X, Y, and Z. (c) Baseline-subtracted VT spectra of mode X fitted to a Gaussian function. Reprinted with permission from Chem. Mater. 2021, 33, 21, 8534–8545.[3] Copyright 2022 American Chemical Society. 67

27. Peak maxima of vibrational mode "X" versus temperature. (a) Peak maxima collected during heating. (b) Peak maxima collected during cooling. Filled data correspond to $Fe(TA)_2$ in the LS state and hollow to the HS state, respectively. Reprinted with permission from Chem. Mater. 2021, 33, 21, 8534–8545.[3] Copyright 2022 American Chemical Society. 68

28. Equilibrium analysis of vibrational mode "X" in $Fe(TA)_2$. Data collected during a cooling cycle. (a) Baseline-subtracted spectra fitted to two species at fixed positions indicated by vertical dashed lines and (b) van't Hoff analysis of equilibrium constants K = [loose]/[tight] versus temperature. The values of [tight] and [loose] were determined from the relative integrated intensities of the high-frequency (blue) and low-frequency (red) species. Reprinted with permission from Chem. Mater. 2021, 33, 21, 8534–8545.[3] Copyright 2022 American Chemical Society. 70

29. VT-DRIFT spectra of $Co(TA)_2$, $Mn(TA)_2$, $Zn(TA)_2$, and $Cu(TA)_2$ and corresponding peak maxima of vibrational mode "X" in each material. Data were collected during cooling cycles unless indicated otherwise. Reprinted with permission from Chem. Mater. 2021, 33, 21, 8534–8545.[3] Copyright 2022 American Chemical Society. 72

30. Total energies of geometry-optimized structures versus metal–triazolate bond lengths of (a) $Mn(TA)_2$, $Co(TA)_2$, $Zn(TA)_2$, and (b) $Cu(TA)_2$. Filled circles correspond to ground-state structures. Reprinted with permission from Chem. Mater. 2021, 33, 21, 8534–8545.[3] Copyright 2022 American Chemical Society. 74

Figure Page

31. Total energies of geometry-optimized $Fe(TA)_2$ structures versus Fe–triazolate bond lengths. Calculations were performed at 0 K. Reprinted with permission from Chem. Mater. 2021, 33, 21, 8534–8545.[3] Copyright 2022 American Chemical Society. 76

32. Cooperativity (Γ) versus temperature for $Fe(TA)_2$. (a) Cooperativity calculated from the heating cycle magnetic susceptibility data. (b) Cooperativity determined from cooling cycle data. Reprinted with permission from Chem. Mater. 2021, 33, 21, 8534–8545.[3] Copyright 2022 American Chemical Society. Reprinted with permission from Chem. Mater. 2021, 33, 21, 8534–8545.[3] Copyright 2022 American Chemical Society. 78

33. Calculated electron density differences Δq for $Fe(TA)_2$ and $[Fe(ptz)_6][BF_4]_2$ between HS and LS states. (a) Electron density maps. (b) Comparison between absolute differences in electron densities in total and per atom. Reprinted with permission from Chem. Mater. 2021, 33, 21, 8534–8545.[3] Copyright 2022 American Chemical Society. 79

34. Pore structure and two types of metal-linker interface in $Fe(TA)_2$ (a). Representation of $[Fe(ptz)_6](BF_4)_2$ with one $[Fe(ptz)_6]_{2+}$ molecule highlighted in yellow (b). Potential energy diagram and molecular orbital diagram of low-spin and high-spin Fe^{2+} species during spin-crossover transition 84

35. Mulliken charge density plot of triazole and propyl-tetrazole linkers. . . 86

36. Potential energy surface of low-spin (blue) and high-spin (red) of $Fe(TA)_2$ extended solid (a) and $[Fe(ptz)_6]_{2+}$ molecular cluster (b). Filled circles indicate the energy of the optimised LS and HS structures used to create other structures. . . 87

37. Energy (black) and a lattice parameters (red) of $Fe(TA)_2$ and Fe-ptz in molecular solid form with increasing number of HS Fe2+ 89

38. Average Fe-N bond length change for Fe^{2+} coordination that undergone LS to HS transition and those that did not as the number of HS Fe^{2+} sites increase in the unit cell. 90

39. Electronic structure of $Fe(TA)_2$ with increasing number of HS Fe2+ 92

40. Changes in electronic structure of Fe-ptz as the number of HS Fe^{2+} sites increase. 92

41. A portion of (a) $Ni_3(HITP)_2$ and (b) $Ni_3(HIB)_2$. The oxidation state and one resonance depiction of each ligand is presented in (c and d), respectively. Atoms are depicted in C – black, N – blue, H – white, and Ni – madder. Reproduced from Phys. Chem. Chem. Phys., 2019,21, 25773-25778[4] with permission from the PCCP Owner Societies. 98

42. Electronic band structures and density of states plots for $Ni_3(HITP)_2$ under five representative hydrostatic pressures. Ni–N antibonding bands drop in energy upon lattice expansion, and are evident above the conduction band at 10 kB. The k-path from L-to-M (0.5,0,0.5-to-0.5,0,0) corresponds to the non-covalent direction and are flat because they are sampling perpendicular to the layer. M-to--to-K sample in the intraplane covalent vectors (0.5,0,0-to-0,0,0-to-0.33,0.33,0). $Ni_3(HITP)_2$ becomes metallic at low pressure. Reproduced from Phys. Chem. Chem. Phys., 2019,21, 25773-25778[4] with permission from the PCCP Owner Societies. 101

43. Electronic band structures and density of states plots for $Ni_3(HIB)_2$ under five representative hydrostatic pressures. LC = lattice constant. Ni–N antibonding bands drop below the Fermi level at 11 kB (LC = 1.10). The k-path from L-to-M (0.5,0,0.5-to-0.5,0,0) corresponds to the non-covalent direction and are flat because they are sampling perpendicular to the layer. M-to--to-K sample in the intraplane covalent vectors (0.5,0,0-to-0,0,0-to-0.33,0.33,0). $Ni_3(HIB)_2$ is persistently a metal at all pressures, and the Ni^{2+} is piezoreduced at 11 kB (LC = 1.10). Reproduced from Phys. Chem. Chem. Phys., 2019,21, 25773-25778[4] with permission from the PCCP Owner Societies. 102

44. A structural (a) and energetic (b) comparison of both $Ni_3(HITP)_2$ and $Ni_3(HIB)_2$ at various pressures. The inset graphs highlight the Ni^{2+} piezoreduction upon expansion of the $Ni_3(HIB)_2$ lattice. Reproduced from Phys. Chem. Chem. Phys., 2019,21, 25773-25778[4] with permission from the PCCP Owner Societies. 103

45. A structural (a) and energetic (b) comparison of both $Ni_3(HITP)_2$ and $Ni_3(HIB)_2$ as lattice constant changes. The inset graphs highlight the Ni^{2+} piezoreduction upon expansion of the $Ni_3(HIB)_2$ lattice. Reproduced from Phys. Chem. Chem. Phys., 2019,21, 25773-25778[4] with permission from the PCCP Owner Societies. 104

46. A structural comparison of both (a) $Ni_3(HITP)_2$ and (b) $Ni_3(HIB)_2$ at various external pressure. Reproduced from Phys. Chem. Chem. Phys., 2019,21, 25773-25778[4] with permission from the PCCP Owner Societies. 105

47. Electronic band structure and density of state of $Ni_3(HITP)_2$ (left) and $Ni_3(HIB)_2$ (right) computed by two different functionals: (a) HSE06 and (b) PBEsol for $Ni_3(HITP)_2$;(c) HSE06 and (d) PBEsol for $Ni_3(HIB)_2$. Reproduced from Phys. Chem. Chem. Phys., 2019,21, 25773-25778[4] with permission from the PCCP Owner Societies. 108

48. An out-of-plane vector (-Z) reveals metallicity in the electronic band structure of $Ni_3(HITP)_2$ (Cmcm space group). From the electron density projection, we can see that the electrons form inter-sheet bonding-type interactions (overlapping yellow lobes), giving rise to electronic delocalization. Reprinted with permission from ACS Appl. Electron. Mater. 2021, 3, 5, 2017–2023.[5] Copyright 2022 American Chemical Society. 110

49. $Ni_3(HIB)_2$ is a bulk metal, independent of sheet slipping. Yet, greater band dispersion for eclipsed stacking structure (a) in the out-of-plane direction (L–M) compared to that of the staggered counterpart (b) for $Ni_3(HIB)_2$. Reprinted with permission from ACS Appl. Electron. Mater. 2021, 3, 5, 2017–2023.[5] Copyright 2022 American Chemical Society. 114

50. (a) Relative energy of bulk structure of $Ni_3(HIB)_2$ in staggered (red) and eclipsed (blue) conformation compare to that of monolayer (gray). (b) Band structures of $Ni_3(HIB)_2$ in eclipsed conformation (first three panels) and $Ni_3(HIB)_2$ monolayer (gray). The interlayer spacings are show above the corresponding panels. Reprinted with permission from ACS Appl. Electron. Mater. 2021, 3, 5, 2017–2023.[5] Copyright 2022 American Chemical Society. 115

Figure Page

51. Effect of bridging linkers insertion on band structures of $Ni_3(HIB)_2$ frameworks: (a) pyrazine (purple), (b) DABCO (blue), and (c) bipyridine (green). The corresponding 3D structure is shown below each of the band structures and DOS. Reprinted with permission from ACS Appl. Electron. Mater. 2021, 3, 5, 2017–2023.[5] Copyright 2022 American Chemical Society. 117

52. Crystal structure of open-framework chalcogenides $TMA_2MGe_4Q_10$, TMA = tetramethyl ammonium, M = Mn, Fe, Co, Ni, Zn, Q = S or Se ($TMA_2MnGe_4S_{10}$ depicted). (a) Local coordination and (b) extended network representations with TMA cations omitted for clarity. Reprinted with permission from Chem. Mater. 2022, 34, 4, 1905–1920.[6] Copyright 2022 American Chemical Society. 122

53. Simulated band structures and pDOS states for as synthesized materials. Reprinted with permission from Chem. Mater. 2022, 34, 4, 1905–1920.[6] Copyright 2022 American Chemical Society. 123

54. Impact of Fe oxidation state on the simulated band structures and pDOS states for TMA_2FeGe_4S/Se_{10}. Reprinted with permission from Chem. Mater. 2022, 34, 4, 1905–1920.[6] Copyright 2022 American Chemical Society. 124

55. Impact of Fe oxidation state on the simulated band structures and pDOS states for TMA_2FeGe_4S/Se_{10}. Reprinted with permission from Chem. Mater. 2022, 34, 4, 1905–1920.[6] Copyright 2022 American Chemical Society. 125

56. Room-temperature Mössbauer spectrum of Fe–Se prepared in-air. Reprinted with permission from Chem. Mater. 2022, 34, 4, 1905–1920.[6] Copyright 2022 American Chemical Society. 127

57. Effect of synthetic preparation on the physical properties of Fe frameworks. (a) Summary of DC conductivities, (b) Mössbauer spectrum of Fe–S prepared in-air, (c) Mössbauer spectrum of Fe–S prepared air-free, (d) Mössbauer spectrum of Fe–Se prepared air-free, (e) diffuse reflectance UV–vis–NIR spectra of Fe–S, and (f) Fe–Se frameworks. Reprinted with permission from Chem. Mater. 2022, 34, 4, 1905–1920.[6] Copyright 2022 American Chemical Society. 128

Figure Page

58. Unit cell of $TMA_2FeGe_4S_{10}$ before (solid color) and after (faded) oxidation of Fe. Reprinted with permission from Chem. Mater. 2022, 34, 4, 1905–1920.[6] Copyright 2022 American Chemical Society. 130

59. Comparison of valence band dispersions of frameworks with different metal ions, chalcogenides, and oxidation states. Diagrams of valence bands with arbitrary energy offsets for clarity. Frameworks with divalent and trivalent metal ions were simulated with two and one TMA+ cations, respectively. Reprinted with permission from Chem. Mater. 2022, 34, 4, 1905–1920.[6] Copyright 2022 American Chemical Society. . . 131

60. Band structures of eclipsed $M_3(HIB)_2$ showing all materials are metallic and the band remain dispersive near the Fermi level for all metal identity. Reprinted with permission from ACS Appl. Electron. Mater. 2021, 3, 5, 2017–2023.[5] Copyright 2022 American Chemical Society. 136

61. (a) Effect of pyrazine insertion on the band structure of $Cr_3(HIB)_2$ and $Fe_3(HIB)_2$. (b) Charge density of a dispersive band that gave rise to out-of-plane metallicity in 2D eclipsed bulk $Cr_3(HIB)_2$ due to orbital overlap. (c) Charge density of dispersive band that gave rise to out-of-plane metallicity in $Cr_3(HIB)_2$(1,4-pyrazine)$_3$ due to covalent interaction in the axial direction. Reprinted with permission from ACS Appl. Electron. Mater. 2021, 3, 5, 2017–2023.[5] Copyright 2022 American Chemical Society. 138

62. Band structures of retrofitted Cr- and Fe-based MOFs. The highlighted paths from L-to-M and T-to-Y show the band dispersion correspond to the axial direction in real space. Reprinted with permission from ACS Appl. Electron. Mater. 2021, 3, 5, 2017–2023.[5] Copyright 2022 American Chemical Society. 139

63. Visualization of the acoustic modes associated with insufficiently tight convergence for phonon calculations. These modes are artificial, and are remedied by unimaginably expensive computations to achieve ¡10-8 eV energetic convergence. The modes shown above map to those highlighted in green in Table S1, Entry 1. The other modes highlighted in green appear similar to what is depicted here. Reprinted with permission from ACS Appl. Electron. Mater. 2021, 3, 5, 2017–2023.[5] Copyright 2022 American Chemical Society. 141

64. bulk $Ni_3(HIB)_2$ computed with various functionals. The GGA+U approach proved to flatten the out-of-plane vector (aligning with the previously reported band structure; J. Am. Chem. Soc., 2017, 139, 13608-13611). The HSE06 electronic band structure was computed from the PBEsol structure, and hence shows qualitatively similar features to the bulk PBEsol structure. The two U values were selected based on their applications to metals (U = 3 eV) and Ni^{2+} in its oxide (U=6.2 eV). Reprinted with permission from ACS Appl. Electron. Mater. 2021, 3, 5, 2017–2023.[5] Copyright 2022 American Chemical Society. 142

LIST OF TABLES

Table Page

1. Relative Energy of Formation for Bipyridine, Pyrazine, and DABCO Retrofitted into $M_3(HIB)_2$ Frameworks (Energies Are Presented in kcal/mol) 119

2. Imaginary frequencies for all MOF from phonon calculations using finite displacement method. Acoustic mode is highlighted in green. 119

3. Calculated relative percentage of each elements (M, Se/S, Ge) from pDOS at the VBM of MGe_4S/Se_{10} materials in vacuum and solvents where M is Mn, Fe, Co, Ni, Zn, Ge, Sn. 126

4. Optical Gap Energies (E_g) as Determined Experimentally from Tauc and Gaussian Plots Compared against Those from Simulated Band Diagrams 130

5. Computed bond lengths and bond orders of metal-ligand bond calculated using DDEC approach. The axial linkers are DABCO, 1,4-pyrazine, and 4,4'-bipyridine 137

CHAPTER I

INTRODUCTION

1.1 A call for new material to address the energy crisis

According to the Oregon Department of Forestry, the 2020 wildfires burned down hundreds of thousands of acres of forest land that forced approximately 40,000 Oregonians to flee their home. On top of that, many wildlife habitats were destroyed in the process killing thousands of organisms within the area. Wildfires are getting increasingly dangerous year after year directly correlated with global warming which is confirmed as a real thread by many science foundation.[7] The global temperature has increased by approximately 2 degrees since 1850 which is only 170 years ago (Figure 1). This increase in global temperature caused many abnormal geographic disasters and human survival on this planet is not guarantee at this rate of increase. Human activities have contributed greatly to global warming including our consumption of fossils fuels placing more greenhouse gasses in the atmosphere. The increase in fossil fuels consumption over the last couple decades is putting the world at risk. Energy consumption will only increase as human needs escalate and as technologies are getting more advanced. The fate of our world relies heavily on us as scientists to reduce fossil fuel consumption by making renewable energy sources more efficient and accessible. Given major effort in making renewable energy the most cheap and available source, the technology we owned at this time is no where near 100% efficiency. Some of the renewable technologies include wind turbines, hydro dams and solar panels all of which produce under 5% of our energy consumption. Both wind turbines and hydro dams are geography dependent meaning that they can only be build in certain area and usually are enormous structures whereas solar panels are much smaller and can

be install on-site (houses, building, garden, etc.). All of these technologies face major problem that prevent renewable energy to become the main source of our energy consumption. For site specific technologies such as wind turbines and hydro dams, improvements in battery technologies with lighter weight and higher storage capacity could reduce the transportation cost and reserve more energy produce on-site. For solar panels,improvements in batteries technology for similar reasons as above and an improvement in the solar panel itself on efficiency and life span could put this technology forward as a major energy sources.

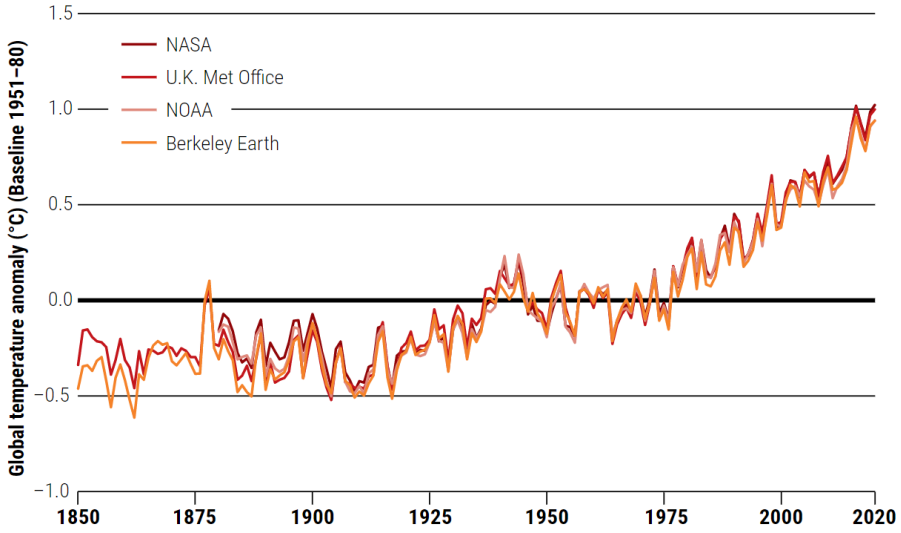

Figure 1. Global temperature plot shows temperatures in 2020 were the hottest on record. Temperatures were about 1°C over a baseline of 1951–80 average temperatures, or about 1.25°C above preindustrial levels. Increase in global temperature since 1850 confirm by various science institutions. Reprint with permission from "Global temperatures in 2020 tied record highs". Copyright 2022 by The American Association for the Advancement of Science and Copyright Clearance Center.

Given the benefits of converting photons to electricity with solar panels, there are still many issues we need to address such as devices' efficiency, reliability, cost, installation issues, panel lifetimes, etc. These issues prevent solar energy to be used at their maximum capacities and make them inaccessible to most people.

One of the major problem with solar panel is its efficiency. An increase in solar panel efficiency is a must in order for this technology to replace conventional non-renewable fuel meaning achieving higher power per unit cost. The issue lies within the ability of the panel to absorb sunlight at a wide range of wavelength and for that reason, single-junction cell can only achieve a maximum of about 31%[8] efficiency. Effort to increase this efficiency include producing multi-junctions solar cell, where multiple layers of materials that can absorb a wider range of wavelength (in compare to single-junction) are install into the same solar panel. Multi-junction solar cell can increase the efficiency of solar panel up to 68%[9,10] (with six junctions) which is comparable to hot carrier solar cell.[11]

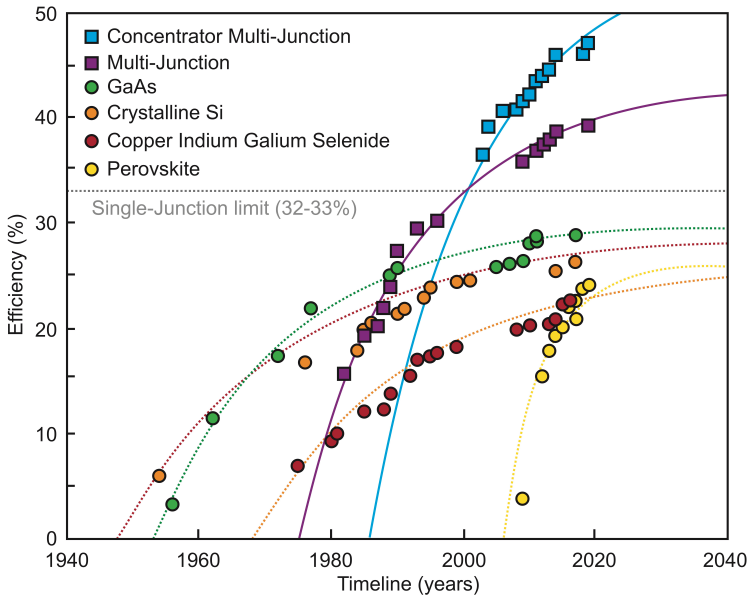

Figure 2. Chronological improvements in the conversion efficiencies of concentrator MJ and MJ solar cells in comparison with those of crystalline Si, GaAs, CIGS, and perovskite single-junction solar cells. Adapted with permission from "Multi-junction solar cells paving the way for super high-efficiency". Copyright 2022 by AIP Publishing and Copyright Clearance Center.

These are the highest percent of efficiency reported up until now, and it is not likely that we can achieve 100% efficiency given there will always be photon

that are outside of the absorb wavelength range and there are a maximum number of junctions that we can stack into a panel. Figure 2 shows the trajectory of various solar cell's efficiency by 2040 and it shows that we are approaching a plateau region in our advancement of solar panel efficiency. However, it it not necessary for us to reach 100% efficiency to replace fossil fuel consumption with renewable energy. Perhaps, we need to keep moving forward in the efficiency advancement of solar panel, but also stepping forward in storage technologies to both, reserve more energy from these renewable energy sources and ease the cost of transportation.

Given the disadvantages of renewable energy mentions above, science is one of the crucial keys to address these disadvantages. One of which involve designing new materials that are cheaper, bio-compatible, more efficient, non-toxic and have longer lifetime. Unfortunately, synthesizing and characterizing materials experimentally are intensive processes that require a great amount of money and times. Furthermore, due to the urgency of global warming, us scientists tend to rush these processes resulting in the lack of understanding of fundamental chemical process and chemical properties which are essential for materials designing. However, with the advancement of technology, we now can understand materials to the electronic level and testing theoretical system at lesser cost using computational chemistry. I believed that computational chemistry is a key for our breakthrough in material design especially for renewable energy technology. Hence, my interest as a chemist has always been elucidating key chemical properties and formulate design principal for solar technology materials using computational chemistry.

1.2 Introducing Metal-Organic Frameworks

In order to address the energy storage issue of all three renewable energy sources mentioned above, we need to design new materials. These new materials

need to satisfy two requirements that allow them to be good candidates for storage technologies. The first requirement is that they need to be conductive so charge transport can occur more readily for the charging and discharging processes.

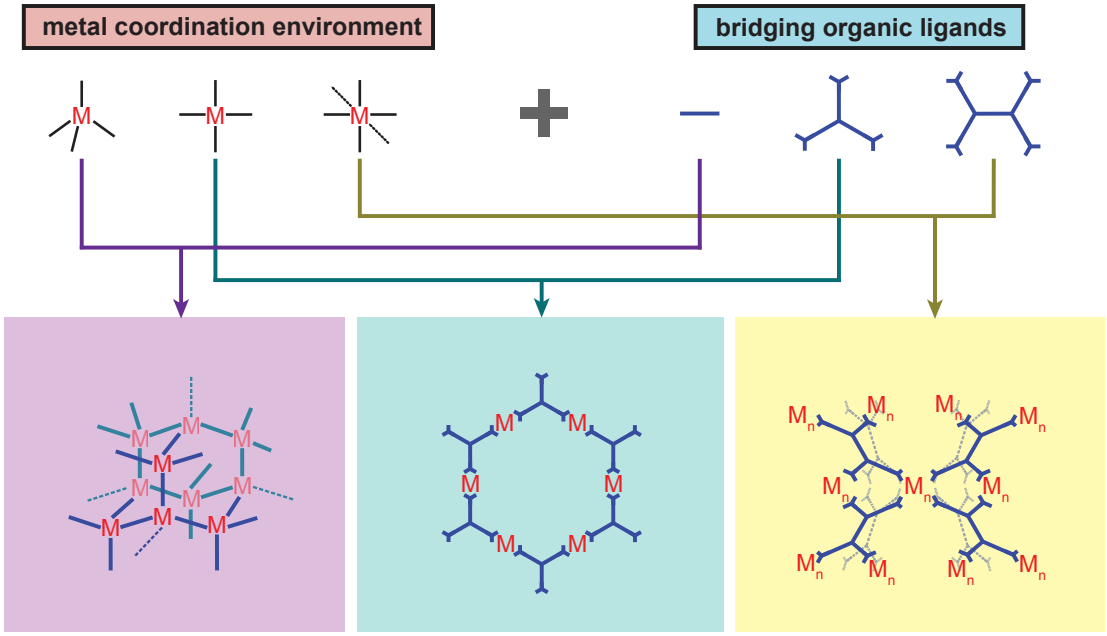

Figure 3. Metal-organic frameworks is a diverse class of materials due to its distinctive building blocks.

The second requirement is that they need to have high surface area. These materials if exist will be most likely use as electrodes in energy storage technologies, and a higher surface area will allow the devices to store more charge. A new class of material with surface area that reach a record in 2012 is metal-organic frameworks (MOFs).[12] MOFs are nano-porous materials that compose of metal components and organic components which serve as building blocks. The metal component are quite diverse ranging from single-metal ion or cluster of metal ions with oxo- or hydroxyl- bridging linkers. The metal ions typically adapt the square planar or octahedral coordination for most MOFs but they can also adapt other configuration such as tetrahedral coordination and others depend

on the metal identity. The organic components are usually linkers with various end group such as O, N, S, etc. that have strong affinity for binding to metal sites. Together, these building blocks can form thousands of different structures by combining different metal identity, different organic linkers, and different metal cluster topology (Figure 3); not to mention that divalent-metal and trivalent-metal are also possibilities.

MOFs can be classify into 3 categories depend on their formation topology: one-dimensional(1D), two-dimensional(2D), and three-dimensional(3D) MOFs. Although it's possible to construct a 1D MOF as a chain that is repeating units of organic linkers and metal ions, it is very unlikely that this type of MOFs is stable and exists in this 1D form in nature. For the purpose of this dissertation, we will only focus on 2D and 3D MOFs which are stable and have been use for various applications ranging from gas separation and storage,[13–16] catalysis,[17] drug delivery,[18,19] to energy-related applications such as light harvesting,[20] thermoelectrics,[21] and supercapacitors[22,23] and many more. The porous structure allows MOFs to be chemically active not only on the surface but also within the materials at the nano-scale which is not very common for other materials. On top of that, due to the rigid structure, MOF's metal clusters and organic linkers are chemically precise allows the ease of modification and elucidation of reaction mechanisms that involve these porous frameworks. Post-synthetic functionalization of the organic linkers is also possible which can change the optical and electronic properties of the MOFs allows precise control over the use of MOFs in applications. For instant, MIL-125, a Ti-based MOFs has shown to be a great candidate for catalysis, posesses a band gap of 3.6 eV.[24] This MOF can be functionalized with NH_2 and the band gap can be reduce to a smaller value, around 2.68 eV[25] which

allows the MOF to be a good photocatalyst.[26] Overall, MOFs are versatile, diverse, and possess incredible surface area making them the most promising candidates for their uses in energy storage technology. The issue lie within their poor charge transport ability.

1.3 The disadvantages of 3D MOFs: poor electrical conductivity

To understand why MOFs possess poor electrical conductivity, we must first discuss how charge transfer happen within a lattice. There are several transport pathways that can occur in a materials: the through-bond pathway, the extended conjugation pathway, and the through-space pathway (Figure 4).

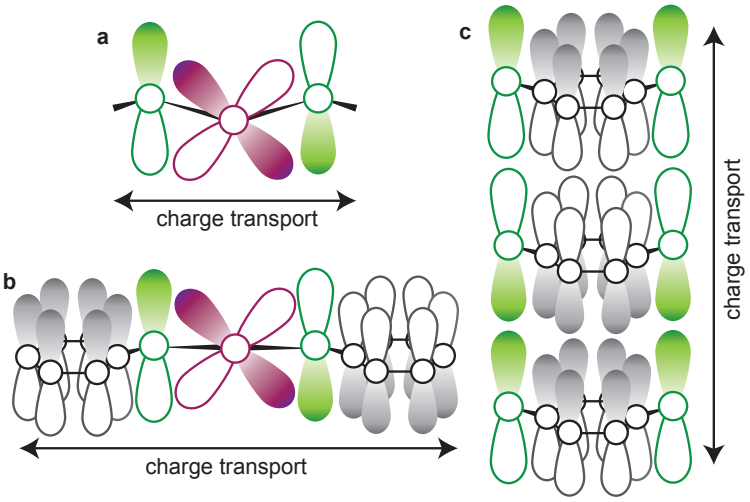

Figure 4. Illustrations of possible charge transport pathways in porous materials (a) through-bond pathway (b) extended conjugation pathway (c) through-space pathway.

The through-bond pathway is very self-explanatory where the overlap of orbitals through bonding interaction between adjacent atoms allow electron/hole to transfer from one site to the other. The extended conjugation pathway occurs when the conjugated orbital of the organic linkers aligns with the orbitals of the metal core forming a unified conjugation network within the same plane allows electrons

to travel between sites within the plane freely through these conjugation network. The through-space pathway occurs when there are overlap between orbitals of non-bonding sites, usually occur in 2D MOFs between the layers. The through-space pathway relies on non-bonding interaction such as $\pi - \pi$ interaction for electron to hop from one site to the other.

The most well-known 3D conductive MOFs is $Fe(TA)_2$ which has a conductivity of 0.3 S/cm in its mix-valence form and is the highest electrical conductivity that was ever reported for 3D MOFs.[27] As excited as this sounds, this conductivity is still super low compare to the conductivity of those materials that have been used in energy storage applications such as graphene with a conductivity above 1000 S/cm.

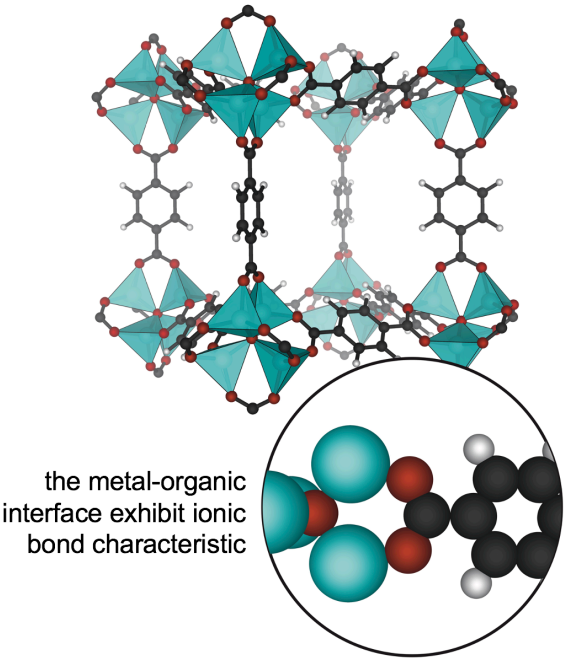

Figure 5. 3D structure of MOF-5 which exhibits large band gap due to the ionic nature of it's metal-organic interface. This perhaps arise from the orbitals orientation of the metal center versus that of the BDC linkers.

The high conductivity found in graphene is due to the amount of orbitals overlap within this materials where all, the extended conjugation pathway, through-space and through-bond pathways can occur. It is easy to elucidate why 3D MOFs have such poor conductivity just by observing the topology of the MOFs. Most 3D MOFs are not suit for the extended conjugation or the through-space pathways which means the only transport pathway that is possible in 3D MOFs is the through-bond pathway. Unfortunately, 3D MOFs exhibit ionic interaction between the metal component and the organic component; and as one should expect, for such ionic materials, charge transport is limited or non-existent (an example is shown in Figure 5). It is inconvenient that material with exceptional surface area as 3D MOFs exhibit such properties that prevent them to be the next generation of material that could be use for energy storage applications.

1.4 Conductive 2D MOFs: balancing between electrical conductivity and surface area

Fortunately, MOF does not only exist in its 3D from, but can also exist as a 2D framework. 2D MOFs is known to exhibit conductivity that is much larger compare to the 3D counterpart. Unlike 3D MOFs, 2D MOFs are somewhat similar to graphene in their topology where both the extended conjugation and the through-space transport pathways are possible. The overlapping between adjacent layers in 2D MOFs allow charge to transfer in the direction orthogonal to the layer and the nature of the metal-organic interface allows both the through-bond and the extended conjugation charge transport pathways to occur for certain MOFs which will be discuss in later chapters. For this reason, most 2D MOFs are metallic or semi-conductive with relatively small band gap and high transport mobility. There are a large number of 2D MOFs out there that are conductive each has its own

advantage and disadvantages. Since the majority of this dissertation is about 2D MOFs and the metal-organic interface covalency in such MOFs, we will discuss that in later chapter. Here, we will briefly discuss 3 family of 2D conductive MOFs.

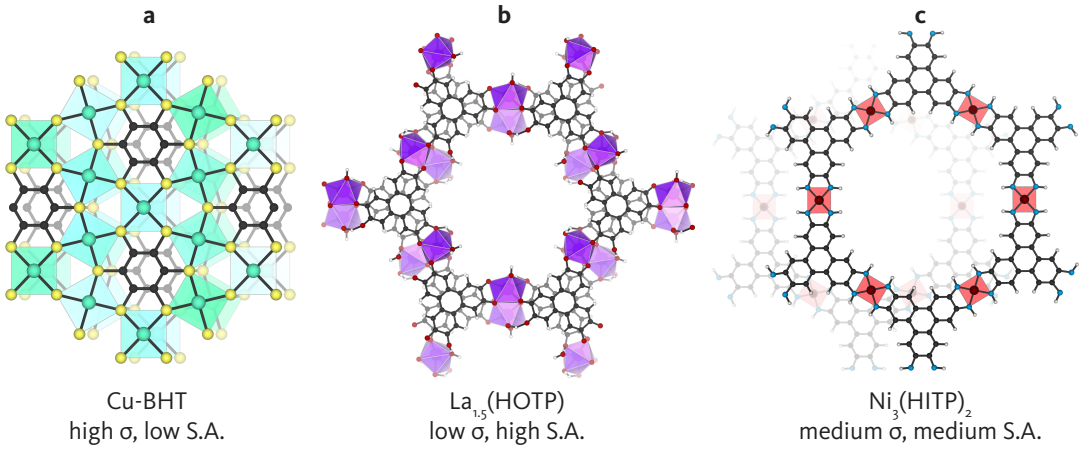

Figure 6. (a) Cu-BHT, a non-porous structure (b) $La_{1.5}$(HOTP) with low conductivity but permanent pores (c) $Ni_3(HITP)_2$ with decent conductivity and slipping structure.

The first 2D MOFs we will talk about is a metallic Cu-based MOF known as Cu-BHT constructs of single-metal ions as metal centers connect to benzenehexathiol (BHT) linkers to form square planar coordination spheres (Figure 6a). The MOF exhibits a conductivity of 1580 S/cm; and an electron/hole mobility of 116 $cm^2V^{-1}s^{-1}$/99 $cm^2V^{-1}s^{-1}$, respectively, which are relatively high for a MOF.[28]. This family of 2D MOFs has the metal ions and small organic linkers packed closely to one another to form a continuous sheet similar to that observed in graphene with no pore. This type of packing maximizes the overlap between orbitals within a layer and between the layers making the material highly conductive. However, this type of packing makes the structure non-porous reduces the surface area of the MOF which defeats the purpose of using MOFs for electronic application in the first place. In order words, it's more convenient to use

graphene instead of this family of MOFs since there is no additional benefit that this family of MOFs can provide and not to mention that graphene materials are much more lighter according to their composition. On the other extreme, a family of 2D MOFs that guarantees the reservation of the porous structure is a group of 2D MOFs that are synthesized using rare earth metals such as Ln and Nd centers (Figure 6b). With the complex coordination that form with Ln and Nd metals and the organic linkers, the metal centers in these 2D MOFs adapt a 3D topology and reserve the porous structure of the MOFs. This allows maximum overlap of orbitals between the layers supporting the through-space transport pathway. With that said, these 2D MOFs exhibit conductivity in the order of 10^{-2} S/cm? which is not feasible for electronic applications. Furthermore, rare earth metals are heavy which means energy storage devices produce using these materials will require more energy to transport which conflict with our intention. Even though this family of MOFs can reserve their porous structure, their poor conductivity and their weight make them inadequate candidates to replace conventional materials that have been use for electronic applications.

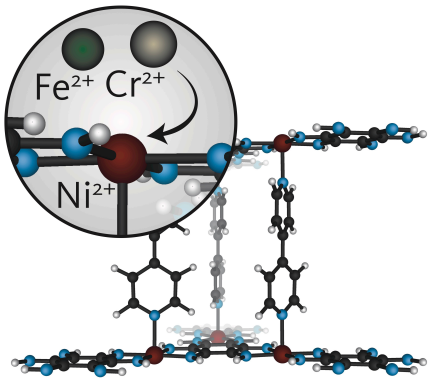

Figure 7. Proposed design principles to modify 2D MOFs to enhance their conductivity and increase their surface area.

The last family of 2D MOFs lies in the middle of the two extremes mentioned above, these are 2D MOFs that construct of single-metal ions, typically Ni or Cu, bind to chatecholates linkers. This family of MOFs was first synthesized by the Yaghi group back in 2012,[29] followed by the Dincă group's work on $Ni_3(HITP)_2$ in 2014 (Figure 6c).[30] $Ni_3(HITP)_2$ is known today as a 2D MOFs with highest conductivity in its family yet still has decent surface area. Unlike Cu-BHT where the porous structure is non-existent and rare earth metal-based MOF where the conductivity is unimpressive, $Ni_3(HITP)_2$ and 2D MOFs in this family exhibit reasonable conductivity and reasonable surface area. However, these "reasonable" properties are not enough for these 2D MOFs to be use in electronic applications. Therefore, in this dissertation, we will focus on innovate design principles to modify this family of 2D MOFs to both, increase their conductivity and surface area via retrofitting and metal-exchange through the lens of DFT (Figure 7).

CHAPTER II

PRACTICAL GUIDE FOR MODELING POROUS FRAMEWORKS AND THE THEORY BEHIND COMPUTATIONAL CHEMISTRY

2.1 Density functional theory and electronic modeling

2.1.1 A short overview of QM/MM methods, Semi-empirical methods, and ab-initio methods.

The used of computational is extremely valuable especially in materials discovery. Computational allows the elucidation of the newly synthesized materials at the electronic level, and at the same time could be used to propose and explore not yet synthesized materials.[31–33] However, computational has different meaning for different field of study, some could be done simply with one click of a button such as simple math with a calculator, others require more intensive machinery and years of theory development. Unfortunately, computational chemistry is on the expensive and complicated side, and the cost scales exponentially with the size of the target system.[34] Within the field of computational chemistry, there are many levels of theory that could be apply depend on the type of the chemical system and what properties one wants to obtain (Figure 8).[34] For large systems such as proteins, DNA, RNA, etc., classical methods, mostly known as molecular mechanic(MM) calculations are usually preferred.[35] These calculations can replicate the behavior of the systems under changing conditions. These types of calculations are usually applied to study large structure folding and thermodynamic parameters. For large system, one can get accurate information such as folding behavior, molecular geometry, heat of formation, dipole moment, etc. However, calculations of these larger systems are not suitable for detailed electronic elucidation because QM/MM calculations are approximations of forces and potential of larger scale quantities such as atoms

and clusters that usually neglect the smaller interactions that involve electrons. Atom or cluster of atoms are often represent as a single unit with a potential and charge that interact with other clusters of atoms with predetermined forces. Many assumptions is considered in a MM calculation therefore one needs to be careful on what type of potential one needs to use and how to balance between accuracy and computational cost. These calculations relies heavily on parameterization and simplification, therefore for material prediction that requires an accuracy to the electronic level, they are typically not very useful.

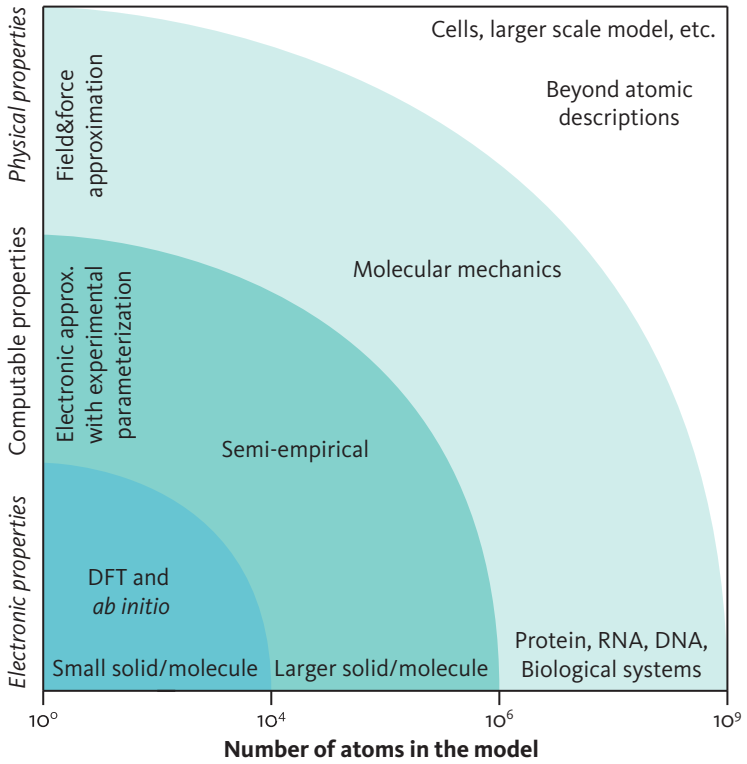

Figure 8. Available computational methods ranging from low cost QM/MM methods for larger systems to ab-initio methods for smaller systems with much higher accuracy.

A somewhat higher level of theory above classical methods are semi-empirical methods that are simplified versions of Hartree-Fock theory where

functionals are replace with parameters that derived from experimental data.[36,37] Unlike MM calculations as described above, most methods fall into this category involve solving heavy mathematical expressions similar to higher level of theory methods, however, the difficult parts of the expression is replaced with numbers in order to speed up the calculation. Most of these methods also rely on correction terms from first-order to third-order expansion to produce comparable data to experimental results. As one might expect, since these calculations depend on experimental parameterization, they are very system specific which means a method that works for a group of compounds might not be accurate for the others. Also notice that these semi-empirical methods are not reliable if they are used to predict the exact values of electronic properties, but they're often used for a general trend prediction amount a group of compounds/solids. Semi-empirical methods, similar to MM methods, can be use to predict properties such as the system lowest energy geometry, electronic band gap, excitation and relaxation energy, etc. with decent accuracy and lower computational cost, but for a smaller size systems, a higher level of method should be used to obtain more accurate and informative predictions. In material study, it is necessary to predict the exact electronic structure in order to elucidate key chemical features that gave rise to the materials' properties observed in experimental set up. Therefore, ab-initio methods are quite important in material study because with the correct choice of methods, one can predict the exact values of the target material properties and the results can be used to explain phenomenon observed in experimental results at the electronic level.[38] Here, we will discuss an ab-initio method called density functional theory (DFT)[39] which is widely used in computational materials chemistry, especially for porous frameworks such as MOFs. One should keep

in mind that the works done in this document do not require the development of quantum methods or implementation of theory into program packages, but rather, we used already available quantum computing packages to obtain electronic properties of materials. The formalism for all methods in this document will not be a detailed mathematical derivations, but rather simplified versions of the theories that was used to complete the works done in this dissertation. DFT has been widely use in solid-state physics since the 1970. DFT is a computational quantum mechanical modeling method that utilizes mathematical derivations and computer programming to study chemistry/materials science as well as biology and physics. DFT is used to elucidate electronic structure (especially the ground state) of many-body-particles systems, particularly molecular systems, and condensed phases. Despite the fact that DFT are consider accurate enough to predict the electronic properties of materials nowadays, there has been countless stepping stones in the development of the model.[40] However, due to the amount of approximations involve, DFT is still lack in its ability to account for inter-molecular interactions, charge transfer interaction, and other electronic properties.[41] The solutions to these problems involve modifying the functionals and/or including correction terms in the calculations in order to produce more accurate prediction of materials.

2.1.2 The Born-Oppenheimer approximation: separation of the electronic and the nuclear wavefunction. In order to understand the flaws of DFT and the developed adjustments, we first will explore the derivation and formalism behind DFT. One can view DFT as a modified version of other approximation that came before it, in particular, the **Born-Oppenheimer approximation (BOA)**.[42] BOA were developed by Max Born and J. Robert Oppenheimer in 1927. They proposed that due to the large differences between

the electronic masses and the masses of the nuclei, the nuclei will move at a much more slower speed compare to that of the electrons which allows us to separate the electronic wavefunction and the nuclear wavefunction while neglecting the cross terms to simplify the Schödinger equation for a many-body many-electrons problems. For instant, the full molecular Hamiltonian is written as:

$$\hat{H} = -\sum_{i=1}^{n}\left(\frac{\hbar^2}{2m_{e_i}}\nabla_{e_i}^2\right) - \sum_{I=1}^{N}\left(\frac{\hbar^2}{2m_{N_I}}\nabla_{N_I}^2\right) + \sum_{i<j}^{n}\left(\frac{e^2}{4\pi\varepsilon_0 r_{ij}}\right) + \sum_{I<J}^{N}\left(\frac{Z_I Z_J e^2}{4\pi\varepsilon_0 r_{IJ}}\right) - \sum_{I}^{N}\sum_{i}^{n}\left(\frac{Z_I e^2}{4\pi\varepsilon_0 r_{Ii}}\right) \tag{2.1}$$

where the first term describes the kinetic energy of the electrons, the second term describes the kinetic energy of the nuclei, the third term describes the repulsion energy between electrons, the forth term describes the repulsion energy between the nuclei, and the last term describes the attraction energy between the nuclei and electrons. Keep in mind that,

$$\nabla = \frac{\partial}{\partial x}i + \frac{\partial}{\partial y}j + \frac{\partial}{\partial z}k = \left(\frac{\partial}{\partial x}, \frac{\partial}{\partial y}, \frac{\partial}{\partial z}\right) \tag{2.2}$$

One can't solve a Schrödinger equation with this Hamiltonian, it is almost impossible for a many-body many-electron system even with the largest supercomputer that we could attain. BOA utilized the mass and velocity differences between the electrons and the nuclei to separate the terms that involve the nuclei from those that involve the electrons in the Hamiltonian which allows us to solve them independently. First, we solve the electronic Schrödinger equation where the nuclei are held fixed,

$$\hat{H}_e = -\sum_{i=1}^{n}\left(\frac{\hbar^2}{2m_{e_i}}\nabla_{e_i}^2\right) + \sum_{i<j}^{n}\left(\frac{e^2}{4\pi\varepsilon_0 r_{ij}}\right) - \sum_{I}^{N}\sum_{i}^{n}\left(\frac{Z_I e^2}{4\pi\varepsilon_0 r_{Ii}}\right) \tag{2.3}$$

where the nuclear variables in the third terms are treat as parameters, then we solve the nuclear Schrödinger equation,

$$\hat{H_n} = -\sum_{I=1}^{N}\left(\frac{\hbar^2}{2m_{N_I}}\nabla_{N_I}^2\right) + \sum_{I<J}^{N}\left(\frac{Z_I Z_J e^2}{4\pi\varepsilon_0 r_{IJ}}\right) \tag{2.4}$$

2.1.3 Density functional theory: replacing electronic particles with electron density. With this, BOA turns an impossible to solve equation to two smaller problems that can be solve independently in sequence. Branching off from this idea, DFT treats the nuclei of the targeted molecules/solid as stationary and the electronic state can be describe by a wavefunction that satisfy the many-electron time-independent Schödinger equation:

$$\hat{H}\Psi = E\Psi \tag{2.5}$$

where,

$$\hat{H} = \hat{T} + \hat{V} + \hat{U} \tag{2.6}$$

For an N-electron system, the kinetic energy is obtain using:

$$\hat{T} = \sum_{i=1}^{N}\left(-\frac{\hbar^2}{2m_i}\nabla_i^2\right) \tag{2.7}$$

The potential energy result from the external field due to the positively charged nuclei is obtain by:

$$\hat{V} = \sum_{i=1}^{N} V(\mathbf{r}_i) \tag{2.8}$$

Lastly, the electron-electron interaction energy can be obtain using:

$$\hat{U} = \sum_{i<j}^{N} U(\mathbf{r}_i, \mathbf{r}_j) \tag{2.9}$$

One of the way to solve this many-body Schödinger equation is by using the **Hartre-Fock method (HF)**.[43] For a many-body system, the HF method is an approximation for determining the wavefunction in the stationary phase. The HF method is the simplest method to approximate the wavefunction of the many-body system by a single Slater determinant, which is an expression that describes the wavefunction of a multi-fermionic system. Although there are many more post-HF methods that attempt to produce a more accurate depiction of the many-body system wavefunction with even more sophisticated expression, it is very unlikely for these methods to be used due to the computational cost given the simplest approximation (HF method) is already only affordable for medium size systems.

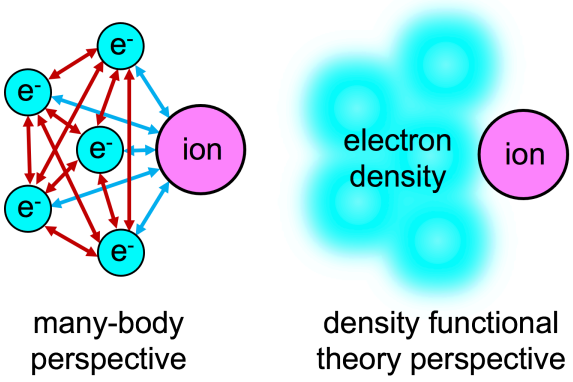

Figure 9. Density functional theory uses electron density to reduce the many particles electronic reality into a single self-interaction electronic cloud.

This is where DFT becomes a promising alternative. DFT is invented base on the concept that there is a one-to-one correspondence between the wavefunction of a molecule with multiple electrons and the electron density of that molecule. This allows us to turn away from the wavefunction approximation, and enables the determine of the system energy using electron density (Figure 9) where:

$$E_{DFT}[\rho] = T[\rho] + E_{ne}[\rho] + J[\rho] + E_{xc}[\rho] \tag{2.10}$$

where T is the electron kinetic energy, E_{ne} is the electron potential energy, J is the electron-electron repulsive energy (Coulombic), and E_{xc} is the electron-electron exchange-correlation energy. This then can be rewritten as:

$$E[\{\Psi_i\}] = -\frac{\hbar^2}{m_e}\sum_i \int \Psi_i^* \nabla^2 \Psi_i d^3r + \int V(\mathbf{r}) n(\mathbf{r}) d^3r + \frac{e^2}{2} \iint \frac{n(\mathbf{r}) n(\mathbf{r'})}{\mathbf{r} - \mathbf{r'}} d^3r d^3r' + E_{ion} + \int \rho \varepsilon_{xc}[\rho, \nabla\rho, \nabla^2\rho, \Psi, ...] dr \tag{2.11}$$

where there first 4 terms of the equation is known, and the last term corresponds to the exchange-correlation functional is an approximation that contain all quantum mechanical terms.

2.1.4 DFT functionals: LDA, GGA, meta-GGA, and hybrid

exchange. This term can be approximate with many different levels of theory including the local density approximation (LDA), the generalised gradient approximation (GGA), meta-GGA, and hybrid exchange, etc.[44] Each of these class of functionals has different level of accuracy and the more accurate functionals are more computationally expensive a.k.a including more mathematical terms (Figure 10). For instant, the LDA functional[45] is one of the simplest where the exchange-correlation energy can be estimate with:

$$E_{xc}[\rho] = \int \rho(\mathbf{r}) \varepsilon_{xc}(\rho(\mathbf{r})) dr \tag{2.12}$$

where $\varepsilon_{xc}(\rho)$ is a function of only the local value of the density. This also known as the zeroth order approximation where there is no gradient term that is included.

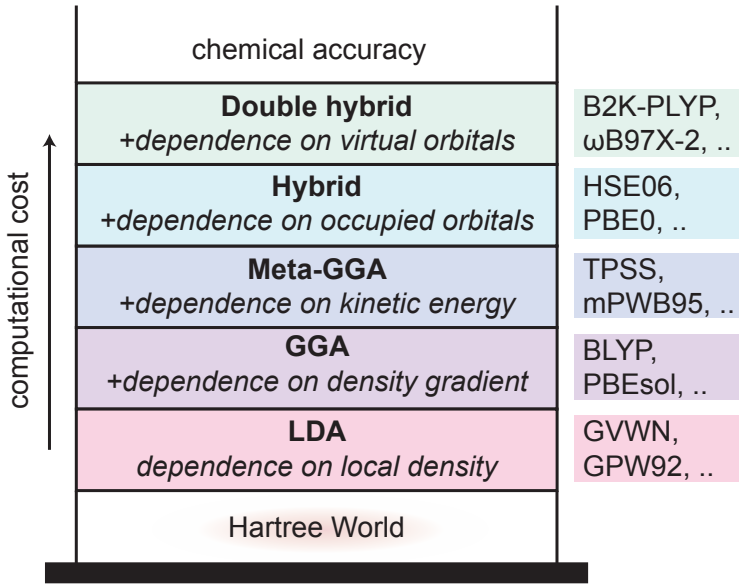

Figure 10. Jacob's Ladder for the five generation of DFT functionals, a depiction of accuracy versus computational cost of functionals and some representative examples

The next level of theory where the gradient is consider is the gradient expansion approximation (GEA)[46] which was found to have un-physical properties and so the GGA functionals[47] are those that contain the first order gradient terms with more reliable prediction power. With GGA, the density and its gradient are both responsible for the energy where the typical form adopted the follow formalism,

$$E_{xc}[\rho] = \int \rho(\mathbf{r})\varepsilon_{xc}(\rho, \nabla\rho)dr \tag{2.13}$$

As one would expect, GGA contains this gradient of the density matrix which improve the accuracy of this method by a significant amount in compare to LDA. This is the class of functional that has been used widely within the literature due to its decent prediction accuracy and its reasonable computational cost. The next level of theory is term the meta-GGA functionals[48,49] where the semi-local information in the Laplacian of the local kinetic energy density is explicitly

considered is taken the form,

$$E_{xc}[\rho] = \int \rho(\mathbf{r})\varepsilon_{xc}(\rho, |\nabla\rho|, \nabla^2\rho, \tau)dr \tag{2.14}$$

where τ is the kinetic energy density. This is a second order expansion of the GGA functionals. However, it has not been used widely in the literature especially for porous frameworks such as MOFs perhaps due to a higher computational cost compare to GGA with minimal improvement on the accuracy. The next level of theory is term the hybrid exchange functionals[50] a.k.a the hyper-GGA which has been used widely in the literature since the improvement of accuracy is quite impressive in compare to GGA especially when it come to predicting the electronic gap of porous materials. This class of exchange-correlation functionals is taking the form of,

$$E_{xc}[\rho] = \frac{1}{2}\int d\vec{\mathbf{r}}d\vec{\mathbf{r}}\text{'} \int_{\lambda=0}^{1} d\lambda \frac{\lambda e^2}{|\vec{\mathbf{r}} - \vec{\mathbf{r}}\text{'}|}[< \rho(\vec{\mathbf{r}})\rho(\vec{\mathbf{r}}\text{'}) >_{\rho,\lambda} - \rho(\vec{\mathbf{r}})\delta(\vec{\mathbf{r}} - \vec{\mathbf{r}}\text{'})] \tag{2.15}$$

where λ is the coupling constant and the expectation value is the density-density correlation function described by the effective potential V_{eff} computed at density $\rho(\mathbf{r})$. These hybrid functionals can sometimes predict the electronic properties to the exact values obtain from experimental, the two widely used hybrid functional out there are B3LYP[51] for molecular system and HSE06[52] for solid systems. One need to considered what type of properties they need to obtain from a calculation and the amount of resources they have for such computation, sometimes, one can get away with using the lower level functional like GGA and still obtain a reasonable result compare to experimental (an optimization calculation for example).

2.2 Geometry Relaxation: Solid and Molecules

Although computational chemistry is view as a tool to support experimental observations and to elucidate chemical properties at the microscopy level, computational chemistry required experimental evidence to validate its findings. Often, x-ray crystallography data of the target material is obtain from experimental, then the structure can be refined after using various characterization methods. The final structure obtained from these processes usually are distorted in topology and composition. A correct representation of the material can be obtain using computational chemistry through a process call geometry relaxation a.k.a. structural optimization. Structural relaxation allows one to obtain the lowest energy conformation of the structure indicating that the structure is stable. Only then, one can obtain accurate geometry information and electronic properties of the materials.

2.2.1 Electronic self-consistency and ionic iterations in an optimization calculation. In order to reach the lowest energy structure, an optimization calculation requires both, the electronic self-consistency (SCF) iteration and ionic iteration to be converged. There are usually many SCF steps that occur within an ionic step. It is important to understand that in order for each new ionic step to take place (where the atoms are display to obtain a new geometry), the electronic self-consistency iteration has to converge meaning the difference in energy between two adjacent SCF steps have to be smaller than a certain threshold. Every ionic step starts with an initial guess of the electronic wavefunction, this guess could be construct base on the information from the previous step or a random guess if this is the first ionic step. Then, the first SCF step takes-in this initial guess wavefunction along with a selected Hamiltonian

to solve the Schödinger equation to obtain a new set of orbitals (or electronic wavefunction). This newly obtain electronic wavefunction is then use along with the selected Hamiltonian to solve the Schödinger equation again, and this will repeat until the difference in energy is below a set threshold (satisfy the SCF convergence criterion). If the SCF convergence criterion is satisfied, then a new ionic step will start. For every ionic step, the SCF iteration should converge with a reasonable energy threshold (determine by the user). Similarly, there is also an energy threshold for the ionic iteration, and the structure is said to reach its lowest energy conformation when the difference of energy between two adjacent ionic steps is below a set threshold (also determine by the user). A common mistake that most beginner computational scientists make is they assume that the final geometry from their calculations is the lowest energy conformation without checking their convergence requirements. One need to make sure that both of these convergence criteria are met before moving on to calculate other properties.

2.2.2 Getting started: refining structure, setting up charge and multiplicity for condense phase calculation. Geometry relaxation can be performed using many different software packages depending on the system size and the license availability. In this chapter, we will focus on two software packages that has been used widely in the literature, VASP (Version 5.4.4)[53] for solid (with periodic boundary conditions) and Gaussian 09 for molecular system (gas phase or in the precense of a solvent). Both of these program packages required the user to own a license, one can also perform such geometry relaxation using other free program package such as CP2K,[54] Quantum Espresso, QChem, ORCA, etc. Before starting a calculation, one should determine what properties they want to obtain from their calculation to decide whether a solid calculation or a molecular

calculation is appropriate. Due to periodic boundary conditions, solid calculations are typically more computationally expensive, so if the target properties can be obtain without a solid calculation, in the case where the target molecular cluster/molecule's interaction with its surrounding are not significant to the study, then a gas phase calculation should be consider.

Solid State Calculation. *Obtaining the structure:* For a solid state calculation, one could obtain the structure from experimental crystallography data as the starting point, or one could find a structure in the literature (for MOF, one can obtain their structure from the online Computation-Ready Experimental Metal-Organic Framework (CoRE MOF) 2019 Dataset and other databases that are readily available). Rarely, if these resources are not suitable for such structure, the structure can be construct using the Materials Studio Program Package with sufficient information about the structure.

Pre-Submission. It is important to have a clean structure before starting your calculation to minimize the computational cost and prevent calculation errors. With solid structure, especially those obtained from x-ray crystallography, it is very likely that the structure is missing some hydrogen atoms or it contains extra hydrogen atoms due to experimental compensation. This usually happens because x-ray crystallography measure the scattering of the incident X-rays by the scatterers a.k.a. the electrons.[55] The heavier atoms will have higher electron density, so the diffraction of this will hinder those with lower electron density. For atom such as hydrogen where the number of electron is one, the diffraction effects from the hydrogen atoms in the pool of all heavier atoms are extremely hard to detect, hence structure obtain from X-ray diffraction methods are not sufficient at positioning hydrogen atoms. For this reason, it is necessary to check your structure

for extra hydrogen or missing hydrogen and adjust the structure accordingly. Other such as water molecules and solvents molecules also should be remove if their interaction with the solid is not what we want to capture in our calculation. Next, it is also necessary to minimize the computational cost by minimize the size of the system.

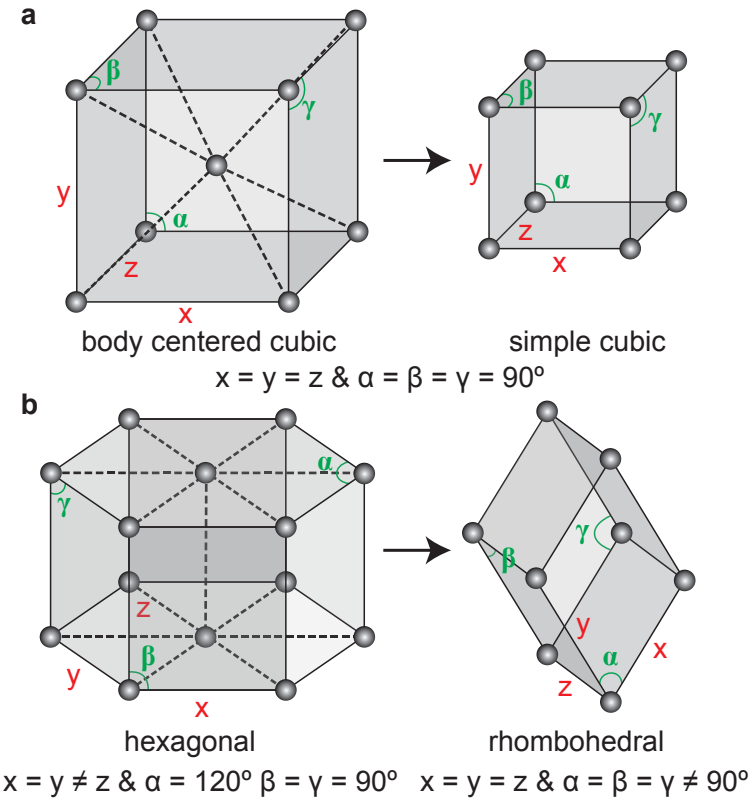

Figure 11. The reduction of a conventional cell into a primitive cell can reduce the number of atoms by multiple magnitudes minimizes the computational cost.

Very often, the the structure provided by experimentalists or those posted on the online database are in the format of a conventional cell (which may or may not be a primitive cell) that might contain additional lattice points. The conventional cell is a unit cell with the full symmetry of the lattice but is not the smallest unit cell. In this case, one should consider reducing their conventional

cell to a primitive cell which is the smallest possible unit cell that contains lattice points only at each of its eight vertices (Figure 11). This cell reduction (can be done via Materials Studio) could reduce the computational cost by multiple orders of magnitude depend on the unit cell. This has been found to be helpful in term of structural relaxation calculation, however, one can keep the conventional cell if the primitive cell is difficult to modify or one is running calculation such as defect and catalytic modeling where a bigger cell is more appropriate.

Charge and multiplicity. It is quite important to figure out the charge and multiplicity of the system before running the calculation. One of the main cause of distorted structure geometry and non-converged structure is from inputting the wrong charge and multiplicity for the system. The type interaction of the atoms within the structure depend directly on the charge density of each specie in the system, if the charge provided are incorrect, the final geometry will contain unreliable geometry (unrealistic bond length, bond angle, bond order, etc.). For instance, in a MIL-125 system, if an incorrect charge were provide for the unit cell, forcing a Ti^{4+} to be a Ti^{3+}, which makes the Ti atom less electronegative, one would expect the bond order of the metal-organic linker interface to decrease, lengthening the bond length of this interface, this might cause the structure to expanse, result in incorrect structure geometry prediction and false electronic behavior. A way to calculate the charge of the unit cell is to count the number of atoms in the cell and total the number of charge carry by the atoms. For instance, a primitive unit cell of MIL-125 contains 8 Ti atoms, 48 C atoms, 36 O atoms, and 28 H atoms. Using the number of C atoms, we find that there are 6 BDC(benzenedicarboxylic) linkers in the unit cell each have 8 C atoms, 4 O atoms and 4 H atoms. This left 12 extra O atoms and 4 extra H atoms to form oxo- and

hydroxyl-bridging linkers. Ti atoms is commonly know to have a charge of +4, and BDC linker has two deprotonation sites making it carries a charge of -2, each oxygen carries a charge of -2 and each hydrogen carries a charge of +1. This can be sum up as Ti_8^{4+} with total charge of +32, BDC_6^{2-} with total charge of -12, O_{12}^{2-} with total charge of -24, and H_4^{1+} with total charge of +4. Adding the total charge give us a net charge of 0 for this unit cell. For a VASP calculation, this is a perfect unit cell since no modification is need to account for a net charge of 0. However, let assume we want to ran a calculation of MIL-125 unit cell where we add 2 extra H^{1+} into the unit cell, then we have to let the program know that this new unit cell has a charge of +2. Unlike other packages, VASP do not allow user to input the charge associated with the unit cell, instead, the calculation will run assuming the unit cell is neutral. To create a charged cell, we need to first run a VASP calculation with no initial charge condition to get the total number of electrons (this should be a quick calculation by setting the SCF step equal to 0). For a unit cell with a +2 charge, we simply subtract two electrons from the total number of electrons of the unit cell and set that as a condition for the optimization. It is also very important to check the multiplicity of your system before running the calculation as this also have an effect of the geometry and the electronic structure of the materials. For instance, for $Fe(TA)_2$, Fe^{2+} has 6 electrons in its valence cell, and in an octahedral coordination environment, these electrons could adopt the low-spin configuration with a total spin of 0 or they could adopt the high-spin configuration with a spin of 4 (see Figure 12). The low-spin configuration will have all the electrons reside in the three t2g orbitals leaving the e_g orbitals empty while the high-spin configuration will have 2 electrons occupy the two e_g orbitals which have higher energy. The high-spin configuration requires the electrons in the lower energy

orbitals (more stable) to occupy a higher energy orbitals, as one could imagine, this raise the energy of the whole system and perhaps decrease the bond order of the system, causing the materials to adopt a different configuration than the low-spin counterpart. Therefore, before submit the calculation, one needs to determine if the materials is high-spin or low-spin and predetermine the spin moment of the system to get the geometry to optimize correctly. In VASP calculation, it's almost always safe to run the calculation as spin-polarized to see what type of spin configuration is prefer at the lowest energy geometry and VASP usually get this correct (align with experimental). However, in other cases, one can run the calculation as a closed-shell system if there are strong experimental evident that the system in fact is closed-shell or the structure is too large for a spin-polarized calculation (where the closed-shell configuration is not against experimental evident). For solids that contained Cu atoms, where antiferromagnetic and ferromagnetic configuration are both possible, one needs to consider trying multiple spin configurations combine with experimental magnetic data to figure out what make the most sense for such materials.

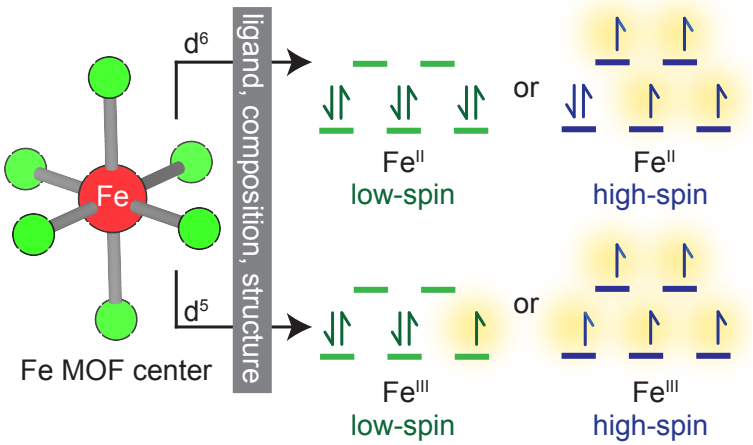

Figure 12. Octahedral Fe metal centers can adopt 4 different charge-multiplicity configurations.

2.2.3 Difficulty in obtaining the first ionic step convergence.

Very often, the first calculation on a new materials or a freshly-clean structure will not go as plan. One might find that the calculations will not get pass the first ionic step where the electronic SCF can reach over 500 iterations. This mean that the first initial guess electronic wavefunction (from the provided initial geometry) is not a reasonable guess that lead to more unreasonable guesses at every iterations. The calculations might goes on until the maximum SCF iterations is reach and the output geometry from this calculation can be fragmented or distorted. For this reason, one needs to check the geometry of their structure very often especially for the first few ionic steps of the optimization. In the case where your structure get distorted to an unreasonable geometry, you first need to evaluate the structure parameters such as number of atoms, charge and multiplicity of the system. For VASP calculation, a bad initial structure can cause many problems because it provided a unrealistic initial guess wavefunction. If the problem with the structure is not visible with eyesight, then we'll have to rely on VASP to correct the structure for us. For a structure to be consider fully optimize, all of the degrees-of-freedom (ionic positions, cell volume, and cell shape) should be allow to change during the calculation. However, with a bad initial guess structure, the calculation might not handle this too well all at once. So instead of allowing all of the degrees of freedom to change at start, once could start with optimizing just the cell volume, then the ionic positions separately or vice versa to obtain a better structure than the initial starting structure. Then a full optimization calculation can be run after this with all degrees-of-freedom allow to change. This method has found to be very helpful in resolving the convergence issue of the first ionic step. A second method to address this problem is to change the electronic minimisation algorithm.

The two algorithms that has been found useful to address this problem are the blocked Davidson iteration scheme and the "Conjugate" algorithm. Notice the change in the minimisation algorithm mention here is to address the first ionic step convergence issue, one can simply change this algorithm when a stable structure is obtained after the first few step to speed up the calculations or for other reasons.

2.2.4 Local minimum and global minimum energy structure. A common mistake is assuming the lowest energy is obtained after one calculation. One needs to be careful in making this assumption although in some fortunate circumstances this might be true, often it is not the case. The completion of a optimization calculation mean that the structure has reached a minimum energy geometry, but does not mean the structure has reach the lowest minimum energy geometry. The obtained geometry after one calculation could locate in a potential energy well of the potential energy surface (a local minimum), one needs to run more calculation to determine if this is in fact the lowest energy structure. One could simple run a optimization using the obtained structure from the first calculation to check and see if this is a lowest energy structure; if this is true, the calculations should stop after one ionic step. However, if that's not the case, one needs to repeat this until the structure is converged after one ionic step. It is also important to notice that the wavefunction should be erase before every rerun or one can simply not write the wavefunction for all optimization calculation. The reason is if a wavefunction is provided, the calculation will start from that wavefunction from the previous run, and the structure will be stuck in the potential energy well starting from the old wavefunction. If all of these considerations are taken into account and your structure converge after one ionic iteration, that means you got an optimized geometry of the material.

2.2.5 Molecular Structure Optimization. For molecular structure calculation, there is no periodic boundary conditions like in the solid case, this reduce the computational cost by a large amount. With that in mind, it is also important to get this calculations done in the right way and not waste computational resources. These calculations can be perform using the Gaussian 09 program package. Similar to solid calculation set up, it is crucial to get the initial structure correctly, this include getting the number of atoms in the structure, the charge, and the multiplicity of the molecular cluster correctly. Unlike in the solid case, the molecular cluster is a close system suspend in either vacuum or in a solvent which simplify all the complication created by periodic boundary conditions. The comment problem that occur for these calculations are often related to a unstable initial geometry, it is recommended that one should optimize their structure with visualization programs such as Avogrado or Materials Studio before feeding the structure into Gaussian calculation, this can make the optimization process in Gaussian 09 goes smoother and faster. Convergence issue in Gaussian 09 also cause by incorrect charge and multiplicity, other minor issues include the chosen basis set does not include the species presented in the structure. A basis set is a set of basis functions which are combined in linear combinations to approximate molecular orbitals, in order words, these are use to construct the wavefunction to solve the Schödinger equation. One should choose the basis set carefully, the rule of thumb for choosing a basis set is to pick the largest computationally affordable basis set. If all of these conditions are satisfied but there are still convergence issues, one should consider switching the minimization algorithm similar to in the solid case. One can also consider lower the convergence criteria to obtain a better starting structure, then perhaps tighten the convergence

criteria again for the optimization of the newly obtained structure. One should be able to obtain a optimized geometry of their molecular cluster following these suggestions.

2.3 Electronic Properties Modeling

An electronic band structure (EBS) and density-of-state (DOS) diagram can be obtain using the lowest energy structure. An EBS along with the DOS is very popular in material study because it can elucidate the chemical origin and the qualitative magnitude of their charge transport properties.

2.3.1 An overview of band theory. In solid-state physics, an electronic band structure describes the ranges of energy that an electron within the solid can occupied.[56] These ranges of energy is term the energy bands ("allowed band") and the ranges of energy where electron can not occupied is term then band gap ("forbidden band"). A band energy is a model describing the behavior of an electron within a solid originate from molecular orbital theory. In a single isolated atom, electrons can occupy atomic orbitals with discrete energy levels. In a small multi-atoms collective, the atoms' interaction split these atomic orbitals into separate molecular orbitals, each also with discrete energy level. If we apply this similar concept to a large multi-atom collective a.k.a a solid materials where thousands of atoms are interacting with one another, the number of molecular orbitals will be immense and the differences in energy between these molecular orbitals are diminutive. Instead of having discrete energy levels like in the small multi-atoms collective, in a solid, we have continuous energy band (which is a collective of molecular energy orbitals) that represents the energy range that electron can populate (Figure 13). Although the molecular orbitals span a large

amount of energy level, they are intervals of energy without a representative molecular orbital which form the band gap.

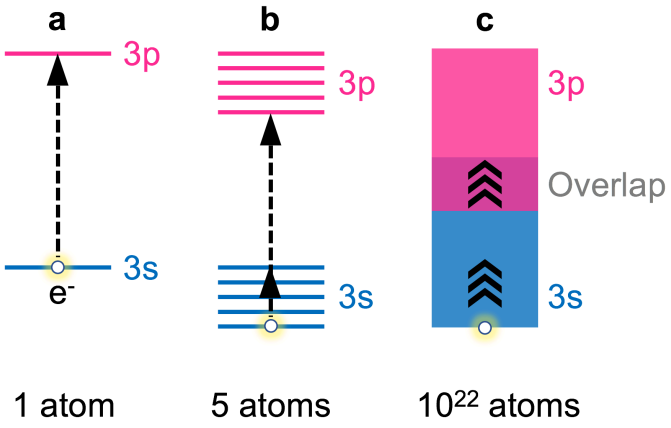

Figure 13. Large numbers of atoms in close proximity allow MOs to form continuous bands. (a) significant energy is required to excite an electrons in a single atom (b) less energy is required for electron excitation as the number of atoms increase (c) overlap permits electrons to freely move between orbitals and/or bands. Notice the two bands do cross in this example, which is not necessarily the case for all materials.

However, these bands can only be imagine as one dimensional representations, which is not very helpful in term of elucidating the transport properties of a material. Fortunately, the periodic nature of the crystal lattice allow one to utilize the crystal's symmetry to map the energy band into ta 2-dimensional plot that provides information about transport properties within the lattice.

2.3.2 EBS is plotted with k-vector in reciprocal space. This 2D plot is what we called a band structure, where the energy of the band is plot as a function of the k-vectors. In mathematical term, these k-vectors a.k.a the wavevectors exist in the reciprocal space or momentum space and is the Fourier transform of vectors from the real space. In chemistry term, these k-vectors are indices that tell us about the phases of the orbitals (whether the orbitals or in-

phase or out-of-phase with one another) and how these different configuration of orbitals phases give rise to a different energy level in a continuous band. The wavevectors are use in DFT to describe the wavefunction through Block's theorem,

$$\Psi(\mathbf{r}) = e^{i\mathbf{k}r}u(\mathbf{r}) \tag{2.16}$$

where r is the position, u is the periodic function that depend on r, and k is the wavevector. These k vector takes on any value inside the Brillouin zone, which is a uniquely defined primitive cell in the reciprocal space. These are wavevectors in the reciprocal space that gave rise to interesting material behavior. These are termed high symmetry points. Figure 14 shows an example of a unit cell in the first Brillouin zone and the high symmetry point in such unit cell.

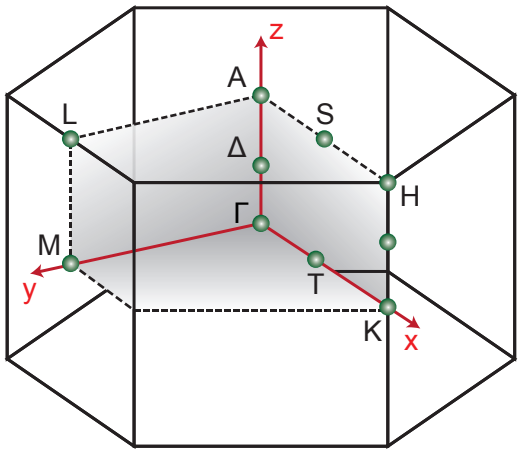

Figure 14. An example of the first Brillouin zone of a hexagonal cell and its high symmetry points in the reciprocal space.

When the band's energy is plot against the wavevectors, one can see the energy representation evolves as a smoothly function with changing k values. In solid state modeling, these wavevectors are multi-dimensional (x,y,z) and a band structure is ideally plot in the 4-dimensional space. This is somewhat difficult consider we are living in a 3-dimensional world, so a band structure is plot as

a 2-dimensional plot along straight line that connecting high-symmetry points. Combine the coordinate of the high-symmetry point and the curvature of the band, one can elucidate what type of interaction give rise to the transport property observed in the material and in what direction will the conductivity be the highest.

2.3.3 Information to look for in EBS. Now that we understand the basics of a EBS, there are features that are important in the the band structure that we need to keep in mind. The first important feature is the electronic band gap. There are many gap that exist within the band structure, but the gap between the valence band (the highest occupied electronic band) and the conduction band (the lowest unoccupied electronic band) is the most crucial in determining the conductivity of the material. This gap tell us the energy needed to promote an electron from the valence band to the conduction band which is necessary for free charge carrier formation. The higher the concentration of free charge carrier, the more likely that the material has good conductivity. There are three types of material: (i) a metallic material with no gap, (ii) a semi-conductive material with a small band gap (typically ¡ 3eV, which usually has good conductivity), (iii) and insulator which possess a large electronic band gap (Figure 15). In term of material design, we want to reduce these gap to make the material more conductive. The second feature is the dispersion of the bands, especially that of the conduction band an the valence band. Since the band structure is though of as a continuous energy range, electrons that reside in any of discrete orbitals within the same band can occupy any other discrete orbitals in the same energy band. In order words, this provide the electron more mobility in term of energy fluctuation and hence they have more mobility to hope from one band to another that cross the same energy level. A curvy valence band in a p-type semiconductor allow hole to transport

readily in the material and a curvy conduction band in a n-type semiconductor allow free electrons to have higher transport mobility, both of these scenarios would result in a highly conductive material.

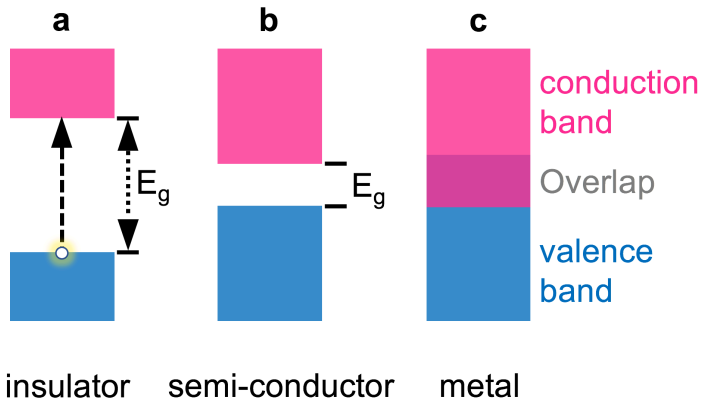

Figure 15. Energy gap between the conduction band and the valence band in (a) an insulator where the gap is significant large (b) semi-conductor where the gap is narrow and (c) a metal where there is no gap allows electron to enter the conduction band freely.

EBS is usually coupled with DOS in the literature. In term of terminology, DOS functions define the number of electronic states per unit volume, per unit energy corresponding to each band. In term of material study, the DOS provide information about which atomic specie in the material is contributing to a electronic band. For instant, in term of MOFs,the DOS help us identify if a band is emerged from the organic component or the inorganic component or the material or both.

2.3.4 Obtaining EBS and DOS. In term of obtaining an EBS and DOS using VASP, one needs the lowest energy structure. According to the previous discussion, the optimized structure should be obtain without the wavefunction. However, it is preferred that the electronic band structure calculation is initialize with a good wavefunction. For this reason, a single-point calculation should be run

with a large k-grid to obtain a good initial wavefunction for the EBS calculation. One also need to determine the sampling k-path for the EBS. In order to do that, one needs to know the space group of their material (Materials Studio can help with this), a k-path should be determine base on the first Brillouin zone along high-symmetry points that would provide the dispersion behavior in all directions in real space. With a good starting wavefunction and a good sampling k-path, one can carry out the EBS and DOS calculation to obtain the electronic structure of the material.

2.4 IR modeling with phonon calculations

2.4.1 Phonon calculation with finite difference method. As discuss above in the DFT section, due to the mass differences between the nuclei and electron, the nuclei is usually treated as a stationary classical particles (BOA). So for a equilibrium geometry, the forces acting on the individual nuclei should equal to 0.

$$F_I(\mathbf{R}_I) = -\frac{\partial E_{tot}(\mathbf{R}_I)}{\partial \mathbf{R}_I} = 0 \tag{2.17}$$

where $\mathbf{R}_n$ is the position of the nuclei, and F_n is the force acting on the nuclei. If the self-consistent ground state electron density is known, one can use the Hellman-Feynman theorem to obtain the atomic force as,

$$F_I(\mathbf{R}_I) = -\int \frac{\partial V_{ion}}{\partial \mathbf{R}_I}(\mathbf{r}, \mathbf{r'}; \mathbf{R}_I) P(\mathbf{r'}, \mathbf{r}) d\mathbf{r} d\mathbf{r'} - \frac{\partial E_{II}(\mathbf{R}_I)}{\partial \mathbf{R}_I} \tag{2.18}$$

where V_{ion} is a local potential characterizing the electron-ion interaction. If the structure is deviates by a small amount from its equilibrium position, then the Hessian matrix (a.k.a. the matrix of the inter-atomic force constants) will dominate the changes in total energy with respect to the atomic positions. The dynamical

matrix will then take the form of:

$$D_{I,J} = -\frac{1}{\sqrt{M_I M_J}} \frac{\partial^2 E_{tot}(\mathbf{R}_I)}{\partial \mathbf{R}_I \partial \mathbf{R}_J} \tag{2.19}$$

where M_I is the mass of the I-th nuclei. All the eigenvalues of D should be real and non-negative if the equilibrium geometry is at the lowest energy configuration. The eigen decomposition of D is,

$$Du_k = \omega_k^2 u_k \tag{2.20}$$

where u_k is the k-th phonon mode and ω_k is the k-th phonon frequency. The easiest way to calculate these phonon frequencies is by using the finite difference (FD) approximation (the frozen phone approach) to obtain the dynamical matrix D where the a-th column of the I,J block can be approximate using:

$$D_{I,J,a} \approx -\frac{1}{\sqrt{M_I M_J}} \frac{\mathbf{F}_I(R_I; \mathbf{R}_J \leftarrow \mathbf{R}_J + he_a) - \mathbf{F}_I(\mathbf{R}_I)}{h} \tag{2.21}$$

where $\mathbf{F}_I(R_I; \mathbf{R}_J \leftarrow \mathbf{R}_J + he_a)$ is the atomic force on the J-th atom, h is the magnitude of the deviation and e_a is the direction of the deviation. This is the simplest method to approximate the phonon frequency and the phonon mode, however, a simple method such as the finite displacement method will produce less accurate data in compare to other complicated method such as density functional perturbation theory (DFPT). Similar idea apply in DFPT method where the evaluation of the dynamical matrix is necessary for the computation of the phonon mode and frequency. Here, however, the formulation is much more complicated compare to in the FD method.

2.4.2 Phonon calculation with density functional perturbation theory. Similar to what was discussed above, we are assuming the forces acting on individual nuclei are negligible and hence we can write an expression for the force as describe in the previous section. However, the dynamical matrix D needs

to be approximate more accurately and systematically for perturbation theory, the matrix can be approximate by:

$$D_{I,J} = -\frac{1}{\sqrt{M_I M_J}} \frac{\partial^2 E_{tot}(\mathbf{R}_I)}{\partial \mathbf{R}_I \partial \mathbf{R}_J} = -\frac{1}{\sqrt{M_I M_J}} \Bigg(\int \frac{\partial V_{ion}}{\partial \mathbf{R}_I}(\mathbf{r}, \mathbf{r'}; \mathbf{R}_I) \frac{\partial P(\mathbf{r'}, \mathbf{r})}{\partial \mathbf{R}_J} d\mathbf{r} d\mathbf{r'} + \int \frac{\partial^2 V_{ion}}{\partial \mathbf{R}_I \partial \mathbf{R}_J}(\mathbf{r}, \mathbf{r'}; \mathbf{R}_I) P(\mathbf{r'}, \mathbf{r}) d\mathbf{r} d\mathbf{r'} + \frac{\partial^2 E_{II}(\mathbf{R}_I)}{\partial \mathbf{R}_I \partial \mathbf{R}_J} \Bigg) \tag{2.22}$$

here, the second integral an be solve readily with all known quantities and the third integral can be solve independently from the electronic states since it's simply account for only the ion-ion interaction. The first integral however involves the electron density and how the perturbation of the atomic positions alter this electron density. The integral can be expand using the chain rule to:

$$\int \frac{\partial V_{ion}(\mathbf{r}, \mathbf{r'}; \mathbf{R}_I)}{\partial \mathbf{R}_I} \frac{\partial P(\mathbf{r'}, \mathbf{r})}{\partial V_{ion}(\mathbf{r''}, \mathbf{r'''})} \frac{\partial V_{ion}(\mathbf{r''}, \mathbf{r'''}; \mathbf{R}_I)}{\partial \mathbf{R}_J} d\mathbf{r} d\mathbf{r'} d\mathbf{r''} d\mathbf{r'''} \tag{2.23}$$

where,

$$\frac{\partial P(\mathbf{r'}, \mathbf{r})}{\partial V_{ion}(\mathbf{r''}, \mathbf{r'''})} \tag{2.24}$$

is the polarizability operator which is a Fréchet derivative that can be apply to the perturbation which contain a local and a non-local component (the last fraction in the equation above). This then becomes a comment form of equation called the Dyson equation, and one can obtain u_k by from solving this math expression. Notice that in order to solve this, the non-local component need to be ignored and each local perturbation requires the solving of a Sternheimer equation by a standard direct of an iterative linear solver. The resulting u_k from solving the Dyson equation for each perturbation is the phonon mode correspond to that perturbation. DFTP calculations require a large amount of computational effort given each phonon mode requires the solving of a large number of heavy mathematical expressions where FD methods is simply an approximation of

the Hessian and dynamical matrix by solving the Kohn-Sham equations self-consistently. For this reason, DFTP calculations tend to scale poorly with larger system size and larger k-grid in compare to FD methods.

2.4.3 Obtaining phonon modes and frequency using VASP. A phonon calculation at the zone-center Γ can be used to both, evaluate the stability of the structure and help visualize the IR/Raman mode. These calculations can be done in VASP, both FD method and DFPT are available. From my personal experience with porous frameworks calculation, FD methods provide comparable result with DFPT which mean FD methods is preferred considering they have lower computational cost. The steps to carry out single-point phonon calculation are very similar to that of the EBS calculation where a single point calculation with a dense k-grid is required to obtain a good initial guess for the wavefunction, then one can follow up with either FD or DFPT calculation to obtain phonon mode and frequency. Notice that to obtain IR spectrum or to visualize the phonon mode, external post-VASP processing packages are required, these are free open-source packages that can be found online.

CHAPTER III

DYNAMIC BONDING OF THE METAL-LIGAND INTERFACE IN 3D MOFS

3.1 Examining metal-organic interface of 3D MOFs: Evidence of dynamic bonding in carboxylate-based MOFs.

3.1.1 An Overview of phase transition in MOFs: a case study of polymorphic transformation of a Zr-based MOF.

MOFs possess outstanding surface area and incredible chemical tunability due to their nano-porous structure yet rigid and stable. So often, MOFs is thought to possess inflexible structure, but can undergoes behavior such as breathing and phase transition such as polymorphic transformation. These transformations usually occur in conjunction of temperature alteration or other modulators. It's difficult to understand how these transformation could occur in a rigid solid structure such as MOFs. For instant, our study on the transformation of the Zr-based MOF, EHU-30 to UiO-66 was my first attempt to elucidate how such transformation like these occur in MOFs. While the theoretical construct for examining polymorphism exists, the discovery and interconversion between MOF polymorphs has been largely neglected due to interest in the intuitive thermodynamic assembly process.[57] Correspondingly, studies that monitor any aspect of the MOF assembly process in situ are rare. In general, two types of polymorphic transformations have been widely recognized: (i) single-crystal-to-single-crystal transformation where the crystal integrity and the long-range structural order are maintained through the transformation process and (ii) dissolution–recrystallization transformation where the components of the crystals reassemble to form a different phase crystal.[58] Metastable kinetic products have been studied to convert into the stable thermodynamic form by applying the appropriate stimuli such as temperature,

pressure, light, solvation, and guest molecule removal or exchange.[59–64] For example, the 8-connected Zr_6O_8 node with tetratopic linkers has been utilized to form different polymorphs by controlling the dihedral angle between the carboxylate bound phenyl and central pyrene, porphyrin, or benzene plane, and conversion of the metastable products to the more stable products was possible by altering the reaction conditions.[65–70]

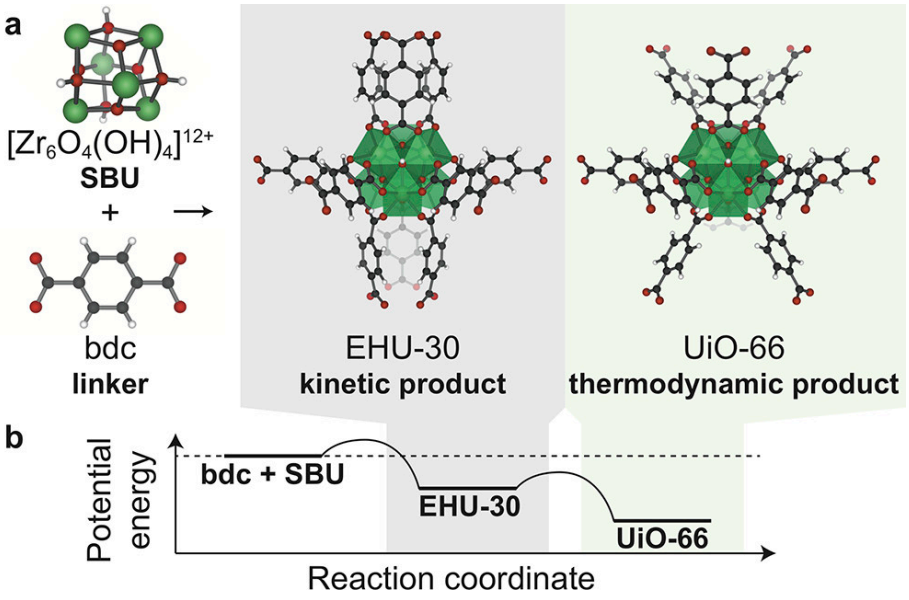

Figure 16. Schematic reaction energy profile and structure of kinetic product EHU-30 and thermodynamic product UiO-66 (C, black; H, pink; O, red; Zr, green). Reprinted with permission from ACS Materials Lett. 2020, 2, 5, 499–504.[1] Copyright 2022 American Chemical Society.

Similarly, conformational differences of ditopic linkers in the Zr-based MOFs have resulted in MOFs with different topologies.[71] These examples highlight that chemical space can be largely expanded if we consider that multitopic linkers are flexible species, rather than rigid pillars, and, in turn, should provide access to a diverse family of compositionally similar scaffolds. UiO-66, first reported in 2008,[72] is one of the most studied MOFs due to its ease of synthesis, exceptional stability, and its ability to be both pre- and postsynthetically functionalized.[73–76]

While there are many reports of defect engineering in UiO-66, resulting in different topologies with different nominal stoichiometries,[77–79] there is only one reported polymorph of UiO-66, EHU-30.[80] Similar to UiO-66, EHU-30 has 12-connected Zr_6 nodes but rather crystallizes in a hex topology as opposed to a fcu topology. The structural dissimilarity arises from three distorted linkers per formula unit, shown schematically in Figure 16.

Herein, we monitor in situ powder X-ray diffraction (PXRD) and in situ1H NMR spectroscopy to determine the structural conversion process of the modulator- and temperature-mediated polymorphic transformation from a kinetic product, EHU-30, to the thermodynamic product, UiO-66 (where UiO-66 is transformed EHU-30) (Figure 16). Scanning electron microscopy (SEM), thermogravimetric analysis (TGA), and gas adsorption isotherms complement the in situ measurements to reveal the necessity of both heat and acetic acid to convert EHU-30 to UiO-66. Density functional theory (DFT) is applied to identify the driving force of this transformation by comparing the linkers in UiO-66 and the distorted linkers of EHU-30. To assess the relative conformational stability of linkers in each MOF, density functional theory (DFT) was employed to determine the energetic penalty for linker distortion in EHU-30. The difference in energy between the bent and linear conformations was found through linker models extracted from the bulk optimized structures of EHU-30 and UiO-66 in order to isolate the effect of linker distortion (Figure 17). The difference in Gibbs free energy, a measure of strain, was found to be 3.0 kcal/mol. In conjunction with the incomplete dissolution of EHU-30 observed in situ, we hypothesized that the population of disconnected linkers observed by NMR was dominated by the formerly bent linkers, which disconnect from the node and reorganize to form the

more stable UiO-66 fcu topology. The computed densities of states are further presented for each polymorph, to demonstrate that both polymorphs are expected to have similar photophysical properties, with their optical gap governed by a ligand-to-ligand transitions occurring in the UV.

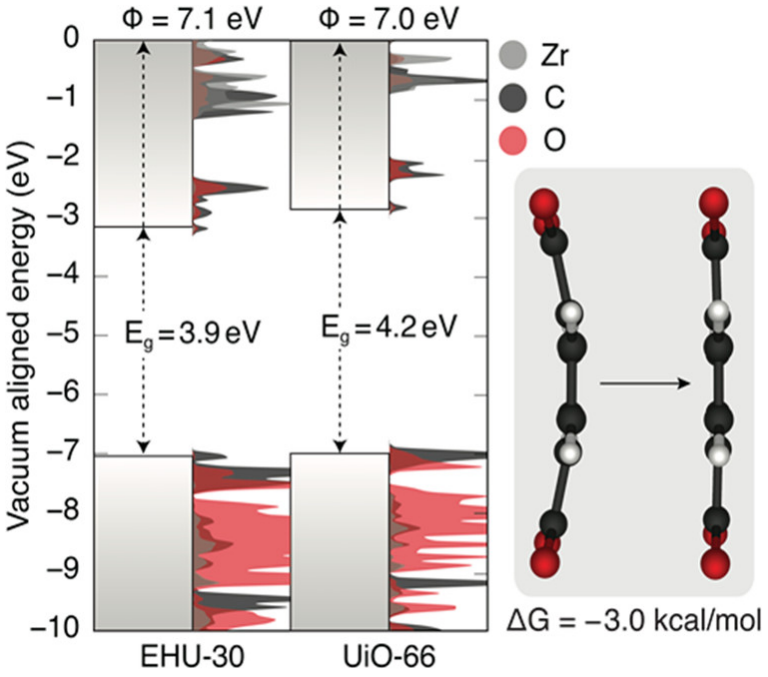

Figure 17. Band edge diagram and theoretical density of states for EHU-30 and UiO-66 demonstrating a subtle difference in frontier band characteristics. A depiction of the bent and linear linkers is additionally presented to illustrate the strain energy stored in the BDC units of EHU-30. Reprinted with permission from ACS Materials Lett. 2020, 2, 5, 499–504.[1] Copyright 2022 American Chemical Society.

We showed the modulator- and temperature-mediated polymorphic transformation of a kinetic MOF product, EHU-30, into its thermodynamic form, UiO-66. The rate of EHU-30 conversion showed a positive correlation with temperature and an inverse correlation with reaction concentration; the conversion conditions are closely related to the synthetic conditions of UiO-66. By monitoring reaction progress with in situ PXRD and 1H NMR, and probing

the energetic relationship between EHU-30 and UiO-66 with DFT, it was found that EHU-30 undergoes a partial dissolution–recrystallization process driven by the rearrangement of linkers to release strain. Therefore, efforts to understand the relationship between kinetic and thermodynamic MOF products and characterizing the intermediate phases of transitions between them will inform the general design of synthetic parameters to target certain phases, which includes the formation of intrinsic defects as well as connectivity. Although we elucidated some aspect of this transformations through examining the before and after polymorphs, we have not yet at this point understand a properties call "dynamic bonding" that gave rise to transformations such as this one in MOFs (which has been thought to be static) that usually require a flexible structure.

3.1.2 Evidence of soft-mode in carboxylate-based MOFs.

Important material phenomena often depend on dynamic distortions to solid lattices, such as ion diffusion through solid electrolytes[81] and surface reconstruction of heterogeneous catalysts.[82] In particular, certain lattice vibrations cause such extreme distortions to equilibrium geometries that they trigger structural phase transitions responsible for wide-ranging functional properties,[83] including ferroelectricity,[84–87] metal–insulator transitions,[88] exciton condensation,[89,90] and multiferroics.[91] Monitoring these phonon modes as a function of temperature reveals that the peak positions redshift and intensities diminish near the phase change critical temperature due to the vibrations transferring energy into the structural reordering process through anharmonic coupling to other phonons.[92] Because these vibrations dissipate energy, they are termed "soft modes". Analysis of such vibrations, and their coupling to magnetic, vibrational, electronic, and other degrees of freedom, offers a microscopic basis for predicting and controlling

phase transitions.[93] Understanding the relationship of lattice dynamics to phase transitions has guided the design of new types of materials, such as metastable phases, for devices with specifically enhanced physical properties. Recently, metal-linker dynamics in the porous coordination polymers known as metal–organic frameworks (MOFs) have been invoked to describe melting mechanisms of MOF liquids[94–97] and glasses.[98–105] These disordered MOF materials attract considerable attention by opening possibilities in the design of porous materials for applications ranging from gas storage to ion exchange membranes, but the metal–ligand dynamics associated with their melting transitions challenge the common conception of MOFs as static structures. Although metal-linker lability helps explain melting and other important behavior, evidence for such dynamic coordination chemistry has only been observed indirectly for carboxylate MOFs.[106–108] Direct measurement of metal-linker lability has been possible for certain ZIFs, however, requiring specialized high-temperature synchrotron techniques.[94,104] The intensifying research into dynamic metal–organic materials would benefit, therefore, from routine methods that probe metal-linker lability, especially for carboxylate MOFs, which constitute the overwhelming majority of MOFs. Although reversible metal-linker coordination is thought to drive MOF crystallization, such dynamic bonding is not commonly thought to occur once the MOF is formed. Dynamic metal-linker bonding is well-documented in analogous one-dimensional coordination polymers, which comprise an important subset of materials termed "dynamic", "adaptable", "stimuli-responsive", or "self-healing covalent networks".[109–112] For example, formation constants (log Kf, Kf = [bound metal linkers]/[unbound metal linkers]) of metal-pyridyl[113] and metal-carbene[114] polymers have been measured to be as small as 3 to 4,

implying that "unbound" states constitute a significant portion of the polymer linkages. Interestingly, formation constants of molecular metal-carboxylate complexes akin to MOF coordination moieties, e.g., zinc-benzoate, range from only 0.1 to 1.5.[115] Structural dynamics in MOFs, instead, conventionally refers to the pressure-induced "breathing" behavior of pore cavities,[116–120] the transient binding of guest molecules,[120–124] and the negative thermal expansion (NTE) of certain MOFs,[125,126,126–130] but labile metal-linker bonding would explain important phenomena, such as the ability of MOFs to undergo postsynthetic exchange,[74,106,131–135] perform catalysis at seemingly saturated metal centers,[136] and readily grow as bulk crystals. Reversible metal-linker bonding could also complement the current mechanistic understanding that dynamic linker motion drives NTE, and, more broadly, guide deliberate control over important MOF functions, while inspiring the design of porous materials with stimuli-responsive, metastable, self-healing, and other adaptable behavior. With challenging the common conception of carboxylate MOFs as static structures, evidence for their labile metal-linker bonding will enable their design in applications that leverage structural dynamics. Here, we demonstrate variable-temperature diffuse reflectance infrared Fourier transform spectroscopy (VT-DRIFTS) combine with DFT as a convenient method for probing MOF metal-linker dynamics. We observe that at higher temperatures, carboxylate stretches red-shift for a general collection of representative carboxylate-based MOF materials, which we ascribe to thermal population of MOF conformations with "loose" metal-carboxylate linkages in equilibrium with a decreased population of "tight" metal-linker states. Importantly, the C–O stretches provide a convenient spectroscopic handle for metal-linker bonding dynamics, due to the coupling of the readily observable

C–O modes to the more elusive M–O modes (Figure 18a). A similar approach has been employed previously, where analysis of linker, rather than metal-linker vibrational modes, provided evidence for dynamic bonding in self-healing metal-pyridyl one-dimensional coordination polymers.[137] Variable-temperature Raman spectroscopy evidenced red-shifting pyridyl stretches at higher temperatures that were attributed to dynamic structural rearrangements.[137] Evidence for the melting mechanism of ZIFs rests on analysis of red-shifting zinc-imidazolate bond stretches, requiring specialized variable-temperature terahertz (THz)/Far-IR synchrotron techniques, due to the low-energy spectral range. In these reports, consistent with analysis of other dynamic and phase-change systems, the red-shifting behavior was attributed to thermal population of the unevenly spaced vibrational excited states of an anharmonic Zn-imidazolate oscillator.[138] Because the states become more closely spaced at higher energies, the apparent vibrational mode shifts to lower wavenumbers. With greater population of higher energy states, the vibrational amplitudes also increase until they reach a critical ratio with respect to the interatomic metal–ligand spacing, termed the Lindemann ratio,[139] causing the material to melt.

3.1.3 Dynamic bonding at the metal-linker interface and shallow potential energy surface allow phase transition in MOFs. Fundamentally, this behavior resembles the ability of soft modes to induce phase transitions through vibrational motion. Here, we demonstrate that similar evidence for melting behavior can be observed for carboxylate MOFs by monitoring the red-shifts of carboxylate stretches coupled to anharmonic metal-linker oscillators. We justify this strategy in terms of molecular orbital arguments and a simple two-state model of tight and loose metal-linker states in thermal equilibrium.

The temperature-induced metal-linker dynamics evidenced in these prototypical MOFs resembles VT-DRIFTS studies of soft modes and phase changes in other classes of materials, including ZIFs, but had not been previously observed for ubiquitous carboxylate MOFs. Evidence for soft modes in carboxylate MOFs have been previously impeded by the difficulty of monitoring low-energy metal-linker vibrations directly, whereas the carboxylate stretches studied here provide a convenient alternative spectroscopic handle. To demonstrate the generality of these findings, we investigate a wide class of carboxylate MOFs that includes iconic examples with diverse structures and metal-linker chemistry. The broad applicability of these results offers a fundamentally different perception of MOFs. In addition to MOFs, we expect VT-DRIFTS to offer a powerful method for probing the stability, dynamics, and structure of other organic–inorganic materials featuring metal–ligand bonds, such as 1-D coordination polymers, porous liquids, and metal–organic cages.[140–142]

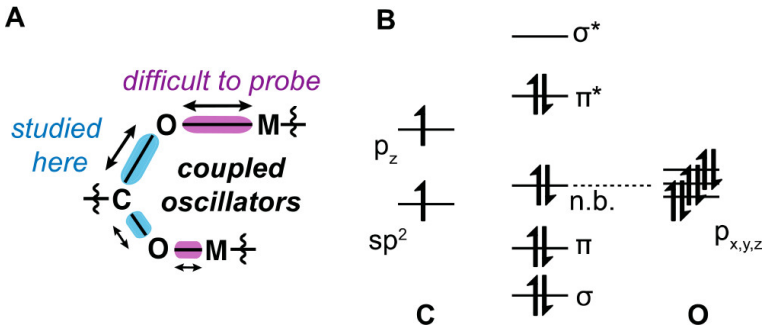

Figure 18. Molecular Orbital (MO) Description of MOF Metal-Carboxylate Interactions (A) Schematic representation of C–O and M–O coupled anharmonic oscillators in metal-carboxylate complexes. (B) MO diagram of carbonyl bond in a carboxylate group. Reprinted with permission from J. Am. Chem. Soc. 2020, 142, 45, 19291–19299.[2] Copyright 2022 American Chemical Society.

Molecular orbital (MO) theory provides a straightforward explanation for why carboxylate stretches might redshift with weaker metal-linker interactions.

Figure 18b illustrates a simplified MO diagram for an individual C–O bond of a carboxylate group. Because the highest energy electrons reside in orbitals that are anti/nonbonding with respect to the C–O bond, they act as the lone pair involved in dative interactions with metal ions. Accordingly, stronger M–O interactions would also enhance C–O bonding by distributing the antibonding density away from the C–O bond vector. Therefore, strong M–O interactions should cause blueshifts to carboxylate stretches, and weak M–O interactions should cause redshifts. Indeed, strongly ionic carboxylate complexes, such as sodium benzoate, show the highest-energy carboxylate stretching modes. For similar reasons, interactions between Lewis acidic metal ions and carbon monoxide induce blueshifts to C–O stretching frequencies. Hence, we hypothesize that if MOF metal-linker bonds exist in equilibrium between "tight" and "loose" states, then high temperatures would produce redshifts by shifting the equilibrium toward weaker C–O interactions. Second, if observed carboxylate bands arise from overlapping spectral components from tight and loose species, then we expect band widths to maximize at temperatures where these species exist in equal mixtures and minimize at temperatures dominated by a single species.

The material HKUST-1 (Cu_3(1,3,5-benzenetricarboxylate)$_2$) was chosen as an initial target for VT-DRIFTS as many seminal studies of MOFs were first demonstrated with this material. Figure 19a plots the spectra collected at 50 °C intervals starting from room temperature, then warmed to 200 °C, and then cooled to 100 °C. Surprisingly, several bands, in addition to the expected asymmetric and symmetric carboxylate stretches, appear to redshift with increased temperature.

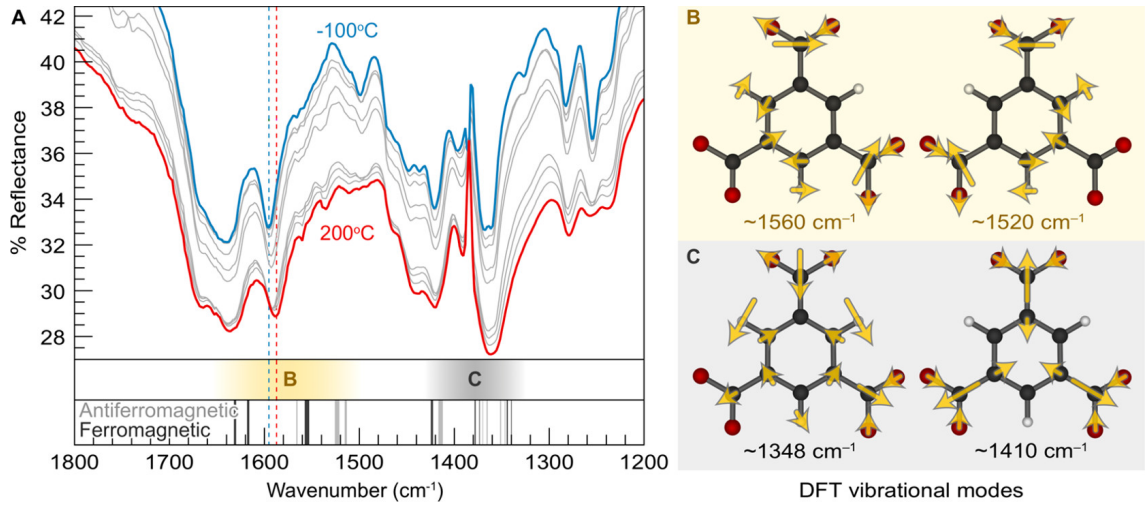

Figure 19. Variable-temperature diffuse reflectance infrared Fourier transform spectra (VT-DRIFTS) and computed phonon modes of HKUST-1. (A) (Top) Experimental spectra collected between 100 and 200 °C under dynamic vacuum. (Bottom) Simulated peak positions of phonon modes with carboxylate character denoted by color intensity and labeled according to modes shown in panel B. (B) Representation of "asymmetric" and (C) "symmetric" carboxylate-based phonon modes projected at the Γ q-point. Reprinted with permission from J. Am. Chem. Soc. 2020, 142, 45, 19291–19299.[2] Copyright 2022 American Chemical Society.

Therefore, we employed density functional perturbation theory for proper assignment of all bands in Figure 19a. For emphasis, only bands with carboxylate character are plotted in Figure 19a. As the Cu paddlewheel dimer in HKUST-1 displays antiferromagnetic ordering below 280 K,[143] which is within the measured temperature regime, spectra were simulated with both antiferromagnetic (AFM) and ferromagnetic (FM) ordering, with the former showing excellent agreement with spectra collected below room temperature (Figure 19a, bottom). To aid in band assignment, vibrational normal modes were projected at the Γ q-point and represented as molecular diagrams (Figure 19b), with arrows denoting vibrational directions and oscillator intensities. Interestingly, all contain carboxylate character, suggesting that the temperature dependence of the data in Figure 19a arises from orbital interactions involving carboxylates specifically.

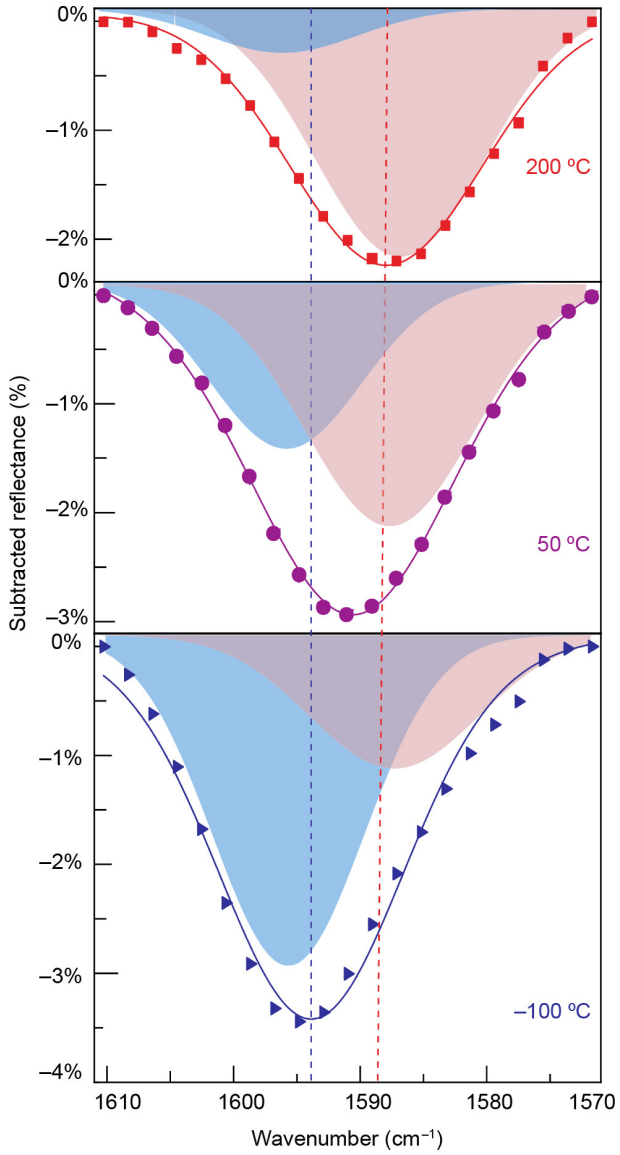

Figure 20. Global curve fittings for representative spectra of the HKUST-1 asymmetric carboxylate stretch. Spectral deconvolution assumed two components with constant peak maxima but variable total areas. Fits produced a species centered at 1596 cm^{-1} (blue) and another at 1587 cm^{-1} (red). Markers denote experimental data and solid lines show Gaussian fits. Reprinted with permission from J. Am. Chem. Soc. 2020, 142, 45, 19291–19299.[2] Copyright 2022 American Chemical Society.

Among these bands, the symmetric carboxylate stretch shows the most distinctive redshift. Notably, the band unique to the AFM magnetic state helps

account for the experimental feature, such as the peak at 1499 cm^{-1}, that disappears above 300 K. We therefore attribute this band to the calculated phonon at 1520 cm^{-1}. Consequently, we explicate the following analysis by focusing on this band in particular, although the symmetric and asymmetric carboxylate stretches of all MOFs considered here exhibit redshifts. Rather than reproduce the observed redshifts from empirical parameters, we investigated whether the experimental data could be simply fitted to two equilibrium species in relative ratios appropriate for labile metal-carboxylate bonds. Indeed, a global population analysis of the symmetric carboxylate stretch for HKUST-1 indicates that the temperature-dependent band can be accurately deconvoluted into a higher-energy component at 1596 cm^{-1} that decreases in intensity and a lower-energy component at 1587 cm^{-1} that increases in intensity with increased temperature (Figure 20).

Importantly, the frequencies of these two components remain unchanged during the data fitting, as expected for a two-state model. Furthermore, this analysis corroborates the evidence for a dominant species existing at either temperature extreme but with nearly equal populations around 50 °C. Figure 21 illustrates this chemical scenario where each component represents ensembles of metal carboxylate species with either long "loose" or short "tight" interactions, each integrated across shallow potential energy surfaces. Through advanced analytical techniques, recent investigations have made considerable progress in characterizing MOF structural disorder and dynamics,[144,145] but experimental evidence for the precise geometries of dynamic systems remains an outstanding challenge.

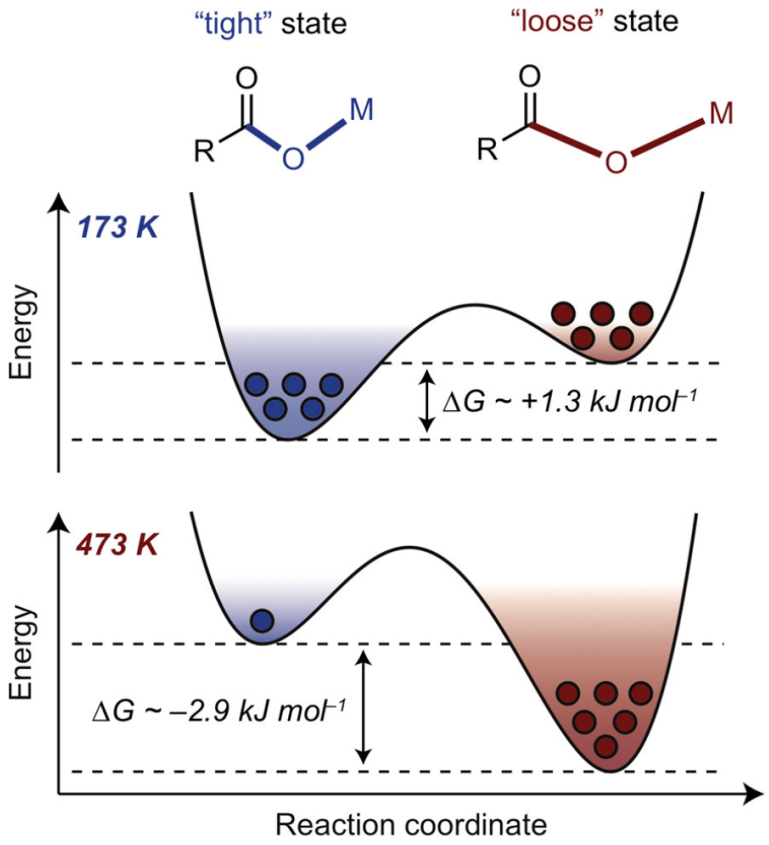

Figure 21. Equilibrium between "Tight" and "Loose" Ensembles of MOF Metal-Carboxylate Populations Existing near Thermoneutral Equilibrium (Top) Conversion of MOF metal-linker bonds between two ensemble-averaged states. (Bottom) Temperature-dependent free energies (ΔG) and relative population according to equilibrium constants derived from experimental data. Reprinted with permission from J. Am. Chem. Soc. 2020, 142, 45, 19291–19299.[2] Copyright 2022 American Chemical Society.

For example, variable temperature X-ray diffraction data of HKUST-1 reveal negative thermal expansion, superficially suggesting bond contraction, rather than expansion, at higher temperatures. After careful consideration, these results can be attributed to large, "trampoline-like" dynamic distortions of the linkers at high temperatures that become time-averaged into a static crystallographic structure disguising the true elongated distances.[125] Nevertheless, evidence for metal-linker dynamics is apparent in the highly disordered carboxylate oxygens, which create

the greatest thermal displacements. For structural insight into the tight and loose configurations of HKUST-1, we therefore computed geometries across a range of contracted and expanded unit cell volumes.

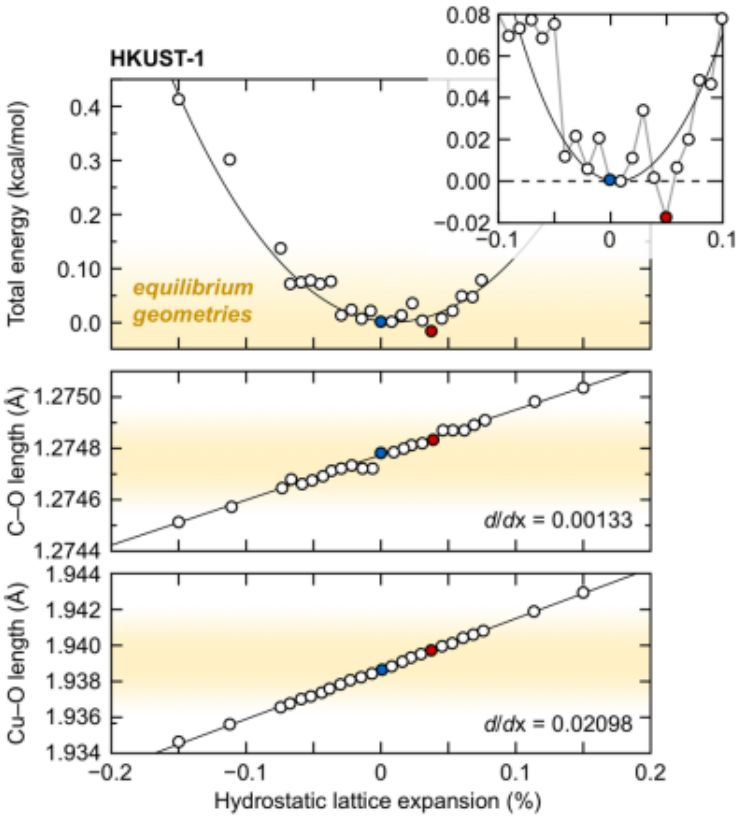

Figure 22. HKUST-1 equation of state. The blue point is the computed equilibrium structure, but other similar energy structures are accessible (emphasized in the yellow gradient). Unlike MOF-5, HKUST-1 a less smooth energy profile near the equilibrium structure. We highlight another minimum energy structure (red), which could be the "loose" geometry. Regardless, the potential energy surface is shallow around the minimum. M-O bond elongates more rapidly than the C-O bond. Reprinted with permission from J. Am. Chem. Soc. 2020, 142, 45, 19291–19299.[2] Copyright 2022 American Chemical Society.

Figure 22 plots the total energies of structures resulting from lattice distortions that correspond to temperatures spanning ±444 K based on reported thermal expansion coefficients.[125] These simulated data contain several important

features that support our model: the shallow depth of the energy well is consistent with numerous, degenerate metal-carboxylate structures; the existence of multiple energetic minima resemble the tight and loose species in thermal equilibrium (highlighted in red and blue as potential candidates); and the direct relationship between Cu–O and C–O distances supports our claim that monitoring carboxylate stretches serves as a proxy for studying MOF metal-carboxylate dynamics.

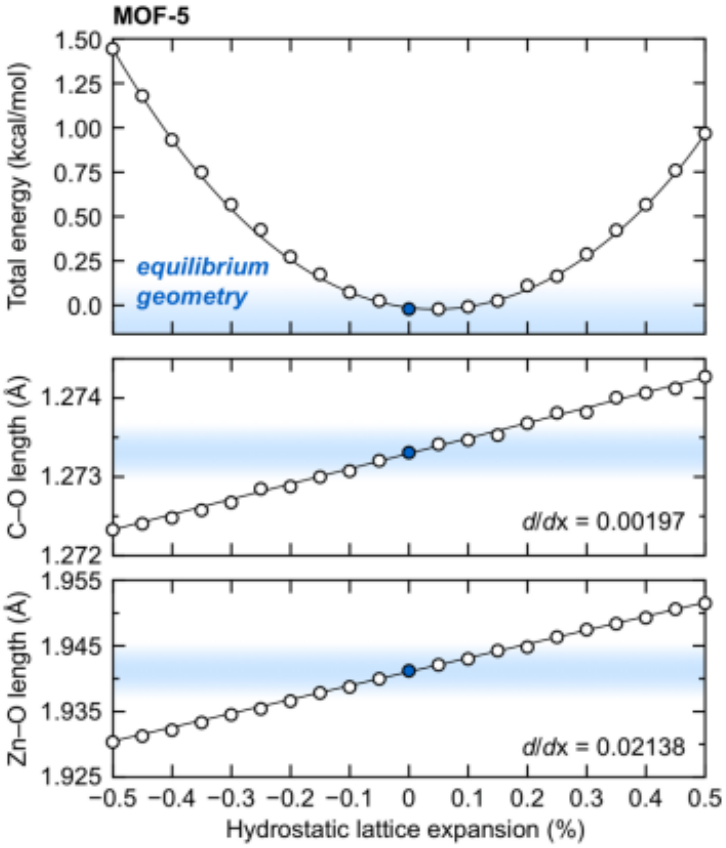

Figure 23. MOF-5 equation of state. The blue point denotes the computed equilibrium structure, but other similar energy structures are accessible (emphasized in the blue gradient). The potential energy surface is shallow around the minimum. M-O bond elongates more rapidly than the C-O bond. Reprinted with permission from J. Am. Chem. Soc. 2020, 142, 45, 19291–19299.[2] Copyright 2022 American Chemical Society.

As expected for coupled anharmonic oscillators, this imbalanced relationship causes the Cu–O bond to be much more sensitive than the C–O carboxylate fragment: over the explored temperature range, the Cu–O bond shows a 20-fold greater slope that covers a considerable bond difference of nearly 0.01 Å compared to just 0.0006 Å for C–O. These results emphasize the remarkable ability of VT-DRIFTS to produce spectral features of such small carboxylate distortions as evidence for major distortions to metal-carboxylate bonds studied only with great difficulty. Similarly, one would expect the shallow energy well where multiple states are within the thermally accessible region can be observed for other carboxylate-based MOFs. An example for MOF-5 is show in Figure 23.

3.1.4 Method. Computational Method. To determine if EHU-30 and UiO-66 were, in fact, polymorphs, the stoichiometry of the neutral bulk materials were compared and found to be identical. The two structures were then optimized with PBEsol[146] as implemented in VASP(5.4.4)[53] using the PAW plane wave method[147] and a 500 eV plane-wave cutoff basis set. A Γ centered 2x2x2 k-grid was converged to ionic, and electronic criteria, of 0.005 eV and $1x10^{-6}$ eV, respectively, accounting for any effects from spin polarization. The normalized energy of EHU-30, taking UiO-66 as the thermodynamic minimum with an energy of 0, is +1.4 eV. These findings support the hypothesis of EHU-30 being the kinetic polymorph of the thermodynamic product UiO-66. Electronic properties for both systems were recovered from a Γ-only single point with the HSEsol06[148] functional on the PBEsol optimized systems. Eigenvalues were aligned to the vacuum level. Interestingly, the density of states for EHU-30 shows a slightly reduced band gap relative to the more common UiO-66 conformer with a high density of states lying near the Fermi and conduction band edges. To calculate the difference in energy

between the bent BDC linkers of the EHU-30 polymorph and the mostly planar BDC linkers in UiO-66, one linker was extracted from each of the bulk optimized structures. A single point frequency calculation was performed at the unrestricted B3LYP level of theory as implemented in Gaussian with a triple zeta Pople basis set augmented by additional diffuse and polarization functions (6-311+G*) in order to recover thermodynamic properties. Linkers were kept in their anionic state with an overall charge of -2. The difference in Gibb's free energy between the planar and distorted structure was found to be 3.04 kcal/mol. Given that half the BDC linkers in EHU-30 are non-planar this would correspond to an additional energy of 0.80 eV per unit cell.

Density Functional Theory (DFT) and finite difference method (FDM) calculations were performed to identify the vibrational frequencies of different MOF systems. Structural optimization for all structures were performed with DFT as implemented in the Vienna ab initio Simulation Package (VASP, version 5.4.4).[53] All structures were equilibrated using the unrestricted GGA-PBEsol exchange–correlation functional[146] except HKUST-1 (antiferromagnetic) where electron spins were set to pair up within each Cu dimer. Ionic relaxation was achieved when all forces were smaller than 0.005 eV/Å. The plane-wave cut off was set at 500 eV, and the SCF convergence criterion was 10^{-6} eV, resulting in electronic convergence of 0.005 eV per atom. An automatic k-grid was used during the optimization with 2x2x2 sampling, except those for MOF-74 where the k-grid was set to be 1x1x4. Symmetry was not enforced. Each optimized structure was then subjected to a single point calculation to obtain the predicted wavefunctions. From the equilibrated structures, vibrational frequencies were obtained via finite differences method implemented in VASP where zone-center (Gamma-point)

frequencies were calculated. Central difference was enforced to allow both negative and positive displacements of ions and the step size was set to be 0.015 Å as default. The unrestricted GGA-PBEsol exchange-correlation functional were used with all convergence criteria similar to those of the optimization calculations. A scale factor of 0.0001 was enforced on the vector field for vibrational frequencies visualization.

3.1.5 Conclusion. Redshifting MOF carboxylate stretches resemble lattice dynamical soft modes observed at temperatures near the phase transition critical temperatures (Tc) for numerous materials, such as ferroelectric perovskites and ZIFs.[149,150] Although described by different physical models, both involve large-amplitude vibrations that drive structural phase changes. According to soft mode theory, the frequency of these critical vibrations redshifts and then vanishes as the material assumes a new structure with unique normal modes. In the data presented here, we attribute the redshift of the carboxylate modes to the gradual transition of a crystalline form into an amorphous structure with weaker metal-carboxylate bonds and a new corresponding set of normal modes. Interestingly, these data resemble the spectral evidence of melting behavior in ZIFs, and yet melting has yet to be observed in carboxylate MOFs. Computational simulations suggest, however, that metal-carboxylate soft modes drive breathing behavior in MOFs,[151] although direct evidence remains an outstanding challenge. These data, therefore, suggest that carboxylate-based MOFs undergo structural distortions associated with melting transitions but decompose before reaching the melting point. A key difference that may explain the absence of melting carboxylate MOFs is that while ZIFs include individual metal ions, carboxylate MOFs often contain multimetallic metal nodes. Upon dissociation from linkers, these complex

inorganic fragments may recombine with nearby dangling linker molecules into any numerous possible polymorphs and amorphous decomposition products rather than remain in a melted phase resembling the original crystalline lattice. Therefore, these results suggest that melting may be achievable in carboxylate MOFs with few competing polymorph phases, perhaps such as those with mononuclear metal sites. While offering evidence for the existence of soft modes invoked to describe MOF liquids, these data provide mechanistic justification of other MOF phenomena requiring dissociation of MOF metal-linker bonds: most notably, single-crystal-to-single-crystal postsynthetic modification (cation exchange and ligand exchange),[74,131,135,152] the ability of MOFs to encapsulate molecules larger than their pore apertures,[153] and the negative thermal expansion of MOFs.[125–128,130,154,155] Identification and analysis of soft modes in phase change MOFs also offers a tool for investigating fundamental aspects of how molecular structure drives phenomena spanning spin crossover transitions, symmetry-lowering distortions, and ferroelectricity.

The contents of this section have been or are intended to be published in whole or in part. The text presented here has been modified from ACS Materials Lett. 2020, 2, 5, 499–504.[1] Copyright 2022 American Chemical Society and J. Am. Chem. Soc. 2020, 142, 45, 19291–19299.[2] Copyright 2022 American Chemical Society.

3.2 Dynamic bonding in non-carboxylated-based single-atom metal center: Fe-based versus others.

3.2.1 Spin crossover transition as a unique property that only occur in $Fe(TA)_2$ in compare to the other analogs. With the understanding of dynamic bonding in carboxylate-based MOFs, and how soft mode trigger phase

transition in MOFs, we then applied the same principle toward a 3D MOF that has been study widely for its unique conductive properties due to its unusual oxidation state and magnetic properties, $Fe(TA)_2$. Switchable behavior in materials is often designed to be abrupt and reversible, have large "memory" (hysteresis), and are triggerable by stimuli near ambient conditions. Spin crossover (SCO) is a leading example of switchable magnetism that arises from paramagnetic systems in equilibrium between high-spin (HS) and low-spin (LS) electronic configurations.[156–159] With stimuli such as thermal energy, light, guest adsorption, or pressure, the equilibria can be reversibly shifted to the magnetic state by influencing the bonding environment of the magnetic center. Relatively low-energy input is required to convert between the spin states in SCO systems because the spin-pairing destabilization energy of the LS state equals the crystal-field destabilization energy of the HS state. As octahedral Fe^{2+} comprises the great majority of SCO systems, it serves as the standard model for explicating key concepts, as follows. Low temperature favors the LS state because $t_{2g}^6 e_g^0$ electronic configurations have less metal–ligand antibonding character and hence greater enthalpic stability compared to the $t_{2g}^4 e_g^2$ HS states, while moderate temperatures, often below 300 K, favor the HS state due to its greater vibrational entropy.[160,161] Due to the impact of SCO on the electronic properties of the magnetic ions, spectroscopy can be used in addition to magnetic measurements to monitor the SCO process, including electronic absorption and ^{57}Fe Mössbauer spectroscopy.[162] Although molecular SCO complexes typically exhibit gradual spin transitions at temperatures below 300 K without magnetic hysteresis, solid-state SCO systems display abrupt transitions with magnetic hysteresis near room temperature, rendering them more useful for readable "on-off" technology.[163] Nearly all solid-

state examples are porous frameworks such as the Prussian Blue analogues or the Hofmann-type networks ($Fe(L)M(CN)_4$, L = pyrazine or pyridine, M = Co, Ni, Pd, Pt),[145,164–173] with $Fe(py)_2Ni(CN)_4$ as the seminal example,[166] while the largest SCO hysteresis has been observed in the metal–organic framework (MOF) Fe(1,2,3-triazolate)$_2$ ($Fe(TA)_2$), as shown in Figure 24.[173] Despite the importance of abrupt and hysteretic spin transitions, the specific chemistry responsible for these long-range phenomena is just beginning to emerge.

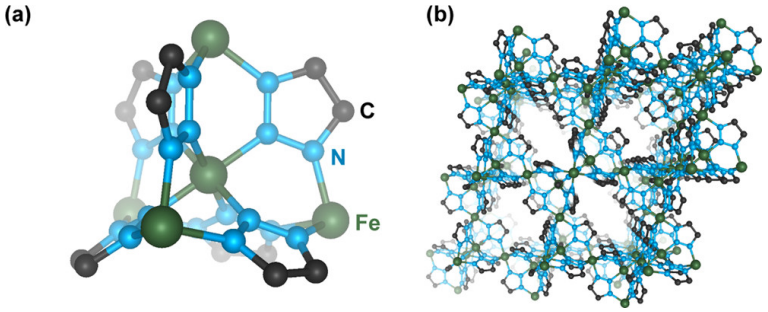

Figure 24. Representation of the $Fe(TA)_2$ metal node (a) and pore structure (b). Reprinted with permission from Chem. Mater. 2021, 33, 21, 8534–8545.[3] Copyright 2022 American Chemical Society.

Several models[174–177] describe "cooperative interactions" as the origin of solid-state SCO behavior and successfully reproduce SCO phenomena, but they generally lack insight into the chemical meaning of such interactions. Despite its ambiguity, cooperativity is a measurable thermodynamic quantity. For example, fitting spin transition equilibrium data of solid systems to a noninteracting model[178] meant for molecular SCO systems grossly overestimates ΔH and ΔS of the spin transition compared to values measured from differential scanning calorimetry. A cooperative interaction parameter Γ is thus employed to account for the apparent thermodynamic stabilization of solid-state systems.[179] Theoretical descriptions of SCO associate Γ with vibronic interactions and coupled anharmonic

oscillations between neighboring magnetic centers.[175,180,181] Although the dominant effect of Γ is to lower ΔH, the large vibrational ΔS of spin transitions has also been identified as a possible contributor to cooperativity.[175] Based on our previous work on dynamic metal–linker bonding in MOFs,[2] we hypothesized that vibrational "soft modes" drive the large cooperativity of SCO frameworks, just as they trigger other types of phase changes through coupled lattice dynamics. Specifically, we propose that certain vibrations act as "soft modes" by driving metal–ligand bonds to convert between strong and weak interactions, thereby enabling the huge volumetric expansion from the condensed LS state into the HS form, as shown in Figure 25a. Recently, we reported that the strong temperature dependence of MOF optical absorption arises in part from this thermally activated dynamic bonding.[182] Furthermore, we propose that this dynamic bonding also serves as the mechanism of both large hysteresis and abrupt transitions of SCO frameworks: the large hysteresis arises from the "expansion pressure" of neighboring HS centers forcing minority LS centers back into the HS state and the vice versa scenario for "compression pressure", causing SCO to occur at lower and higher temperatures, respectively, compared to the expected T1/2 for a system without cooperative interactions (Figure 25b). Dynamic bonding would therefore assist in the reversible bond configurations and coupled motion of neighboring atoms in this mechanism, while also causing the abrupt transitions because as lattice phonons, they drive the collective motion of the entire lattice simultaneously.

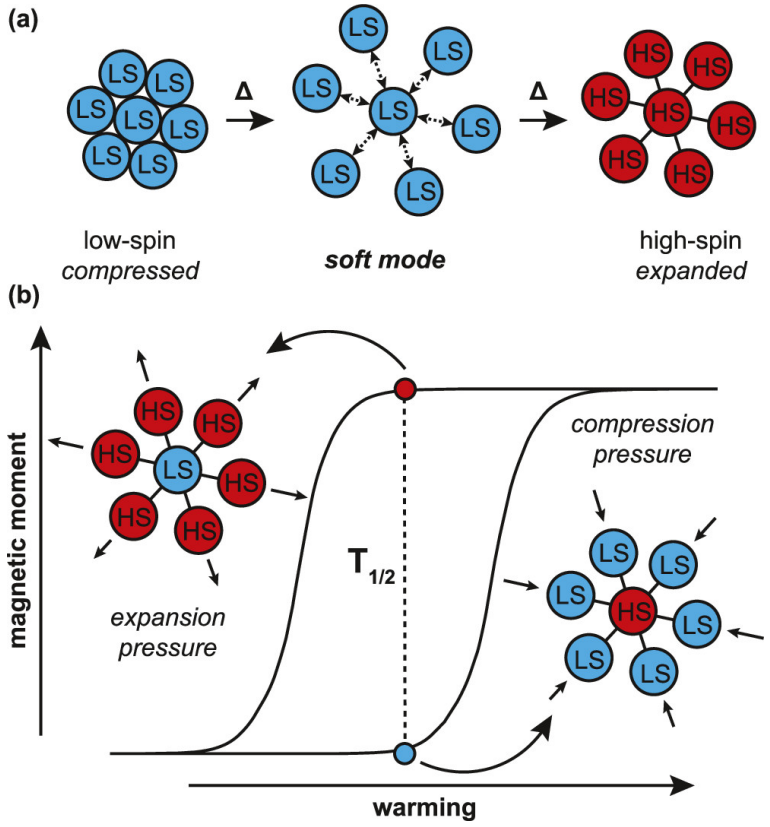

Figure 25. Representation of Bonding and Hysteresis Phenomena in Spin Crossover Behavior (a) Thermal-induced bond expansion and soft modes. (b) Magnetic hysteresis and abrupt transitions with depictions of elastic interactions between neighboring ions. Reprinted with permission from Chem. Mater. 2021, 33, 21, 8534–8545.[3] Copyright 2022 American Chemical Society.

3.2.2 Soft mode and its role in inducing spin crossover transition in $Fe(TA)_2$.

In this work, we report a combined experimental–computational investigation into the origin of the exceptional SCO cooperativity of $Fe(TA)_2$. Variable-temperature diffuse reflectance infrared vibrational spectroscopy (VT-DRIFTS) provides evidence for dynamic metal–linker bonding in the family of isostructural $M(TA)_2$ materials (M = Mn, Fe, Co, Cu, Zn) reminiscent of the "loose–tight" equilibrium phase change observed for conventional carboxylate MOFs.[2] In addition to dynamic bonding, the vibrational spectra of $Fe(TA)_2$ depict

hallmark signatures of soft modes at the SCO critical temperature, suggesting a microscopic origin of cooperativity. Thermodynamic analysis of the SCO equilibrium also allows cooperativity to be quantified, revealing an unusually large magnitude that explains the wide magnetic hysteresis. Finally, computational analysis suggests that this large cooperativity arises from the ionic and polarizable bonding inherent to MOF materials and other systems with metal ions bridged by azolates and similar ligands. Compared to other classes of SCO molecules and materials, these results explain why ionically bound networks of metal–organic bridges are uniquely well-suited building blocks for switchable magnetism, while raising fundamental questions concerning the general importance of dynamic bonding in the phase-change behavior of porous materials.

To identify the origin of the unexpected SCO behavior of $Fe(TA)_2$ and its relation to cooperativity, we investigated the dynamic bonding of $M(TA)_2$ frameworks. Bulk powder XRD of $Fe(TA)_2$ was obtained by the original Yaghi et al. method. Briefly, $FeCl_2$ was combined with 1,2,3-triazole in DMF under air-free conditions and heated to 120 °C affording a pink solid, with PXRD analysis confirming the phase purity. The related isostructural frameworks with Mn, Co, and Zn were also prepared according to the original report by Yaghi et al.[183] while the Cu material was prepared by the Volkmer procedure.[184] To explore whether $M(TA)_2$ frameworks engage in the same "loose–tight" dynamic bonding equilibrium as carboxylate MOFs, VT-DRIFT spectra were recorded between 173 and 623 K under dynamic vacuum. In Figure 26a the 173 K (LS) and 623 K (HS) spectra of $Fe(TA)_2$ are plotted with computed vibrational transitions of both HS and LS materials (Figure 26b), showing a good overall agreement.

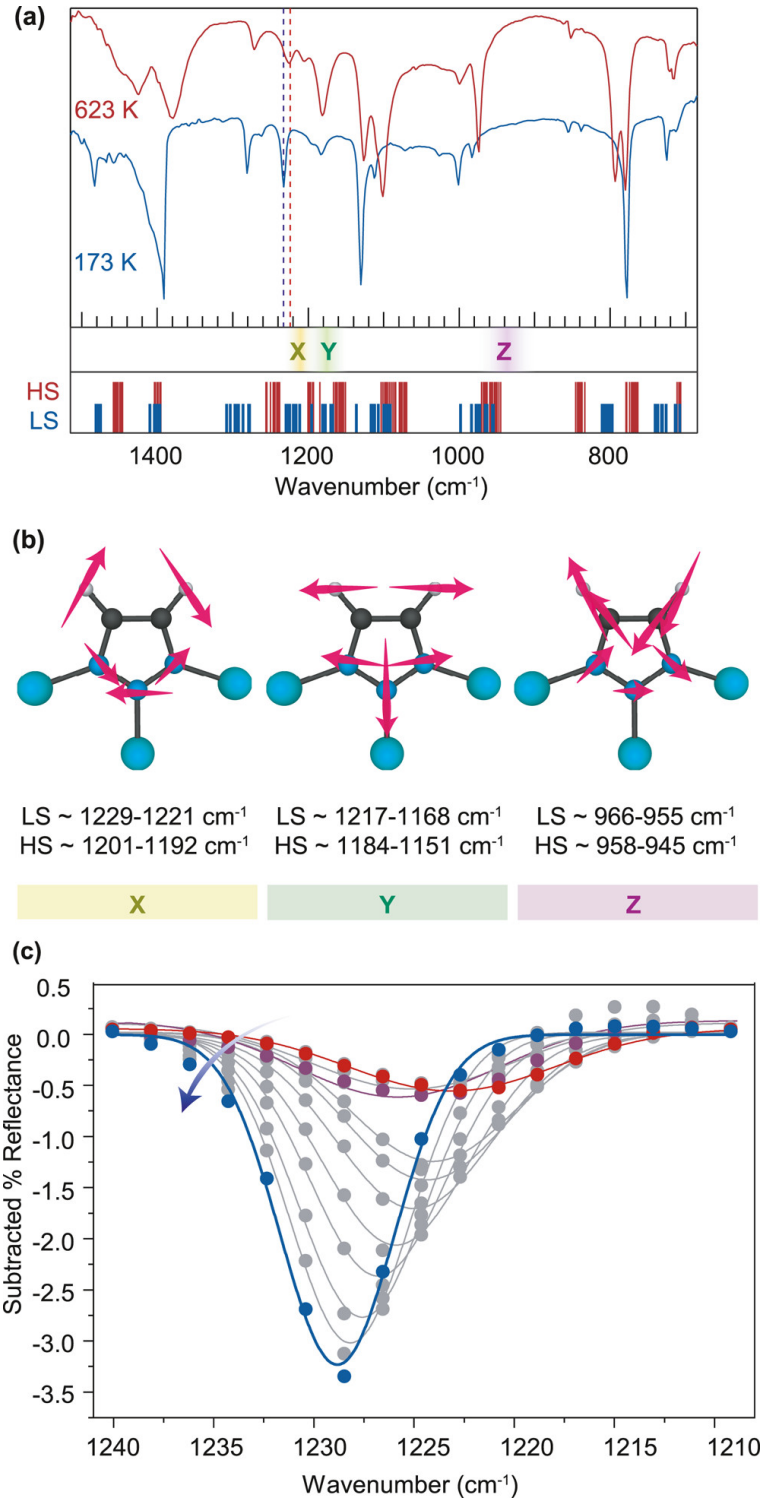

Figure 26. VT-DRIFT spectra of $Fe(TA)_2$. (a) Spectra collected at 623 and 173 K of HS and LS phases, respectively. (b) Computed vibrational modes corresponding to frequency regions X, Y, and Z. (c) Baseline-subtracted VT spectra of mode X fitted to a Gaussian function. Reprinted with permission from Chem. Mater. 2021, 33, 21, 8534–8545.[3] Copyright 2022 American Chemical Society.

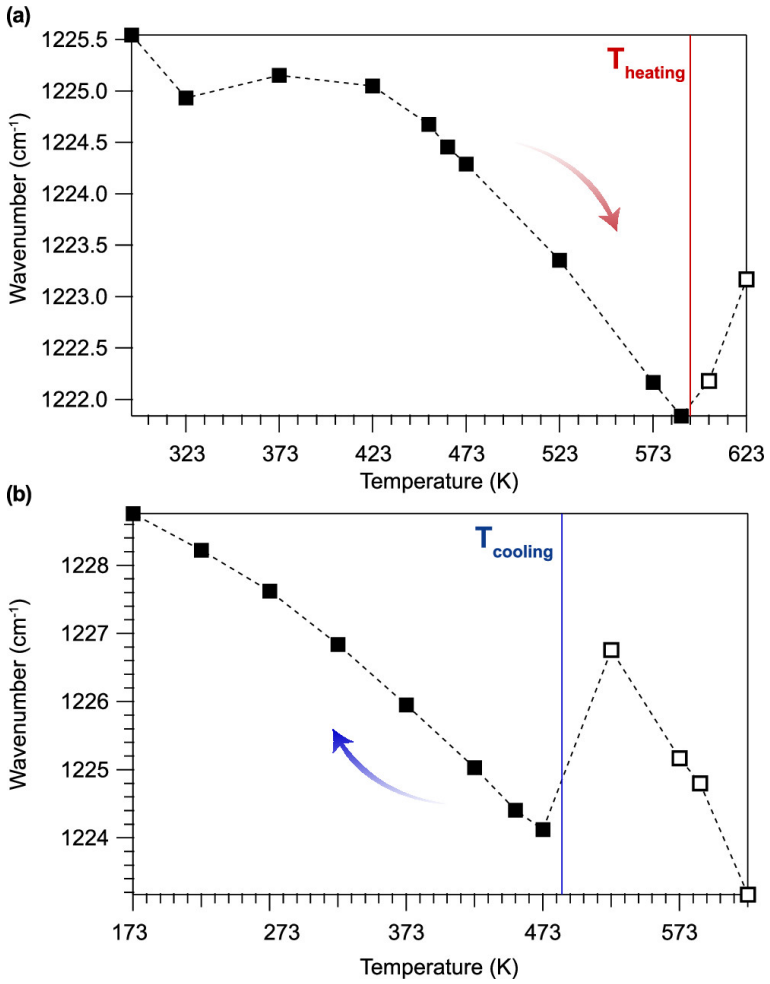

Figure 27. Peak maxima of vibrational mode "X" versus temperature. (a) Peak maxima collected during heating. (b) Peak maxima collected during cooling. Filled data correspond to $Fe(TA)_2$ in the LS state and hollow to the HS state, respectively. Reprinted with permission from Chem. Mater. 2021, 33, 21, 8534–8545.[3] Copyright 2022 American Chemical Society.

As expected for two different phases, the LS and HS spectra show considerable differences, with several bands disappearing and new bands appearing with decreased temperature (Figure 26a). This effect is also apparent in the different expected bands from the calculated phonon modes. Figure 26a,b highlights vibrations labeled X, Y, and Z that persist with temperature, which, as calculations suggest, involve triazolate-based stretches. Interestingly, vibration X,

centered at around 1230 cm^{-1}, displays temperature dependence whereas Y and Z do not. Figure 26c plots the baseline-subtracted spectra of vibration X for $Fe(TA)_2$ during a cooling cycle. Although carboxylate MOFs exhibit carboxylate stretches that red-shift linearly at higher temperatures, close inspection indicates that this triazolate mode exhibits both red- and blue-shifts with temperature.

Figure 27a plots the peak maxima of vibration X in $Fe(TA)_2$ during a heating cycle, revealing a red-shift–blue-shift inflection centered at Theating, while Figure 27b shows a similar trend centered at Tcooling during a cooling cycle. A red-shift–blue-shift inflection is hallmark evidence of the special class of vibrations known as soft modes that trigger phase transitions by pushing the atomic positions from one phase to the positions of another. As the material approaches the T_c of a phase transition, soft modes impart increasing amounts of energy to the surrounding lattice through coupled anharmonic oscillations. As a result, the soft mode red-shifts in the frequency because the vibration loses energy to the lattice undergoing a phase change. Beyond T_c, however, the soft mode blue-shifts toward its new frequency in the new phase.[83,185] Previously, we demonstrated red-shifting carboxylate stretches in carboxylate MOFs and proposed that they arise from metal–carboxylate bond weakening and equilibrium between "tight" and "loose" conformations. Although a blue shift was not observed in these studies, we hypothesized that the critical temperature of a phase change into the "loose" conformation present beyond the decomposition temperature of the MOFs. The data in Figure 27, however, show both an inflection centered at the SCO T_c and the continuation of red shifting at the highest temperatures, therefore exhibiting characteristics of both "tight–loose" and SCO equilibria. During heating, these data indicate red-shifted slopes () of 0.020 cm^{-1} K_{-1}, but upon cooling, the slope

increases to 0.035 cm^{-1} K_{-1} in the HS form and then 0.016 cm^{-1} K_{-1} in the LS form. If depends on the metal–ligand bonding strength, then the greater slope reflects the expected weaker bonding of HS species.

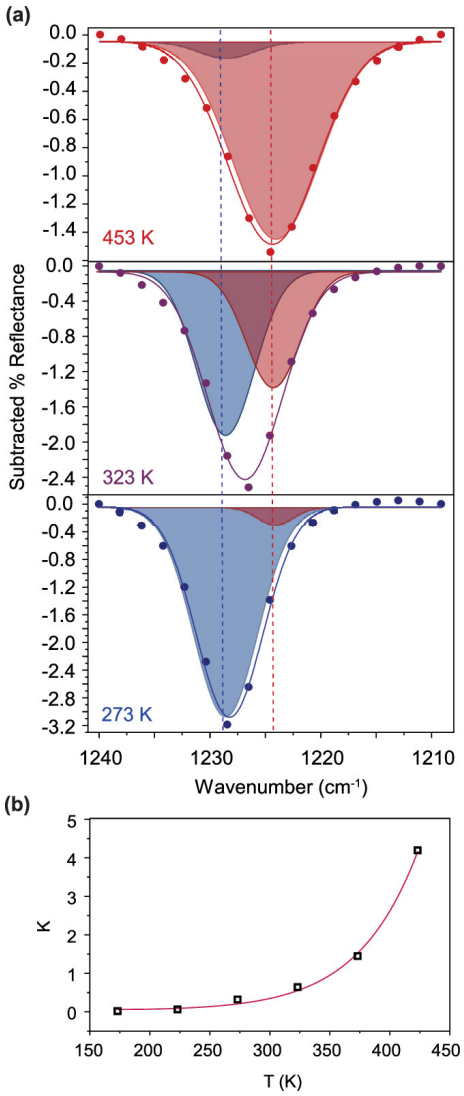

Figure 28. Equilibrium analysis of vibrational mode "X" in $Fe(TA)_2$. Data collected during a cooling cycle. (a) Baseline-subtracted spectra fitted to two species at fixed positions indicated by vertical dashed lines and (b) van't Hoff analysis of equilibrium constants K = [loose]/[tight] versus temperature. The values of [tight] and [loose] were determined from the relative integrated intensities of the high-frequency (blue) and low-frequency (red) species. Reprinted with permission from Chem. Mater. 2021, 33, 21, 8534–8545.[3] Copyright 2022 American Chemical Society.

The slight change in the red-shifted slopes in the LS phases before and after the heating cycle may indicate fatigue in the crystalline lattice, as has been observed previously in SCO solids.[186,187] To investigate whether the temperature-dependent spectra arise from equilibrium phase changes, spectra of vibration X were examined by population analysis, producing excellent fits with a low-temperature higher-frequency species centered at 1228 cm^{-1} (blue) and a high-temperature lower-frequency species centered at 1224 cm^{-1} (red) (Figure 28). These data derive from a cooling cycle with $Fe(TA)_2$ in the LS state. Akin to prior analysis of carboxylate stretches in MOFs, the positions of both species remain constant across all temperatures, while relative areas change with the high-frequency species giving way to the low-frequency species. Just as weaker metal–carboxylate binding would lead to lower-frequency C–O stretches by increasing the antibonding electron density in the C–O bond vector, weaker metal–triazolate bonding at higher temperatures would produce lower-frequency triazolate stretches. These results strongly suggest that $Fe(TA)_2$ exists in equilibrium between species with strong and weak metal–triazolate bonding, but the microscopic origin remained unclear because both SCO and "loose–tight" transitions could give rise to weaker bonding. To determine whether $Fe(TA)_2$ engages in a "tight–loose" equilibrium in addition to SCO behavior, we investigated the Mn, Co, Cu, and Zn analogues by VT-DRIFTS. Figure 29 shows the spectra of all materials collected between 173 and 623 K. Although $Fe(TA)_2$ displays a single temperature-dependent vibration, the non-SCO analogues exhibit several temperature-dependent bands, which, as calculations suggest, possess a triazolate character.

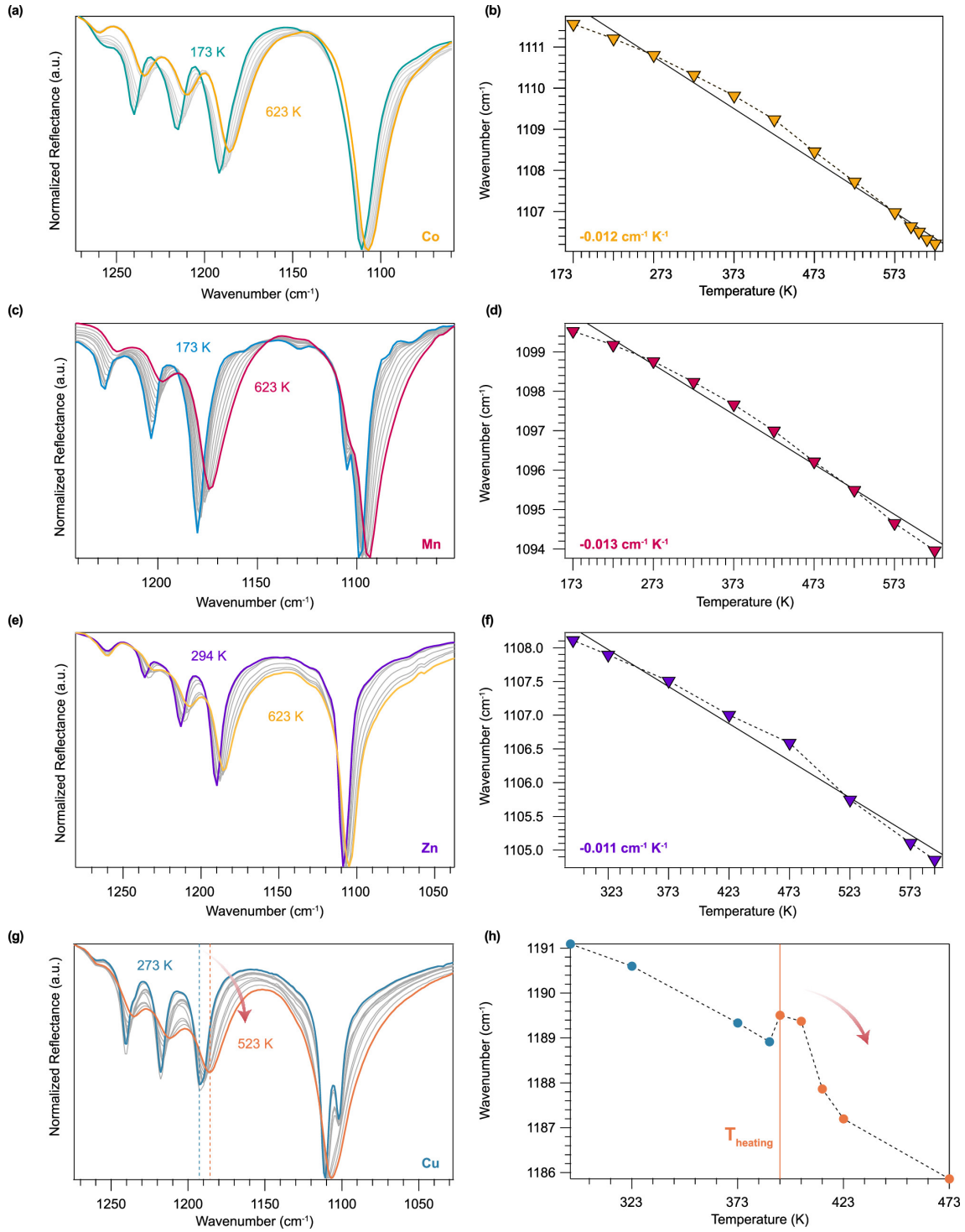

Figure 29. VT-DRIFT spectra of $Co(TA)_2$, $Mn(TA)_2$, $Zn(TA)_2$, and $Cu(TA)_2$ and corresponding peak maxima of vibrational mode "X" in each material. Data were collected during cooling cycles unless indicated otherwise. Reprinted with permission from Chem. Mater. 2021, 33, 21, 8534–8545.[3] Copyright 2022 American Chemical Society.

Unlike $Fe(TA)_2$, these bands only red-shift at higher temperatures. Although all spectra appear qualitatively similar, we focused our investigation on a single phonon mode in all materials around 1180 cm^{-1}, which also appears as the only temperature-dependent mode (vibration X) in $Fe(TA)_2$. As shown in Figure 29b,d,f, the peak maxima of this mode in $Mn(TA)_2$, $Co(TA)_2$, and $Zn(TA)_2$ linearly red-shift at higher temperatures with slopes of around 0.01 cm^{-1} K_{-1}, which are half as steep as those in $Fe(TA)_2$. Shallow slopes could arise from systems with either less dynamic bonding or from equilibria between species with similar vibrational frequencies, such as ensembles of metal–ligand conformations with degenerate potential energies. Because these slopes are smaller than the measured for carboxylate MOFs, we expect that they arise from stronger and less dynamic metal–nitrogen bonding. Unlike the Mn, Co, and Zn analogues, $Cu(TA)_2$ undergoes a phase transition from tetragonal-to-cubic symmetry.[184] Interestingly, the peak maximum of $Cu(TA)_2$ during the warming cycle exhibits a red-shift–blue-shift inflection at the critical temperature (Figure 29h), suggesting that this vibration also serves as a soft mode for $Cu(TA)_2$. Population analysis of this mode in the Mn, Co, Cu, and Zn analogues also supports the presence of two-state equilibria, strongly suggesting that $M(TA)_2$ materials undergo a "tight–loose" equilibrium even in the absence of SCO. Interpreting these fits in terms of "tight–loose" ensembles affords conventional 300 K formation constants (Kf = [tight]/[loose]) of all $M(TA)_2$ materials. Comparing $\ln(K_f)$ values, indicates that the non-phase-change materials (Mn, Co, and Zn) possess the most dynamic bonding. van't Hoff analysis of the Mn, Co, Cu, and Zn analogues produces ΔH and ΔS comparable to carboxylate MOFs, but with considerably larger ΔC_p. Notably, the ΔH and K_f are the smallest for the Mn and Zn analogues,

consistent with the labile bonding expected for these ions lacking crystal-field stabilization energies. Comparatively, the ΔH and ΔS values of $Fe(TA)_2$ are approximately twice as large as the other analogues, but they are smaller than the SCO parameters, suggesting that they arise from a "tight–loose" rather than SCO equilibrium.

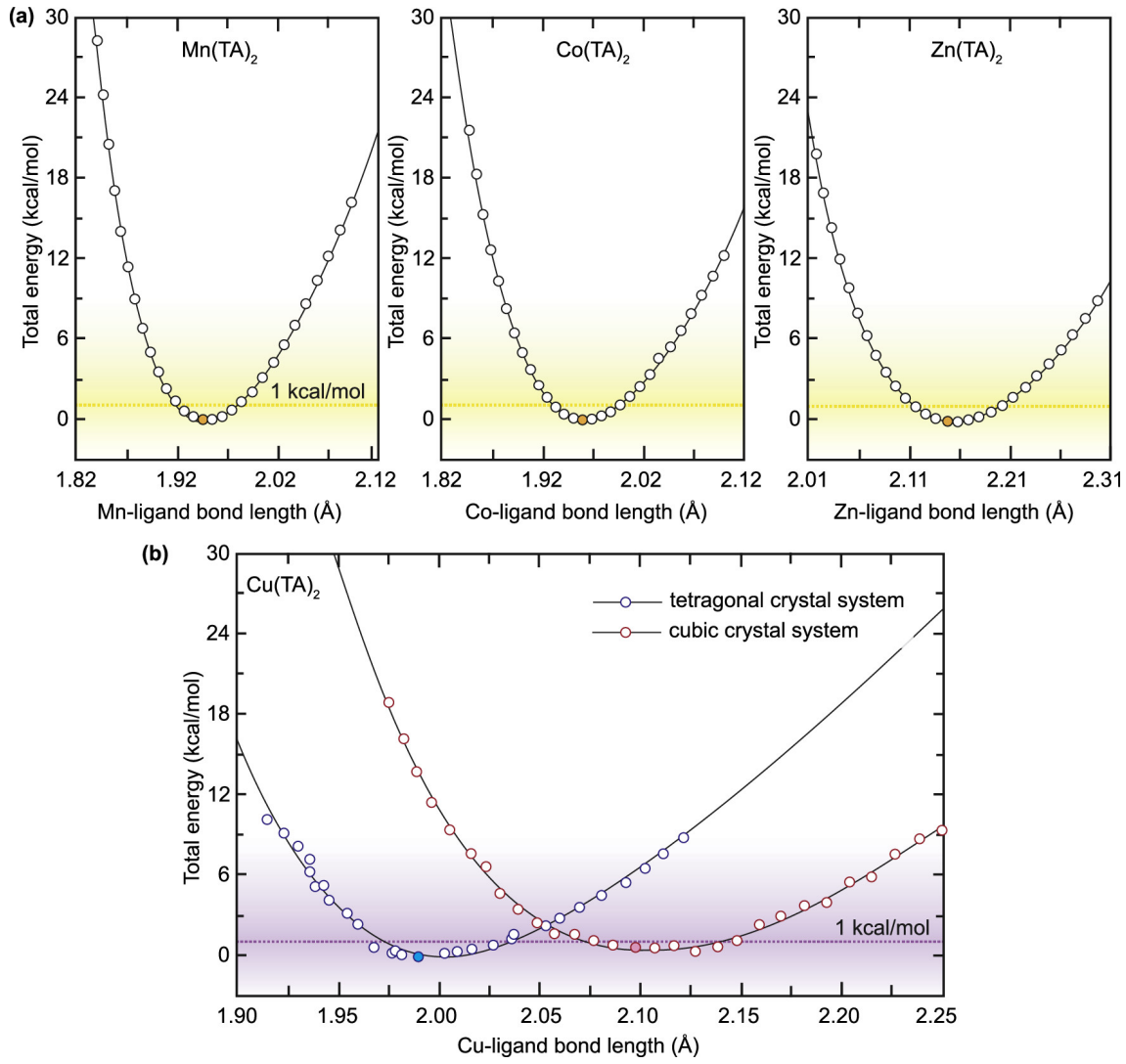

Figure 30. Total energies of geometry-optimized structures versus metal–triazolate bond lengths of (a) $Mn(TA)_2$, $Co(TA)_2$, $Zn(TA)_2$, and (b) $Cu(TA)_2$. Filled circles correspond to ground-state structures. Reprinted with permission from Chem. Mater. 2021, 33, 21, 8534–8545.[3] Copyright 2022 American Chemical Society.

Nevertheless, the larger thermodynamic parameters and the presence of only a single soft mode for $Fe(TA)_2$ imply that it proceeds through a markedly different equilibrium process. We propose that vibrations X, Y, and Z red-shift in $M(TA)_2$ materials where only the "tight–loose" equilibrium is relevant, whereas only mode X red-shifts in $Fe(TA)_2$ because it acts as the soft mode driving a separate, competing equilibrium, i.e., the low-spin-to-high-spin phase change. In other words, mode X red-shifts in $Fe(TA)_2$ because it acts as a soft mode to drive SCO, whereas modes X, Y, and Z red-shift in the other materials as a consequence of weakened metal–ligand interactions caused by dynamic bonding.

To further understand the dynamic bonding of $M(TA)_2$ materials, we computed the energies of different metal–ligand conformations. Figure 30 plots the energies of $Mn(TA)_2$, $Co(TA)_2$, $Zn(TA)_2$, and $Cu(TA)_2$ geometries with metal–ligand bond distances that were systematically altered. These "equation of state" diagrams result from uniformly compressing or elongating the entire unit cell volumes and allowing geometries to relax. Energies reflect only enthalpy since the calculations correspond to 0 K. Each data point therefore corresponds to an equilibrium geometry with variable metal–ligand distances. These diagrams are therefore analogous to single-configurational or "reaction" coordinate diagrams. In support of the presence of "tight–loose" equilibria, numerous conformations are accessible through ambient thermal energy, which is indicated by horizontal lines as 1 kcal mol–1. These calculations also reproduce the tetragonal-to-cubic phase change of $Cu(TA)_2$ and demonstrate that both phases possess nearly degenerate conformations that would give rise to "tight–loose" equilibria and red-shifted . Metal–ligand bond distances could be quantified as a function of temperature by experimentally measuring the thermal expansion coefficients (TECs) of all

materials. All TECs resemble values determined for conventional carboxylated MOFs showing values of around 10^{-6} K_{-1}, except MOF-5 and HKUST-1, which display negative TECs due to a structural mechanism that likely arises from dynamic bonding.[125,127,130] The larger TEC parameters for $Fe(TA)_2$ and $Cu(TA)_2$ are consistent with the large volume changes resulting from their phase changes. With experimental TECs, the corresponding metal–ligand conformations could be identified at each temperature. For example, comparing 173 and 623 K geometries, the metal–triazolate bond distances of $Mn(TA)_2$ shift from 1.94 to 1.95 Å, $Co(TA)_2$ from 1.97 to 1.98 Å, $Cu(TA)_2$ from 1.99 to 2.01 Å, and $Zn(TA)_2$ from 2.15 to 2.16 Å. Taken together, these experimental and computational results support the presence of dynamic metal–ligand bonding in the general family of $M(TA)_2$ frameworks.

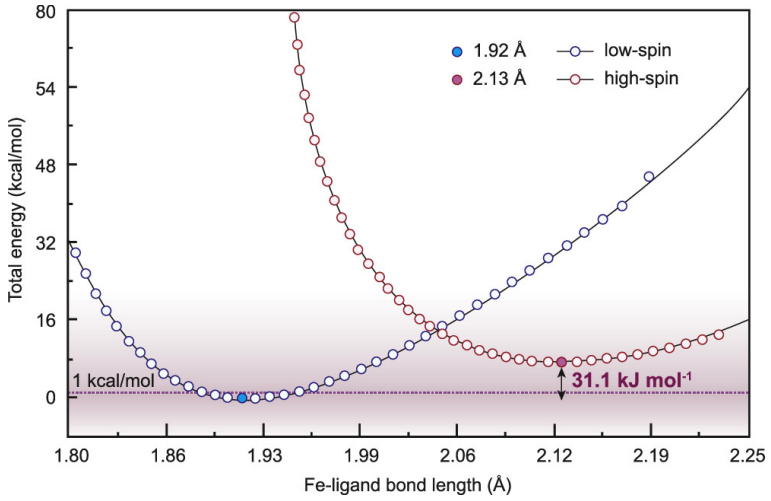

Figure 31. Total energies of geometry-optimized $Fe(TA)_2$ structures versus Fe–triazolate bond lengths. Calculations were performed at 0 K. Reprinted with permission from Chem. Mater. 2021, 33, 21, 8534–8545.[3] Copyright 2022 American Chemical Society.

To understand the relationship between "tight–loose" and SCO behavior in $Fe(TA)_2$, we investigated the energies of iron–triazolate conformations as

a function of temperature. Figure 31 plots the energies of LS (blue) and HS (red) $Fe(TA)_2$ conformations with varying iron–nitrogen bond distances. These calculations reproduce the experimental ground-state geometries (filled circles) and the experimentally determined ΔH with high accuracy: the energetic difference between the LS and HS energy curves produces a ΔH of 31.1 kJ mol–1, in excellent agreement with 31.2 kJ mol–1 measured by differential scanning calorimetry. The presence of nearly degenerate iron–nitrogen conformations within ambient thermal energy also corroborates the ability of $Fe(TA)_2$ to engage in dynamic bonding. As indicated in Figure 31, the TECs imply that metal–ligand bonds in the LS phase could elongate from 1.91 to 1.93 Å at 583 K prior to SCO. Although the relative energies of the LS and HS curves shift with increased temperature due to entropy, these results suggest that SCO may be enabled by the weakening of iron–nitrogen interactions through dynamic bonding in the LS phase. In other words, vibrational soft modes might serve as the microscopic origin of the unusual SCO cooperativity of $Fe(TA)_2$.

3.2.3 Another unique properties of Fe-based analog: cooperativity in MOFs.

For quantitative analysis of cooperativity (Γ) in $Fe(TA)_2$, previously reported magnetic susceptibility data[173] were interpreted in terms of the Slichter–Drickamer model.[179] Figure 32 plots Γ versus temperature for both cooling and heating cycles by using experimental values for ΔH and ΔS and magnetic susceptibility data to determine n_{HS}, the fraction of HS species at each temperature point. In both cycles, Γ becomes infinite at T_c and levels at large values approximately between 10 and 20 kJ mol^{-1}. A few studies, if any have quantified the value of Γ in SCO frameworks even though they exhibit the largest

cooperativity. Most reports on Γ have focused on molecular crystals with weak intermolecular interactions, giving Γ values between 1 and 5 kJ mol^{-1}.[188]

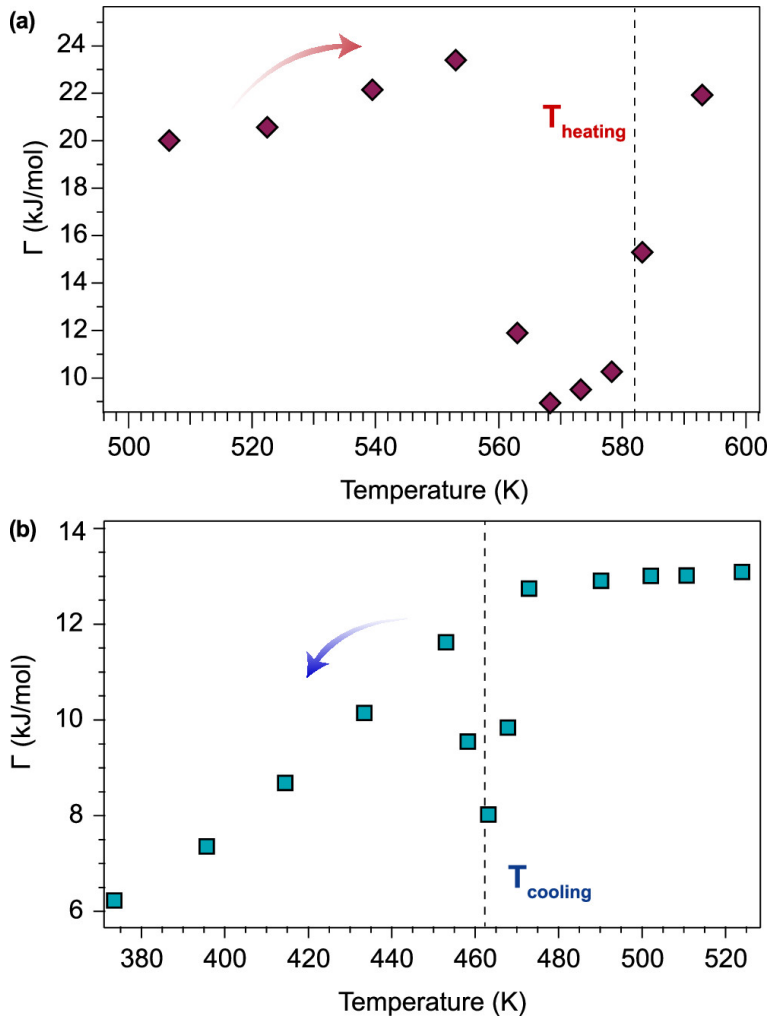

Figure 32. Cooperativity (Γ) versus temperature for $Fe(TA)_2$. (a) Cooperativity calculated from the heating cycle magnetic susceptibility data. (b) Cooperativity determined from cooling cycle data. Reprinted with permission from Chem. Mater. 2021, 33, 21, 8534–8545.[3] Copyright 2022 American Chemical Society. Reprinted with permission from Chem. Mater. 2021, 33, 21, 8534–8545.[3] Copyright 2022 American Chemical Society.

A a Γ value of 20 kJ mol^{-1} corresponds to a thermal energy of 2400 K, which is consistent with early predictions[175] that abrupt SCO transitions arise when Γ ¿ $k_B T_c$. Given the Theating and Tcooling of 582 K and 465, respectively,

Γ would correspond to a $k_B T_c$ of roughly 4–5. This analysis, therefore, provides quantitative evidence of the unusually large SCO cooperativity of $Fe(TA)_2$.

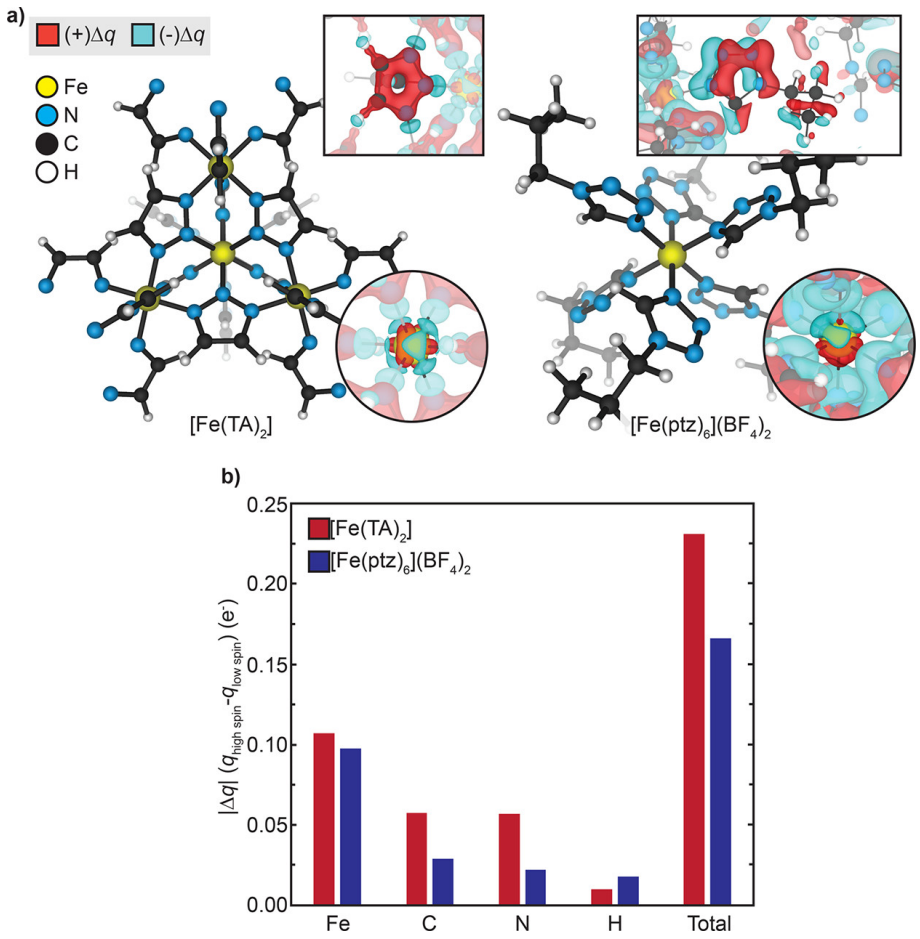

Figure 33. Calculated electron density differences Δq for $Fe(TA)_2$ and $[Fe(ptz)_6][BF_4]_2$ between HS and LS states. (a) Electron density maps. (b) Comparison between absolute differences in electron densities in total and per atom. Reprinted with permission from Chem. Mater. 2021, 33, 21, 8534–8545.[3] Copyright 2022 American Chemical Society.

With numerical support for large cooperativity and evidence that it relates to vibrational soft modes, we sought deeper microscopic insight into its origin in $Fe(TA)_2$. Previous theoretical reports contended that cooperativity arises from fluctuations in the Madelung field of a SCO material. According to this model, the greater the difference in the electrostatic interactions between the LS and HS

states, the greater the energetic driving force (cooperativity) for magnetic centers to drive each other through the spin transition. Quantitatively, the magnitude of cooperativity depends directly on the difference in the metal–ligand bond polarizations $\Delta\Delta V$ and the electron density distributions Δq of the LS versus HS states,[189] i.e., $\Gamma = \Delta q \times \Delta\Delta V$. To explore the ability of this model to account for the large Γ in $Fe(TA)_2$, we calculated Δq for both $Fe(TA)_2$ and a related molecular crystal of $[Fe(ptz)_6][BF_4]_2$ (ptz = 1-propyltetrazolate). Figure 33a shows the increased (red) and decreased (blue) Δq of both systems in the HS state relative to the LS states. In both systems, electron density shifts away from the metal–ligand bonding orbitals toward the ligand accepting orbitals. Additionally, inspection of the metal centers indicates rearrangement of electron density within the d-orbitals, as expected for a spin transition. For quantitative comparison of Δq, Figure 33b plots $-\Delta q-$ as a histogram. Although $Fe(TA)_2$ shows slightly higher changes in the electron density on the Fe centers, it exhibits a far larger change on the ligands to produce a total $-\Delta q-$ nearly 50% greater per formula unit compared to the molecular analogue. Considered together, these results, therefore, suggest that the large cooperativity of $Fe(TA)_2$, and perhaps frameworks in general, derives from vibrational soft modes that induce large differences in electron density along the metal–ligand unit. Compared to other molecular and solid-state SCO materials, we propose that MOFs occupy a perfect middle-ground state between the weak intermolecular interactions of molecular crystals and the strong covalent bonding of conventional semiconductors. Due to ionic metal–linker interactions that engage in dynamic bonding with high polarizability, cooperativity is especially strong, leading to a unique SCO behavior. The importance of dynamic bonding in driving SCO might also explain the strong size dependence of SCO particles, where large domain

sizes exhibit larger hysteresis windows at higher temperatures and more abrupt transitions.[190–195] Specifically, we expect greater bond dynamics in smaller particles due to their more flexible structures, thereby permitting SCO with less thermal energy compared to large domain sizes.

3.2.4 Method. Computational Method. Structural relaxation for all structures was performed with DFT calculations as implemented in the Vienna Ab initio Simulation Package (VASP, version 5.4.4).[53] All calculations were performed with a plane-wave cut off at 500 eV and the unrestricted GGA-PBEsol exchange–correlation functional.[146] The ionic convergence criterion was set to 0.005 eV Å–1 and the electronic convergence criterion was set to 10–6 eV. The automatic k-grid used for all optimizations was $3 \times 3 \times 3$. Symmetry was not enforced for these calculations. The optimized room temperature (RT) structures of the Zn, Co, and Mn analogues were obtained by spin-polarized calculations. The high-temperature structures were obtained by expanding the cells and then optimized by spin-polarized calculations with restricted changes in the cell volume and shape. The Fe analogues were obtained by similar methods as above, but for the RT structure, the spin moments on all Fe atoms were set to 0, and for the HT structures, the spin moment for each Fe atom was set to 4. Similarly, for the Cu analogue, the spin moment for RT and HT were set to match the experimentally reported data.[184] Energy profiles for all structures were obtained by a similar technique where the unit cell is compressed and expanded from optimized ground-state structures and then reoptimized with restricted change in the cell shape and volume. Vibrational frequency calculations were obtained via the finite difference method (FDM) as implemented in VASP where zone-center (Γ-point) frequencies were calculated. The calculations were carried out with the unrestricted GGA-

PBEsol exchange–correlation functional and with similar convergence criteria as relaxation calculations. Electronic properties for all systems were obtained from single-point calculations at the Γ-point with the HSEsol06 functional.[196]

3.2.5 Conclusion. In conclusion, VT-DRIFTS provides evidence for both dynamic metal–linker bonding in the family of $M(TA)_2$ MOFs and hallmark signatures of soft modes at the SCO temperature of $Fe(TA)_2$. These results suggest that the unusual SCO cooperativity of $Fe(TA)_2$ derives from the particularly dynamic vibrations of MOFs, in general. Modeling magnetic susceptibility data allows quantification of cooperativity, affording energetic values several orders of magnitude larger than that reported for nonframework systems. To identify the origin of this large cooperativity, computational analysis of electron density in the HS and LS $Fe(TA)_2$ structures was performed, revealing a much larger difference across metal–linker bonds compared to molecular analogues. As predicted by previous theoretical studies, such considerable changes in bond polarization, as induced by collective vibrations, trigger fluctuations in the Madelung fields thereby electrostatically stabilizing spin transitions. These results, therefore, provide a microscopic mechanism and quantitative analysis of SCO cooperativity for outlining the general design of materials with cooperative magnetism.

The contents of this section have been or are intended to be published in whole or in part. The text presented here has been modified from Chem. Mater. 2021, 33, 21, 8534–8545.[3] Copyright 2022 American Chemical Society.

3.3 Fe-based MOFs: Cooperativity differentiate MOFs from molecular solids

3.3.1 MOFs versus molecular solid analog. Metal-organic frameworks (MOFs) are nanoporous materials with high surface area[197–199]

making them outstanding candidates for industrial applications such as gas absorption/separation,[14,15] catalysis,[17] and perhaps electronic applications.[20–23] Despite their solidified physical form, most MOFs possess large charge-localization making them behave similarly to molecular solid where the metal clusters and the organic linkers act as separate chemical entities.[200] This behavior is somewhat hindered in 2D catecholate-based conductive MOFs and a few others due to their extended conjugation systems but most likely presence in 3D MOFs with minimal orbital overlaps. This allows MOFs to be modeled as either molecular clusters or extended solids yet capture accurate chemical properties of the materials including electronic properties, magnetic properties, catalytics pathways, etc.[201] Recent studies have shown a handful of 3D MOFs exhibit dynamic bondings that can initiate phase transition at high temperature further emphasizing the molecular properties of these frameworks over their solid physical form.[2,3] However, given the similarity in chemical behavior of MOFs with molecular solids, there are properties that differentiate them from molecular systems. One of such properties includes cooperativity during spin crossover transitions in MOFs that are driven by dynamic bonds between the metal clusters and the organic linkers that seems to be lacking in a molecular solid system. Spin-crossover in MOFs with large cooperativity has a distinguishing MOF framework with their molecules counterpart. In our previous study,[3] we have found that dynamic bonding of the metal-organic interface gave rise to the cooperative effect which is the main driving force of spin crossover transition in iron-triazolate. To quantify the magnitude of cooperativity, we calculated the differences in electron distribution in high-spin (HS) and low-spin(LS) analog revealing a larger cooperative effect in the MOF compared to the molecular solid analog. Iron-triazolate ($Fe(TA)_2$) is one unique system that

undergoes thermal-induced spin-crossover transition. The MOF is composed of single-iron atoms bound to the 1,2,3-triazole linkers at all nitrogen sites. Even though there have been studies that indicate this MOF as a 3D conductive MOFs, their conductivity is still not impressive even in their mix-valence form.[27] Their spin crossover properties however, raise interesting phenome-non that can be used as study concept and design principles for other porous solid frameworks.

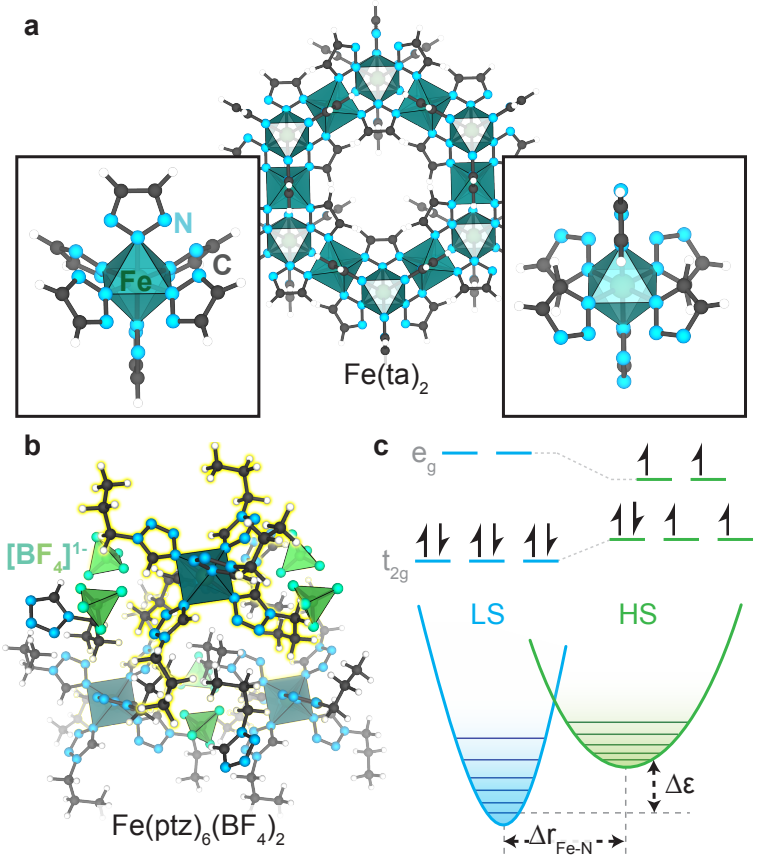

Figure 34. Pore structure and two types of metal-linker interface in $Fe(TA)_2$ (a). Representation of $[Fe(ptz)_6](BF_4)_2$ with one $[Fe(ptz)_6]_{2+}$ molecule highlighted in yellow (b). Potential energy diagram and molecular orbital diagram of low-spin and high-spin Fe^{2+} species during spin-crossover transition

In this work, we will be comparing between $Fe(TA)_2$ and an iron-complex molecular solid that can also exhibit thermal-induced spin-crossover transition

$[Fe(ptz)_6](BF_4)_2$ (ptz=1-propyltetrazole), we'll name this system Fe-ptz for this work. The structure is composed of single Fe^{2+} atoms bind to 1-propyltetrazole linkers with charge balance counter ions $[BF_4]_{1-}$ surrounding each cluster. Unlike $Fe(TA)_2$, this system tends to stay in its HS configuration and the LS configuration can only be obtained with slow cooling of the materials to a threshold that is relatively low compared to room temperature. We observed a subtle difference in the Fe-N bond length between these two materials in their LS configurations due to the difference in electron distribution in the organic linkers, while uncovering that the spin crossover transition in Fe-ptz is less favourable in the molecular solid form while cooperativity in the MOF framework allows $Fe(TA)_2$ to undergo LS to HS transition that would otherwise won't happen in the molecular cluster form. We provide further evidence that cooperativity is the driving force in $Fe(TA)_2$ for spin crossover transitions and compare that to the lack of cooperativity in the molecular solid Fe-ptz. We also found a correlation between the electronic properties of $Fe(TA)_2$ with the magnitude of cooperative effects among the metal sites. Together, this computational study provides plenty of evidence that although MOFs inhibit charge localization similar to molecular solid, there are physical properties and electronic properties that exist in MOFs that do not occur to similar molecular analogs.

3.3.2 A closer look at how cooperativity in $Fe(TA)_2$ distinguishing the framework from similar molecular solid.

Although the Fe^{2+} centers for both structures adopt an octahedral coordination sphere, the structures are somewhat different in terms of the organic linkers and the metal-linker bond length. The average Fe-N bond length in $Fe(TA)_2$ is 1.91 A and the average Fe-N bond length in the molecular system is about 0.016 A longer. The

denser electron density on nitrogen atoms in the triazole linkers might account for this shorter Fe-N bond length in the MOF. As shown in Figure 35, each nitrogen atoms on the triazole linker possess a charge of -0.159 to -0.163 e- while in the propyl-tetrazole linker, the charge density on nitrogen atoms is less uniform, localized mostly on the nitrogen attach to the carbon tail.

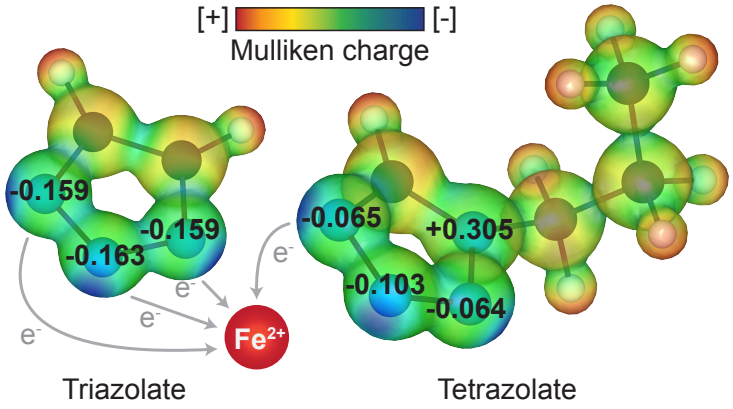

Figure 35. Mulliken charge density plot of triazole and propyl-tetrazole linkers.

The nitrogen binding site for Fe^{2+} on the propyl-tetrazole linker has a charge of -0.065 e-, which is relatively small compared to that of those in the triazole linkers; this explains the longer bond length in the molecular solid compared to the MOF. Furthermore,the higher electron density in the triazole linkers contribute to a larger orbital splitting between the e_g and the t_{2g} compared to that of $[Fe(ptz)_6]_{2+}$, making HS cluster structure of $Fe(TA)_2$ unstable and not obtainable in the molecular form. We performed geometry relaxation on cluster structures of $Fe(TA)_2$ and $[Fe(ptz)_6]_{2+}$, both LS structures reached convergence, where only the HS structure of $[Fe(ptz)_6]_{2+}$ is obtainable. This signified the role of cooperativity in the spin crossover transition that occur in $Fe(TA)_2$ that HS Fe^{2+} bind to the 1,2,3-triazole linkers which can only be obtained via solid form. We then examine the potential energy surface of the Fe-ptz cluster. Figure 36 shows the energies

of the molecular cluster for Fe-ptz as a function of increasing Fe-N bond length (approximately 0.01 A increment). The average increase in Fe-N bond length is about 0.19 A going from LS to HS configuration which is very similar to that of the $Fe(TA)_2$ in our previous studies (1.91 A to 1.93 A).

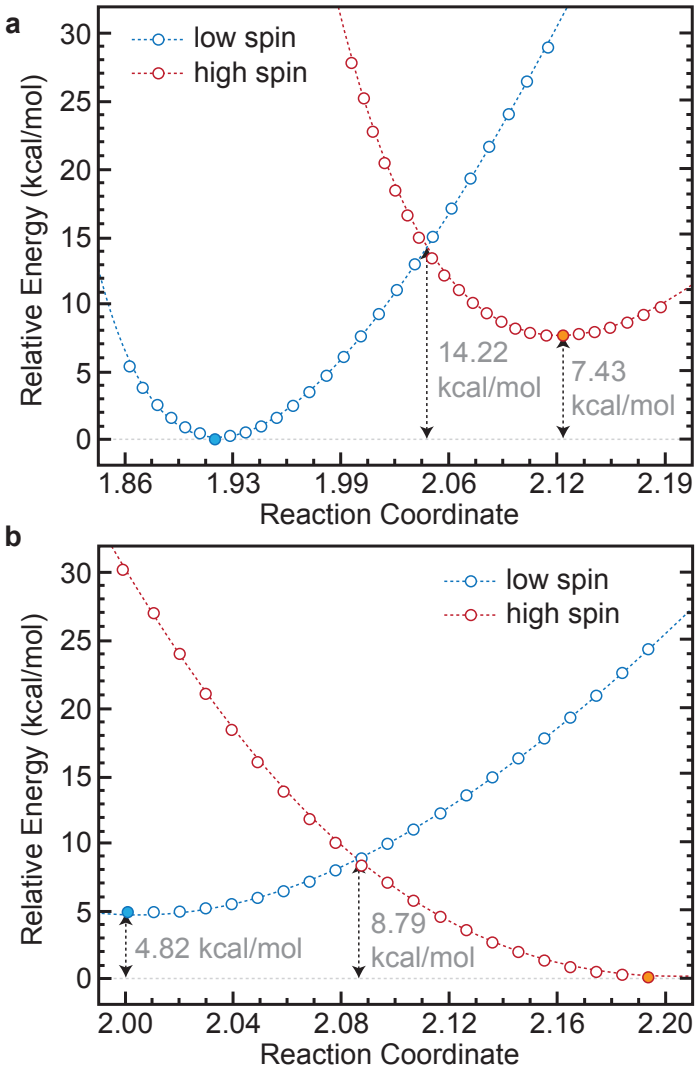

Figure 36. Potential energy surface of low-spin (blue) and high-spin (red) of $Fe(TA)_2$ extended solid (a) and $[Fe(ptz)_6]_{2+}$ molecular cluster (b). Filled circles indicate the energy of the optimised LS and HS structures used to create other structures.

However, the $Fe(TA)_2$ potential energy surface, the HS configuration is more favorable, with an energy that is 4.82 kcal/mol lower than that compared to the LS configuration. In $Fe(TA)_2$ solid structure, this energy difference is about 7.43 kcal/mol, but more favorable for the low spin system.[3] The energetic barrier going from LS to HS is 3.97 kcal/mol and HS to LS is 8.79 kcal/mol. Interestingly, for the Fe-ptz molecular solid, the HS state is more obtainable in experimental setting and the LS state can only obtain by slow cooling the materials under a certain temperature threshold, and since DFT is design to fit with experimental data, it is sensible that the HS state for the molecule is more favorable than the high spin-state.

Furthermore, as discussed previously, due to the lower electron density on the nitrogen that binds to the Fe^{2+} atom, Fe-ptz has a smaller orbital splitting energy between the e_g and t_{2g} orbitals, making HS state more accessible. We also model the cluster structures without the charge neutral agents $[BF_4]_{1-}$ which exist in the molecular solid, these negatively charged molecules might play a role in stabilizing the carbon tails, pushing more electron toward the nitrogen atoms in the ring, allow the LS configuration to be somewhat stable relative to the HS configuration. To examine this, we performed calculation of Fe-ptz as a molecular solid with $[BF_4]_{1-}$ molecules. Our result shows that the energy difference between the HS and LS Fe-ptz in the molecular solid form wth $[BF_4]_{1-}$ ions increased from 4.82 kcal/mol to 11.64 kcal/mol. This increase of energy comes from both the presence of the $[BF_4]_{1-}$ ions and also other $[Fe(ptz)_6]_{2+}$ molecules. One can say that spin crossover transition of $[Fe(ptz)_6]_{2+}$ is less favorable in their molecular solid form compared to single molecules form. For $Fe(TA)_2$, our previous work has shown that cooperativity facilitates spin crossover transition.[3] The ratio of

HS/LS Fe^{2+} in the framework can either hinder or pushforward the spin crossover transition. We investigated the lattice parameters and the change in energy of the MOF and the molecular solid systems as HS/LS Fe^{2+} ratio increases. For Fe-ptz, as we increase the number of HS Fe_{2+}, we observe a constant decrease in energy and an increase in a lattice parameter almost in a linear fashion (Figure 37b). This agrees with our molecular cluster calculations as HS Fe-ptz is lower in energy compared to that of the LS analogs, as the number of HS clusters appear in the molecular solid, the energy of the whole system drops and each cluster seems to behave discreetly with respect to one another.

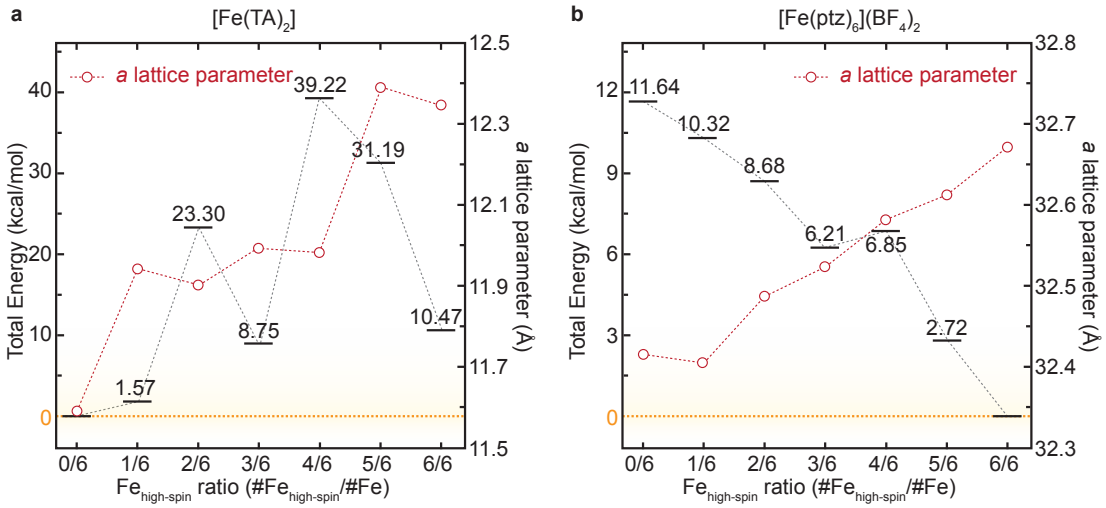

Figure 37. Energy (black) and a lattice parameters (red) of $Fe(TA)_2$ and Fe-ptz in molecular solid form with increasing number of HS Fe2+

On the other hand, the spin state of each Fe^{2+} cluster in $Fe(TA)_2$ is dependent on their surrounding Fe^{2+} cluster. There are several minima in the $Fe(TA)_2$'s energy surface, at HS/LS ratio of 3/6 and 6/6 (all HS) and several maxima, at 2/6 and 4/6. Notice that unlike in Fe-ptz, where the maximum and minimum energy are at all LS and all HS, respectively, the all HS structure of $Fe(TA)_2$ is at a local minimum hence it will be much more stable because it need

to overcome that transition barrier at 4/6 and 2/6 HS/LS Fe^{2+} ratio. The energy plot of $Fe(TA)_2$ also demonstrate cooperativity exist with $Fe(TA)_2$ where if enough energy is provide for the systems to reach 2/6 and 4/6 HS/LS Fe^{2+} ratio, getting to 3/6, 5/6 and all HS Fe^{2+} are favourable. The more HS Fe^{2+} sites exist in the systems, the easier for LS to HS crossover transition to occur. One can also see the increase in a lattice parameter is not as constant as seen in Fe-ptz as the number of HS Fe^{2+} increases, the first big expansion of the unit cell happen after a LS to HS transition at one Fe^{2+} site, and the final large cell expansion occurs with 5 Hs Fe+ emphasise the cooperativity effects in $Fe(TA)_2$ where the 5th HS Fe^{2+} sites in a 6 Fe^{2+} sites unit cell cause a significant cell expansion that force the last Fe^{2+} site to also adopts the high spin configuration (a drop in energy of 20.72 kcal/mol).

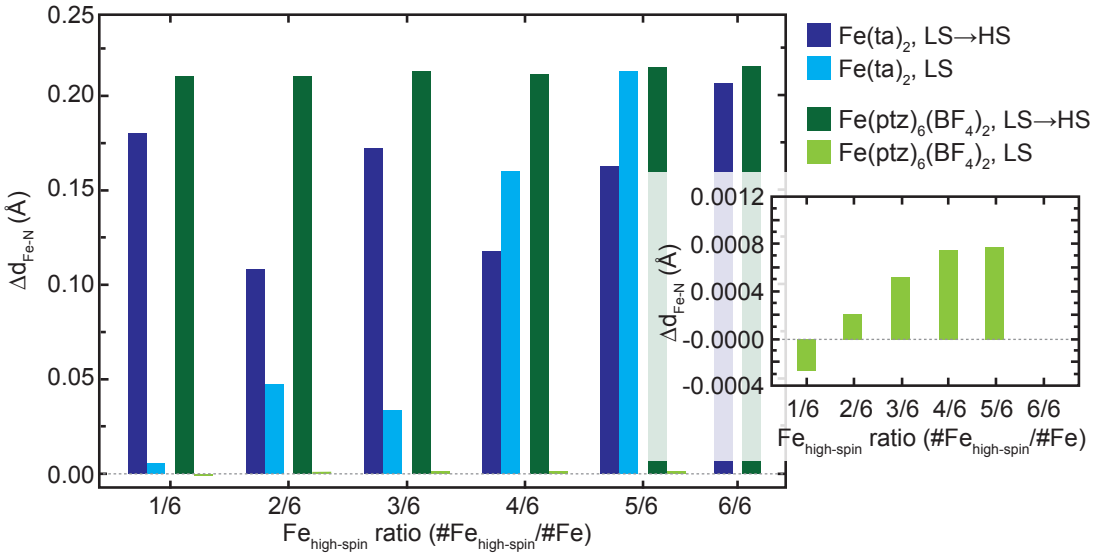

Figure 38. Average Fe-N bond length change for Fe^{2+} coordination that undergone LS to HS transition and those that did not as the number of HS Fe^{2+} sites increase in the unit cell.

To further support our hypothesis, we calculated the average Fe-N bond length change as we increase the number of HS Fe^{2+} sites in $Fe(TA)_2$ and Fe-ptz

(Figure 38). For those sites that underwent a LS to HS transition, the change in Fe-N bond length is relatively constant for Fe-ptz (dark green) which agree with the result obtained about where each Fe^{2+} cluster behaves separately for each other. If the ionic bond between the metal-organic interfaces in MOFs make them act similar to molecular solids, we would expect to see similar result as Fe-ptz, however, their are relatively large fluctuation of these changes because unlike a molecular solid, MOF act as a networks that the change in metal-organic bond length at cluster has a direct effects on the other (demonstrated as dark blue bars in Figure 38). For the sites that did not undergo a LS to HS transition in Fe-ptz, we see a negligible change in Fe-N bond length compared to that of those sites that underwent transition (light green, right panel). In $Fe(TA)_2$, even if the Fe^{2+} does not undergo spin crossover transition, the Fe-N still undergoes some changes and the stronger the the cooperativity effect is, the larger the increase in Fe-N bond length. For instance, as we conclude from Figure 37a, the cooperativity effect is the strongest at 4/6 and 5/6 HS/LS Fe^{2+} ratio, which is shown here to have the largest change in Fe-N bond length for those Fe^{2+} that do not undergo transition.

3.3.3 Cooperativity's effect on the electronic properties of Fe-based MOFs. Although MOFs can be modelled as molecules, and electronic information can be retrieved very accurately, we still lose a lot of information that can only be obtained from extended solid modelling such as cooperativity as shown above. Not only the cooperativity play an important role in alter the physical properties of the materials itself, it also play an important role in altering the electronic structure of the materials since the metal-organic bond length, bonding type (covalent/ionic), and electron configurations are factors that affect the carrier concentration and mobility in a material. We hypothesise that cooperative effects

not only enforce spin-crossover transition, but also enhance the bonding interaction between the metal-organic interfaces.

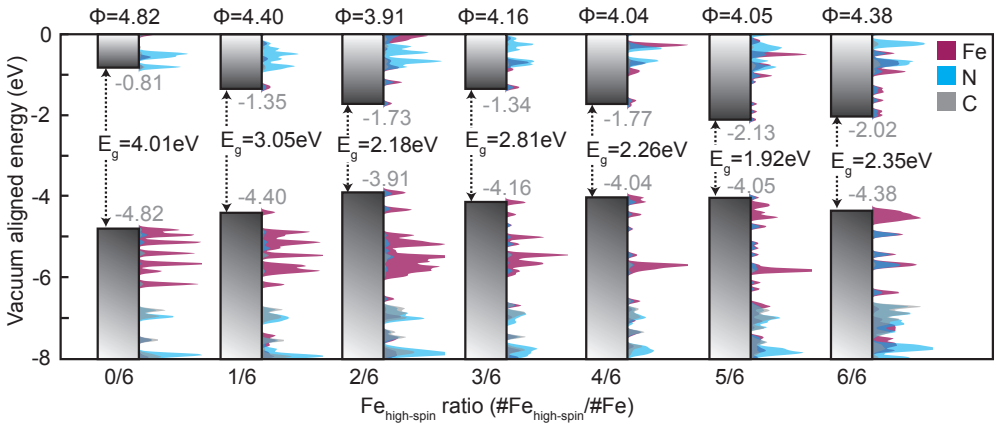

Figure 39. Electronic structure of $Fe(TA)_2$ with increasing number of HS Fe2+

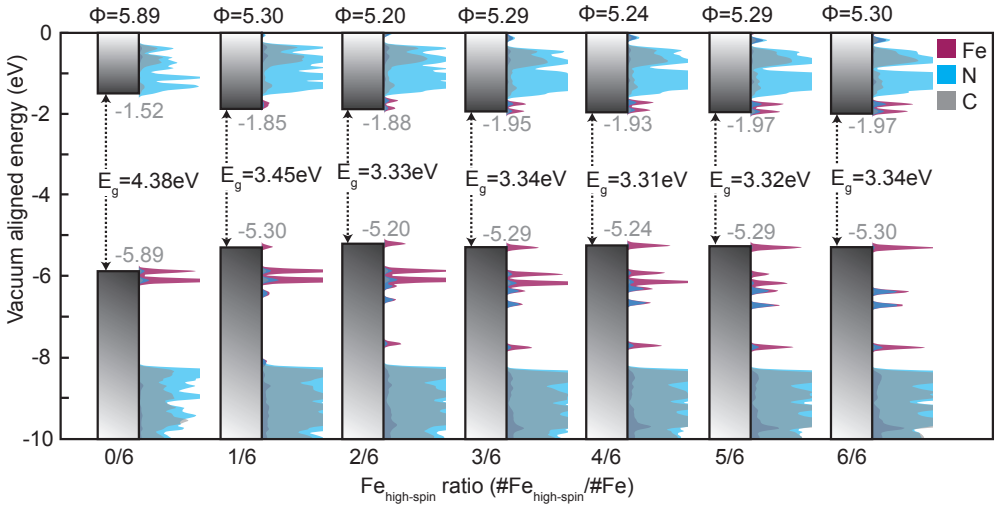

Figure 40. Changes in electronic structure of Fe-ptz as the number of HS Fe^{2+} sites increase.

As one would expect, when a material transitions from a LS state to a HS state, the band gap would decrease due to orbital delocalization and the increase in electrons' energies. In fact, that was found to be true for Fe-ptz, the transition from LS to HS reduces the band gap by approximately 1 eV for all HS/LS Fe^{2+}

ratio (Figure 40). Since each clusters in Fe-ptz act on their own, the band gap stays almost constant having 1 HS Fe^{2+} to 6 HS Fe_{2+}. Interestingly, a LS to HS transition in Fe-ptz allows both the conduction band and valence band to contain Fe characteristic as opposed to no Fe DOS in the LS configuration. This could give rise to design principles for similar materials where band edge control is necessary.

For ionic material such as MOFs, we would expect similar consequences where the reduction of band gap will occur when a single HS Fe^{2+} is introduced to the systems and the band gap will stay constant for concurrence of HS Fe_{2+}. The former was found to be true where the band gap of $Fe(TA)_2$ dropped by 0.96 eV after the introduction of a HS Fe_{2+}, but the band gap did not stay constant after more concurrence of more HS Fe_{2+}. In fact, the band gap reduces to 2.18 eV at a 2/6 HS/LS Fe^{2+} ratio (Figure 39). One would expect to see a larger reduction of band gap for each additional HS Fe^{2+} sites following this trend, however, the band gap go back up to 2.81 eV with one more additional HS Fe_{2+}, decrease again with 4 and 5 HS Fe^{2+} site and go back up with 6 HS Fe_{2+}. Notice that the lowest band gap occurs at 5HS/1LS Fe^{2+} ratio where we proposed that the cooperativity effect is the largest according to the Fe-N bond length changes and the energy surface of $Fe(TA)_2$ (Figure 37 and Figure 38). These affect not only the spin configuration of the material forcing the last LS Fe^{2+} centre to adopt the HS configuration but at the sametimes strengthen the bonds that exist within the frameworks and enhance charge delocalization. This demonstrates that $Fe(TA)_2$ are a lot different from their molecular solid analog Fe-ptz in terms of their electronic properties that are mostly driven by cooperativity.

3.3.4 Method. Computational Method. Structures of $Fe(TA)_2$ and $[Fe(ptz)_6](BF_4)_2$ were obtained, each containing 6 iron atoms within the unit

cells. Electronic relaxations were performed on both structures with an enforced spin of 0 on all Fe atoms corresponding to the LS state of both structures. The ionic convergence criterion was set to 0.005 eV A^{-1} and the electronic convergence criterion was set to be 10_{-6} eV. The projected augmented wave (PAW) basis set[147] was used and the plane wave cutoff was set to be 500 eV. All optimizations were performed with the PBEsol exchange correlation functional.[146] All calculations with periodic boundary condition were performed with the Vienna Ab initio Simulation Package (VASP, version 5.4.4.).[53] $Fe(TA)_2$ structure was optimized with an automatic k-grid of 3 x 3 x 3 while the molecular solid,$[Fe(ptz)_6](BF_4)_2$ was optimized with a k-grid of 1 x 1 x 1 due to its large structure. HS iron exhibits 4 unpaired electrons, so each of these optimized unit cells was then used for structure relaxations with enforced spin of 4, 8, 12, 16, 20, and 24, corresponding to an increased number of high spin iron from 1 to 6 in the unit cells. To obtain more accurate energy of these structures, a single-point calculation at the Gamma-point was performed on each of these structures with similar convergence criterion as above with the hybrid exchange-correlation functional, HSEsol06.[148] Electronic structures were plotted using these calculations. Molecular structure of $[Fe(ptz)_6]_{2+}$ was extracted from the optimized bulk structure and cluster structure of $Fe(TA)_2$ were also extracted from the optimized bulk structure of $Fe(TA)_2$. Both of the extracted molecular structures were subjected to structural relaxation for both HS and LS state. All cluster calculations were performed with DFT as implemented in the Gaussian 09 software package. Relaxation calculations were performed with tight convergence criterion with the 6-311G basis sets including double-zeta polarization and diffuse functions. The PBE exchange-correlation functional was used for the optimizations for these structures. $Fe(TA)_2$ cluster HS model did

not converge with several attempts of initial structure manipulation and loose convergence criteria. For $[Fe(ptz)_6]_{2+}$, the final Fe-N bond lengths were measured for both HS and LS, then a series of 20 geometries were created by interpolating between the HS and LS Fe-N bond lengths. Each structure was then subjected under modredundant calculations with freeze Fe-N bond lengths for both HS and LS configurations. These were carried out with PBE exchange-correlation functionals and similar basis sets mentioned above. Single-point calculations were performed using the optimized geometries obtained from the previous calculations with the HSE06 functionals to obtain more accurate energies to plot the potential energy surfaces in Figure 36. The two linkers shown in Figure 35 were also extracted from the bulk optimized structures, both were then optimized using the 6-311G basis sets (including double-zeta polarization and diffuse functions) and the HSE06 functionals, and the respective charge density plot were created from these results.

3.3.5 Conclusion. In this work, we elucidate the properties that differentiate a 3D MOF, $Fe(TA)_2$ from their molecular solid analog Fe-ptz. Although they both exhibit charge localization and are very similar structurally in their LS configuration, the lack of cooperativity between the Fe^{2+} clusters in the molecular solid is making spin crossover transition less favourable in these systems compared to that of the MOF materials. For Fe-ptz, we found that the lack of electron localization on the metal-binding-nitrogen is causing a weaker bond between the metal and the organic linkers contributing to a smaller splitting between the eg and t2g orbital making the HS configuration energetically favourable compare to the LS configuration. This energetic effect is even larger when these molecules were modelled as an extended solid with charge

balance counter ions $[BF_4]_{1-}$. The opposite was found for $Fe(TA)_2$ where their HS molecular form is not obtainable and the cooperativity was found to be a major driving force for the extended solid HS configuration. This cooperativity effect was at its strongest when the HS/LS Fe^{2+} ratio was at 5/6 where we overcame the highest transition barrier and where the final expansion of the solid happened. We also demonstrate that this cooperative effect has a major contribution to enhance delocalization reducing the electronic band gap which was not the case in the molecular solid Fe-ptz. Overall, our computational studies emphasise the importance of cooperativity in spin crossover transition in MOFs, and differentiate them from their molecular solid analog. Even though MOFs can be model as molecules, one need to keep in mind that there are crucial information that would be lost such as the effect of cooperativity that can only be retrieved from extended solid modelling of the MOFs.

CHAPTER IV

COVALENCY IN METAL-LIGAND INTERFACE IN 2D CONDUCTIVE MOFS

4.1 Evidence of Covalency in Metal-Linker Interface in 2D Conductive MOFs

4.1.1 The challenge of utilizing MOFs in electronic applications due to their ionic bonding characteristic. Previous studies of MOFs have shown that this class of structurally diverse materials are unique due to their porous architecture and resultant high surface areas.[197–199] The application of a particular MOF depends on the chemistry of both the inorganic metal ions/clusters and the organic linkers. Considering their structure and composition, MOFs have been decidedly useful in gas separation and storage,[13–16] catalysis,[17] drug delivery,[18,19] and energy-related applications such as light harvesting,[20] thermoelectrics,[21] and supercapacitors.[22,23] In case of the latter, a MOF's utility is intimately related to its electrical conductivity. Thus improving electronic delocalization is paramount if these scaffolds will be useful in energy storage devices.[202–205] However, most MOFs are wide gap electrical insulators with heavy charge carrier effective masses.[206**?** ,207] These properties stem from their highly ionic metal–ligand interface.[200] Furthermore, the only successful route to doping a metal–organic framework relies on the redox properties of the ligand and/or metal. This approach has been fruitful; redox-induced charge hopping[13,27,208–210] has been shown to result in increased electrical conductivity. But given most charge carriers are formed thermally, the band gap, and nature of the frontier orbitals and their corresponding energetics is of critical importance for generating conductive scaffolds.

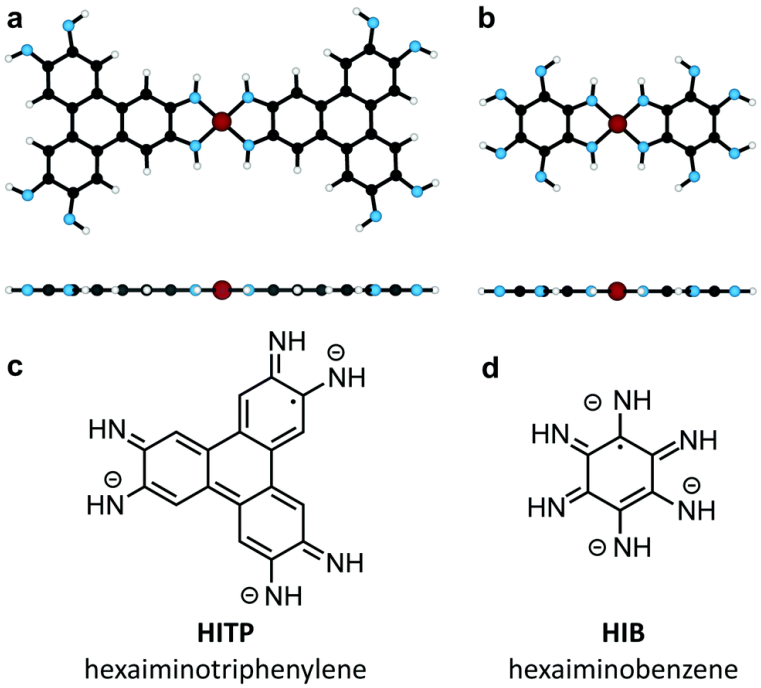

Figure 41. A portion of (a) $Ni_3(HITP)_2$ and (b) $Ni_3(HIB)_2$. The oxidation state and one resonance depiction of each ligand is presented in (c and d), respectively. Atoms are depicted in C – black, N – blue, H – white, and Ni – madder. Reproduced from Phys. Chem. Chem. Phys., 2019,21, 25773-25778[4] with permission from the PCCP Owner Societies.

Two of the highest performing conductive MOFs, $Ni_3(HITP)_2$ (HITP 2,3,6,7,10,11-hexaiminotriphenylene) and $Ni_3(HIB)_2$ (HIB hexaiminobenzene) are 2D-connected bulk metals (truncated building blocks are shown in Figure 41), with corresponding electrical conductivities of 60 S cm[1 30,211] and 8 S cm[1],[212] respectively. Despite their structural similarities, monolayer $Ni_3(HITP)_2$ features a discrete 0.2 eV band gap;[213] electrons are thought to conduct in the bulk material in the non-covalent -stacked direction, perpendicular to the covalent sheets.[214] Foster and colleagues further explored this by demonstrating that $Ni_3(HITP)_2$ undergoes a metal-to-semiconductor transition by separating its sheets (either through chemical pillaring or otherwise).[213] Conversely, $Ni_3(HIB)_2$ is metallic in-plane but insulating in the bulk non-covalent directions.[212] The electronic

dissimilates between these two scaffolds are governed by the electronic differences of the ligand (one resonance structure for each are shown in Figure 41c and d). In both syntheses the ligand is required to be triply oxidized and deprotonated six times to yield a charge neutral scaffold. Ideally, these 2D connected MOFs would feature metallic character in all directions, minimizing the reliance of crystallographic packing in the non-covalent axis. However, without augmenting the composition of the MOF, there are no reports of the installation of a semiconductor-to-metal transition in the $Ni_3(HITP)_2$ monolayer. Here we propose the application of pressure to modulate the electronic structure of these conductive scaffolds in order to obtain novel electronic properties from these promising conductive scaffolds.

4.1.2 Pressure modulation as a way to probe the metal-organic interface in MOFs. Hydrostatic pressure, both positive and negative, may be experimentally applied mechanically, or by thermal expansion, gas adsorption,[215,216] etc. In some cases, this process can result in amorphization, phase transitions, and other structural changes of the frameworks,[217–220] but MOFs are known to be stable up to relatively high pressure and temperature.[102,221,222] With this in mind, the effect of pressure on the electronic structure of both $Ni_3(HITP)_2$ and $Ni_3(HIB)_2$ has not been previously examined. Here, we demonstrate that under facile lattice expansion, $Ni_3(HITP)_2$ becomes an in-plane metal. Further, we observe $Ni_3(HIB)_2$ undergoes electronic re-ordering to reduce Ni^{2+} to $Ni^{1.33+}$ while oxidising each ligand by 1e, an effect we term "piezoreduction".

Models of bulk $Ni_3(HITP)_2$ and $Ni_3(HIB)_2$ are complicated because the interplane potential energy surface is relatively shallow.[27] However, much can be gained from examination of the monolayer, as a single sheet allows us to monitor

the electronic properties within the covalent plane without having to examine the emergences of magnetic ordering or other secondary effects. Following the procedure detailed in the computational methods, we assess the effect of pressure through the lens of the electronic band structure, density of states, and magnetic properties in the monolayer. Based on prior work,[223] we hypothesized that the addition of pressure would stabilize bonding interactions, while destabilizing their antibonding partners.[224] Further, since the metal–ligand bonds are weaker than the organic covalent bonds of the ligand, geometric alterations to the framework are expected to be most evident at the metal–ligand interface. Thus, we hypothesize that bands that contain Ni–N bond characteristics will display larger energetic shifts than, for example, bands associated with the conjugated carbon backbone.

Lattice contractions are expected to also increase band dispersion due to increased inter-atomic interactions.[224] $Ni_3(HITP)_2$ exhibits a minor increase in band curvature (+0.05 eV, Figure 42a) compared to its equilibrium structure. Similarly, $Ni_3(HIB)_2$ is persistently a metal even and at high pressure (43 kB, Figure 43a) metallic bands become marginally more disperse (+0.03 eV).

Conversely, one might expect that a hydrostatic expansion of the frameworks would feature a similar but opposite electronic response to that of a contraction (i.e. a band gap/dispersion reduction with lattice expansion). Through the application of negative pressure (i.e. stretching the framework) we note that $Ni_3(HITP)_2$ features a reduced band gap by 9 meV at 8 kB and, at an applied pressure of approximately 10 kB the material becomes metallic (Figure 42d and e). The metallicity evidently arises from the installation of degeneracy of carbon-based bands at the -point. Importantly, the addition of negative pressure provides a novel route to converting $Ni_3(HITP)_2$ into a 2D metal, as evidenced by the non-

zero density of states at the Fermi level (Figure 42e). This result has obvious implications for the expected electrical conductivity of the framework, as in-plane conduction would no longer be thermally activated. Additionally, while the metallic transition may not have been experimentally isolated due to difficulties in growing single crystals and measuring their conductivity, we expect that in plane conduction does contribute to the bulk, pressed-pellet measurements. Furthermore, the metallic transition occurs around 10 kB, pressures that should be accessible at high gas loadings or accessible at high temperatures.

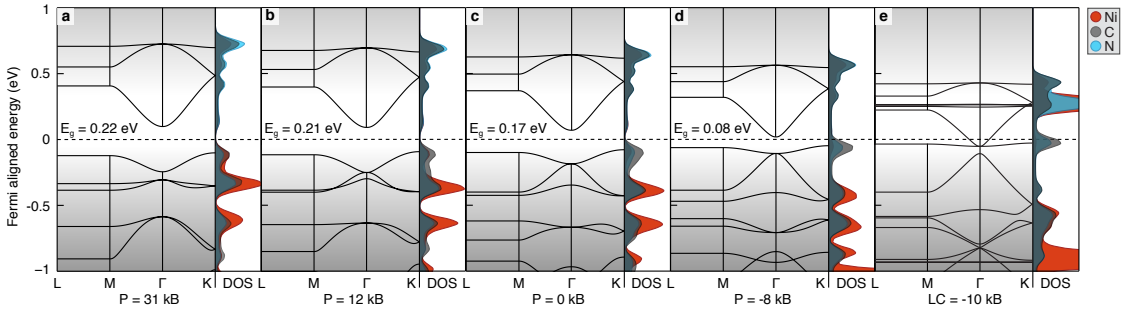

Figure 42. Electronic band structures and density of states plots for $Ni_3(HITP)_2$ under five representative hydrostatic pressures. Ni–N antibonding bands drop in energy upon lattice expansion, and are evident above the conduction band at 10 kB. The k-path from L-to-M (0.5,0,0.5-to-0.5,0,0) corresponds to the non-covalent direction and are flat because they are sampling perpendicular to the layer. M-to--to-K sample in the intraplane covalent vectors (0.5,0,0-to-0,0,0-to-0.33,0.33,0). $Ni_3(HITP)_2$ becomes metallic at low pressure. Reproduced from Phys. Chem. Chem. Phys., 2019,21, 25773-25778[4] with permission from the PCCP Owner Societies.

The electronic band structure of monolayer $Ni_3(HITP)_2$ also reveals the emergence of Ni–N centred bands appearing at low pressures. These bands drop from much higher energy at 8 kB (not visible in Figure 42d), to immediately above the conduction band (Figure 42e). Although these bands play no role in determining the electronic properties of the framework, their rapid decrease in

energy between 8 kB and 10 kB suggests that the energetics of the Ni–N interface is extremely sensitive to interatomic distance, and this interaction is antibonding in character. The bond lengths and associated energetics of this lattice contortion are presented in Figure 44, Figure 45 and Figure 46.

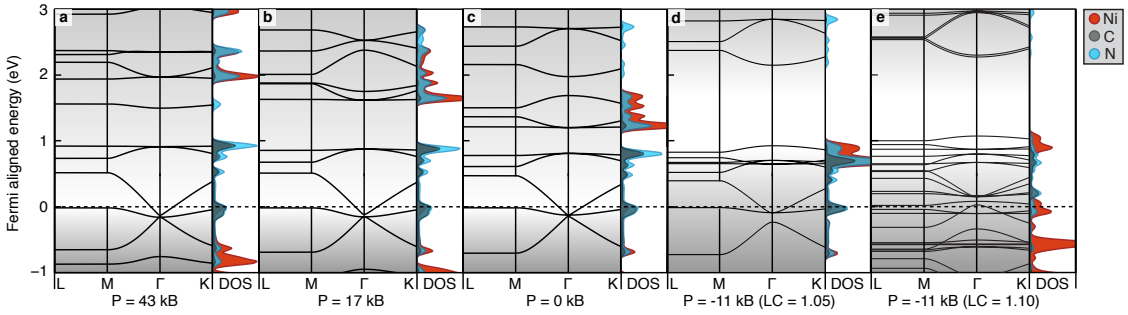

Figure 43. Electronic band structures and density of states plots for $Ni_3(HIB)_2$ under five representative hydrostatic pressures. LC = lattice constant. Ni–N antibonding bands drop below the Fermi level at 11 kB (LC = 1.10). The k-path from L-to-M (0.5,0,0.5-to-0.5,0,0) corresponds to the non-covalent direction and are flat because they are sampling perpendicular to the layer. M-to--to-K sample in the intraplane covalent vectors (0.5,0,0-to-0,0,0-to-0.33,0.33,0). $Ni_3(HIB)_2$ is persistently a metal at all pressures, and the Ni^{2+} is piezoreduced at 11 kB (LC = 1.10). Reproduced from Phys. Chem. Chem. Phys., 2019,21, 25773-25778[4] with permission from the PCCP Owner Societies.

4.1.3 Unusual redox behavior as evidence of covalency in metal-organic interface. Contrastingly, monolayer $Ni_3(HIB)_2$ is persistently metallic upon both framework expansion and contraction. However, we noted that the converged structure of 10 percent-expanded $Ni_3(HIB)_2$ features a non-zero magnetic moment, corresponding to approximately 0.66 unpaired electrons per Ni. This electronic structure is at odds with any plausible electronic configuration for square planar Ni^{2+}. We first assumed that the magnetic moment was due to an asymmetry in the expanded lattice resulting in an orbital degeneracy of d_{z^2} and d_{x2y2}. However, examination of the converged material reveals that the

structure is indeed symmetric. In fact, Ni^{2+} had been reduced by 0.66e per Ni, to $Ni^{1.33+}$. These two electrons are fully delocalised, in line with a Robin-Day type III classification. Bader analysis supported this observation as evidenced by an increase in charge density on the nickel atoms.[225]

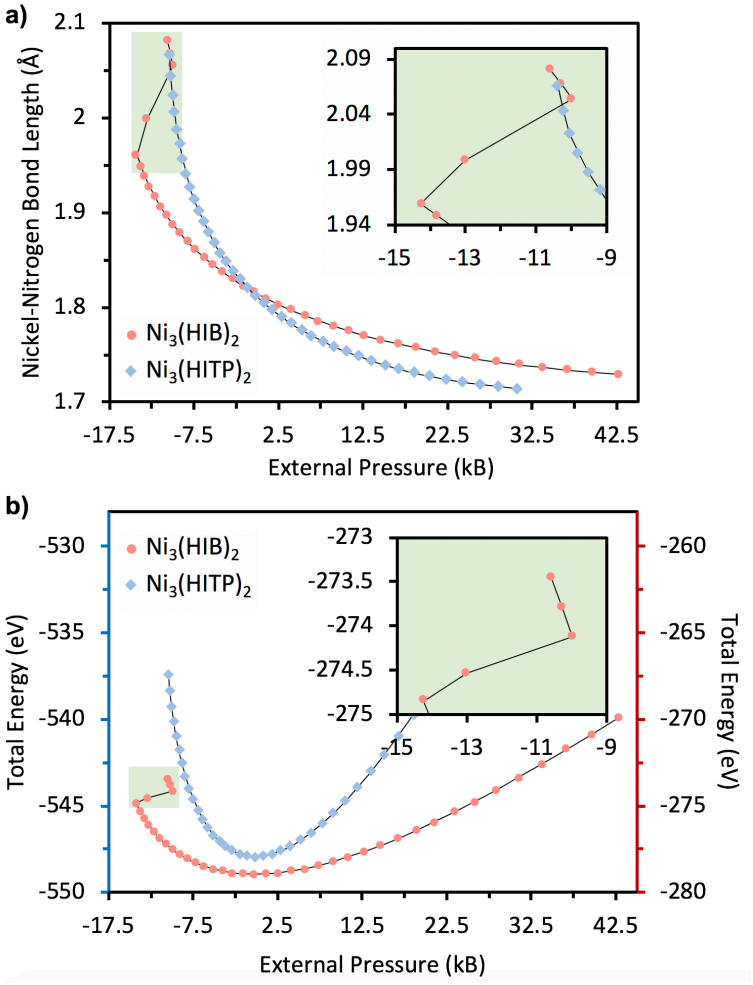

Figure 44. A structural (a) and energetic (b) comparison of both $Ni_3(HITP)_2$ and $Ni_3(HIB)_2$ at various pressures. The inset graphs highlight the Ni^{2+} piezoreduction upon expansion of the $Ni_3(HIB)_2$ lattice. Reproduced from Phys. Chem. Chem. Phys., 2019,21, 25773-25778[4] with permission from the PCCP Owner Societies.

We surmised that this reduction event was motivated by the electronic structure of the ligand, which may be thought of as a trianionic radical (one

resonance form is shown in Figure 41). While these electrons are paired and delocalized across the C-based -system in the equilibrium structure, elongation of the Ni–N bond results in piezoreductive transfer of a ligand centred electron to the neighbouring Ni (Figure 44).

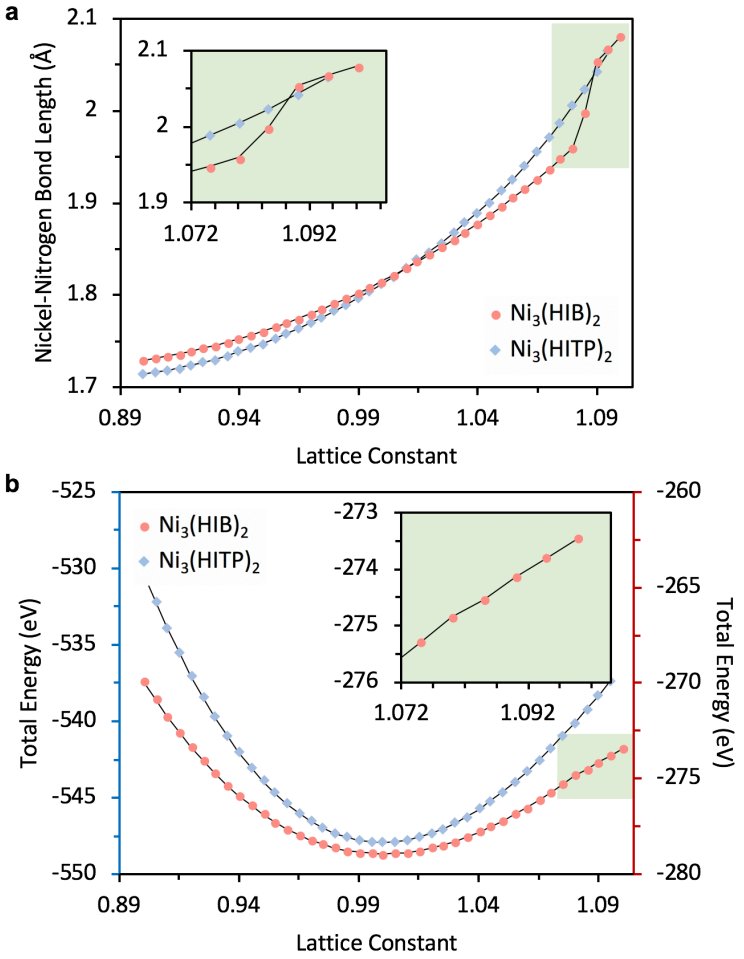

Figure 45. A structural (a) and energetic (b) comparison of both $Ni_3(HITP)_2$ and $Ni_3(HIB)_2$ as lattice constant changes. The inset graphs highlight the Ni^{2+} piezoreduction upon expansion of the $Ni_3(HIB)_2$ lattice. Reproduced from Phys. Chem. Chem. Phys., 2019,21, 25773-25778[4] with permission from the PCCP Owner Societies.

Beyond the electronic differences between the two structures, e.g. the piezoreductive transition observed in $Ni_3(HIB)_2$, and the semiconductor-to-metal

transition in $Ni_3(HITP)_2$, the materials have different energetic responses to pressure. Figure 44a presents the explicit comparison of pressure to Ni–N bond length.

Here, we observe three features; (i) the equilibrium Ni–N bond length does not depend on the ligand, (ii) as the lattice is contracted $Ni_3(HITP)_2$ more rapidly contracts in the Ni–N bond than that observed for $Ni_3(HIB)_2$ and, (iii) as the lattice is expanded the piezoreductive transition occurs when the Ni–N bond length begins to exceed 2 Å.

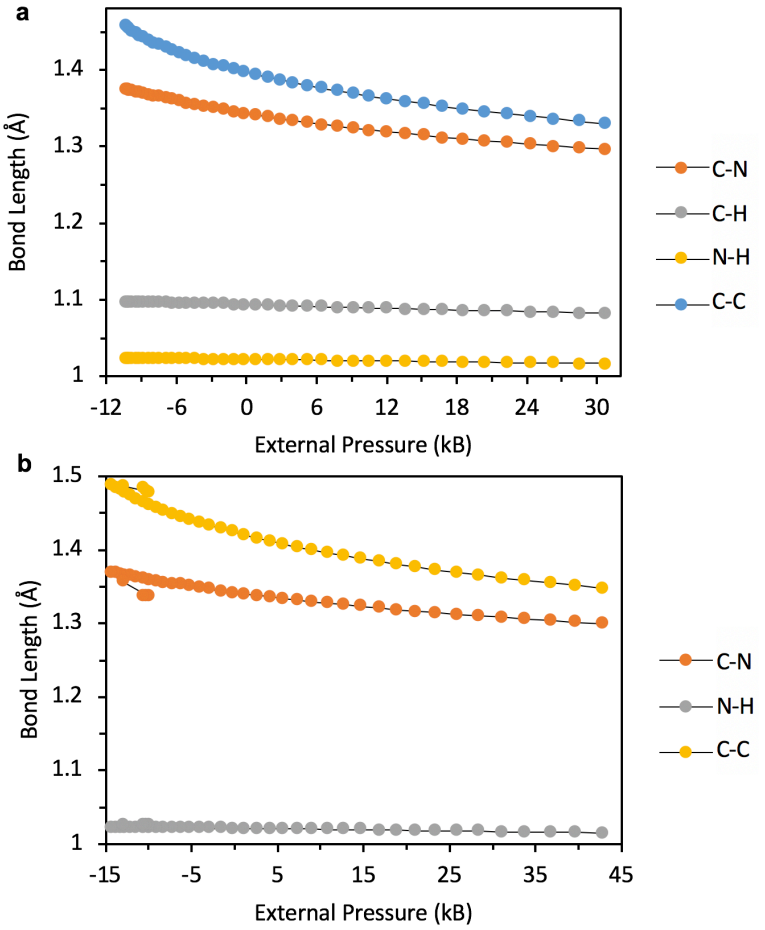

Figure 46. A structural comparison of both (a) $Ni_3(HITP)_2$ and (b) $Ni_3(HIB)_2$ at various external pressure. Reproduced from Phys. Chem. Chem. Phys., 2019,21, 25773-25778[4] with permission from the PCCP Owner Societies.

The difference in Ni–N contraction can be attributed to the increased rigidity of the HITP ligand owing to an increase in dense covalent C–C bonds. Examination of total energy versus pressure (Figure 44b) reveals a similar trend; $Ni_3(HIB)_2$ has a more shallow potential energy surface indicating that the HITP material is more rigid. Although we do not observe piezoreductive event in $Ni_3(HITP)_2$ the Ni–N bands do drop in energy upon lattice expansion. In $Ni_3(HIB)_2$ these bands drop below the Fermi level as external pressure decreases, and a formal reduction event occurs.

Perhaps this transition is most obviously depicted by comparison of the Ni–N bond lengths, and corresponding energies (Figure 44). Energetically, this transition occurs with an input of 94 kcal/mol, and should be accessible in the laboratory setting.

4.1.4 Method. Computational Method. Structural optimization of monolayer $Ni_3(HIB)_2$ and $Ni_3(HITP)_2$ were performed with DFT as implemented in the Vienna ab initio Simulation Package (VASP, version 5.4.4).[226] Both structures were equilibrated in a 20 Å vacuum using the unrestricted GGA-PBEsol exchange–correlation functional.[227] Ionic relaxation was achieved when all forces were smaller than 0.005 eV $Å^1$. The plane-wave cut off was set at 500 eV and the SCF convergence criterion was 10^6 eV, resulting in electronic convergence of 0.005 eV per atom. An automatic k-grid was used during the optimization with $4 \times 4 \times 1$ sampling, and yielded indistinguishable results comparted to $6 \times 6 \times 1$ meshes. Symmetry was not enforced. From the equilibrated structures of $Ni_3(HIB)_2$ and $Ni_3(HITP)_2$ hydrostatic pressure was applied by scaling lattice constants in 0.5% increments. By allowing the stress tensor to be calculated at every electronic step while restricting the cell shape and cell volume to change, the external pressure was

calculated at each lattice constant. Single point calculations were performed with a $4 \times 4 \times 1$ which is a sufficient k-grid to model monolayer metallic $Ni_3(HIB)_2$. For $Ni_3(HITP)_2$, a higher k-grid of $6 \times 6 \times 1$ were used to closely monitor the behaviour of the bands at the Fermi level and the flat bands corresponding to the Ni–N antibonding orbitals which are indistinguishable. These calculations were used to construct the electronic band structures and corresponding density of states for both MOFs at different pressures points. It should be noted that the DFT calculations employed here are known to systematically underestimate the band gap energy, especially for semiconductors,[146,228] so a larger band gap/dispersion perturbations may be possible in an experimental setting. The HSE06 hybrid functional was also examined and shows qualitatively similar properties to the PBEsol functional. For this study, the most important feature is the closing of the band gap and shift in energy of the Ni-N orbital that cause the change in magnetic properties. For this reason, we chose to use the PBEsol functional for all calculation to minimize computation cost. Hybrid functional such as HSE06 might produce higher quality band structures but very expensive and only contain similar information that can be capture by calculation at the GGA level (Figure 47). As show below, both structure for $Ni_3(HITP)_2$ displace a band gap correspond to a semi-conductive material and no band gap for $Ni_3(HIB)_2$. Both functionals are consistence with one another, hence PBEsol is sufficient for this study.

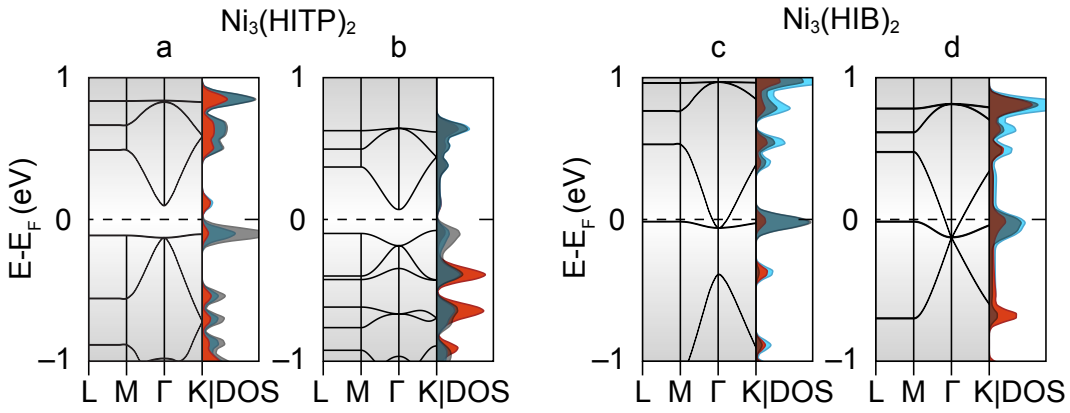

Figure 47. Electronic band structure and density of state of $Ni_3(HITP)_2$ (left) and $Ni_3(HIB)_2$ (right) computed by two different functionals: (a) HSE06 and (b) PBEsol for $Ni_3(HITP)_2$;(c) HSE06 and (d) PBEsol for $Ni_3(HIB)_2$. Reproduced from Phys. Chem. Chem. Phys., 2019,21, 25773-25778[4] with permission from the PCCP Owner Societies.

Bader charge analysis was performed using the package by Henkelman and colleagues[229] (version 1.03) with a core charge density correction on optimized $Ni_3(HIB)_2$ monolayer with lattice constant scaling of 100% and 110% to calculate the total charge differences of Ni atoms.

4.1.5 Conclusion. External pressure modulation of monolayer conductive MOFs such as $Ni_3(HIB)_2$ and $Ni_3(HITP)_2$, leads to exotic electronic property transitions including band gap closing in semi-conductive monolayer of $Ni_3(HITP)_2$. The emergence of magnetic moments in the metallic monolayer is a result of the piezo-reductive transition of the metal centres. As external pressure increases, slight changes in the electronic band structures occur for both monolayers. Interestingly, $Ni_3(HITP)_2$ demonstrates a notable contraction in band gap energy as the lattice became progressively expanded, eventually becoming metallic at 10 kB. Additionally, lattice expansion showed that indeed the Ni–N interface was the most labile and, in the case of $Ni_3(HIB)_2$, a piezoreduction

occurs when the Ni–N bond length is expanded by approximately 10Hydrostatic pressure therefore provides a pathway for electronic structure modifications in both semi-conducting and metallic materials. We expect these findings will aid in the development of novel MOF-based sensors, as well as serve as a general design consideration in the synthesis of other compressible, conductive MOFs.

The contents of this section have been or are intended to be published in whole or in part. The text presented here has been modified from Phys. Chem. Chem. Phys., 2019,21, 25773-25778[4] with permission from the PCCP Owner Societies.

4.2 Sheet Orientation and Its Relative Effects on Electronic Properties

4.2.1 A proposed pathway to increase conductivity in MOFs: 2D metallic MOFs into 3D metallic MOFs. Metal–organic frameworks (MOFs) are typically celebrated for their ultrahigh surface area[12] and porous geometries,[230] which enable their use as separation[231] and adsorption media[232,233] and site isolated catalysts.[234] Yet, their generally poor electrical conductivity prevents their use in most electronic applications.[235] Efforts to increase the conductivity of MOFs have involved synthesizing novel materials with reduced or zero bandgaps through ligand selection,[236] doping by mixed valency,[27] and defect engineering.[237,238] Although a handful of electrically conductive MOFs have been reported,[239] their conductivities are often below 10^{-2} S/cm, limiting their utility.[200] Increasing MOF conductivity would enable the formation of innovative energy storage and sensing technologies. In general, electrical conductivity depends on three properties: (i) the number of charge carriers, (ii) their charge, and (iii) their mobility. In insulating, undoped MOFs (i.e., those with discrete bandgaps), the charge carrier mobility is often limited by flat bands arising from the highly ionic metal–ligand interface.[206,239,240]

In those cases, the charge of the carriers is ±1 for a hole or electron. Subsequently, several recent studies characterize and quantify the number and identity of the charge carriers, and most examples show increasing conductivity with chemical oxidation, that is, the formation of holes.[241,242]

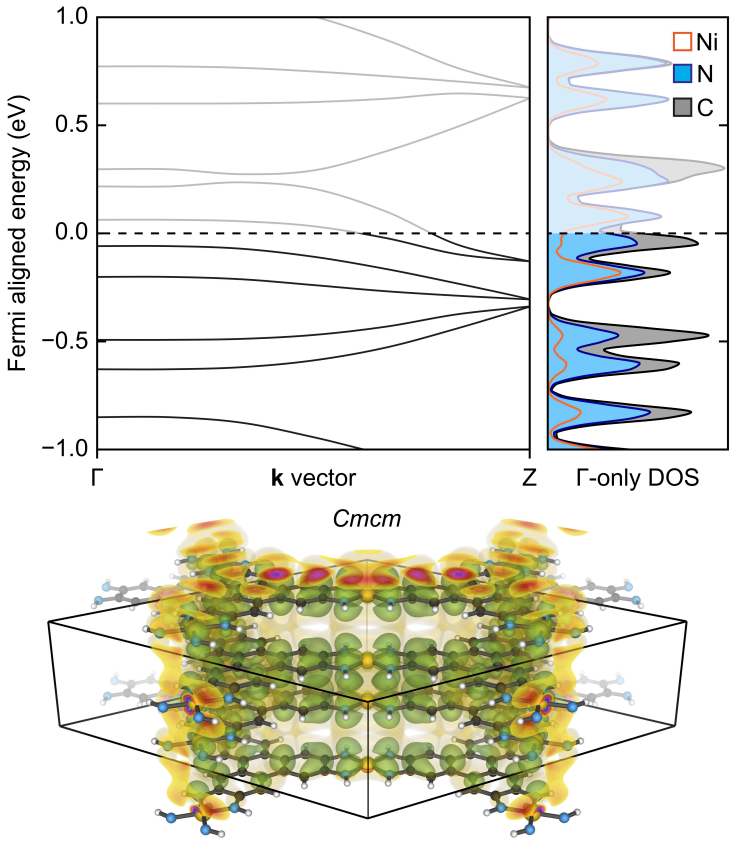

Figure 48. An out-of-plane vector (-Z) reveals metallicity in the electronic band structure of $Ni_3(HITP)_2$ (Cmcm space group). From the electron density projection, we can see that the electrons form inter-sheet bonding-type interactions (overlapping yellow lobes), giving rise to electronic delocalization. Reprinted with permission from ACS Appl. Electron. Mater. 2021, 3, 5, 2017–2023.[5] Copyright 2022 American Chemical Society.

Yet, the mobility and directionality of conduction are still limited by the scaffold geometry.[201] The highest performing MOF conductors do not feature an explicit bandgap: in other words, the MOFs are metallic. These scaffolds (e.g., $Ni_3(HITP)_2$,[243] $Ni_3(HIB)_2$,[212] etc.[244]) feature more covalent metal–ligand bonds. Similar to graphitic materials,[245] the -orbitals from the linkers create delocalized bands that exhibit dispersion both in and out of the covalently connected plane.

Yet, the electronic structure of 2D metal–organic graphene analogues is nuanced. There is increasing evidence to suggest that the linkers are oxidized during the formation of these MOFs, rendering them no longer aromatic.[246–249] Considering the most well-studied 2D conductive MOF, $Ni_3(HITP)_2$ (HITP 2,3,6,7,10,11-hexaiminotriphenylene),[23,30,250–254] each HITP linker must be assigned a formal oxidation state of 3– to satisfy the charge neutrality condition. Therefore, each linker would host an odd number of electrons (assuming a single deprotonation has occurred for each amine).

However, previous work has elucidated that a monolayer of this material features a discrete bandgap and no unpaired electrons.[4] Each pair of linkers can therefore be thought of as a closed-shell 4/–2 pair (a resonance structure of 3/–3): a Robin–Day Class III system.[255] While the monolayer features a narrow but discrete bandgap, metallicity is observed in the bulk vdW form (where weak dispersion interactions between stacked linkers arise from -orbital overlap).[256] This manifests as the emergence of metallic bands in the bulk electronic band structure along the out-of-plane (-stacked) –Z vector (Figure 48). Broadly, linker-based radicals are thought to be stabilized by two mechanisms: (i) formation of a curved (disperse) band in-plane, delocalizing the electrons within the covalent sheet, and

(ii) formation of a curved band out-of-plane, delocalizing the electrons in the vdW direction.

Another consideration for these 2D analogues is the range of accessible sheet stacking arrangements. The potential energy surface of sheet slipping in $Ni_3(HITP)_2$ is shallow; with a penalty of <0.7 eV for all parallel-displaced configurations[30] the pores could be thermally distorted by sheets slipping up to 0.1 nm in the a/b plane under ambient conditions. The pores could be further occluded by sheets slipping past one another, perhaps under extreme conditions (e.g., high heat and pressure). While the implications for electrical conductivity appear to be minimal based on these partially sheet-slipped band structures,[256] diminished porosity undermines MOF utility for energy storage applications. One emergent strategy to maintain the porosity of conductive 2D MOFs is to strengthen the intersheet interactions via retrofitting (a form of postsynthetic ligand modification[257,258] known to affect both the electronic and structural properties of materials[128,259,260]). The general concept is that the sheets can be held in place by installing a linker to connect the formally square planar Ni^{2+}, yielding octahedral Ni^{2+} and a 3D-connected scaffold. In a recent study, Foster and colleagues demonstrated that the installation of such pillars in $Ni_3(HITP)_2$ created a wide bandgap material,[256] highlighting the importance of d_{z^2} orbitals on the metals in facilitating Class III delocalization of the ligand. In other words, the pillars destroyed the out-of-plane covalency and resulted in a semiconductor. Thus, the results showed that retrofitting a MOF whose monolayer features a bandgap seems to yield a 3D-connected insulator. Here, we examine a different family of 2D MOF conductors based on a recently reported structure, $Ni_3(HIB)_2$ (HIB hexaiminobenzene).[212] Unlike the triphenylene-based materials, the monolayer

is metallic.[4] The three-electron oxidation of triphenylene can be thought of as yielding a relatively stable quinone monoradical.[30] We believe metallicity emerges in $Ni_3(HIB)_2$ because the same three electron oxidation of a single benzene ring results in a half-populated HIB band, which by definition is metallic. The bulk material is also metallic with metallically dispersed bands in the a/b plane, independent of sheet stacking configuration (see the M–K vectors in Figure 49). We have previously studied and contrasted $Ni_3(HITP)_2$ and $Ni_3(HIB)_2$,[4] revealing dissimilarities in their electronic structure motivated by the in-plane metallicity of the latter. Metallicity in $Ni_3(HIB)_2$ monolayer makes bulk metallicity independent of the stacking orientation and intersheet spacing. In contrast, $Ni_3(HITP)_2$ conducts primarily out-of-plane, and increasing intersheet spacing hinders charge transport throughout the material. Resultantly, the previous 2D to 3D retrofitting study turns a 2D conductive MOF into a 3D semiconductor by reducing band dispersion and introducing a bandgap. Instead, we propose modifying $Ni_3(HIB)_2$, allowing the formation of 3D MOFs that retain the metallic character of the 2D MOF. This work introduces intersheet bridging linkers into $Ni_3(HIB)_2$ that induce a change in metallicity and band dispersion of the newly formed 3D-connected material. We show that while this procedure does yield a metal, it is likely due to material instability rather than the desired retrofitted 3D conductor. To overcome this challenge, we propose alternative compositions that may be more thermodynamically accessible. This study further emphasizes the importance of the dz2 orbital occupancy in forming disperse bands and stable MOF conductors.

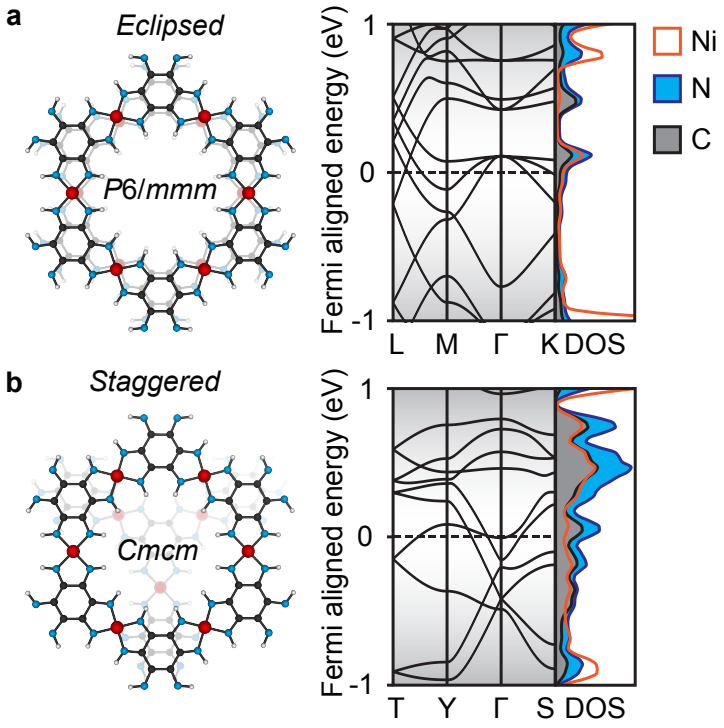

Figure 49. $Ni_3(HIB)_2$ is a bulk metal, independent of sheet slipping. Yet, greater band dispersion for eclipsed stacking structure (a) in the out-of-plane direction (L–M) compared to that of the staggered counterpart (b) for $Ni_3(HIB)_2$. Reprinted with permission from ACS Appl. Electron. Mater. 2021, 3, 5, 2017–2023.[5] Copyright 2022 American Chemical Society.

4.2.2 Challenges in investigating 2D MOFs: A closer look at layers orientation's effect on electronic properties and the material's porosity. While the absolute electronic structure of individual HIB linkers depends on the extent of oxidation, the -bonding network within each ligand remains intact. Thus, we term this direction the "covalent plane". These sheets are held together by much weaker electrostatic interactions between the layers—we term this direction "out-of-plane". Bulk electronic properties depend on the sheet stacking orientations (Figure 49).

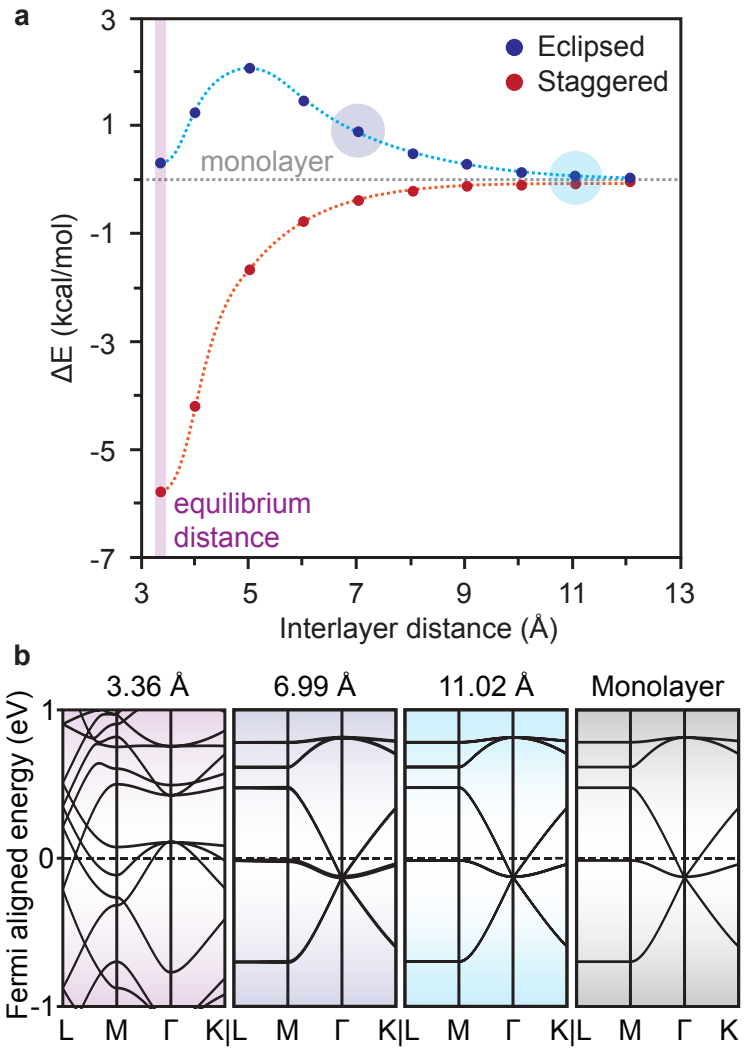

Figure 50. (a) Relative energy of bulk structure of $Ni_3(HIB)_2$ in staggered (red) and eclipsed (blue) conformation compare to that of monolayer (gray). (b) Band structures of $Ni_3(HIB)_2$ in eclipsed conformation (first three panels) and $Ni_3(HIB)_2$ monolayer (gray). The interlayer spacings are show above the corresponding panels. Reprinted with permission from ACS Appl. Electron. Mater. 2021, 3, 5, 2017–2023.[5] Copyright 2022 American Chemical Society.

When these 2D sheets are in their eclipsed stacking conformation, one would expect the overlap between organic -orbitals of adjacent layers to be maximized, along with the repulsion of Ni d_{z^2} orbitals. Deviation from the eclipsed stacking structure reduces the orbital overlap and therefore band dispersion in this direction.

This effect is reflected in the k-path from L-to-M and T-to-Y (out-of-plane). However, the impact of stacking conformations on the band dispersion in the covalent plane is not as clear (see the k-path M–K and YS). Regardless, both staggered and eclipsed conformations are persistently metallic, as evidenced by the band crossing the computed Fermi level and the nonzero density of states (DOS). The eclipsed structure is, however, energetically disfavored by 6 kcal/mol (Figure 50a). At the interlayer distance of 3.36 Å—the experimentally reported interlayer distance for this framework[212]—it is unlikely for $Ni_3(HIB)_2$ to obtain the eclipsed structure. As we artificially exfoliate the layers by progressively stepping them apart, both forms converge to the energy of a free monolayer. Interestingly, however, the eclipsed structure exhibits the most disfavored orientation at an interlayer distance of 5 Å, suggesting that eclipsed layers may be metastable (see also the absence of imaginary frequency in Table 2). Increasing interlayer spacing reduces the electrostatic interaction between the sheets. Therefore, the metallicity is diminished in the out-of-plane direction, as shown in Figure 50b (see the flattening of the bands from L-to-M at the interlayer distance of 6.99 and 11.02 Å). The k-path M–K reveals the impact on the electronic properties of the material in the covalent plane. Although the increase in interlayer distance reduces the number of bands crossing the Fermi level, the metallicity of the material remains unchanged (shown in Figure 50b). Still, we do not know whether the addition of an axial ligand to the Ni^{2+} atoms will be energetically preferable to forming the bulk 2D material.

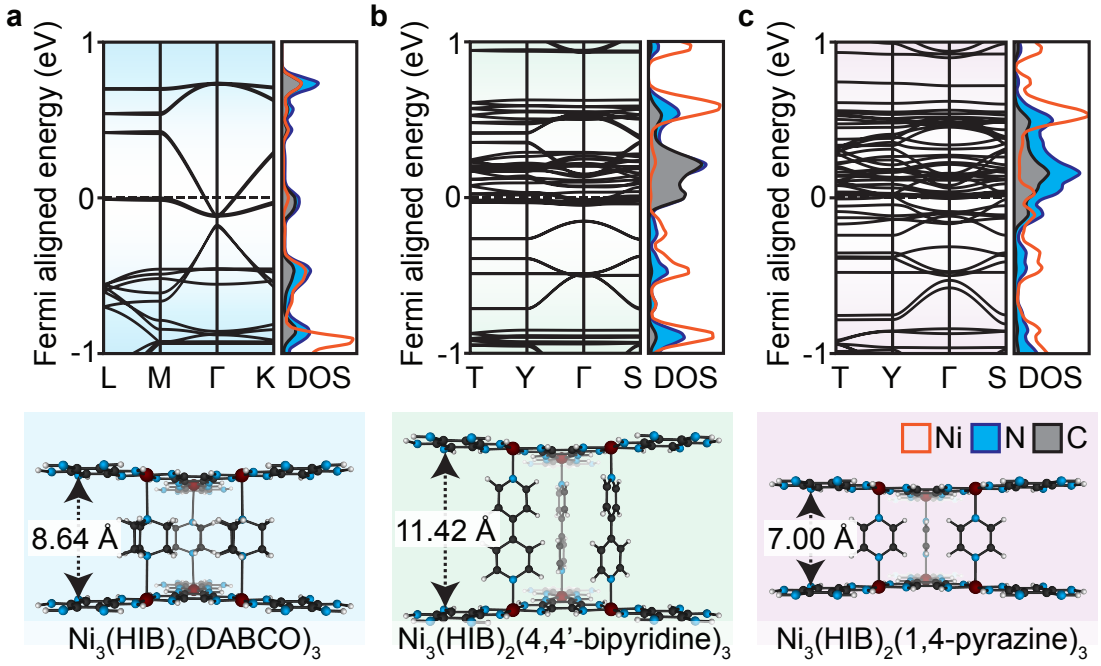

Figure 51. Effect of bridging linkers insertion on band structures of $Ni_3(HIB)_2$ frameworks: (a) pyrazine (purple), (b) DABCO (blue), and (c) bipyridine (green). The corresponding 3D structure is shown below each of the band structures and DOS. Reprinted with permission from ACS Appl. Electron. Mater. 2021, 3, 5, 2017–2023.[5] Copyright 2022 American Chemical Society.

4.2.3 Retroffitting of $Ni_2(HIB)_3$ revealing the role of d-orbital occupancy in maintaining the metal-organic interface covalency. We seek to link the coordinatively unsaturated nodes of metallic $Ni_3(HIB)_2$ monolayers by using extrinsic ligands. Three potential bridging organic linker candidates are explored: 1,4-pyrazine, DABCO (1,4-diazabicyclo[2.2.2]octane), and 4,4-bipyridine, all of which are commonly used linkers in the MOF field.[261–263] Retrofitting these linkers results in interlayer spacing of 7 Å (pyrazine), 9 Å (DABCO), and 11 Å $(bipyridine)_3$. In each case, the sheets are sufficiently far apart (per Figure 50b) to minimize -stacking interactions between the covalent sheets. The 3D-connected retrofitted structures of $Ni_3(HIB)_2$ are shown in Figure 51. First, we consider the effect of a pure -donor linkage through the inclusion of DABCO (Figure 51a). From

an energetic perspective, the DABCO linkers insertion was thermodynamically disfavored by 2.30 kcal/mol (Table 1). Our phonon calculations revealed imaginary frequencies in the geometrically equilibrated structures, suggesting the material is not dynamically stable. We also noted that the DABCO–Ni bond length converged to 3.06 Å (beyond what any reasonable metal–ligand bond might be), so we employed the density-derived electrostatic and chemical approach (DDEC)[264] to evaluate the bond orders for these bonds. The metal–ligand bond order in the out-of-plane direction is 0.07, which is very weak compared to the in-plane metal–NH bond (bond order of 0.78, bond length of 1.82 Å). For comparison, the bond orders in nonretrofitted $Ni_3(HIB)_2$ bulk and monolayer Ni–NH bonds are 0.78 and 0.84, respectively. The decreasing bond order in bulk $Ni_3(HIB)_2$ compared to that of the monolayer is one avenue to assess the importance of the vdW stacking. Considering the long DABCO–Ni bond, the band structure remains very similar to that of the monolayer (Figure 51a), which further indicates that the DABCO linkers are likely not interacting with the $Ni_3(HIB)_2$ layers. We attribute this to square-planar Ni^{2+} being a weak Lewis acid and axial ligation forming high-spin octahedral Ni^{2+}. Because the d_{z^2} orbital is formally occupied in the square-planar complex, -donor ligands form a nonbonding interaction. Both pyrazine and 4,4-bipyridine are -donors but better -acceptors than DABCO. Retrofitted $Ni_3(HIB)_2$(1,4-pyrazine)$_3$ and $Ni_3(HIB)_2$(4,4-bipyridine)$_3$ result in metal–ligand bond lengths of 2.11 and 2.15 Å for the pyrazine and bipyridine analogues, respectively (Figure 51b,c). In the former, a bond order of 0.38 was found for the metal–ligand bond in the out-of-plane direction, which is relatively low compared to the in-plane metal ligation (bond order 0.53). Similarly, for $Ni_3(HIB)_2$(4,4-bipyridine)$_3$, a bond order of 0.36 was found for the metal–ligand bond in the out-of-plane direction (compared to a

Table 1. Relative Energy of Formation for Bipyridine, Pyrazine, and DABCO Retrofitted into $M_3(HIB)_2$ Frameworks (Energies Are Presented in kcal/mol)

	Ni	**Cr**	**Fe**
4,4-bipyridine	61.85	–110.42	–81.23
1,4-pyrazine	68.61	–115.64	–74.20
DABCO	2.30	–64.49	–23.99

Table 2. Imaginary frequencies for all MOF from phonon calculations using finite displacement method. Acoustic mode is highlighted in green.

MOF	**Number of Imaginary Frequency (cm^{-1})**	**Acoustic Frequency (cm^{-1})**	**Non-acoustic Frequency (cm^{-1})**
$Ni_3(HIB)_2$	3	4.17, 5.02, 7.32	
$Ni_3(HIB)_2$	3	4.10, 6.29, 16.82	
$Ni_3(HIB)_2$	3	8.58, 14.94, 18.05	
$Ni_3(HIB)_2(DABCO)_3$	10		7.51, 8.28, 16.53, 19.94, 27.53, 34.50, 45.15, 48.72, 54.54, 71.59
$Ni_3(HIB)_2$(1,4-pyrazine)$_3$	6	4.98	8.70, 12.02, 15.85, 17.86, 49.81
$Ni_3(HIB)_2$(4,4'-bipyridine)$_3$	4	11.66, 16.72	23.59, 28.23
$Cr_3(HIB)_2$ monolayer	3	3.51, 8.16, 10.53	
$Cr_3(HIB)_2$ eclipsed	3	4.24, 7.80, 13.86	
$Cr_3(HIB)_2(DABCO)_3$	5		2.98, 14.11, 19.44, 40.89, 56.85
$Cr_3(HIB)_2$(1,4-pyrazine)$_3$	3	9.80, 12.40, 16.14	
$Cr_3(HIB)_2$(4,4'-bipyridine)$_3$	4	10.86	17.12, 21. 22, 24.75
$Fe_3(HIB)_2$	3	4.92, 7.07, 10.17	
$Fe_3(HIB)_2$ eclipsed	5	1.14, 2.99, 5.19	39.64, 44.70
$Fe_3(HIB)_2(DABCO)_3$	3	9.01, 10.51	15.72
$Fe_3(HIB)_2$(1,4-pyrazine)$_3$	3	9.58, 11.81, 15.46	
$Fe_3(HIB)_2$(4,4'-bipyridine)$_3$	3	10.12, 16.33, 20.31	

bond order of 0.52 for the metal–ligand bond in the covalent plane). The inclusion of a -acceptor dramatically reduces the in-plane bonding interactions. As a result, these inclusions are highly energetically unfavorable: the insertion of bipyridine and pyrazine linkers into the framework increases the Gibbs free energy by 61.85 and 68.61 kcal/mol, respectively (Table 1). Again, the presence of imaginary frequencies revealed that these structures are not dynamically stable (Table 2).

4.2.4 Conclusion. In sum, a retrofitting approach using only -donors results in the Ni-MOF preferring nonbonded (or simply intercalated) pillars. The -accepting ligands result in a bond, but at extreme energetic penalty due to

reorganization of the Ni^{2+} d orbitals, inhibiting the binding of fifth and sixth axial ligands. Hence, retrofitting $Ni_3(HIB)_2$ with the pillars creates unstable materials, independent of their properties.

The contents of this section have been or are intended to be published in whole or in part. The text presented here has been modified from ACS Appl. Electron. Mater. 2021, 3, 5, 2017–2023.[5] Copyright 2022 American Chemical Society.

4.3 The Effects of Metal Identity: Fe-based centers enhance conductivity and transport properties in porous frameworks

4.3.1 Selecting the appropriate metal for retrofitting: a case study using open-framework chalcogenides. Given the energetic penalty of creating octahedral Ni^{2+}, we now examine the possibility of altering metal composition to minimize the d_{z^2} repulsive interaction. To do so, we expand our study to include other divalent transition metals in the form of $Cu_3(HIB)_2$, $Fe_3(HIB)_2$, and $Cr_3(HIB)_2$. The Cu^{2+} material has been previously synthesized,[212] but it is also a late transition metal with filled d_{z^2} orbitals. We hypothesized that retrofitted $Cu_3(HIB)_2$ would exhibit similar properties to $Ni_3(HIB)_2$ since they have filled d_{z^2} orbitals. Indeed, our attempt to obtain a model for $Cu_3(HIB)_2(DABCO)_3$ resulted in much the same as we observed for the Ni^{2+} system—intercalated and nonbonding. As a result, we turned our interest to the Cr^{2+} and Fe^{2+} systems. We selected Fe^{2+} and Cr^{2+} because it allows us to depopulate the valence orbitals in steps while minimizing the computational difficulties of computing magnetic ordering of other first-row transition metals (e.g., Mn^{2+} and Co^{2+}). In addition, both Cr^{2+} and Fe^{2+} form high-spin complexes in square-planar coordination spheres, leaving the d_{z^2} orbitals partially filled. The partially filled dz2 orbitals

can readily accept extra electrons from the bridging linkers to form octahedral coordination spheres. Additionally, both Fe and Cr have been used in the formation of MOFs.[265,266] Fe^{2+} metal center possesses unique conductive properties because of (i) its unique oxidation state and (ii) its spin crossover transition properties. Fe-based materials usually exhibit better charge transport mobility and hence higher conductivity. This was demonstrated in our study of the open-framework chalcogenides.

Open-framework chalcogenides offer an alternative family of nanoporous materials, featuring main-group-chalcogenide clusters linked by transition-metal ions through covalent bonds. Like MOFs, these materials are available with a variety of metal ions, chalcogenides, and clusters, furnishing a diverse collection of networks with varying pore sizes and shapes. Although these materials have been widely studied for decades and frequently termed semiconductors,[267–280] few, if any, studies have examined their basic conductivity properties.[271,274,279] As three-dimensional (3-D) frameworks, these materials serve as low-density analogues to conventional metal chalcogenides, opening fundamental studies into the relationship of semiconductor form and function. These materials also benefit from well-defined porosity, unlike two-dimensional (2-D) metal chalcogenides whose surface areas can become inaccessible through intersheet aggregation.[281,282] While new examples of conductive MOFs remain hotly pursued, many open-framework chalcogenides have already been reported and simply await studies into the relationship between their nanoporosity and semiconductor behavior. In this study, we report a combined experimental–computational investigation into the iconic family of materials $TMA_2MGe_4Q_10$ (M = Mn, Fe, Co, Ni, Zn; Q = S, Se, TMA = tetramethyl

ammonium), as shown in Figure 52, first reported by Yaghi et al. prior to the advent of modern MOF chemistry.[267]

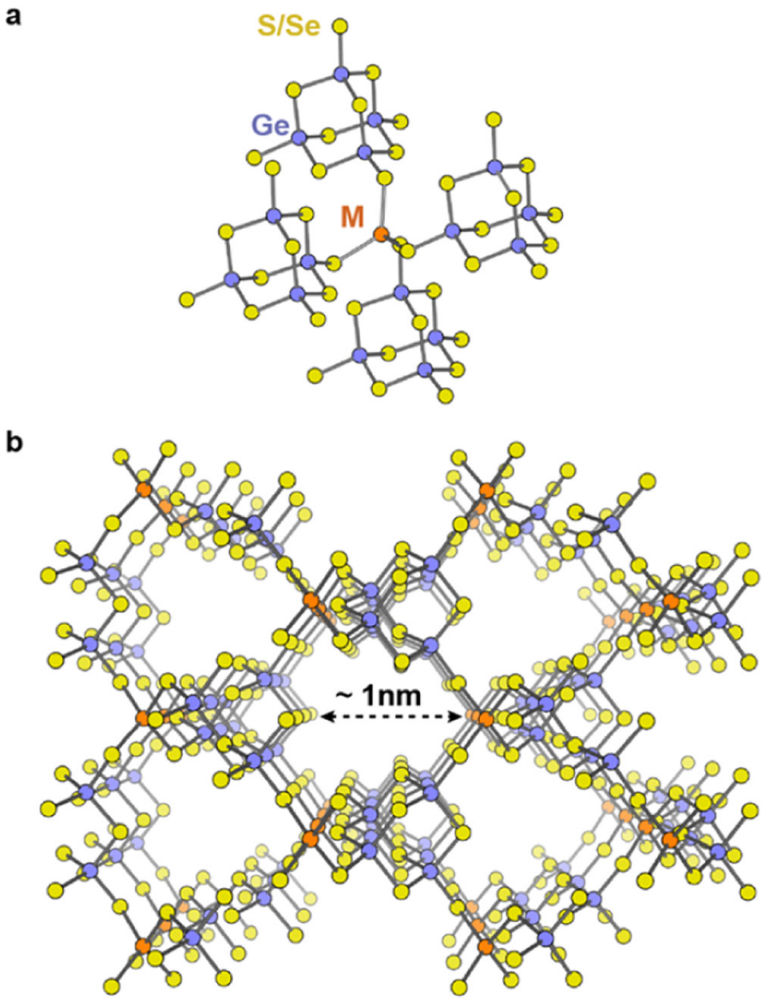

Figure 52. Crystal structure of open-framework chalcogenides $TMA_2MGe_4Q_10$, TMA = tetramethyl ammonium, M = Mn, Fe, Co, Ni, Zn, Q = S or Se ($TMA_2MnGe_4S_{10}$ depicted). (a) Local coordination and (b) extended network representations with TMA cations omitted for clarity. Reprinted with permission from Chem. Mater. 2022, 34, 4, 1905–1920.[6] Copyright 2022 American Chemical Society.

A reexamination of these frameworks presents new insights into their optical, magnetic, and electronic behaviors, revealing the sensitivity of these properties to subtle differences in composition and their tunability through

molecular redox chemistry. The charge transport of the frameworks is especially sensitive to these variables, with conductivities differing across several orders of magnitude and in the basic mechanism of transport. A key insight from the anomalously high conductivity of the Fe analogue is that charge mobilities and charge carrier densitiesthe essential parameters governing conductivitycan be tuned through molecular chemistry in the form of metal–ligand bond covalency and redox chemistry. These results provide direct confirmation of open-framework chalcogenides as porous semiconductors, while opening myriad investigations into their tunable charge transport behavior.

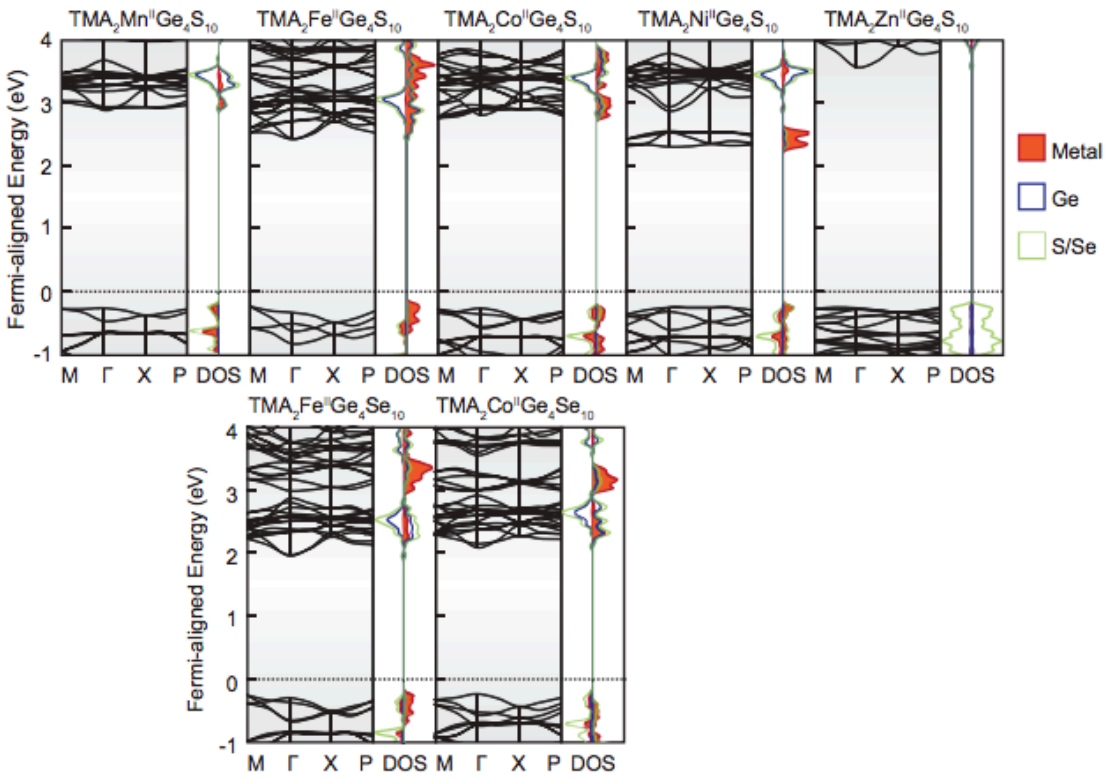

Figure 53. Simulated band structures and pDOS states for as synthesized materials. Reprinted with permission from Chem. Mater. 2022, 34, 4, 1905–1920.[6] Copyright 2022 American Chemical Society.

To understand the relationship of the tunable compositions and the electronic properties of the $TMA_2MGe_4Q_10$ frameworks, we computed the band diagrams for a variety of chalcogenides and first-row transition-metal ions in divalent and trivalent oxidation states, as summarized in Figure 53 and Figure 54. Figure 55 plots the conduction band and valence band electron densities and corresponding density-of-state (DOS) diagrams of Fe–S, Ni–S, and Zn–S as representative examples. Although these materials differ only in metal ions, the atomic character of the band-edge orbitals diverges considerably.

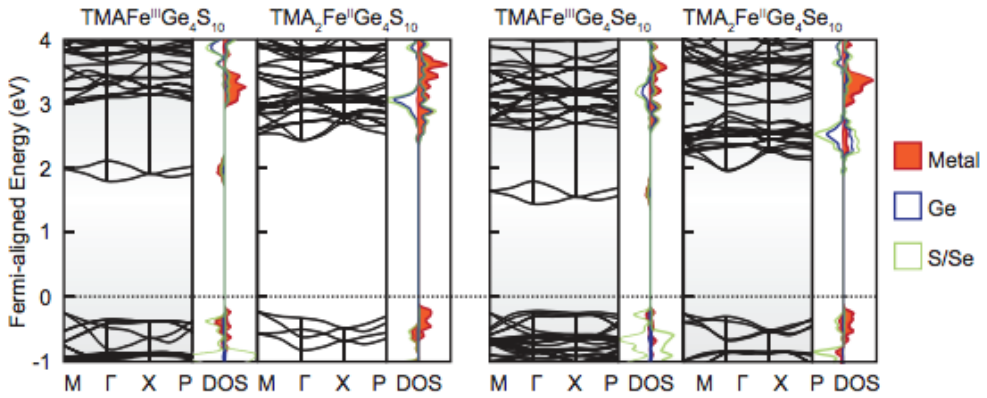

Figure 54. Impact of Fe oxidation state on the simulated band structures and pDOS states for TMA_2FeGe_4S/Se_{10}. Reprinted with permission from Chem. Mater. 2022, 34, 4, 1905–1920.[6] Copyright 2022 American Chemical Society.

For example, whereas Fe and Ni d-orbitals contribute to both band edges in Fe–S and Ni–S, respectively, S p-orbitals dominate both band edges in Zn–S. These differences are due to high-energy unpaired d electrons in Fe–S and Ni–S, which contribute substantially to the band edge(s), whereas Zn–S has no such electrons in its closed d shell. The partial atomic orbital character can be quantified for each material, as summarized in Table 3, revealing considerable differences in bond covalency, as well. For example, d-orbitals comprise 84% of the valence band in Fe–S, whereas Ni and Zn d-orbitals make up 54% in Ni–S and just 4% in

Zn–S. Bond covalency also depends strongly on the metal ion oxidation state and chalcogenide identity.

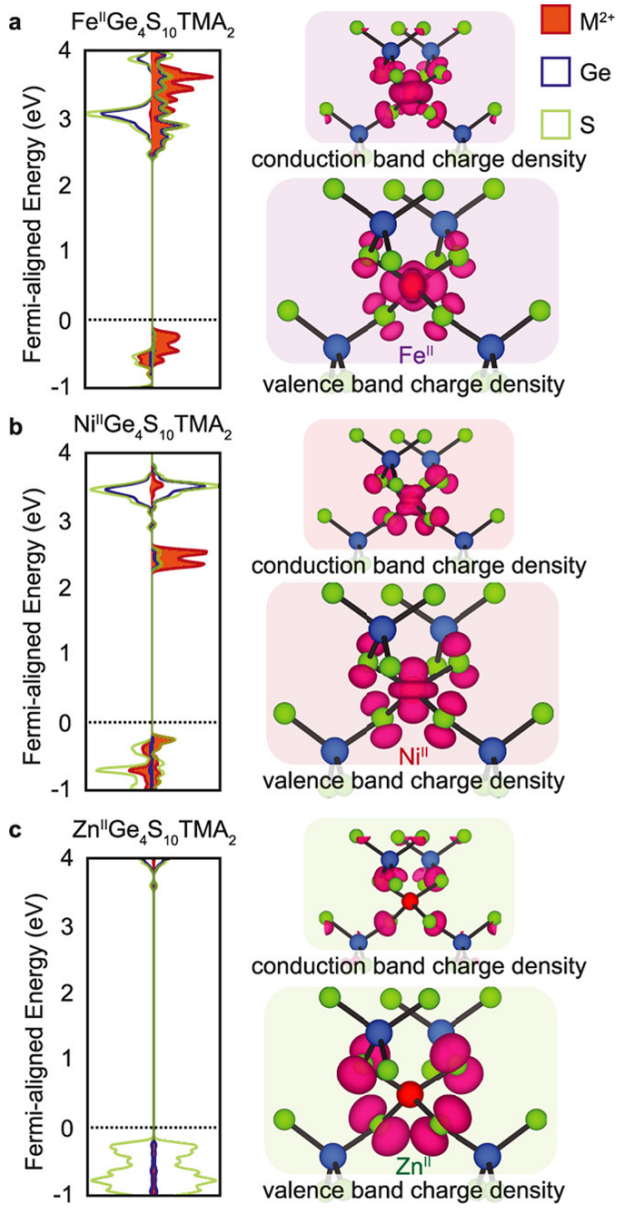

Figure 55. Impact of Fe oxidation state on the simulated band structures and pDOS states for TMA_2FeGe_4S/Se_{10}. Reprinted with permission from Chem. Mater. 2022, 34, 4, 1905–1920.[6] Copyright 2022 American Chemical Society.

For example, upon oxidation, the Fe d-orbital valence band contribution drops from 84 to 72% in Fe^{3+}-S and from 71% in Fe–Se to 39% in Fe^{3+}–Se. These

significant differences in the electronic structures of these materials on the basis of oxidation state and chalcogenide provide a basis for understanding their diverse magnetic, optical, and charge transport behaviors.

Table 3. Calculated relative percentage of each elements (M, Se/S, Ge) from pDOS at the VBM of MGe_4S/Se_{10} materials in vacuum and solvents where M is Mn, Fe, Co, Ni, Zn, Ge, Sn.

Materials	**Percent Occupancy of Element (%) with TMA**		
	Metal DOS	***S/Se DOS***	***Ge DOS***
$Mn^{II}Ge_4S_{10}$	39	56	5
$Co^{II}Ge_4S_{10}$	49	47	4
$Fe^{II}Ge_4S_{10}$	48	47	5
$Ni^{II}Ge_4S_{10}$	45	51	4
$Zn^{II}Ge_4S_{10}$	4	92	4
$Ge^{IV}Ge_4S_{10}$	5	95	5
$Sn^{IV}Ge_4S_{10}$	1	94	5
$Mn^{II}Ge_4Se_{10}$	31	64	5
$Co^{II}Ge_4Se_{10}$	31	64	5
$Fe^{II}Ge_4Se_{10}$	71	22	7
$Ni^{II}Ge_4Se_{10}$	33	63	4
$Zn^{II}Ge_4Se_{10}$	4	93	3
$Ge^{IV}Ge_4Se_{10}$	6	94	6
$Sn^{IV}Ge_4Se_{10}$	2	93	6
$Fe^{III}Ge_4S_{10}$	38	57	5
$Fe^{III}Ge_4Se_{10}$	39	55	6

To investigate the oxidation state of iron in Fe–Se, we turned to Mössbauer spectroscopy, which probes the oxidation state, coordination environment, and spin state of the iron center. At 300 K, the Mössbauer spectrum of Fe–Se (Figure 56) has a single doublet with an isomer shift of 0.393 mm/s and a quadrupole splitting of 0.568 mm/s, which we assign as high-spin Fe^{3+}, indicating the material is isovalent Fe^{3+}. We hypothesize that the Fe^{2+} starting material used in the synthesis of the Fe–Se framework facilitates spontaneous electron transfer to the cluster, generating an Fe^{3+} site and a cluster-based radical. This in situ oxidation is

supported by the fact that tetrahedral Fe^{2+} coordination complexes have been shown to oxidize at milder potentials when coordinated by selenium vs sulfur donors.[283] The Fe^{3+} spin and the radical would be strongly antiferromagnetically coupled via direct coupling, as reflected in the low magnetic moment of the Fe–Se framework. However, depend on synthesis conditions, the oxidation level of Fe change accordingly, but the Fe-analog likely to exist in the mixed-valence state with the presences of both Fe^{3+} and Fe^{2+} (Figure 57).

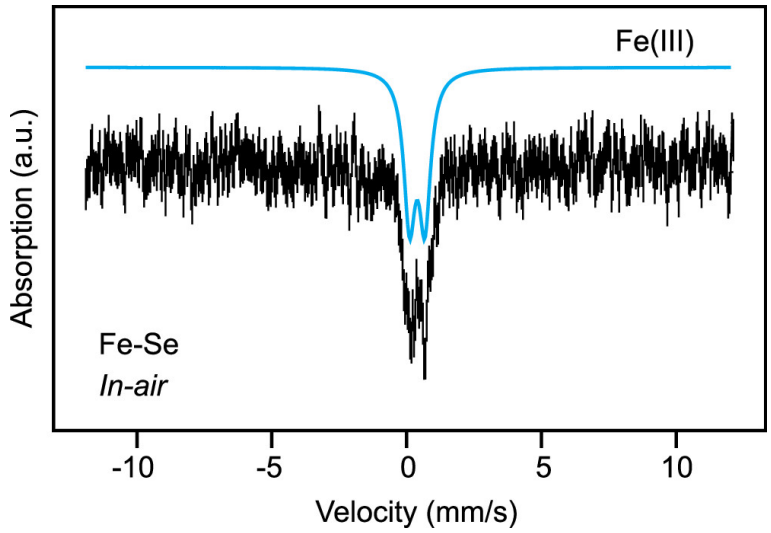

Figure 56. Room-temperature Mössbauer spectrum of Fe–Se prepared in-air. Reprinted with permission from Chem. Mater. 2022, 34, 4, 1905–1920.[6] Copyright 2022 American Chemical Society.

To experimentally explore the electronic structures of the framework materials, their optical absorption spectra were measured by diffuse reflectance UV–vis–NIR spectroscopy. For the frameworks lacking allowed d–d transitions (Mn–S and Zn–S), the optical gaps arise from charge-transfer events from chalcogenide p-orbital to germanium empty sp^3 orbitals, with varying degrees of contributions from the metal d-orbital to the valence bands depending on the degree of metal–ligand covalency. For open-shell frameworks, the DOS diagrams in

Figures 55, Figure 53, and Figure 54 suggest that the band-gap transitions involve a combination of both S-to-Ge and ligand field transitions.

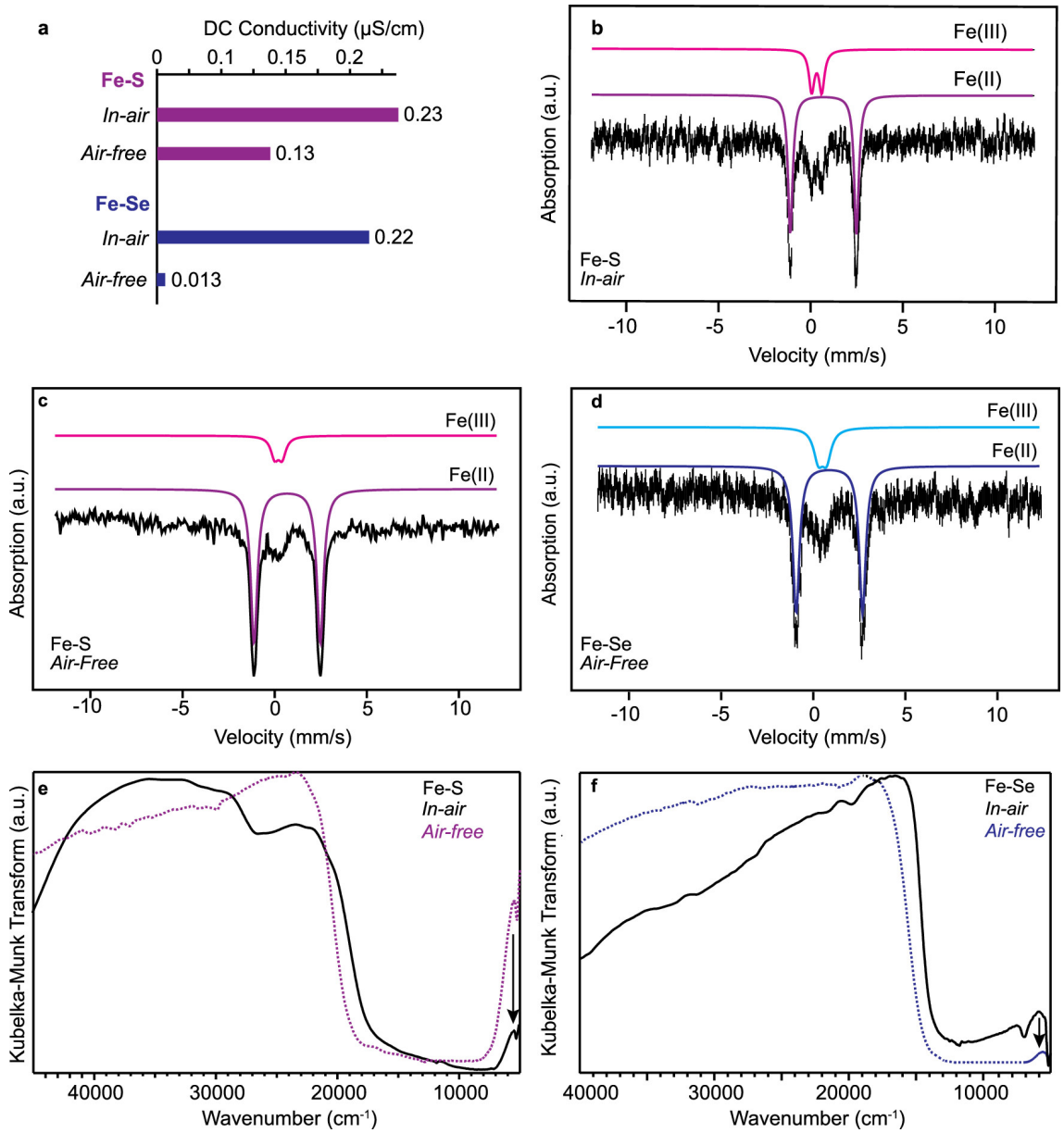

Figure 57. Effect of synthetic preparation on the physical properties of Fe frameworks. (a) Summary of DC conductivities, (b) Mössbauer spectrum of Fe–S prepared in-air, (c) Mössbauer spectrum of Fe–S prepared air-free, (d) Mössbauer spectrum of Fe–Se prepared air-free, (e) diffuse reflectance UV–vis–NIR spectra of Fe–S, and (f) Fe–Se frameworks. Reprinted with permission from Chem. Mater. 2022, 34, 4, 1905–1920.[6] Copyright 2022 American Chemical Society.

The experimentaly UV-vis-NIR spectra indicate a substantial narrowing of band-gap transitions for the open-shell systems, which agrees with density functional theory (DFT) calculations that the conduction band involves both low-lying d-orbitals and Ge-based orbitals stabilized by approximately 1 eV relative to the wider optical gap Zn–S. Indeed, the Mn–S and Zn–S frameworks display optical gaps similar to the parent $TMA_2Ge_4S_{10}$ cluster, whereas the open-shell frameworks exhibit narrowed gaps, suggesting that optical properties depend on the availability of d–d transitions, bond covalency, and electrostatic stabilization of atomic orbitals induced by the linking metal ions. The optical gap transitions of most materials could be assigned using Gaussian fits, which produced the best agreement with optical gaps determined by DFT when the band-edge orbitals were dominated by linking metal d-orbitals (Fe–S, Fe–Se, Co–S, and Ni–S) or sulfur p-orbitals (Zn–S). In contrast, Tauc plot analysis, traditionally reserved for defective and amorphous semiconductors, provided the best fits for Mn–S and Co–Se, which calculations suggest bear nearly equal contributions of chalcogenide and linking metal orbitals in the band-edge orbitals. Table 4 summarizes the experimentally derived optical gaps with values determined from simulated band structures. Together, these data demonstrate the wide tunability of the framework optical properties, with selenium increasing valence band edges relative to sulfur and M^{2+} d-orbitals dominating both band edges to produce optical gaps spanning 2.0–3.6 eV.

4.3.2 High conductivity in Fe-based frameworks: the role of mixed-valency and oxidation level. To understand the role of redox chemistry in the charge transport mechanism, specifically a "charge hopping" versus band-type model, we compared the band diagrams of the framework materials bearing different metal ions, chalcogenides, and redox states. Specifically, we examined the

Table 4. Optical Gap Energies (E_g) as Determined Experimentally from Tauc and Gaussian Plots Compared against Those from Simulated Band Diagrams

Material	**Experimental E_g (eV)**	**Simulated E_g (eV)**
Zn-S	3.6	3.8
Mn-S	3.4	3.2
Ni-S	2.7	2.6
Co-S	3.0	3.0
Fe-S	2.7	2.7
Fe-Se	2.0	2.2/1.9 (Fe^{3+})
Co-Se	2.2	2.3

dispersions of the valence bands because holes act as the dominant charge carriers. Figure 59 summarizes the widths of the valence bands, indicating that the Fe^{2+}–Q frameworks exhibit the greatest band dispersion.

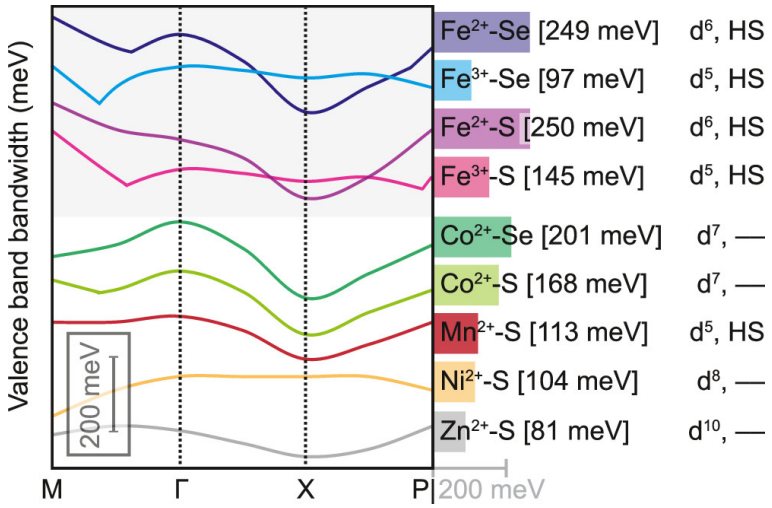

Figure 58. Unit cell of $TMA_2FeGe_4S_{10}$ before (solid color) and after (faded) oxidation of Fe. Reprinted with permission from Chem. Mater. 2022, 34, 4, 1905–1920.[6] Copyright 2022 American Chemical Society.

This result is expected as these bonds are the most covalent, while Zn–S shows the least covalency due to the low metal ion character. Interestingly, calculations of the Fe^{3+}-based frameworks show lower bandwidths compared to those of the Fe^{2+} analogues. Inspection of the geometry-optimized structures

reveals a contraction of the unit cell upon oxidation to form Fe^{3+} (Figure 58). Calculations also predict that this physical distortion causes a change in the optical gap, which helps explain the agreement between Fe and Se prepared in-air with an optical gap of 2.0 eV compared with the simulated band structure of Fe^{3+}–Se (1.9 eV). These results also imply that the superior conductivity of Fe frameworks, specifically those containing Fe^{2+}, arises from the greater mobility of holes in the dispersive valence bands.

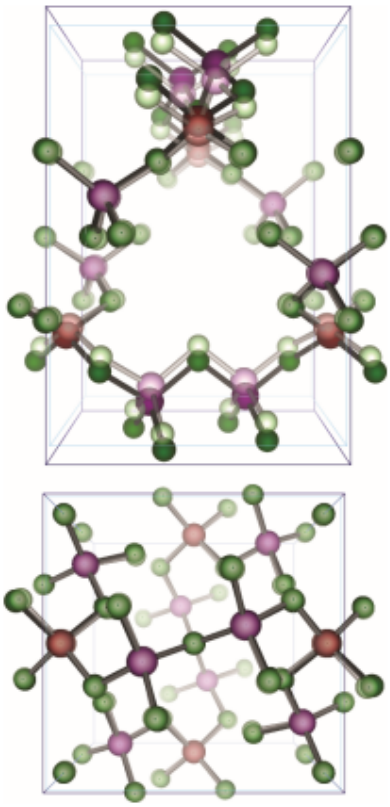

Figure 59. Comparison of valence band dispersions of frameworks with different metal ions, chalcogenides, and oxidation states. Diagrams of valence bands with arbitrary energy offsets for clarity. Frameworks with divalent and trivalent metal ions were simulated with two and one TMA+ cations, respectively. Reprinted with permission from Chem. Mater. 2022, 34, 4, 1905–1920.[6] Copyright 2022 American Chemical Society.

These results suggest a band-type charge transport mechanism for the Fe-containing frameworks and a redox-hopping-type mechanism for the Mn, Co, Ni, and Zn materials. Generally, band-type transport leads to higher conductivities in materials with greater bond covalency and, hence, high charge mobilities, while redox hopping depends on chemical factors that promote outer-sphere electron transfer, as outlined by Marcus theory.[284] Specifically, redox hopping benefits from materials with redox sites in close proximity by improving the likelihood of charge transfer and with mixed valency to provide both donor charges and acceptor orbitals.[208] Experimental measurements indicate that holes act as the dominant charge carriers, implying that the curvatures of valence bands should dictate charge mobilities, while our calculations predict that Fe^{2+} frameworks possess greater valence bandwidths. The experimentally collected EIS spectra corroborate this assignment by showing that Fe–S charge transport involves pure electronic movement, whereas Zn–S conductivity involves the transfer of both electrons and ions, as expected for outer-sphere electron transfer to be accompanied by charge-balancing ions. While band dispersions for pristine Fe^{2+}–Se and Fe^{2+}–S are comparable, the dispersion drop is far more significant for Fe^{3+}–Se than for Fe^{3+}–S, with bands comparable to the flat valence band of Zn–S. High conductivity in these frameworks requires both higher charge carrier densities and dispersive band curvatures (high carrier mobility) but that a critical amount of oxidation causes the frameworks to distort into materials with lower charge mobilities. The redox-dependent conductivity supports the assignment of a band-type mechanism for the Fe frameworks, as well, and explains the superior conductivity of the Fe frameworks. If the mechanism involved redox hopping, then conductivity would maximize with Fe^{2+}/Fe^{3+} in a 50:50 mixture, with conductivity decreasing

beyond this mixture, as has been observed for redox polymers.[285,286] For band-type materials, conductivity generally improves in materials with greater charge carrier concentrations. However, "overoxidation" of the Fe–S and Fe–Se frameworks to form the Fe^{3+} variants causes significant distortions to the lattices that flatten the valence bands and reduce hole mobility.

The general tendency of Fe^{2+} to engage in facile redox chemistry, therefore, implies that the higher conductivity of the Fe frameworks arises from their ability to form dilute charge carrier concentrations. Accordingly, the partial oxidation of Mn–S led to greater DC conductivity by forming an oxidized Mn species. If oxidation had led to dilute concentrations of Ni_{3+} and Co^{3+}, rather than oxidized sulfides, we predict that Ni–S and Co–S also would have demonstrated improved conductivity. Instead, we propose that the Mn, Co, and Ni frameworks show similar charge transport to Zn–S when prepared in air despite their more dispersive valence bands because, like Zn–S, their charge transport involves intra- and intercluster hopping, rather than through bonds. Similarly, among MOF families that can be prepared with a variety of metal ions, the Fe derivatives often exhibit conductivities several orders of magnitude higher and smaller activation energies. Further investigations suggest that Fe promotes charge transport with its high-energy Fe d-orbitals susceptible to oxidation and, hence, $Fe^{2+/3+}$ mixed valency,[287] akin to the Fe frameworks studied here. The conductivity of the Fe–S and Fe–Se frameworks represents rare examples of the three-dimensional band-type transport in porous frameworks. High conductivity in MOFs often arises from charge delocalization along infinite one-dimensional (1-D) chains of inorganic ligands, such as chalcogenides,[288,289] and metal ions within otherwise 3-D frameworks. In this "through-bond" transport mechanism, orbitals are

conjugated along the chains but not across the organic cores of the linkers. In rare cases, the chains are 2-D or 3-D,[290] but orbital overlap does not involve the entire material in an "extended conjugation" fashion. Extended conjugation has been observed in MOFs that employ "redox noninnocent"[291] or "fully conjugated" linkers,[241,292,293] although the examples with the highest conductivities are typically 2-D sheets. For frameworks based on polyoxometalate clusters,[294] the exceptional conductivity of the Fe variants likely arises from redox-type hopping, rather than from band-type transport, due to the ionic nature of Fe^{2+}–O2– bonds. The computed electron density in Figures 55 and Figure 53 and Table 3 shows that the valence bands of most of the frameworks involve the metal d-orbitals and chalcogenide p-orbitals but not the Ge atoms, whereas the conduction bands involve all elements. Hole transport, therefore, does not proceed strictly by "extended conjugation", whereas n-type doping would lead to such a mechanism. Although open-framework chalcogenides comprise a large and important family of materials, few reports have investigated their charge transport properties. The DC conductivities of the MSn_4Se_{10}2– (M = Fe, Mn) frameworks were ascribed primarily to ion transport and reported to be as low as 10^{-10} S/cm, (28) compared to the 10^{-6} S/cm reported here for $FeGe_4S_{10}$2–, which is dominated by electron transport. Such low electronic conductivity is surprising given the covalency of the Fe–S bonds, but it may be explained by low charge carrier densities afforded by the air-free synthetic conditions. Finally, these results reveal mixed-conducting and magnetic ordering behavior previously unknown for open-framework chalcogenides. The ferromagnetic ordering of $TMA_2FeGe_4S_{10}$ observed at 2.75 K provides the first validation of an earlier computational study on this family of material, which predicted ferromagnetism in the Fe variant but not the other analogues.[295] This

study also predicted half-metallicity, which has yet to be reported. The absence of ferromagnetic ordering in Fe–Se likely reflects the increased distance between Fe sites and/or the Fe sites being predominantly Fe^{3+} centers. This may explain the absence of magnetic ordering in the previously studied $TMA_2FeSn_4Se_{10}$.[276] Although open-framework chalcogenides have been widely studied as ionic conductors, the EIS data demonstrate hallmark evidence of mixed ion–electron conductivity. Given the ability of these materials to be prepared with other cations, such as Cs,[277] K,[271] and Li,[279] their propensity for cation exchange,[267] and the variable pore sizes and environments, coupled with the tunable electronic conductivity reported here, these results reveal that open-framework chalcogenides comprise an attractive new class of mixed conductors for studying energy storage and other electrochemical technologies.

4.3.3 A 3D metallic MOF: retrofitted $Fe_3(HIB)_2$. Following this study on the unique property of Fe centers, we proposed that retrofitting an Fe-based 2D MOFs will produce a prominent porous structure with acceptable conductivity for electronic applications. The electronic band structures of eclipsed of $Fe_3(HIB)_2$ and $Cr_3(HIB)_2$ are presented in Figure 60. These 2D-connected materials show similar band dispersion behavior to that of the Ni analogue; bands cross the computed Fermi level in both the out-of-plane and the covalent plane directions. As expected, the increased interlayer distance also flattened the band dispersion in the out-of-plane direction (see Figure 61 and Figure 62).

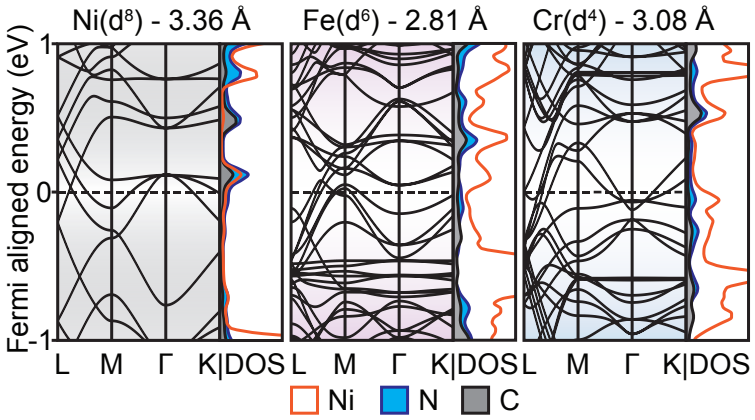

Figure 60. Band structures of eclipsed $M_3(HIB)_2$ showing all materials are metallic and the band remain dispersive near the Fermi level for all metal identity. Reprinted with permission from ACS Appl. Electron. Mater. 2021, 3, 5, 2017–2023.[5] Copyright 2022 American Chemical Society.

The retrofitted MOFs yield metal–axial ligand bond lengths of 1.95 Å (pyrazine), 1.98 Å (bipyridine)$_3$, 2.16 Å (DABCO) for Fe^{2+} analogues, and 2.04 Å (pyrazine), 2.06 Å (bipyridine)$_3$, and 2.24 Å (DABCO) for the Cr^{2+} analogues. The formation of a bonding interaction between DABCO with Cr^{2+} and Fe^{2+} metal centers clearly shows that earlier transition metals can form pure -bonding interaction with axial linkers. Furthermore, there is a slight elongation of the in-plane Fe^{2+} bonds after retrofitting (compared to the nonretrofitted structure, see Table 5) which can be rationalized by increased e– density associated with the metal repulsing the M–pillar bond.

The bond orders for the metal–axial ligands were computed to be 0.32 (DABCO), 0.53 (pyrazine), and 0.51 (bipyridine)$_3$ for the Fe^{2+} analogues and 0.27 (DABCO), 0.45 (pyrazine), and 0.42 (bipyridine)$_3$ for the Cr^{2+} analogues. These bond orders are somewhat smaller than those computed for the metal–ligand bonds in the covalent direction (approximately 0.1–0.2 lower for pyrazine and bipyridine linkers and 0.3–0.4 lower for DABCO linker, Table 5). These weaker

Table 5. Computed bond lengths and bond orders of metal-ligand bond calculated using DDEC approach. The axial linkers are DABCO, 1,4-pyrazine, and 4,4'-bipyridine

MOF	M-L Bond length (Å)		M-L Bond order	
	M-HIB	M-axial linker	M-HIB	M-axial linker
$Ni_3(HIB)_2$ monolayer	1.82		0.84	
$Ni_3(HIB)_2$ eclipsed	1.82		0.78	
$Ni_3(HIB)_2(DABCO)_3$	1.82	3.06	0.78	0.07
$Ni_3(HIB)_2$(1,4-pyrazine)$_3$	1.99	2.11	0.53	0.38
$Ni_3(HIB)_2$(4,4'-bipyridine)$_3$	2.01	2.15	0.52	0.36
$Cr_3(HIB)_2$ monolayer	1.95		0.72	
$Cr_3(HIB)_2$ eclipsed	1.95		0.71	
$Cr_3(HIB)_2(DABCO)_3$	1.96	2.24	0.59	0.27
$Cr_3(HIB)_2$(1,4-pyrazine)$_3$	1.97	2.04	0.57	0.45
$Cr_3(HIB)_2$(4,4'-bipyridine)$_3$	1.96	2.06	0.56	0.42
$Fe_3(HIB)_2$ monolayer	1.85		0.84	
$Fe_3(HIB)_2$ eclipsed	1.85		0.81	
$Fe_3(HIB)_2(DABCO)_3$	1.89	2.16	0.70	0.32
$Fe_3(HIB)_2$(1,4-pyrazine)$_3$	1.90	1.95	0.65	0.53
$Fe_3(HIB)_2$(4,4'-bipyridine)$_3$	1.89	1.98	0.66	0.51

(longer) bonds result from the nonuniform distribution of electron density between metal orbitals and the in-plane and out-of-plane ligands due to their different shape and orientation.[296] These factors contribute to the Jahn–Teller distortion observed in the coordination sphere of our retrofitted structures, which commonly occurs for octahedral complexes.[297,298] The metal–axial ligand bond orders for $Fe_3(HIB)_2(DABCO)_3$ and $Cr_3(HIB)_2(DABCO)_3$ are small but still support the existence of a -bond interaction between the DABCO linker and the Fe^{2+} and Cr^{2+} metal centers. The formation of these axial metal–ligand bonds is supported by the observed Jahn–Teller distortions and the decrease in bond order of the metal–ligand bonds in the covalent direction. This decrease in bond order is not observed for the $Ni_3(HIB)_2(DABCO)_3$ structure, where the metal–axial ligand bond order is significantly smaller (0.07).

The electronic band structures of the 3D retrofitted MOFs (for Cr and Fe) show the retainment of band dispersion in the covalent direction after bridging linker insertion (M–K, Figure 61).

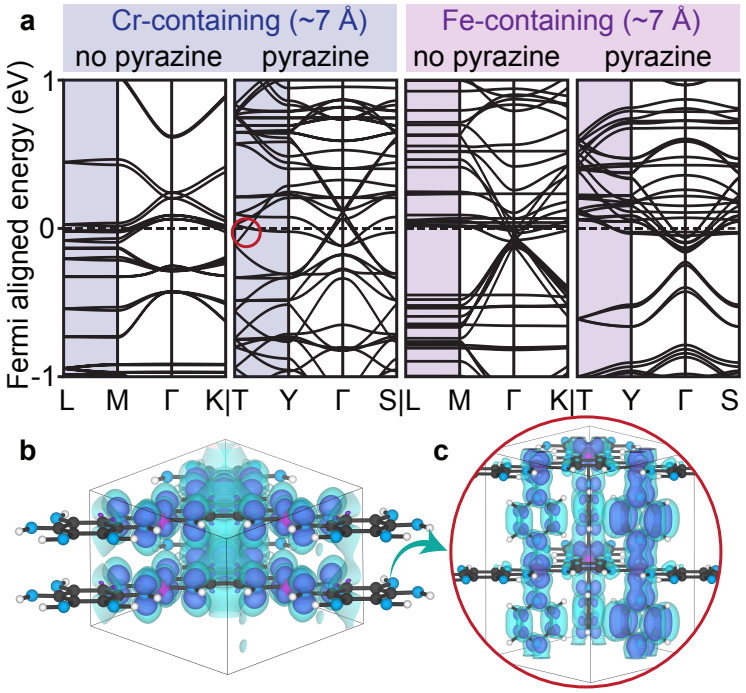

Figure 61. (a) Effect of pyrazine insertion on the band structure of $Cr_3(HIB)_2$ and $Fe_3(HIB)_2$. (b) Charge density of a dispersive band that gave rise to out-of-plane metallicity in 2D eclipsed bulk $Cr_3(HIB)_2$ due to orbital overlap. (c) Charge density of dispersive band that gave rise to out-of-plane metallicity in $Cr_3(HIB)_2$(1,4-pyrazine)$_3$ due to covalent interaction in the axial direction. Reprinted with permission from ACS Appl. Electron. Mater. 2021, 3, 5, 2017–2023.[5] Copyright 2022 American Chemical Society.

Interestingly, for these earlier transition metals, retrofitting also allows the materials to regain dispersion in the out-of-plane direction without the – orbital interactions that exist between the layers when they were closer to each other: an example is shown in Figure 61a, T–Y, along with the charge density comparison before and after retrofitting in Figure 61b,c. Electronic band structures for other retrofitted MOFs depicting similar results can be found in Figure 62. This out-of-

plane covalency is due to the metal–axial ligand bonding interaction (formed from -type interactions hindered by d_{z^2} occupancy in Ni^{2+} analogues). Our calculations suggest that the -bond interaction allows delocalization of charge in the out-of-plane direction via the through-bond charge transport pathway. In $Cr_3(HIB)_2$(1,4-pyrazine)$_3$, the partial charge density from the dispersive, metallic band in the out-of-plane direction (shown in Figure 61c) reveals the Cr–pyrazine bonding interaction. A similar interaction was present in the Fe^{2+} analogue but was not observed in the Ni^{2+} analogue, which possesses flatter bands in the out-of-plane direction (see Figure 51c).

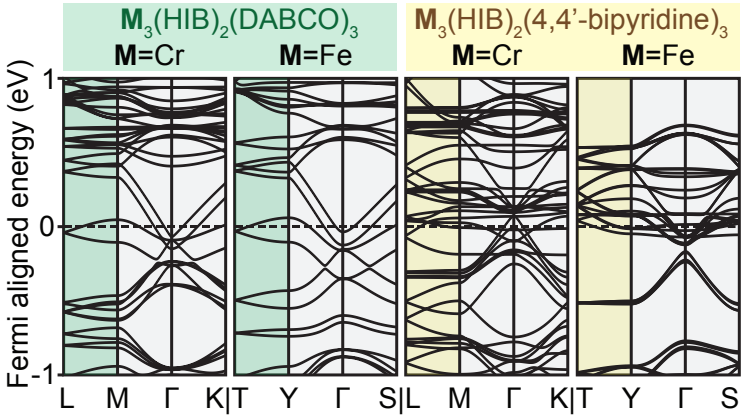

Figure 62. Band structures of retrofitted Cr- and Fe-based MOFs. The highlighted paths from L-to-M and T-to-Y show the band dispersion correspond to the axial direction in real space. Reprinted with permission from ACS Appl. Electron. Mater. 2021, 3, 5, 2017–2023.[5] Copyright 2022 American Chemical Society.

In sum, all metal–axial ligand bond orders for the Fe- and Cr-based retrofitted MOFs are large compared to the Ni-based retrofitted MOFs. Early transition metals are better retrofitting candidates because they allow both -donation and -backbonding interactions from the axial linkers. Furthermore, the formation energies of these 3D retrofitted MOFs from their 2D parent frameworks are largely negative (Table 1), indicating that for Cr^{2+} and Fe^{2+} forming octahedral

coordination spheres from their initial square-planar coordination spheres is energetically favorable.

Unfortunately, phonon calculations for some of the retrofitted 3D MOFs reveal imaginary frequencies (see Table 2). These negative modes would suggest that corresponding structures may not be thermodynamically metastable. However, these frequencies may instead correspond to artificial ring rotations between the retrofitted linkages, particularly given the formation energies are so favorable.

4.3.4 Method. Computational Method. Structural equilibration of both the eclipsed and staggered Ni_3(HIB) was performed with DFT as implemented in the Vienna ab initio Simulation Package (VASP, ver. 5.4.4).[226] The structures were relaxed by using the unrestricted GGA-PBEsol exchange–correlation functional. Ionic relaxation was achieved when all forces were smaller than 0.005 eV $Å^{-1}$.[227] The plane-wave cutoff was set at 500 eV, and the SCF convergence criterion was 10^{-6} eV. An automatically generate k-grid was used during the optimization with $2 \times 2 \times 4$ sampling meshes. Symmetry was not enforced in the case of Jahn–Teller or other distortions. The interlayer distances were then increased from 3.3 to 12 Å at 1 Å increments. Each structure was then fully equilibrated with a constant volume but variable ionic positions and lattice parameters to create the potential energy surfaces in the noncovalent direction. Retrofitting was then performed by adding pyrazines, DABCO, and bipyridine linkers in the eclipsed structure. These structures were then equilibrated by using the same criteria. Other metal derivatives were created by substituting Ni and converged by using the same parameters.

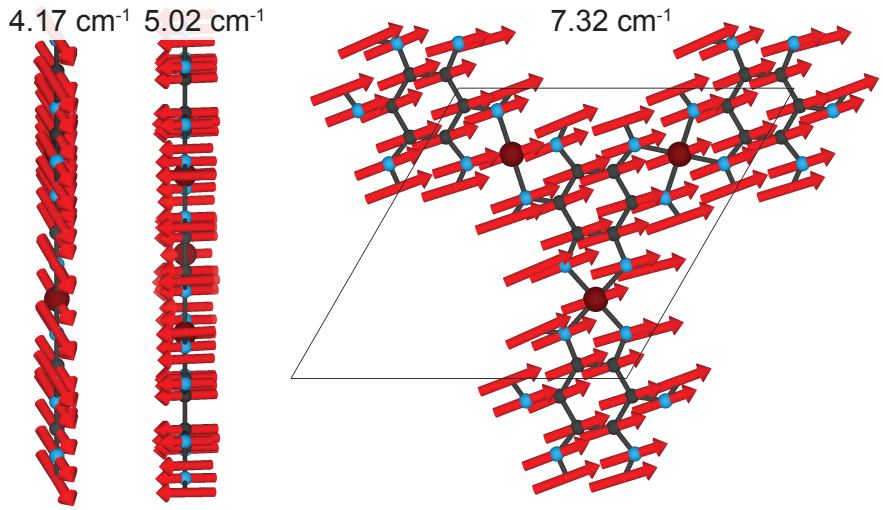

Figure 63. Visualization of the acoustic modes associated with insufficiently tight convergence for phonon calculations. These modes are artificial, and are remedied by unimaginably expensive computations to achieve ¡10-8 eV energetic convergence. The modes shown above map to those highlighted in green in Table S1, Entry 1. The other modes highlighted in green appear similar to what is depicted here. Reprinted with permission from ACS Appl. Electron. Mater. 2021, 3, 5, 2017–2023.[5] Copyright 2022 American Chemical Society.

All optimized structures were used for electronic band structures and corresponding density-of-states calculations at the GGA-PBEsol level of theory since all materials are metallic, and qualitative analysis of band curvature is not thought to change dramatically by using a hybrid functional in this case.[201] Additionally, PBEsol significantly reduced the computational expense. GGA+U calculations and HSE06 functionals were also explored on the bulk staggered structure of $Ni_3(HIB)_2$ to clarify that GGA-PBEsol functional is sufficient for this study. Two U parameters were selected (3 and 6.2 eV) as recommended by the literature on related materials (Figure 64).[299–301]

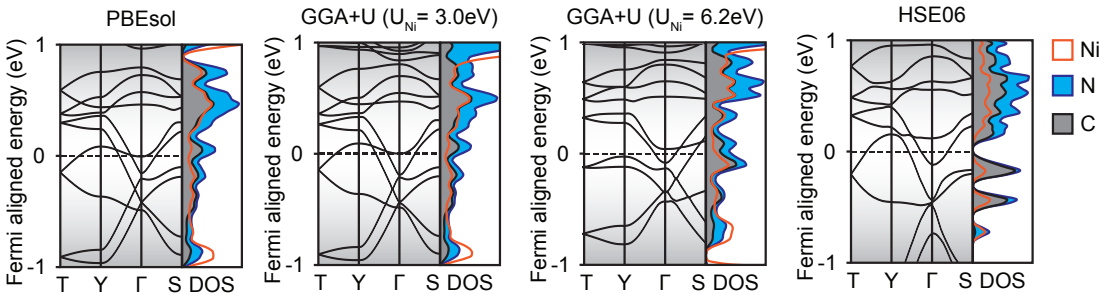

Figure 64. bulk $Ni_3(HIB)_2$ computed with various functionals. The GGA+U approach proved to flatten the out-of-plane vector (aligning with the previously reported band structure; J. Am. Chem. Soc., 2017, 139, 13608-13611). The HSE06 electronic band structure was computed from the PBEsol structure, and hence shows qualitatively similar features to the bulk PBEsol structure. The two U values were selected based on their applications to metals (U = 3 eV) and Ni^{2+} in its oxide (U=6.2 eV). Reprinted with permission from ACS Appl. Electron. Mater. 2021, 3, 5, 2017–2023.[5] Copyright 2022 American Chemical Society.

Phonon modes and frequencies were obtained via the finite differences method as implemented in VASP at the zone-center (-point). Central difference was enforced, and the step size was set to be 0.015 Å as default. The unrestricted GGA-PBEsol exchange-correlation functional was used with the same convergence criteria as above.

4.3.5 Conclusion. Together, our study demonstrates that 3D conductive MOFs can be generated by retrofitting covalent 2D sheets that house square planar metals with partially, or unoccupied, d_{z^2} orbitals using neutral N-donor pillar ligands. The $Ni_3(HIB)_2$ framework exhibits more dispersive bands, especially in the out-of-plane direction, when adopting the eclipsed stacking conformation. However, the eclipsed structure is energetically unfavorable compared to the staggered configuration. Because of d_{z^2} orbital occupancy, retrofitting the $Ni_3(HIB)_2$ scaffold with bipyridine, pyrazine, and DABCO generates thermodynamically destabilized structures. However, incorporating transition

metals with reduced d_{z^2} density form bonding interactions with both DABCO and the aromatic linkages. The resulting materials are thermodynamically stable and potentially dynamically metastable. Although direct synthesis of the Cr and Fe analogues ($Fe_3(HIB)_2$ and $Cr_3(HIB)_2$) may not be tractable, ligand pillaring approaches and metal exchange may afford synthetic access to these structures and the emergence of a novel class of 3D-connected electrical conductors.

The contents of this section have been or are intended to be published in whole or in part. The text presented here has been modified from ACS Appl. Electron. Mater. 2021, 3, 5, 2017–2023.[5] Copyright 2022 American Chemical Society and Chem. Mater. 2022, 34, 4, 1905–1920.[6] Copyright 2022 American Chemical Society.

CHAPTER V

CONCLUSION

Unfortunately, the electrical conductivity of metal-organic frameworks is often less than 10^3 S/cm[30,212,287] making the materials unfit for electronic applications even though the material possess incredible surface area and precise chemical motifs. The nano-porous structure allows MOFs to host chemical reaction both on the surface of the MOFs and within the core of the materials. Furthermore, with the simple framework topology, where organic ligands bind to metal clusters at very specific binding sites, the chemical structure of the framework can be determine and control very accurately on its surface and inside the pore; this allows chemical reaction such as catalysis and adsorption on the framework to be control readily. These advantages allow MOFs to become the most prominent candidates for electronic storage applications such as batteries and capacitors. These storage applications rely heavily on the two properties of the electrode's materials: (i) their surface area[302–306] (ii) and their electrical conductivity.[307] Higher surface area means more charge can be store and high electrical conductivity mean high charge mobility and higher charge carrier concentration. MOFs are extremely suitable in term of satisfying the first requirement of high surface area[12] and in addition, the porous structure allows the reduction of electrode volume while maintaining the high reactive sites concentration. However, most MOFs do not satisfied the second condition of having reasonable electrical conductivity, especially 3D MOFs. In fact, most 3D MOFs are non-conductive due to the ionic nature of the metal-organic interfaces. Up until now, only 2D conductive MOFs are known to be feasible for electronic applications such as supercapacitor[23] and chemiresistive sensors[248] because these 2D layers

possess overlapping π-π orbitals interactions between layers and more covalency charateristic at the metal-organic interface compare to 3D MOFs. Given that these 2D MOFs are somewhat conductive and perhaps satisfy the second condition mentioned above, they do not possess chemical define topology as seen in 3D MOFs where the layers of the 2D MOFs are not static but are constantly slipping. The slipping motion destroys the porous feature and reduces the framework's surface area. Moreover, unlike 3D MOFs where conductivity are highly uniform throughout the frameworks, 2D MOFs possess different conductivity in different directions depend on whether if π-π orbitals overlapping or extended conjugated orbitals is responsible for charge transport pathway in that direction. This gave rise to misalignment issues and difficulty in control the conduction direction if MOFs is used for electronic applications. It's safe to assume that both 2D and 3D MOFs in there current forms are not the best candidates for electronic storage applications. Studies of MOFs should be then focus on exploring new building blocks and topology instead of focus on improving the already existed MOFs. Hence, in this work, we used DFT to elucidate some keys concepts relating to the metal-organic interface which dictate charge transport properties in order to propose design principles for a 3D conductive MOF with reasonable charge transport properties and at the same time, possess a chemical precise porous structure. In our pressure modulation study, we elucidated that the electronic structure of a 2D MOF, specifically, $Ni_3(HIB)_2$ and $Ni_3(HITP)_2$ can be alter via metal-organic interface modification.[4] For a semi-conductive material such as $Ni_3(HITP)_2$ monolayer, the band gap can be reduce or widen by stretching and compressing the metal-organic interface due to stabilization and destabilization of the anti-bonding orbitals. While this is interesting, we also observed a redox event that occur within the $Ni_3(HIB)_2$

monolayer between the metal centers and the organic linkers when we elongated the bond. This allowed us to conclude that unlike 3D MOFs, this class of 2D MOFs possesses more covalency characteristic in their metal-organic interface compare to 3D MOFs because for an ionic bonding interaction, electron density would be more localized and electron transfer should not occur between the metal centers and the organic linkers. Although this study did not provide in depth details on the electron transfer mechanism, one can deduce that the extended conjugated orbitals network is necessary for the electron transfer reaction to happen. Furthermore, this phenomenon happen more readily in $Ni_3(HIB)_2$ in compare to $Ni_3(HITP)_2$ at similar pressure, which means the size of the organic linker has some impact on the covalency of this metal-organic interface, more specifically, smaller conjugated linker means more covalency within the metal-organic interface. Notice, one would argue that $Ni_3(HITP)_2$ has higher conductivity than $Ni_3(HIB)_2$, which is different from this convalency characteristic that we are exploring in this study. $Ni_3(HITP)_2$ is a metallic material in the direction that is perpendicular to the sheet meaning the bulk conductivity for this MOF depend mostly on the overlapping of orbitals between the layers and not the extended conjugation network within each layer. In the monolayer form, $Ni_3(HIB)_2$ is a metallic material and $Ni_3(HITP)_2$ is a semi-conductor - aka, free charge carriers formation and charge transport would occur more readily in $Ni_3(HIB)_2$. In sum, the conclusion from this study provides the first two design principles that is in order to increase the covalency between the metal-organic interface (which should enhance the MOF conductivity), (1) one need to consider a design where the metal orbitals and the organic linkers can form an extended conjugation network and (2) smaller conjugated organic linkers seems to maximize the covalency characteristic within the metal-organic interface.

As mentions above, conductive MOFs need to contain the extended conjugation network, which only exist in 2D layers and is almost non-existent in 3D MOFs. However, one could imagine forming a 3D MOF from a 2D MOF (where extended orbitals conjugation already exist) via retrofitting. In fact, this has been proposed by Foster et. al. on $Ni_3(HITP)_2$[256] and Choi et. al. had shown that this post-synthetic pillar insertion method can be carry out experimentally in another 2D MOF, Cu-THQ[308]. Retrofitting does not only serve the purpose of allowing the MOF to be 3D, but also prevent the MOF from slipping retaining the porosity and increasing the surface area. Both of these studies are stepping stones toward better conductive MOFs. However, as mentioned in our previous study, one must consider carefully when it comes to choose the 2D MOF for retrofitting. In the study of $Ni_3(HITP)_2$, the metallic 2D MOF turned into a semi-conductive 3D MOF after retrofitting due to the destruction of the overlapping orbitals between the layers which govern the transport mobility of this MOF. In the experimental study, Cu-THQ was chosen, and pillar insertion enhances the surface area of this MOF, but did not increase the conductivity of such MOF. We proposed the retrofitting of $Ni_3(HIB)_2$ which possesses very high covalency characteristic within the metal-organic interface.[5] However, our computational results show that retrofitting $Ni_3(HIB)_2$ did not produce a good conductive candidate, instead, we reduced some of the convalency within the layers due to the introduction of pillars that turned the square-planar Ni centers into octahedral coordinations. This was shown to be unfavorable as depicted by the positive formation energy and in our phonon calculations where the retrofitted MOFs were not meta-stable. Inserting the negatively charged linkers onto the negatively charged d_{z^2} orbitals of $Ni_3(HIB)_2$ is unfavorable. Furthermore, this pillars insertion disrupted the extended

conjugation network that existed within the layers, causing the electronic bands to flatten correspond to a diminishing charge mobility for the MOF. Although, we learned that for pillar insertion, the length of the bridging linker has little effect on the electronic structure and the binding affinity of the linker to the metal center, on the other hand, the linker conjugation network play an important role in whether if the bridging linker will bind to the framework. From this study, we learned that (3) for retrofitting, it is preferable for the bridging linkers to be aromatic.

Perhaps retrofitting a 2D MOF into a 3D MOF will only make the MOF more ionic and reduce its conductivity. Given the ionic characteristic, all 3D MOFs may behave like molecular solids. Similarly to our studies on 2D MOFs, we explored the metal-organic interface of several 3D MOFs under temperature modifications using IR spectroscopy combined with computational analysis.[2] We demonstrate, through the use of variable-temperature diffuse reflectance infrared Fourier transform spectroscopy (VT-DRIFTS) aided by ab initio plane wave density functional theory, that melting behavior in zeolitic imidazolate frameworks and carboxylate-based framework, i.e., reversible metal-linker bonding are driven by specific vibrational modes. This can be observed for carboxylate MOFs by monitoring the red-shifts of carboxylate stretches coupled to anharmonic metal-carboxylate oscillators. We investigate a wide class of carboxylate MOFs that includes iconic examples with diverse structures and metal-linker chemistry. These metal-linker dynamics resemble the ubiquitous soft modes that trigger important phase transitions in diverse classes of materials while offering a fundamentally new perspective for the design of next-generation metal–organic materials. Dynamic bonding interaction in these MOFs explain why most 3D MOFs are ionic and possess insufficient charge transport mobility. We also provided evidence that

dynamic bonding also exists in triazolate-based MOFs, especially those that can undergoes phase transition such as $Fe(TA)_2$ and $Cu(TA)_2$.[3] Furthermore, we provided evident that unlike other analog, $Fe(TA)_2$ frameworks possess cooperative interactions which are responsible for the useful properties of spin crossover (SCO) materialslarge hysteresis windows, critical temperatures near room temperature, and abrupt transitions. Variable-temperature vibrational spectroscopy provides evidence that "soft modes" associated with dynamic metal–linker bonding trigger the cooperative SCO transition. Thermodynamic analysis also confirms a cooperativity magnitude much larger than those of other SCO systems, while electron density calculations of $Fe(TA)_2$ support previous theoretical predictions that large cooperativity arises in materials where SCO produces considerable differences in metal–ligand bond polarities between different spin states. Taken together, this combined experimental–computational study provides a microscopic basis for understanding cooperative magnetism and highlights the important role of dynamic bonding in the functional behavior of framework materials. Given that 3D MOFs are ionic, depend on the metal centers, properties such as cooperativity might be beneficial for enhancing conductivity. In fact, our study had shown that the effect of cooperativity combine with spin crossover transition can reduce the band gap in $Fe(TA)_2$ by a significant amount which was not observed in the molecular solid counterpart. The Fe center, with its complex oxidation state and magnetic flexibility is a good candidate for 3D conductive MOFs. In fact, the mix-valency in $Fe(TA)_2$ enhances the MOF conductivity by 9-folds.[27] The takeaway from this investigation on the metal-organic interface in 3D MOFs has lead us to believe that (4) single-metal Fe center is most suitable for creating a 3D conductive MOFs. In fact, we had conducted an transmetallation study on $Ni_3(HIB)_2$

retrofitted structure and found that retrofitted $Fe_3(HIB)_2$ allows the retention of dispersion of electronic bands and the reservation of the metallic characteristic of the material. Furthermore, the negative formation energies showed that these Fe-based 3D retrofitted MOFs are favorable and the structures were shown to be meta-stable without imaginary phonon frequency.[5] All together, we conclude that in order to create a 3D conductive MOFs that can be use for eletronic and energy storage applications, one should considers the following design principles: Starting from a 2D MOFs that have (1) an extended conjugation network within the layers, (2) and small conjugated organic linkers. (3) Retrofit said MOF using aromatic bridging linkers and most importantly (4) the metal centers should be single-Fe ions. In order words, $Fe_3(HIB)_2(pyrazine)_3$ is the best candidate for electronic applications if someone can make it.

REFERENCES

[1] Lee, S.-J.; Mancuso, J. L.; Le, K. N.; Malliakas, C. D.; Bae, Y.-S.; Hendon, C. H.; Islamoglu, T.; Farha, O. K. *ACS Materials Lett.* **2020**, *2*, 499–504, Publisher: American Chemical Society.

[2] Andreeva, A. B.; Le, K. N.; Chen, L.; Kellman, M. E.; Hendon, C. H.; Brozek, C. K. *J. Am. Chem. Soc.* **2020**, *142*, 19291–19299, Publisher: American Chemical Society.

[3] Andreeva, A. B.; Le, K. N.; Kadota, K.; Horike, S.; Hendon, C. H.; Brozek, C. K. *Chem. Mater.* **2021**, *33*, 8534–8545, Publisher: American Chemical Society.

[4] N. Le, K.; H. Hendon, C. *Physical Chemistry Chemical Physics* **2019**, *21*, 25773–25778, Publisher: Royal Society of Chemistry.

[5] Le, K. N.; Mancuso, J. L.; Hendon, C. H. *ACS Appl. Electron. Mater.* **2021**, *3*, 2017–2023, Publisher: American Chemical Society.

[6] McKenzie, J.; Le, K. N.; Bardgett, D. J.; Collins, K. A.; Ericson, T.; Wojnar, M. K.; Chouinard, J.; Golledge, S.; Cozzolino, A. F.; Johnson, D. C.; Hendon, C. H.; Brozek, C. K. *Chem. Mater.* **2022**, Publisher: American Chemical Society.

[7] Voosen, P. *Science* **2021**, *371*, 334–335, Publisher: American Association for the Advancement of Science.

[8] Green, M.; Dunlop, E.; Hohl-Ebinger, J.; Yoshita, M.; Kopidakis, N.; Hao, X. *Progress in Photovoltaics: Research and Applications* **2021**, *29*, 3–15, _eprint: https://onlinelibrary.wiley.com/doi/pdf/10.1002/pip.3371.

[9] Yamaguchi, M.; Dimroth, F.; Geisz, J. F.; Ekins-Daukes, N. J. *Journal of Applied Physics* **2021**, *129*, 240901, Publisher: American Institute of Physics.

[10] Geisz, J. F.; France, R. M.; Schulte, K. L.; Steiner, M. A.; Norman, A. G.; Guthrey, H. L.; Young, M. R.; Song, T.; Moriarty, T. *Nature Energy* **2020**, *5*, 326–335, Number: 4 Publisher: Nature Publishing Group.

[11] Qian, J.; Ernst, M.; Wu, N.; Blakers, A. *Sustainable Energy & Fuels* **2019**, *3*, 1439–1447, Publisher: The Royal Society of Chemistry.

[12] Farha, O. K.; Eryazici, I.; Jeong, N. C.; Hauser, B. G.; Wilmer, C. E.; Sarjeant, A. A.; Snurr, R. Q.; Nguyen, S. T.; Yazaydın, A. ; Hupp, J. T. *J. Am. Chem. Soc.* **2012**, *134*, 15016–15021, Publisher: American Chemical Society.

[13] Xie, K.; Fu, Q.; Xu, C.; Lu, H.; Zhao, Q.; Curtain, R.; Gu, D.; Webley, P. A.; Qiao, G. G. *Energy Environ. Sci.* **2018**, *11*, 544–550.

[14] Ding, M.; Flaig, R. W.; Jiang, H.-L.; Yaghi, O. M. *Chem. Soc. Rev.* **2019**, *48*, 2783–2828.

[15] Farha, O. K.; Özgür Yazaydın, A.; Eryazici, I.; Malliakas, C. D.; Hauser, B. G.; Kanatzidis, M. G.; Nguyen, S. T.; Snurr, R. Q.; Hupp, J. T. *Nature Chemistry* **2010**, *2*, 944–948.

[16] Liang, W.; Bhatt, P. M.; Shkurenko, A.; Adil, K.; Mouchaham, G.; Aggarwal, H.; Mallick, A.; Jamal, A.; Belmabkhout, Y.; Eddaoudi, M. *Chem* **2019**, *5*, 950–963.

[17] Metzger, E. D.; Comito, R. J.; Wu, Z.; Zhang, G.; Dubey, R. C.; Xu, W.; Miller, J. T.; Dincă, M. *ACS Sustainable Chem. Eng.* **2019**, *7*, 6654–6661.

[18] Horcajada, P.; Serre, C.; Vallet-Regí, M.; Sebban, M.; Taulelle, F.; Férey, G. *Angew. Chem. Int. Ed. Engl.* **2006**, *45*, 5974–5978.

[19] An, J.; Geib, S. J.; Rosi, N. L. *J. Am. Chem. Soc.* **2009**, *131*, 8376–8377.

[20] Lee, C. Y.; Farha, O. K.; Hong, B. J.; Sarjeant, A. A.; Nguyen, S. T.; Hupp, J. T. *J. Am. Chem. Soc.* **2011**, *133*, 15858–15861.

[21] Lin, C.-C.; Huang, Y.-C.; Usman, M.; Chao, W.-H.; Lin, W.-K.; Luo, T.-T.; Whang, W.-T.; Chen, C.-H.; Lu, K.-L. *ACS Appl. Mater. Interfaces* **2019**, *11*, 3400–3406.

[22] Vlad, A.; Balducci, A. *Nature Materials* **2017**, *16*, 161–162.

[23] Sheberla, D.; Bachman, J. C.; Elias, J. S.; Sun, C.-J.; Shao-Horn, Y.; Dincă, M. *Nat Mater* **2017**, *16*, 220–224.

[24] Hendon, C. H.; Tiana, D.; Fontecave, M.; Sanchez, C.; D'arras, L.; Sassoye, C.; Rozes, L.; Mellot-Draznieks, C.; Walsh, A. *Journal of the American Chemical Society* **2013**, *135*, 10942–10945, Publisher: American Chemical Society.

[25] Li, Y.; Fu, Y.; Ni, B.; Ding, K.; Chen, W.; Wu, K.; Huang, X.; Zhang, Y. *AIP Advances* **2018**, *8*, 035012.

[26] Vitillo, J. G.; Presti, D.; Luz, I.; Llabrés i Xamena, F. X.; Bordiga, S. *The Journal of Physical Chemistry C* **2020**, *124*, 23707–23715, Publisher: American Chemical Society.

[27] Park, J. G.; Aubrey, M. L.; Oktawiec, J.; Chakarawet, K.; Darago, L. E.; Grandjean, F.; Long, G. J.; Long, J. R. *J. Am. Chem. Soc.* **2018**, *140*, 8526–8534.

[28] Huang, X.; Sheng, P.; Tu, Z.; Zhang, F.; Wang, J.; Geng, H.; Zou, Y.; Di, C.-a.; Yi, Y.; Sun, Y.; Xu, W.; Zhu, D. *Nature Communications* **2015**, *6*, 7408, Number: 1 Publisher: Nature Publishing Group.

[29] Hmadeh, M. et al. *Chemistry of Materials* **2012**, *24*, 3511–3513, Publisher: American Chemical Society.

[30] Sheberla, D.; Sun, L.; Blood-Forsythe, M. A.; Er, S.; Wade, C. R.; Brozek, C. K.; Aspuru-Guzik, A.; Dincă, M. *J. Am. Chem. Soc.* **2014**, *136*, 8859–8862.

[31] Krstić, P. S.; Dean, D. J.; Zhang, X. G.; Keffer, D.; Leng, Y. S.; Cummings, P. T.; Wells, J. C. *Computational Materials Science* **2003**, *28*, 321–341.

[32] Westermayr, J.; Gastegger, M.; Schütt, K. T.; Maurer, R. J. *The Journal of Chemical Physics* **2021**, *154*, 230903, Publisher: American Institute of Physics.

[33] Lipkowitz, K. B.; Cundari, T. R.; Boyd, D. B. *Reviews in Computational Chemistry, Volume 26*; John Wiley & Sons, 2008; Google-Books-ID: KuJTWueg1NgC.

[34] Jensen, F. *Israel Journal of Chemistry* **2022**, *62*, e202100027, _eprint: https://onlinelibrary.wiley.com/doi/pdf/10.1002/ijch.202100027.

[35] Senn, H. M.; Thiel, W. *Angewandte Chemie International Edition* **2009**, *48*, 1198–1229, _eprint: https://onlinelibrary.wiley.com/doi/pdf/10.1002/anie.200802019.

[36] Cui, Q.; Elstner, M. *Physical Chemistry Chemical Physics* **2014**, *16*, 14368–14377, Publisher: Royal Society of Chemistry.

[37] Stewart, J. J.; Davis, L. P.; Burggraf, L. W. *Journal of Computational Chemistry* **1987**, *8*, 1117–1123, _eprint: https://onlinelibrary.wiley.com/doi/pdf/10.1002/jcc.540080808.

[38] Friesner, R. A. *Proceedings of the National Academy of Sciences* **2005**, *102*, 6648–6653, Publisher: Proceedings of the National Academy of Sciences.

[39] Parr, R. G. *Annual Review of Physical Chemistry* **1983**, *34*, 631–656, _eprint: https://doi.org/10.1146/annurev.pc.34.100183.003215.

[40] Seminario, J. M. *Recent Developments and Applications of Modern Density Functional Theory*; Elsevier, 1996.

[41] Burke, K. *The Journal of Chemical Physics* **2012**, *136*, 150901, Publisher: American Institute of Physics.

[42] Woolley, R. G.; Sutcliffe, B. T. *Chemical Physics Letters* **1977**, *45*, 393–398.

[43] McWeeny, R. *Physical Review* **1959**, *114*, 1528–1529, Publisher: American Physical Society.

[44] Giese, T. J.; York, D. M. *The Journal of Chemical Physics* **2010**, *133*, 244107.

[45] Jackson, K.; Pederson, M. R. *Physical Review B* **1990**, *42*, 3276–3281, Publisher: American Physical Society.

[46] Sahni, V.; Gruenebaum, J.; Perdew, J. P. *Physical Review B* **1982**, *26*, 4371–4377, Publisher: American Physical Society.

[47] Perdew, J. P. *Physica B: Condensed Matter* **1991**, *172*, 1–6.

[48] M. del Campo, J.; Gázquez, J. L.; Trickey, S. B.; Vela, A. *Chemical Physics Letters* **2012**, *543*, 179–183.

[49] Simón, L.; M. Goodman, J. *Organic & Biomolecular Chemistry* **2011**, *9*, 689–700, Publisher: Royal Society of Chemistry.

[50] Schwabe, T.; Grimme, S. *Physical Chemistry Chemical Physics* **2007**, *9*, 3397–3406, Publisher: Royal Society of Chemistry.

[51] Tirado-Rives, J.; Jorgensen, W. L. *Journal of Chemical Theory and Computation* **2008**, *4*, 297–306, Publisher: American Chemical Society.

[52] Deák, P.; Aradi, B.; Frauenheim, T.; Janzén, E.; Gali, A. *Physical Review B* **2010**, *81*, 153203, Publisher: American Physical Society.

[53] Kresse, G.; Furthmüller, J. *Computational Materials Science* **1996**, *6*, 15–50.

[54] Kühne, T. D. et al. *The Journal of Chemical Physics* **2020**, *152*, 194103, Publisher: American Institute of Physics.

[55] Smyth, M. S.; Martin, J. H. J. *Molecular Pathology* **2000**, *53*, 8–14.

[56] Singleton, J. *Band Theory and Electronic Properties of Solids*; OUP Oxford, 2001; Google-Books-ID: MftzBAAAQBAJ.

[57] Shen, P.; He, W.-W.; Du, D.-Y.; Jiang, H.-L.; Li, S.-L.; Lang, Z.-L.; Su, Z.-M.; Fu, Q.; Lan, Y.-Q. *Chemical Science* **2014**, *5*, 1368–1374, Publisher: The Royal Society of Chemistry.

[58] Van Vleet, M. J.; Weng, T.; Li, X.; Schmidt, J. *Chemical Reviews* **2018**, *118*, 3681–3721, Publisher: American Chemical Society.

[59] Zaczek, A. J.; Catalano, L.; Naumov, P.; Korter, T. M. *Chemical Science* **2019**, *10*, 1332–1341, Publisher: The Royal Society of Chemistry.

[60] Wang, K.; Liu, J.; Yang, K.; Liu, B.; Zou, B. *The Journal of Physical Chemistry C* **2014**, *118*, 8122–8127, Publisher: American Chemical Society.

[61] Mir, M. H.; Koh, L. L.; Tan, G. K.; Vittal, J. J. *Angewandte Chemie International Edition* **2010**, *49*, 390–393, _eprint: https://onlinelibrary.wiley.com/doi/pdf/10.1002/anie.200905898.

[62] Bobrovs, R.; Seton, L.; Actiņš, A. *CrystEngComm* **2014**, *16*, 10581–10591, Publisher: The Royal Society of Chemistry.

[63] Chen, X.-D.; Zhao, X.-H.; Chen, M.; Du, M. *Chemistry – A European Journal* **2009**, *15*, 12974–12977, _eprint: https://onlinelibrary.wiley.com/doi/pdf/10.1002/chem.200902306.

[64] Qin, T.; Gong, J.; Ma, J.; Wang, X.; Wang, Y.; Xu, Y.; Shen, X.; Zhu, D. *Chemical Communications* **2014**, *50*, 15886–15889, Publisher: The Royal Society of Chemistry.

[65] Gong, X.; Noh, H.; Gianneschi, N. C.; Farha, O. K. *Journal of the American Chemical Society* **2019**, *141*, 6146–6151, Publisher: American Chemical Society.

[66] Shaikh, S. M.; Usov, P. M.; Zhu, J.; Cai, M.; Alatis, J.; Morris, A. J. *Inorganic Chemistry* **2019**, *58*, 5145–5153, Publisher: American Chemical Society.

[67] Karadeniz, B.; Žilić, D.; Huskić, I.; Germann, L. S.; Fidelli, A. M.; Muratović, S.; Lončarić, I.; Etter, M.; Dinnebier, R. E.; Barišić, D.; Cindro, N.; Islamoglu, T.; Farha, O. K.; Friščić, T.; Užarević, K. *Journal of the American Chemical Society* **2019**, *141*, 19214–19220, Publisher: American Chemical Society.

[68] Bai, Y.; Dou, Y.; Xie, L.-H.; Rutledge, W.; Li, J.-R.; Zhou, H.-C. *Chemical Society Reviews* **2016**, *45*, 2327–2367, Publisher: The Royal Society of Chemistry.

[69] Lyu, J.; Zhang, X.; Otake, K.-i.; Wang, X.; Li, P.; Li, Z.; Chen, Z.; Zhang, Y.; Wasson, M. C.; Yang, Y.; Bai, P.; Guo, X.; Islamoglu, T.; Farha, O. K. *Chemical Science* **2019**, *10*, 1186–1192, Publisher: The Royal Society of Chemistry.

[70] Wasson, M. C.; Lyu, J.; Islamoglu, T.; Farha, O. K. *Inorganic Chemistry* **2019**, *58*, 1513–1517, Publisher: American Chemical Society.

[71] Yuan, S.; Zou, L.; Li, H.; Chen, Y.-P.; Qin, J.; Zhang, Q.; Lu, W.; Hall, M. B.; Zhou, H.-C. *Angewandte Chemie International Edition* **2016**, *55*, 10776–10780, _eprint: https://onlinelibrary.wiley.com/doi/pdf/10.1002/anie.201604313.

[72] Cavka, J. H.; Jakobsen, S.; Olsbye, U.; Guillou, N.; Lamberti, C.; Bordiga, S.; Lillerud, K. P. *Journal of the American Chemical Society* **2008**, *130*, 13850–13851, Publisher: American Chemical Society.

[73] Kandiah, M.; Nilsen, M. H.; Usseglio, S.; Jakobsen, S.; Olsbye, U.; Tilset, M.; Larabi, C.; Quadrelli, E. A.; Bonino, F.; Lillerud, K. P. *Chemistry of Materials* **2010**, *22*, 6632–6640, Publisher: American Chemical Society.

[74] Kim, M.; Cahill, J. F.; Su, Y.; Prather, K. A.; Cohen, S. M. *Chemical Science* **2011**, *3*, 126–130, Publisher: The Royal Society of Chemistry.

[75] DeStefano, M. R.; Islamoglu, T.; Garibay, S. J.; Hupp, J. T.; Farha, O. K. *Chemistry of Materials* **2017**, *29*, 1357–1361, Publisher: American Chemical Society.

[76] Taddei, M.; Wakeham, R. J.; Koutsianos, A.; Andreoli, E.; Barron, A. R. *Angewandte Chemie International Edition* **2018**, *57*, 11706–11710, _eprint: https://onlinelibrary.wiley.com/doi/pdf/10.1002/anie.201806910.

[77] Wu, H.; Chua, Y. S.; Krungleviciute, V.; Tyagi, M.; Chen, P.; Yildirim, T.; Zhou, W. *Journal of the American Chemical Society* **2013**, *135*, 10525–10532, Publisher: American Chemical Society.

[78] Shearer, G. C.; Chavan, S.; Ethiraj, J.; Vitillo, J. G.; Svelle, S.; Olsbye, U.; Lamberti, C.; Bordiga, S.; Lillerud, K. P. *Chemistry of Materials* **2014**, *26*, 4068–4071, Publisher: American Chemical Society.

[79] Shearer, G. C.; Chavan, S.; Bordiga, S.; Svelle, S.; Olsbye, U.; Lillerud, K. P. *Chemistry of Materials* **2016**, *28*, 3749–3761, Publisher: American Chemical Society.

[80] Perfecto-Irigaray, M.; Beobide, G.; Castillo, O.; Silva, I. d.; García-Lojo, D.; Luque, A.; Mendia, A.; Pérez-Yáñez, S. *Chemical Communications* **2019**, *55*, 5954–5957, Publisher: The Royal Society of Chemistry.

[81] Famprikis, T.; Canepa, P.; Dawson, J. A.; Islam, M. S.; Masquelier, C. *Nature Materials* **2019**, *18*, 1278–1291, Number: 12 Publisher: Nature Publishing Group.

[82] Sachs, C.; Hildebrand, M.; Völkening, S.; Wintterlin, J.; Ertl, G. *Science* **2001**, *293*, 1635–1638, Publisher: American Association for the Advancement of Science.

[83] Scott, J. F. *Reviews of Modern Physics* **1974**, *46*, 83–128, Publisher: American Physical Society.

[84] Cochran, W. *Advances in Physics* **1960**, *9*, 387–423, Publisher: Taylor & Francis _eprint: https://doi.org/10.1080/00018736000101229.

[85] Dunnett, K.; Narayan, A.; Spaldin, N. A.; Balatsky, A. V. *Physical Review B* **2018**, *97*, 144506, Publisher: American Physical Society.

[86] Miyata, K.; Zhu, X.-Y. *Nature Materials* **2018**, *17*, 379–381, Number: 5 Publisher: Nature Publishing Group.

[87] Jiang, M. P. et al. *Nature Communications* **2016**, *7*, 12291, Number: 1 Publisher: Nature Publishing Group.

[88] O'Hara, A.; Demkov, A. A. *Physical Review B* **2015**, *91*, 094305, Publisher: American Physical Society.

[89] Wang, Z.; Rhodes, D. A.; Watanabe, K.; Taniguchi, T.; Hone, J. C.; Shan, J.; Mak, K. F. *Nature* **2019**, *574*, 76–80, Number: 7776 Publisher: Nature Publishing Group.

[90] Kogar, A.; Rak, M. S.; Vig, S.; Husain, A. A.; Flicker, F.; Joe, Y. I.; Venema, L.; MacDougall, G. J.; Chiang, T. C.; Fradkin, E.; van Wezel, J.; Abbamonte, P. *Science* **2017**, *358*, 1314–1317, Publisher: American Association for the Advancement of Science.

[91] Shuvaev, A. M.; Hemberger, J.; Niermann, D.; Schrettle, F.; Loidl, A.; Ivanov, V. Y.; Travkin, V. D.; Mukhin, A. A.; Pimenov, A. *Physical Review B* **2010**, *82*, 174417, Publisher: American Physical Society.

[92] Cowley, R. A. *Integrated Ferroelectrics* **2012**, *133*, 109–117, Publisher: Taylor & Francis _eprint: https://doi.org/10.1080/10584587.2012.663634.

[93] Fleury, P. A. *Annual Review of Materials Science* **1976**, *6*, 157–180, _eprint: https://doi.org/10.1146/annurev.ms.06.080176.001105.

[94] Gaillac, R.; Pullumbi, P.; Beyer, K. A.; Chapman, K. W.; Keen, D. A.; Bennett, T. D.; Coudert, F.-X. *Nature Materials* **2017**, *16*, 1149–1154, Number: 11 Publisher: Nature Publishing Group.

[95] Costa Gomes, M.; Pison, L.; Červinka, C.; Padua, A. *Angewandte Chemie International Edition* **2018**, *57*, 11909–11912, _eprint: https://onlinelibrary.wiley.com/doi/pdf/10.1002/anie.201805495.

[96] Longley, L. et al. *Chemical Science* **2019**, *10*, 3592–3601, Publisher: The Royal Society of Chemistry.

[97] Bumstead, A. M.; Gómez, M. L. R.; Thorne, M. F.; Sapnik, A. F.; Longley, L.; Tuffnell, J. M.; Keeble, D. S.; Keen, D. A.; Bennett, T. D. *CrystEngComm* **2020**, *22*, 3627–3637, Publisher: The Royal Society of Chemistry.

[98] Bennett, T. D.; Horike, S. *Nature Reviews Materials* **2018**, *3*, 431–440, Number: 11 Publisher: Nature Publishing Group.

[99] Ogawa, T.; Takahashi, K.; Nagarkar, S. S.; Ohara, K.; Hong, Y.-l.; Nishiyama, Y.; Horike, S. *Chemical Science* **2020**, *11*, 5175–5181, Publisher: The Royal Society of Chemistry.

[100] Horike, S.; Nagarkar, S. S.; Ogawa, T.; Kitagawa, S. *Angewandte Chemie International Edition* **2020**, *59*, 6652–6664, _eprint: https://onlinelibrary.wiley.com/doi/pdf/10.1002/anie.201911384.

[101] Chen, W.; Horike, S.; Umeyama, D.; Ogiwara, N.; Itakura, T.; Tassel, C.; Goto, Y.; Kageyama, H.; Kitagawa, S. *Angewandte Chemie International Edition* **2016**, *55*, 5195–5200, _eprint: https://onlinelibrary.wiley.com/doi/pdf/10.1002/anie.201600123.

[102] Zhou, C. et al. *Nat Commun* **2018**, *9*, 1–9.

[103] Hou, J. et al. *Nature Communications* **2019**, *10*, 2580, Number: 1 Publisher: Nature Publishing Group.

[104] Hou, J. et al. *Journal of the American Chemical Society* **2020**, *142*, 3880–3890, Publisher: American Chemical Society.

[105] Umeyama, D.; Funnell, N. P.; Cliffe, M. J.; Hill, J. A.; Goodwin, A. L.; Hijikata, Y.; Itakura, T.; Okubo, T.; Horike, S.; Kitagawa, S. *Chemical Communications* **2015**, *51*, 12728–12731, Publisher: The Royal Society of Chemistry.

[106] Brozek, C. K.; Michaelis, V. K.; Ong, T.-C.; Bellarosa, L.; López, N.; Griffin, R. G.; Dincă, M. *ACS Central Science* **2015**, *1*, 252–260, Publisher: American Chemical Society.

[107] Krylov, A.; Vtyurin, A.; Petkov, P.; Senkovska, I.; Maliuta, M.; Bon, V.; Heine, T.; Kaskel, S.; Slyusareva, E. *Physical Chemistry Chemical Physics* **2017**, *19*, 32099–32104, Publisher: The Royal Society of Chemistry.

[108] Hoffman, A. E. J.; Vanduyfhuys, L.; Nevjestić, I.; Wieme, J.; Rogge, S. M. J.; Depauw, H.; Van Der Voort, P.; Vrielinck, H.; Van Speybroeck, V. *The Journal of Physical Chemistry C* **2018**, *122*, 2734–2746, Publisher: American Chemical Society.

[109] Rao, Y.-L.; Chortos, A.; Pfattner, R.; Lissel, F.; Chiu, Y.-C.; Feig, V.; Xu, J.; Kurosawa, T.; Gu, X.; Wang, C.; He, M.; Chung, J. W.; Bao, Z. *Journal of the American Chemical Society* **2016**, *138*, 6020–6027, Publisher: American Chemical Society.

[110] Williams, K. A.; Boydston, A. J.; Bielawski, C. W. *Chemical Society Reviews* **2007**, *36*, 729–744, Publisher: The Royal Society of Chemistry.

[111] Norris, B. C.; Bielawski, C. W. *Macromolecules* **2010**, *43*, 3591–3593, Publisher: American Chemical Society.

[112] Williams, K. A.; Dreyer, D. R.; Bielawski, C. W. *MRS Bulletin* **2008**, *33*, 759–765.

[113] Dobrawa, R.; Würthner, F. *Journal of Polymer Science Part A: Polymer Chemistry* **2005**, *43*, 4981–4995, _eprint: https://onlinelibrary.wiley.com/doi/pdf/10.1002/pola.20997.

[114] Lewis, A. K. d. K.; Caddick, S.; Cloke, F. G. N.; Billingham, N. C.; Hitchcock, P. B.; Leonard, J. *Journal of the American Chemical Society* **2003**, *125*, 10066–10073, Publisher: American Chemical Society.

[115] Bunting, J. W.; Thong, K. M. *Canadian Journal of Chemistry* **1970**, *48*, 1654–1656, Publisher: NRC Research Press.

[116] Grosch, J. S.; Paesani, F. *Journal of the American Chemical Society* **2012**, *134*, 4207–4215, Publisher: American Chemical Society.

[117] Yot, P. G.; Ma, Q.; Haines, J.; Yang, Q.; Ghoufi, A.; Devic, T.; Serre, C.; Dmitriev, V.; Férey, G.; Zhong, C.; Maurin, G. *Chemical Science* **2012**, *3*, 1100–1104, Publisher: The Royal Society of Chemistry.

[118] Ghoufi, A.; Benhamed, K.; Boukli-Hacene, L.; Maurin, G. *ACS Central Science* **2017**, *3*, 394–398, Publisher: American Chemical Society.

[119] Parent, L. R.; Pham, C. H.; Patterson, J. P.; Denny, M. S.; Cohen, S. M.; Gianneschi, N. C.; Paesani, F. *Journal of the American Chemical Society* **2017**, *139*, 13973–13976, Publisher: American Chemical Society.

[120] Nishida, J.; Tamimi, A.; Fei, H.; Pullen, S.; Ott, S.; Cohen, S. M.; Fayer, M. D. *Proceedings of the National Academy of Sciences* **2014**, *111*, 18442–18447, Publisher: Proceedings of the National Academy of Sciences.

[121] Mao, V. Y.; Milner, P. J.; Lee, J.-H.; Forse, A. C.; Kim, E. J.; Siegelman, R. L.; McGuirk, C. M.; Zasada, L. B.; Neaton, J. B.; Reimer, J. A.; Long, J. R. *Angewandte Chemie International Edition* **2020**, *59*, 19468–19477, _eprint: https://onlinelibrary.wiley.com/doi/pdf/10.1002/anie.201915561.

[122] McDonald, T. M. et al. *Nature* **2015**, *519*, 303–308, Number: 7543 Publisher: Nature Publishing Group.

[123] Kong, X.; Scott, E.; Ding, W.; Mason, J. A.; Long, J. R.; Reimer, J. A. *Journal of the American Chemical Society* **2012**, *134*, 14341–14344, Publisher: American Chemical Society.

[124] Brozek, C. K.; Ozarowski, A.; Stoian, S. A.; Dincă, M. *Inorganic Chemistry Frontiers* **2017**, *4*, 782–788, Publisher: The Royal Society of Chemistry.

[125] Wu, Y.; Kobayashi, A.; Halder, G. J.; Peterson, V. K.; Chapman, K. W.; Lock, N.; Southon, P. D.; Kepert, C. J. *Angewandte Chemie International Edition* **2008**, *47*, 8929–8932, _eprint: https://onlinelibrary.wiley.com/doi/pdf/10.1002/anie.200803925.

[126] Lock, N.; Christensen, M.; Wu, Y.; Peterson, V. K.; Thomsen, M. K.; Piltz, R. O.; Ramirez-Cuesta, A. J.; McIntyre, G. J.; Norén, K.; Kutteh, R.; Kepert, C. J.; Kearley, G. J.; Iversen, B. B. *Dalton Transactions* **2013**, *42*, 1996–2007, Publisher: The Royal Society of Chemistry.

[127] Zhou, W.; Wu, H.; Yildirim, T.; Simpson, J. R.; Walker, A. R. H. *Physical Review B* **2008**, *78*, 054114, Publisher: American Physical Society.

[128] Schneider, C.; Bodesheim, D.; Ehrenreich, M. G.; Crocellà, V.; Mink, J.; Fischer, R. A.; Butler, K. T.; Kieslich, G. *J. Am. Chem. Soc.* **2019**, *141*, 10504–10509, Publisher: American Chemical Society.

[129] Redfern, L. R.; Ducamp, M.; Wasson, M. C.; Robison, L.; Son, F. A.; Coudert, F.-X.; Farha, O. K. *Chemistry of Materials* **2020**, *32*, 5864–5871, Publisher: American Chemical Society.

[130] Lock, N.; Wu, Y.; Christensen, M.; Cameron, L. J.; Peterson, V. K.; Bridgeman, A. J.; Kepert, C. J.; Iversen, B. B. *The Journal of Physical Chemistry C* **2010**, *114*, 16181–16186, Publisher: American Chemical Society.

[131] Brozek, C. K.; Dincă, M. *Chemical Society Reviews* **2014**, *43*, 5456–5467, Publisher: The Royal Society of Chemistry.

[132] Brozek, C. K.; Dincă, M. *Chemical Science* **2012**, *3*, 2110–2113, Publisher: The Royal Society of Chemistry.

[133] Brozek, C. K.; Bellarosa, L.; Soejima, T.; Clark, T. V.; López, N.; Dincă, M. *Chemistry – A European Journal* **2014**, *20*, 6871–6874, _eprint: https://onlinelibrary.wiley.com/doi/pdf/10.1002/chem.201402682.

[134] Takaishi, S.; DeMarco, E. J.; Pellin, M. J.; Farha, O. K.; Hupp, J. T. *Chemical Science* **2013**, *4*, 1509–1513, Publisher: The Royal Society of Chemistry.

[135] Cohen, S. M. *Journal of the American Chemical Society* **2017**, *139*, 2855–2863, Publisher: American Chemical Society.

[136] Leus, K.; Muylaert, I.; Vandichel, M.; Marin, G. B.; Waroquier, M.; Speybroeck, V. V.; Voort, P. V. D. *Chemical Communications* **2010**, *46*, 5085–5087, Publisher: The Royal Society of Chemistry.

[137] Bode, S.; Zedler, L.; Schacher, F. H.; Dietzek, B.; Schmitt, M.; Popp, J.; Hager, M. D.; Schubert, U. S. *Advanced Materials* **2013**, *25*, 1634–1638, _eprint: https://onlinelibrary.wiley.com/doi/pdf/10.1002/adma.201203865.

[138] Shen, Y. C.; Upadhya, P. C.; Linfield, E. H.; Davies, A. G. *Applied Physics Letters* **2003**, *82*, 2350–2352, Publisher: American Institute of Physics.

[139] Chakravarty, C.; Debenedetti, P. G.; Stillinger, F. H. *The Journal of Chemical Physics* **2007**, *126*, 204508, Publisher: American Institute of Physics.

[140] Leong, W. L.; Vittal, J. J. *Chemical Reviews* **2011**, *111*, 688–764, Publisher: American Chemical Society.

[141] Gosselin, A. J.; Rowland, C. A.; Bloch, E. D. *Chemical Reviews* **2020**, *120*, 8987–9014, Publisher: American Chemical Society.

[142] Cooper, A. I. *ACS Central Science* **2017**, *3*, 544–553, Publisher: American Chemical Society.

[143] Tiana, D.; Hendon, C. H.; Walsh, A. *Chemical Communications* **2014**, *50*, 13990–13993, Publisher: The Royal Society of Chemistry.

[144] Lee, S.; Bürgi, H.-B.; Alshmimri, S. A.; Yaghi, O. M. *Journal of the American Chemical Society* **2018**, *140*, 8958–8964, Publisher: American Chemical Society.

[145] Rodríguez-Velamazán, J. A.; González, M. A.; Real, J. A.; Castro, M.; Muñoz, M. C.; Gaspar, A. B.; Ohtani, R.; Ohba, M.; Yoneda, K.; Hijikata, Y.; Yanai, N.; Mizuno, M.; Ando, H.; Kitagawa, S. *Journal of the American Chemical Society* **2012**, *134*, 5083–5089, Publisher: American Chemical Society.

[146] Perdew, J. P.; Burke, K.; Ernzerhof, M. *Phys. Rev. Lett.* **1996**, *77*, 3865–3868.

[147] Blöchl, P. E. *Physical Review B* **1994**, *50*, 17953–17979, Publisher: American Physical Society.

[148] Krukau, A. V.; Vydrov, O. A.; Izmaylov, A. F.; Scuseria, G. E. *The Journal of Chemical Physics* **2006**, *125*, 224106, Publisher: American Institute of Physics.

[149] Sirenko, A. A.; Bernhard, C.; Golnik, A.; Clark, A. M.; Hao, J.; Si, W.; Xi, X. X. *Nature* **2000**, *404*, 373–376, Number: 6776 Publisher: Nature Publishing Group.

[150] Zhou, J.-J.; Hellman, O.; Bernardi, M. *Physical Review Letters* **2018**, *121*, 226603, Publisher: American Physical Society.

[151] Hoffman, A. E. J.; Wieme, J.; Rogge, S. M. J.; Vanduyfhuys, L.; Speybroeck, V. V. *Zeitschrift für Kristallographie - Crystalline Materials* **2019**, *234*, 529–545, Publisher: Oldenbourg Wissenschaftsverlag.

[152] Liu, L.; Li, L.; Ziebel, M. E.; Harris, T. D. *Journal of the American Chemical Society* **2020**, *142*, 4705–4713, Publisher: American Chemical Society.

[153] Morabito, J. V.; Chou, L.-Y.; Li, Z.; Manna, C. M.; Petroff, C. A.; Kyada, R. J.; Palomba, J. M.; Byers, J. A.; Tsung, C.-K. *Journal of the American Chemical Society* **2014**, *136*, 12540–12543, Publisher: American Chemical Society.

[154] Rimmer, L. H. N.; Dove, M. T.; Goodwin, A. L.; Palmer, D. C. *Physical Chemistry Chemical Physics* **2014**, *16*, 21144–21152, Publisher: The Royal Society of Chemistry.

[155] Balestra, S. R. G.; Bueno-Perez, R.; Hamad, S.; Dubbeldam, D.; Ruiz-Salvador, A. R.; Calero, S. *Chemistry of Materials* **2016**, *28*, 8296–8304, Publisher: American Chemical Society.

[156] Nicolazzi, W.; Bousseksou, A. *Comptes Rendus Chimie* **2018**, *21*, 1060–1074.

[157] Takahashi, K. *Inorganics* **2018**, *6*, 32, Number: 1 Publisher: Multidisciplinary Digital Publishing Institute.

[158] Kitazawa, T. *Crystals* **2019**, *9*, 382, Number: 8 Publisher: Multidisciplinary Digital Publishing Institute.

[159] Gütlich, P.; Hauser, A.; Spiering, H. *Angewandte Chemie International Edition in English* **1994**, *33*, 2024–2054, _eprint: https://onlinelibrary.wiley.com/doi/pdf/10.1002/anie.199420241.

[160] Gütlich, P., Goodwin, H., Eds. *Spin Crossover in Transition Metal Compounds I*; Topics in Current Chemistry; Springer: Berlin, Heidelberg, 2004; Vol. 233.

[161] Halcrow, M. A. *Spin-Crossover Materials: Properties and Applications*; John Wiley & Sons, 2013; Google-Books-ID: BC8OmFkLWLwC.

[162] Chorazy, S.; Charytanowicz, T.; Pinkowicz, D.; Wang, J.; Nakabayashi, K.; Klimke, S.; Renz, F.; Ohkoshi, S.-i.; Sieklucka, B. *Angewandte Chemie International Edition* **2020**, *59*, 15741–15749, _eprint: https://onlinelibrary.wiley.com/doi/pdf/10.1002/anie.202007327.

[163] Kahn, O. *Current Opinion in Solid State and Materials Science* **1996**, *1*, 547–554.

[164] Valverde-Muñoz, F. J.; Kazan, R.; Boukheddaden, K.; Ohba, M.; Real, J. A.; Delgado, T. *Inorganic Chemistry* **2021**, *60*, 8851–8860, Publisher: American Chemical Society.

[165] Ohtani, R.; Yoneda, K.; Furukawa, S.; Horike, N.; Kitagawa, S.; Gaspar, A. B.; Muñoz, M. C.; Real, J. A.; Ohba, M. *Journal of the American Chemical Society* **2011**, *133*, 8600–8605, Publisher: American Chemical Society.

[166] Kitazawa, T.; Gomi, Y.; Takahashi, M.; Takeda, M.; Enomoto, M.; Miyazaki, A.; Enoki, T. *Journal of Materials Chemistry* **1996**, *6*, 119–121, Publisher: The Royal Society of Chemistry.

[167] Southon, P. D.; Liu, L.; Fellows, E. A.; Price, D. J.; Halder, G. J.; Chapman, K. W.; Moubaraki, B.; Murray, K. S.; Létard, J.-F.; Kepert, C. J. *Journal of the American Chemical Society* **2009**, *131*, 10998–11009, Publisher: American Chemical Society.

[168] Sciortino, N. F.; Scherl-Gruenwald, K. R.; Chastanet, G.; Halder, G. J.; Chapman, K. W.; Létard, J.-F.; Kepert, C. J. *Angewandte Chemie International Edition* **2012**, *51*, 10154–10158, _eprint: https://onlinelibrary.wiley.com/doi/pdf/10.1002/anie.201204387.

[169] Zenere, K. A.; Duyker, S. G.; Trzop, E.; Collet, E.; Chan, B.; Doheny, P. W.; Kepert, C. J.; Neville, S. M. *Chemical Science* **2018**, *9*, 5623–5629, Publisher: The Royal Society of Chemistry.

[170] Sciortino, N. F.; Neville, S. M.; Létard, J.-F.; Moubaraki, B.; Murray, K. S.; Kepert, C. J. *Inorganic Chemistry* **2014**, *53*, 7886–7893, Publisher: American Chemical Society.

[171] Kosaka, W.; Nomura, K.; Hashimoto, K.; Ohkoshi, S.-i. *Journal of the American Chemical Society* **2005**, *127*, 8590–8591, Publisher: American Chemical Society.

[172] Boström, H. L. B.; Cairns, A. B.; Liu, L.; Lazor, P.; Collings, I. E. *Dalton Transactions* **2020**, *49*, 12940–12944, Publisher: The Royal Society of Chemistry.

[173] Grzywa, M.; Röß-Ohlenroth, R.; Muschielok, C.; Oberhofer, H.; Błachowski, A.; Żukrowski, J.; Vieweg, D.; von Nidda, H.-A. K.; Volkmer, D. *Inorganic Chemistry* **2020**, *59*, 10501–10511, Publisher: American Chemical Society.

[174] Ohnishi, S.; Sugano, S. *Journal of Physics C: Solid State Physics* **1981**, *14*, 39–55, Publisher: IOP Publishing.

[175] Zimmermann, R.; König, E. *Journal of Physics and Chemistry of Solids* **1977**, *38*, 779–788.

[176] Kambara, T. *The Journal of Chemical Physics* **1981**, *74*, 4557–4565, Publisher: American Institute of Physics.

[177] Sasaki, N.; Kambara, T. *Journal of Physics C: Solid State Physics* **1982**, *15*, 1035–1071, Publisher: IOP Publishing.

[178] Hauser, A.; Guetlich, P.; Spiering, H. *Inorganic Chemistry* **1986**, *25*, 4245–4248, Publisher: American Chemical Society.

[179] Slichter, C. P.; Drickamer, H. G. *The Journal of Chemical Physics* **1972**, *56*, 2142–2160, Publisher: American Institute of Physics.

[180] Sorai, M.; Seki, S. *Journal of Physics and Chemistry of Solids* **1974**, *35*, 555–570.

[181] Willenbacher, N.; Spiering, H. *Journal of Physics C: Solid State Physics* **1988**, *21*, 1423–1439, Publisher: IOP Publishing.

[182] Fabrizio, K.; Lazarou, K. A.; Payne, L. I.; Twight, L. P.; Golledge, S.; Hendon, C. H.; Brozek, C. K. *Journal of the American Chemical Society* **2021**, *143*, 12609–12621, Publisher: American Chemical Society.

[183] Gándara, F.; Uribe-Romo, F. J.; Britt, D. K.; Furukawa, H.; Lei, L.; Cheng, R.; Duan, X.; O'Keeffe, M.; Yaghi, O. M. *Chemistry – A European Journal* **2012**, *18*, 10595–10601, _eprint: https://onlinelibrary.wiley.com/doi/pdf/10.1002/chem.201103433.

[184] Grzywa, M.; Denysenko, D.; Hanss, J.; Scheidt, E.-W.; Scherer, W.; Weil, M.; Volkmer, D. *Dalton Transactions* **2012**, *41*, 4239–4248, Publisher: The Royal Society of Chemistry.

[185] Venkataraman, G. *Bulletin of Materials Science* **1979**, *1*, 129–170.

[186] Sanchis-Gual, R.; Torres-Cavanillas, R.; Coronado-Puchau, M.; Giménez-Marqués, M.; Coronado, E. *Journal of Materials Chemistry C* **2021**, *9*, 10811–10818, Publisher: The Royal Society of Chemistry.

[187] Brooker, S. *Chemical Society Reviews* **2015**, *44*, 2880–2892, Publisher: The Royal Society of Chemistry.

[188] Shen, F.-X.; Pi, Q.; Shi, L.; Shao, D.; Li, H.-Q.; Sun, Y.-C.; Wang, X.-Y. *Dalton Transactions* **2019**, *48*, 8815–8825, Publisher: The Royal Society of Chemistry.

[189] Kepenekian, M.; Le Guennic, B.; Robert, V. *Physical Review B* **2009**, *79*, 094428, Publisher: American Physical Society.

[190] Torres-Cavanillas, R.; Sanchis-Gual, R.; Dugay, J.; Coronado-Puchau, M.; Giménez-Marqués, M.; Coronado, E. *Advanced Materials* **2019**, *31*, 1900039, _eprint: https://onlinelibrary.wiley.com/doi/pdf/10.1002/adma.201900039.

[191] Forestier, T.; Kaiba, A.; Pechev, S.; Denux, D.; Guionneau, P.; Etrillard, C.; Daro, N.; Freysz, E.; Létard, J.-F. *Chemistry – A European Journal* **2009**, *15*, 6122–6130, _eprint: https://onlinelibrary.wiley.com/doi/pdf/10.1002/chem.200900297.

[192] Boldog, I.; Gaspar, A. B.; Martínez, V.; Pardo-Ibañez, P.; Ksenofontov, V.; Bhattacharjee, A.; Gütlich, P.; Real, J. A. *Angewandte Chemie International Edition* **2008**, *47*, 6433–6437, _eprint: https://onlinelibrary.wiley.com/doi/pdf/10.1002/anie.200801673.

[193] Larionova, J.; Salmon, L.; Guari, Y.; Tokarev, A.; Molvinger, K.; Molnár, G.; Bousseksou, A. *Angewandte Chemie International Edition* **2008**, *47*, 8236–8240, _eprint: https://onlinelibrary.wiley.com/doi/pdf/10.1002/anie.200802906.

[194] Coronado, E.; Galán-Mascarós, J. R.; Monrabal-Capilla, M.; García-Martínez, J.; Pardo-Ibáñez, P. *Advanced Materials* **2007**, *19*, 1359–1361, _eprint: https://onlinelibrary.wiley.com/doi/pdf/10.1002/adma.200700559.

[195] Volatron, F.; Catala, L.; Rivière, E.; Gloter, A.; Stéphan, O.; Mallah, T. *Inorganic Chemistry* **2008**, *47*, 6584–6586, Publisher: American Chemical Society.

[196] Kroeber, J.; Audiere, J.-P.; Claude, R.; Codjovi, E.; Kahn, O.; Haasnoot, J. G.; Groliere, F.; Jay, C.; Bousseksou, A. *Chemistry of Materials* **1994**, *6*, 1404–1412, Publisher: American Chemical Society.

[197] Cheetham, A. K.; Rao, C. N. R.; Feller, R. K. *Chem. Commun.* **2006**, 4780–4795.

[198] Chae, H. K.; Siberio-Pérez, D. Y.; Kim, J.; Go, Y.; Eddaoudi, M.; Matzger, A. J.; O'Keeffe, M.; Yaghi, O. M. *Nature* **2004**, *427*, 523–527.

[199] Furukawa, H.; Cordova, K. E.; O'Keeffe, M.; Yaghi, O. M. *Science* **2013**, *341*, 1230444.

[200] N, N.; Maity, K.; Saha, S. *Elaboration and Applications of Metal-organic Frameworks*; 2018; pp 655–686.

[201] Mancuso, J. L.; Mroz, A. M.; Le, K. N.; Hendon, C. H. *Chem. Rev.* **2020**, *120*, 8641–8715.

[202] Zhang, X.; Dong, P.; Song, M.-K. *Batteries & Supercaps* **2019**, *2*, 591–626.

[203] Spoerke, E. D.; Small, L. J.; Foster, M. E.; Wheeler, J.; Ullman, A. M.; Stavila, V.; Rodriguez, M.; Allendorf, M. D. *J. Phys. Chem. C* **2017**, *121*, 4816–4824.

[204] Zhang, H.; Liu, X.; Wu, Y.; Guan, C.; K. Cheetham, A.; Wang, J. *Chemical Communications* **2018**, *54*, 5268–5288.

[205] Fang, X.; Zong, B.; Mao, S. *Nano-Micro Lett.* **2018**, *10*, 64.

[206] Walsh, A.; Butler, K. T.; Hendon, C. H. *MRS Bulletin* **2016**, *41*, 870–876.

[207] Hendon, C. H.; Walsh, A.; Dincă, M. *Inorganic Chemistry* **2016**, *55*, 7265–7269, Publisher: American Chemical Society.

[208] Lin, S.; M. Usov, P.; J. Morris, A. *Chemical Communications* **2018**, *54*, 6965–6974.

[209] Ahrenholtz, S. R.; Epley, C. C.; Morris, A. J. *J. Am. Chem. Soc.* **2014**, *136*, 2464–2472.

[210] Sun, L.; Hendon, C. H.; Park, S. S.; Tulchinsky, Y.; Wan, R.; Wang, F.; Walsh, A.; Dincă, M. *Chem. Sci.* **2017**, *8*, 4450–4457.

[211] Sun, L.; Liao, B.; Sheberla, D.; Kraemer, D.; Zhou, J.; Stach, E. A.; Zakharov, D.; Stavila, V.; Talin, A. A.; Ge, Y.; Allendorf, M. D.; Chen, G.; Léonard, F.; Dincă, M. *Joule* **2017**, *1*, 168–177.

[212] Dou, J.-H.; Sun, L.; Ge, Y.; Li, W.; Hendon, C. H.; Li, J.; Gul, S.; Yano, J.; Stach, E. A.; Dincă, M. *J. Am. Chem. Soc.* **2017**, *139*, 13608–13611.

[213] Foster, M. E.; Sohlberg, K.; Spataru, C. D.; Allendorf, M. D. *J. Phys. Chem. C* **2016**, *120*, 15001–15008.

[214] Foster, M. E.; Sohlberg, K.; Allendorf, M. D.; Talin, A. A. *J. Phys. Chem. Lett.* **2018**, *9*, 481–486.

[215] Shi, Y.-X.; Li, W.-X.; Zhang, W.-H.; Lang, J.-P. *Inorg. Chem.* **2018**, *57*, 8627–8633.

[216] Krause, S.; Bon, V.; Senkovska, I.; Többens, D. M.; Wallacher, D.; Pillai, R. S.; Maurin, G.; Kaskel, S. *Nat Commun* **2018**, *9*, 1–8.

[217] Jiang, K.; Zhang, L.; Hu, Q.; Zhao, D.; Xia, T.; Lin, W.; Yang, Y.; Cui, Y.; Yang, Y.; Qian, G. *Journal of Materials Chemistry B* **2016**, *4*, 6398–6401.

[218] Moggach, S. A.; Bennett, T. D.; Cheetham, A. K. *Angewandte Chemie* **2009**, *121*, 7221–7223.

[219] Hu, Y. H.; Zhang, L. *Phys. Rev. B* **2010**, *81*, 174103.

[220] Ortiz, A. U.; Boutin, A.; Fuchs, A. H.; Coudert, F.-X. *J Chem Phys* **2013**, *138*, 174703.

[221] Young Jung, J.; Karadas, F.; Zulfiqar, S.; Deniz, E.; Aparicio, S.; Atilhan, M.; T. Yavuz, C.; Min Han, S. *Physical Chemistry Chemical Physics* **2013**, *15*, 14319–14327.

[222] Graham, A. J.; Allan, D. R.; Muszkiewicz, A.; Morrison, C. A.; Moggach, S. A. *Angewandte Chemie International Edition* **2011**, *50*, 11138–11141.

[223] Hendon, C. H.; Wittering, K. E.; Chen, T.-H.; Kaveevivitchai, W.; Popov, I.; Butler, K. T.; Wilson, C. C.; Cruickshank, D. L.; Miljanić, O. ; Walsh, A. *Nano Lett.* **2015**, *15*, 2149–2154.

[224] Hoffmann, R. *Angew. Chem. Int. Ed. Engl.* **1987**, *26*, 846–878.

[225] Xu, M.; Xiao, P.; Stauffer, S.; Song, J.; Henkelman, G.; Goodenough, J. B. *Chem. Mater.* **2014**, *26*, 3089–3097.

[226] Kresse, G.; Furthmüller, J. *Phys. Rev. B* **1996**, *54*, 11169–11186.

[227] Perdew, J. P.; Ruzsinszky, A.; Csonka, G. I.; Vydrov, O. A.; Scuseria, G. E.; Constantin, L. A.; Zhou, X.; Burke, K. *Phys. Rev. Lett.* **2008**, *100*, 136406.

[228] Kumar, A.; Banerjee, K.; Foster, A. S.; Liljeroth, P. *Nano Lett.* **2018**, *18*, 5596–5602.

[229] Tang, W.; Sanville, E.; Henkelman, G. *J. Phys.: Condens. Matter* **2009**, *21*, 084204.

[230] Schoedel, A.; Yaghi, O. M. *Macrocyclic and Supramolecular Chemistry*; John Wiley & Sons, Ltd, 2016; pp 200–219, Section: 9 _eprint: https://onlinelibrary.wiley.com/doi/pdf/10.1002/9781119053859.ch9.

[231] Li, J.-R.; Sculley, J.; Zhou, H.-C. *Chemical Reviews* **2012**, *112*, 869–932, Publisher: American Chemical Society.

[232] Ghanbari, T.; Abnisa, F.; Wan Daud, W. M. A. *Science of The Total Environment* **2020**, *707*, 135090.

[233] Petit, C. *Current Opinion in Chemical Engineering* **2018**, *20*, 132–142.

[234] Liu, L.; Corma, A. *Nature Reviews Materials* **2021**, *6*, 244–263, Number: 3 Publisher: Nature Publishing Group.

[235] Kung, C.-W.; Han, P.-C.; Chuang, C.-H.; Wu, K. C.-W. *APL Materials* **2019**, *7*, 110902, Publisher: American Institute of Physics.

[236] Degaga, G. D.; Pandey, R.; Gupta, C.; Bharadwaj, L. *RSC Adv.* **2019**, *9*, 14260–14267.

[237] Bueken, B.; Van Velthoven, N.; Krajnc, A.; Smolders, S.; Taulelle, F.; Mellot-Draznieks, C.; Mali, G.; Bennett, T. D.; De Vos, D. *Chemistry of Materials* **2017**, *29*, 10478–10486, Publisher: American Chemical Society.

[238] Dissegna, S.; Epp, K.; Heinz, W. R.; Kieslich, G.; Fischer, R. A. *Advanced Materials* **2018**, *30*, 1704501, _eprint: https://onlinelibrary.wiley.com/doi/pdf/10.1002/adma.201704501.

[239] Xie, L. S.; Skorupskii, G.; Dincă, M. *Chem. Rev.* **2020**, *120*, 8536–8580.

[240] Hendon, C. H.; Rieth, A. J.; Korzyński, M. D.; Dincă, M. *ACS Cent. Sci.* **2017**, *3*, 554–563, Publisher: American Chemical Society.

[241] Clough, A. J.; Orchanian, N. M.; Skelton, J. M.; Neer, A. J.; Howard, S. A.; Downes, C. A.; Piper, L. F. J.; Walsh, A.; Melot, B. C.; Marinescu, S. C. *J. Am. Chem. Soc.* **2019**, *141*, 16323–16330.

[242] Bhardwaj, S. K.; Bhardwaj, N.; Kaur, R.; Mehta, J.; Sharma, A. L.; Kim, K.-H.; Deep, A. *J. Mater. Chem. A* **2018**, *6*, 14992–15009.

[243] Nguyen, D. K.; Schepisi, I. M.; Amir, F. Z. *Chemical Engineering Journal* **2019**, *378*, 122150.

[244] Dong, R.; Zhang, Z.; Tranca, D.; Zhou, S.; Wang, M.; Adler, P.; Liao, Z.; Liu, F.; Sun, Y.; Shi, W.; Zhang, Z.; Zschech, E.; Mannsfeld, S.; Felser, C.; Feng, X. *Nature Communications* **2018**, *9*.

[245] Kim, K. K.; Kim, S. M.; Lee, Y. H. *Acc. Chem. Res.* **2016**, *49*, 390–399, Publisher: American Chemical Society.

[246] Dou, J.-H. et al. *Nature Materials* **2021**, *20*, 222–228, Number: 2 Publisher: Nature Publishing Group.

[247] Day, R. W.; Bediako, D. K.; Rezaee, M.; Parent, L. R.; Skorupskii, G.; Arguilla, M. Q.; Hendon, C. H.; Stassen, I.; Gianneschi, N. C.; Kim, P.; Dincă, M. *ACS Cent. Sci.* **2019**, *5*, 1959–1964, Publisher: American Chemical Society.

[248] Stassen, I.; Dou, J.-H.; Hendon, C.; Dincă, M. *ACS Cent. Sci.* **2019**, *5*, 1425–1431, Publisher: American Chemical Society.

[249] Yang, L.; He, X.; Dincă, M. *J. Am. Chem. Soc.* **2019**, *141*, 10475–10480, Publisher: American Chemical Society.

[250] Chen, S.; Dai, J.; Zeng, X. C. *Phys. Chem. Chem. Phys.* **2015**, *17*, 5954–5958, Publisher: The Royal Society of Chemistry.

[251] Sun, F.; Chen, X. *Electrochemistry Communications* **2017**, *82*, 89–92.

[252] Miner, E. M.; Fukushima, T.; Sheberla, D.; Sun, L.; Surendranath, Y.; Dincă, M. *Nature Communications* **2016**, *7*, 10942, Number: 1 Publisher: Nature Publishing Group.

[253] He, Y.; Talin, A. A.; Allendorf, M. D. *ECS J. Solid State Sci. Technol.* **2017**, *6*, N236, Publisher: IOP Publishing.

[254] You Tie, D.; Chen, Z. *RSC Advances* **2015**, *5*, 55186–55190, Publisher: Royal Society of Chemistry.

[255] Murase, R.; Leong, C. F.; D'Alessandro, D. M. *Inorg. Chem.* **2017**, *56*, 14373–14382.

[256] Foster, M. E.; Sohlberg, K.; Spataru, C. D.; Allendorf, M. D. *J. Phys. Chem. C* **2016**, *120*, 15001–15008.

[257] Karagiaridi, O.; Bury, W.; Tylianakis, E.; Sarjeant, A. A.; Hupp, J. T.; Farha, O. K. *Chem. Mater.* **2013**, *25*, 3499–3503, Publisher: American Chemical Society.

[258] Karagiaridi, O.; Bury, W.; Mondloch, J. E.; Hupp, J. T.; Farha, O. K. *Angewandte Chemie International Edition* **2014**, *53*, 4530–4540, _eprint: https://onlinelibrary.wiley.com/doi/pdf/10.1002/anie.201306923.

[259] Schneider, C.; Bodesheim, D.; Keupp, J.; Schmid, R.; Kieslich, G. *Nature Communications* **2019**, *10*, 4921, Number: 1 Publisher: Nature Publishing Group.

[260] Kapustin, E. A.; Lee, S.; Alshammari, A. S.; Yaghi, O. M. *ACS Cent. Sci.* **2017**, *3*, 662–667, Publisher: American Chemical Society.

[261] Siemensmeyer, K.; Peeples, C. A.; Tholen, P.; Schmitt, F.-J.; Çoşut, B.; Hanna, G.; Yücesan, G. *Advanced Materials* **2020**, *32*, 2000474, _eprint: https://onlinelibrary.wiley.com/doi/pdf/10.1002/adma.202000474.

[262] Kawamura, A.; Greenwood, A. R.; Filatov, A. S.; Gallagher, A. T.; Galli, G.; Anderson, J. S. *Inorg. Chem.* **2017**, *56*, 3349–3356.

[263] Ha, H.; Kim, Y.; Kim, D.; Lee, J.; Song, Y.; Kim, S.; Park, M. H.; Kim, Y.; Kim, H.; Yoon, M.; Kim, M. *Chemistry – A European Journal* **2019**, *25*, 14414–14420, _eprint: https://chemistry-europe.onlinelibrary.wiley.com/doi/pdf/10.1002/chem.201903210.

[264] A. Manz, T. *RSC Advances* **2017**, *7*, 45552–45581, Publisher: Royal Society of Chemistry.

[265] Férey, G.; Mellot-Draznieks, C.; Serre, C.; Millange, F.; Dutour, J.; Surblé, S.; Margiolaki, I. *Science* **2005**, *309*, 2040–2042, Publisher: American Association for the Advancement of Science.

[266] Aziz, A.; Ruiz-Salvador, A. R.; Hernández, N. C.; Calero, S.; Hamad, S.; Grau-Crespo, R. *Journal of Materials Chemistry A* **2017**, *5*, 11894–11904, Publisher: The Royal Society of Chemistry.

[267] Yaghi, O. M.; Sun, Z.; Richardson, D. A.; Groy, T. L. *Journal of the American Chemical Society* **1994**, *116*, 807–808, Publisher: American Chemical Society.

[268] Rangan, K. K.; Billinge, S. J. L.; Petkov, V.; Heising, J.; Kanatzidis, M. G. *Chemistry of Materials* **1999**, *11*, 2629–2632, Publisher: American Chemical Society.

[269] Bag, S.; Kanatzidis, M. G. *Journal of the American Chemical Society* **2010**, *132*, 14951–14959, Publisher: American Chemical Society.

[270] Bag, S.; Kanatzidis, M. G. *Journal of the American Chemical Society* **2008**, *130*, 8366–8376, Publisher: American Chemical Society.

[271] Haddadpour, S.; Melullis, M.; Staesche, H.; Mariappan, C. R.; Roling, B.; Clérac, R.; Dehnen, S. *Inorganic Chemistry* **2009**, *48*, 1689–1698, Publisher: American Chemical Society.

[272] Rangan, K. K.; Trikalitis, P. N.; Kanatzidis, M. G. *Journal of the American Chemical Society* **2000**, *122*, 10230–10231, Publisher: American Chemical Society.

[273] MacLachlan, M. J.; Coombs, N.; Bedard, R. L.; White, S.; Thompson, L. K.; Ozin, G. A. *Journal of the American Chemical Society* **1999**, *121*, 12005–12017, Publisher: American Chemical Society.

[274] Zhang, J.; Bu, X.; Feng, P.; Wu, T. *Accounts of Chemical Research* **2020**, *53*, 2261–2272, Publisher: American Chemical Society.

[275] MacLachlan, M. J.; Coombs, N.; Ozin, G. A. *Nature* **1999**, *397*, 681–684, Number: 6721 Publisher: Nature Publishing Group.

[276] Tsamourtzi, K.; Song, J.-H.; Bakas, T.; Freeman, A. J.; Trikalitis, P. N.; Kanatzidis, M. G. *Inorganic Chemistry* **2008**, *47*, 11920–11929, Publisher: American Chemical Society.

[277] Bowes, C. L.; Lough, A. J.; Malek, A.; Ozin, G. A.; Petrov, S.; Young, D. *Chemische Berichte* **1996**, *129*, 283–287, _eprint: https://onlinelibrary.wiley.com/doi/pdf/10.1002/cber.19961290307.

[278] Trikalitis, P. N.; Rangan, K. K.; Bakas, T.; Kanatzidis, M. G. *Nature* **2001**, *410*, 671–675, Number: 6829 Publisher: Nature Publishing Group.

[279] Duchardt, M.; Haddadpour, S.; Kaib, T.; Bron, P.; Roling, B.; Dehnen, S. *Inorganic Chemistry* **2021**, *60*, 5224–5231, Publisher: American Chemical Society.

[280] Ahari, H.; Garcia, A.; Kirkby, S.; Ozin, G. A.; Young, D.; Lough, A. J. *Journal of the Chemical Society, Dalton Transactions* **1998**, 2023–2028, Publisher: The Royal Society of Chemistry.

[281] Mas-Ballesté, R.; Gómez-Navarro, C.; Gómez-Herrero, J.; Zamora, F. *Nanoscale* **2011**, *3*, 20–30, Publisher: The Royal Society of Chemistry.

[282] Li, Y.; Jiang, X.; Fu, Z.; Huang, Q.; Wang, G.-E.; Deng, W.-H.; Wang, C.; Li, Z.; Yin, W.; Chen, B.; Xu, G. *Nature Communications* **2020**, *11*, 261, Number: 1 Publisher: Nature Publishing Group.

[283] Levesanos, N.; Liyanage, W. P. R.; Ferentinos, E.; Raptopoulos, G.; Paraskevopoulou, P.; Sanakis, Y.; Choudhury, A.; Stavropoulos, P.; Nath, M.; Kyritsis, P. *European Journal of Inorganic Chemistry* **2016**, *2016*, 5332–5339, _eprint: https://onlinelibrary.wiley.com/doi/pdf/10.1002/ejic.201600833.

[284] Shuai, Z.; Li, W.; Ren, J.; Jiang, Y.; Geng, H. *The Journal of Chemical Physics* **2020**, *153*, 080902, Publisher: American Institute of Physics.

[285] Wilbourn, K.; Murray, R. W. *The Journal of Physical Chemistry* **1988**, *92*, 3642–3648, Publisher: American Chemical Society.

[286] Feldman, B. J.; Burgmayer, P.; Murray, R. W. *Journal of the American Chemical Society* **1985**, *107*, 872–878, Publisher: American Chemical Society.

[287] Sun, L.; Hendon, C. H.; Park, S. S.; Tulchinsky, Y.; Wan, R.; Wang, F.; Walsh, A.; Dincă, M. *Chem. Sci.* **2017**, *8*, 4450–4457.

[288] Xie, L. S.; Sun, L.; Wan, R.; Park, S. S.; DeGayner, J. A.; Hendon, C. H.; Dincă, M. *J. Am. Chem. Soc.* **2018**, *140*, 7411–7414.

[289] Sun, L.; Hendon, C. H.; Minier, M. A.; Walsh, A.; Dincă, M. *Journal of the American Chemical Society* **2015**, *137*, 6164–6167, Publisher: American Chemical Society.

[290] Park, J. G.; Aubrey, M. L.; Oktawiec, J.; Chakarawet, K.; Darago, L. E.; Grandjean, F.; Long, G. J.; Long, J. R. *J. Am. Chem. Soc.* **2018**, *140*, 8526–8534.

[291] DeGayner, J. A.; Jeon, I.-R.; Sun, L.; Dincă, M.; Harris, T. D. *Journal of the American Chemical Society* **2017**, *139*, 4175–4184, Publisher: American Chemical Society.

[292] Huang, X.; Zhang, S.; Liu, L.; Yu, L.; Chen, G.; Xu, W.; Zhu, D. *Angewandte Chemie International Edition* **2018**, *57*, 146–150, _eprint: https://onlinelibrary.wiley.com/doi/pdf/10.1002/anie.201707568.

[293] Clough, A. J.; Skelton, J. M.; Downes, C. A.; de la Rosa, A. A.; Yoo, J. W.; Walsh, A.; Melot, B. C.; Marinescu, S. C. *Journal of the American Chemical Society* **2017**, *139*, 10863–10867, Publisher: American Chemical Society.

[294] Chen, L.; San, K. A.; Turo, M. J.; Gembicky, M.; Fereidouni, S.; Kalaj, M.; Schimpf, A. M. *Journal of the American Chemical Society* **2019**, *141*, 20261–20268, Publisher: American Chemical Society.

[295] Wang, J.; Zhao, L.; Gong, K. *Journal of Magnetism and Magnetic Materials* **2008**, *320*, 1696–1699.

[296] Conradie, J. *Inorganica Chimica Acta* **2019**, *486*, 193–199.

[297] Echigo, T.; Kimata, M. *Phys Chem Minerals* **2008**, *35*, 467.

[298] Zhang, X.; Lawson Daku, M. L.; Zhang, J.; Suarez-Alcantara, K.; Jennings, G.; Kurtz, C. A.; Canton, S. E. *J. Phys. Chem. C* **2015**, *119*, 3312–3321, Publisher: American Chemical Society.

[299] Le, K. N.; Hendon, C. H. *Phys. Chem. Chem. Phys.* **2019**,

[300] Jain, A.; Hautier, G.; Ong, S. P.; Moore, C. J.; Fischer, C. C.; Persson, K. A.; Ceder, G. *Phys. Rev. B* **2011**, *84*, 045115, Publisher: American Physical Society.

[301] Cococcioni, M.; de Gironcoli, S. *Phys. Rev. B* **2005**, *71*, 035105, Publisher: American Physical Society.

[302] Mano, N. *Current Opinion in Electrochemistry* **2020**, *19*, 8–13.

[303] Sharma, V.; Singh, I.; Chandra, A. *Scientific Reports* **2018**, *8*, 1307, Number: 1 Publisher: Nature Publishing Group.

[304] Sharma, V.; Biswas, S.; Chandra, A. *Advanced Energy Materials* **2018**, *8*, 1800573, _eprint: https://onlinelibrary.wiley.com/doi/pdf/10.1002/aenm.201800573.

[305] Zhu, Z.; Jiang, H.; Guo, S.; Cheng, Q.; Hu, Y.; Li, C. *Scientific Reports* **2015**, *5*, 15936, Number: 1 Publisher: Nature Publishing Group.

[306] Xing, L.; Dong, Y.; Hu, F.; Wu, X.; Umar, A. *Dalton Transactions* **2018**, *47*, 5687–5694, Publisher: The Royal Society of Chemistry.

[307] Li, H.; Guo, H.; Huang, K.; Liu, B.; Zhang, C.; Chen, X.; Xu, X.; Yang, J. *Applied Physics A* **2018**, *124*, 763.

[308] Choi, J. Y.; Flood, J.; Stodolka, M.; Pham, H. T. B.; Park, J. *ACS Nano* **2022**, *16*, 3145–3151, Publisher: American Chemical Society.